GFRP BARS IN CONCRETE TOWARD CORROSION-FREE RC STRUCTURES: BOND BEHAVIOR, CHARACTERIZATION, AND LONG-TERM DURABILITY PREDICTION

A Dissertation
Submitted to the Graduate Faculty
of the
North Dakota State University
of Civil and Environmental Engineering

By

Fei Yan

In Partial Fulfillment of the Requirements
for the Degree of
DOCTOR OF PHILOSOPHY

Major Department:
Civil and Environmental Engineering

November 2016

Fargo, North Dakota

North Dakota State University
Graduate School

Title

GFRP Bars in Concrete toward Corrosion-Free RC Structures: Bond Behavior, Characterization, and Long-Term Durability Prediction

By

Fei Yan

The Supervisory Committee certifies that this ***disquisition*** complies with North Dakota State University's regulations and meets the accepted standards for the degree of

DOCTOR OF PHILOSOPHY

SUPERVISORY COMMITTEE:

Dr. Zhibin Lin
Chair

Dr. Ying Huang

Dr. Mijia Yang

Dr. Fardad Azarmi

Dr. Jerry Gao

Dr. Long Jiang

Approved:

November 14, 2016
Date

Dr. Dinesh Katti
Department Chair

ABSTRACT

Corrosion of steel reinforcements is the leading causes of malfunction or even failures of reinforced concrete (RC) structures nationwide and worldwide for many decades. This arises up to substantial economic burden on repairs and rehabilitations to maintain and extend their service life of those RC public projects. The inherent natures of glass fiber-reinforced polymers (GFRP) bars, from their superior corrosion resistance to high strength-to-weight ratio, have promoted their acceptance as a viable alternative for steel reinforcement in civil infrastructures. Comprehensive understanding of the bond between GFRP bars and concrete, in particular under in-service conditions or extremely severe events, enables scientists and engineers to provide their proper design, assessment and long-term predictions, and ultimately to implement them toward the corrosion-free concrete products.

This research aims to develop a holistic framework through an experimental, analytical and numerical study to gain deep understanding of the bond mechanism, behavior, and its long-term durability under harsh environments. The bond behavior and failure modes of GFRP bar to concrete are investigated through the accelerated aging tests with various environmental conditions, including alkaline and/or saline solutions, freezing-thawing cycles. The damage evolution of the bond is formulated from Damage Mechanics, while detailed procedures using the Arrhenius law and time shift factor approach are developed to predict the long-term bond degradation over time. Besides, the machine learning techniques of the artificial neural network integrated with the genetic algorithm are used for bond strength prediction and anchorage reliability assessment.

Clearly, test data allow further calibration and verification of the analytical models and the finite element simulation. Bond damage evolution using the secant modulus of the bond-slip

curves could effectively evaluate the interface degradation against slip and further identify critical factors that affect the bond design and assessment under the limit states. Long-term prediction reveals that the moisture content and elevated temperature could impact the material degradation of GFRP bars, thereby affecting their service life. In addition, the new attempt of the Data-to-Information concept using the machine learning techniques could yield valuable insight into the bond strength prediction and anchorage reliability analysis for their applications in RC structures.

ACKNOWLEDGEMENTS

I fully acknowledge the financial support provided by ND NASA EPCoR (FAR0023941), ND NSF EPSCoR (FAR0022364) and US DOT (FAR0025913). The results, discussion, and opinions reflected in this dissertation are those of the research team only and do not necessarily represent those of the sponsors.

First and foremost, I would like to thank my advisor, Dr. Zhibin Lin, who constantly and patiently passed on the valuable knowledge and skills to me, guiding me to become a better research scientist. I could always find him in his office whenever I met academic bottlenecks and cannot move forward on my research. He inspired me to be more scientific and rigorous on my Ph.D. study.

My sincere appreciation dedicates to my co-advisor, Dr. Ying Huang. The general advices you provided on my academic writing and publishing benefit me a lot and would contribute to the my future work.

I would like to express my gratitude to my doctoral committee who continuously challenged and encouraged me to explore more insightful research. Dr. Yang, Dr. Gao and Dr. Azarmi provided great help on the experimental study in this dissertation. The durability test cannot be implemented without your supports. I also appreciate Dr. Long Jiang, their feedback and suggestions helped me to develop a better dissertation.

Great thanks to my colleagues at North Dakota State University: Mingli Li, Xingyu Wang, Hong Pan, and Mohsen Azimi. Thank you for your contributions and help on the experimental study.

Special thanks to my family. I am incredibly grateful for you all who always support me along the way.

DEDICATION

To my parents, my brother, and my wife.

TABLE OF CONTENTS

ABSTRACT iii

ACKNOWLEDGEMENTS v

DEDICATION vi

LIST OF TABLES xv

LIST OF FIGURES xvii

LIST OF ABBREVIATIONS xxi

LIST OF SYMBOLS xxii

1. INTRODUCTION 1

1.1. Background 1

1.2. Problem Statement 5

1.2.1. Bond Behavior and Its Predictive Models 5

1.2.2. Bond Durability and Its Predictive Models 7

1.2.3. Bond Development Associated with Damage Evolution 10

1.2.4. Reliability Assessment for GFRP-Concrete Anchorage 10

1.3. Research Significance 11

1.4. Research Objectives 12

1.5. Organization of the Dissertation 14

1.6. References 16

2. LITERATURE REVIEW 22

2.1. Introduction 22

2.2. Bond Behavior and Modeling of GFRP Bars to Concrete 24

2.2.1. Bond Stress-Slip Behavior and Its Modeling 24

2.2.2. BPE and Modified BPE Models 25

2.2.3. Malvar's Model 27

2.2.4. CMR Model 28
2.2.5. Parameters Determined for the Existing Bond-Slip Models 28
2.2.6. Bond Strength Specified in Existing Design Provisions 31
2.2.6.1. ACI 440.1R-06 31
2.2.6.2. Canadian standards association 32
2.2.6.3. Canadian highway bridge design code 32
2.2.6.4. Japanese design code 33
2.2.6.5. Comparisons of national and international design specifications 34
2.3. Critical Factors and Their Impacts on Failure Modes and Bond Strength of GFRP Bars to Concrete 36
2.3.1. Failure Mode and Bond Strength Associated with Concrete Compressive Strength 36
2.3.1.1. Failure mode 36
2.3.1.2. Bond strength 37
2.3.2. Failure Mode and Bond Strength Associated with Concrete Cover 39
2.3.2.1. Failure mode 39
2.3.2.2. Bond strength 41
2.3.3. Failure Mode and Bond Strength Associated with Embedment Length 42
2.3.3.1. Failure mode 42
2.3.3.2. Bond strength 43
2.3.4. Failure Mode and Bond Strength Associated with Bar Diameter 45
2.3.4.1. Failure mode 45
2.3.4.2. Bond strength 45
2.3.5. Failure Mode and Bond Strength Associated with Bar Surface Conditions 46
2.3.5.1. Failure mode 46
2.3.5.2. Bond strength 47

2.3.6. Failure Mode and Bond Strength Associated with Enhancement of Concrete from Transverse Reinforcement 48

2.3.6.1. Enhancement from transverse reinforcement confinement 48

2.3.6.2. Enhancement from fiber-reinforced concrete matrix 49

2.3.7. Failure Mode and Bond Strength Associated with Bar Casting Position 50

2.4. Environmental Conditions and Their Impacts on Bond Behavior and Bond Strength of FRP Bars 50

2.4.1. Freeze-Thaw Cycles 50

2.4.2. Wet-Dry Cycles 52

2.4.3. Alkaline Solutions 53

2.4.4. High Temperatures 54

2.5. Conclusions 56

2.6. References 57

3. EXPERIMENTAL STUDY ON BOND DURABILITY OF GFRP BARS IN CONCRETE EXPOSED TO HARSH ENVIRONMENTAL AGENTS: FREEZE-THAW CYCLES AND ALKALINE-SALINE SOLUTIONS 70

3.1. Introduction 70

3.2. Background and Research to Date 71

3.2.1. Bond Durability 71

3.2.2. Statement of the Problem 73

3.3. Experimental Study 74

3.3.1. Sample Design 74

3.3.1.1. Material selection and sample size determination 74

3.3.1.2. Material properties 76

3.3.2. Environmental Aging Design 79

3.3.2.1. Freeze-thaw cycles 79

3.3.2.2. Alkaline-saline solutions 82

3.3.3. Pullout Test Design 82
3.4. Experimental Results and Discussion 83
3.4.1. Mode of Failure 85
3.4.2. Weight Loss 87
3.4.3. Relative Dynamic Modulus of Elasticity and Durability Factor 90
3.4.4. Bond Behavior and Durability 94
3.4.4.1. Bond stress-slip response 94
3.4.4.2. Bond strength and its corresponding slip 96
3.5. Calibration of Analytical Models Considering Environmental Effects 98
3.6. Conclusions 102
3.7. References 104
4. BOND DURABILITY ASSESSMENT AND LONG-TERM DEGRADATION PREDICTION FOR GFRP BARS TO FIBER-REINFORCED CONCRETE UNDER SALINE SOLUTIONS 109
4.1. Introduction 109
4.2. Experimental Program 112
4.2.1. Specimen Design 112
4.2.1.1. Statistical data 112
4.2.1.2. Materials 114
4.2.2. Environmental Aging Design 117
4.2.3. Pullout Test Design 118
4.3. Experimental Results and Discussion 119
4.3.1. Mode of Failure 121
4.3.2. Bond Stress-Slip Response 122
4.3.3. Adhesion Stress 124
4.3.4. Bond Strength 125

4.4. Calibration of Analytical Models Considering Environmental Effect 127
4.5. Prediction of Long-Term Bond Strength Degradation under Saline Environment 131
4.5.1. Arrhenius Relation and Time Shift Factor Method 131
4.5.2. Prediction Procedure 133
4.5.2.1. Evaluation of validity for the predictive models 133
4.5.2.2. Derivation of the time shift factor formula 135
4.5.2.3. Prediction of long-term bond strength retention 136
4.5.3. Application in Representative Cold and Warm Regions 138
4.6. Conclusions 139
4.7. References 141
5. BOND BEHAVIOR OF GFRP BAR-CONCRETE INTERFACE: DAMAGE EVOLUTION ASSESSMENT AND FE SIMULATION IMPLEMENTATIONS 146
5.1. Introduction 146
5.2. Bond Damage Evolution at the Bar-Concrete Interface 150
5.2.1. Analytical Models Accounting for FRP-Concrete Bond 150
5.2.2. Bond Damage Evolution Equations 152
5.3. Finite Element Modeling 154
5.3.1. Experimental Program Overview 155
5.3.2. Geometry Modeling 156
5.3.2.1. Finite element modeling simplifications 156
5.3.2.2. GFRP bar and concrete matrix 158
5.3.2.3. Bar-concrete interface 158
5.3.3. Material Modeling 159
5.3.3.1. GFPR bar 160
5.3.3.2. Concrete matrix 160
5.3.3.3. Bar-concrete interface 162

5.3.4. Boundary Conditions and Loading Conditions 163
5.3.5. Modeling Validation 164
5.3.5.1. Bond-slip relation in plain concrete 164
5.3.5.2. Bond-slip relation in fiber-reinforced concrete 166
5.4. Bond Damage Assessment 168
5.4.1. Damage Evolution Patterns 168
5.4.1.1. Plain concrete specimens 168
5.4.1.2. Fiber-reinforced concrete specimens 171
5.4.2. Critical Factors and Their Impacts on Damage Evolutions 173
5.4.2.1. Palin concrete specimens 173
5.4.2.2. Fiber-reinforced concrete specimens 175
5.5. Conclusions 176
5.6. References 178
6. EVALUATION AND PREDICTION OF BOND STRENGTH OF GFRP-BAR REINFORCED CONCRETE USING ARITIFICIAL NEURAL NETWORK AND GENETIC ALGORITHM 184
6.1. Introduction 184
6.2. Hybrid Modeling Strategy 187
6.2.1. Framework of Hybrid Modeling 187
6.2.2. Data Acquisition and Preprocessing 189
6.2.3. ANN Modeling for Bond Strength 190
6.2.3.1. Architecture and working principle of ANN 190
6.2.3.2. Training parameter settings 193
6.2.3.3. Performance assessment indices 194
6.2.4. ANN Optimized by GA 195
6.2.4.1. Synthesized working principle of ANN-GA 195

6.2.4.2. Parameters settings of GA 197
6.2.4.3. Fitness function 198
6.3. Bond Strength Prediction by Other Methods 199
6.3.1. Multi-nonlinear Regression 199
6.3.2. Design Equations 200
6.4. Modeling Applications 201
6.4.1. Database Creation and Data Preprocessing 201
6.4.2. Modeling Implementations 202
6.4.3. Performance Assessment 204
6.5. Conclusions 209
6.6. References 210
7. NEW STRATEGY FOR ANCHORAGE RELIABILITY ASSESSMENT OF GFRP BARS TO CONCRETE USING HYBRID ARTIFICIAL NEURAL NETWORK AND GENETIC ALGORITHM 215
7.1. Introduction 215
7.2. ANN-based Anchorage Reliability Assessment 217
7.2.1. Framework of ANN-based Anchorage Reliability Assessment 217
7.2.2. Data Selection and Processing 219
7.2.3. Performance Function Modeling for Anchorage Reliability 222
7.2.3.1. Performance function definition 222
7.2.3.2. Modeling performance function based on design standards 223
7.2.3.3. Modeling performance function based on the ANN and GA 224
7.2.3.4. Performance function prediction and validation 227
7.2.4. ANN-based Anchorage Reliability Assessment 231
7.2.4.1. ANN-based performance function derivation 231
7.2.4.2. ANN-based FOSM method 233

7.2.4.3. ANN-based MCS method 234
7.3. Implementation to GFRP Bar Anchorage Reliability Assessment 235
7.3.1. Target Reliability Index 235
7.3.2. Development Length Estimation 236
7.3.3. Reliability Index Estimation 239
7.3.3.1. Performance function modeling with the ANN-GA model 239
7.3.3.2. ANN-based FOSM method 240
7.3.3.3. ANN-based MCS method 243
7.4. Designed Graphical User Interface (GUI) System for FRP Bar Anchorage Reliability Assessment 243
7.5. Conclusions 245
7.6. References 246
8. CONCLUSIONS AND RECOMMENDATIONS 252
8.1. Conclusions 252
8.1.1. Durability Performance and Bond Degradation Prediction 252
8.1.1.1. Experimental investigation 252
8.1.1.2. Analytical investigation 253
8.1.2. Bond Damage Evolution 254
8.1.3. New Strategy for Bond Behavior Modeling and the Application in Practical Use 256
8.2. Recommendations 257

LIST OF TABLES

Table		Page
1-1.	Material and Physical Properties of Fibers (derived from Nanni et al., 2014)	4
1-2.	Material and Physical Properties of resin matrix (derived from Nanni et al., 2014)	4
1-3.	Physical Properties of Reinforcing bars (ACI Committee, 2006)	5
2-1.	Factors for determining bond strength in the national and international design codes	35
3-1.	Material properties of 12.7 mm diameter GFRP bars (as reported by manufacturer)	77
3-2.	Composition and characteristics of concrete	79
3-3.	Pullout test results of GFRP-concrete specimens exposed to different environmental conditions	84
3-4.	Weight loss of conditioned specimens	89
3-5.	Relative dynamic modulus of elasticity	91
3-6.	Fitting parameters of the mBPE model and CMR model	101
3-7.	Mean values of the parameters considering different environmental conditions	102
4-1.	Material properties of 12.7 mm diameter GFRP bars (as reported by manufacturer)	115
4-2.	Fiber properties	116
4-3.	Composition of concrete mix	117
4-4.	Pullout test results for both plain concrete and FRC specimens	120
4-5.	Fitting parameters of the mBPE model and CMR model	130
4-6.	Mean values of the parameters with and without considering alkaline-saline environment	130
4-7.	Bond strength retention over 75-year service lifetime	135
4-8.	Critical parameters using the time shift factor method	136
4-9.	Prediction of bond strength retention under different environmental conditions	138

5-1. Material properties of the specimens used in the pullout tests 155

5-2. Fitting parameters of the mBPE model and CMR model for plain concrete specimens 164

5-3. Fitting parameters of the mBPE model and CMR model for FRC specimens 166

5-4. Fitting parameters of the lognormal distribution and Weibull distribution 170

5-5. Fitting parameters of the lognormal distribution and Weibull distribution 172

6-1. Variables affecting bond strength considered in existing design codes 185

6-2. Variables involved in the fitness function 198

6-3. Bond strength calculations by design standards 201

6-4. Statistical characteristics of influencing factors on bond strength..... 202

6-5. Parameter initializations for GA 203

7-1. Statistical characteristics of variables affecting bond strength 220

7-2. Bond strength predicted by national and international design standards..... 224

7-3. Parameter initializations for the GA 227

7-4. Corrected statistical characteristics of design variables..... 239

LIST OF FIGURES

Figure — Page

1-1. Annual corrosion cost in the infrastructure category (derived from Koch et al., 2002) 2

1-2. Typical corrosion-induced damages on (a) abutment and (b) pier (Gergely et al., 1998; Hansson, 1995) 3

2-1. BPE model for steel bar 26

2-2. Modified BPE model for FRP bar 26

2-3. Dispersion conditions of fitting parameters β and sr 29

2-4. Discrete conditions of fitting parameter α 30

2-5. Discrete conditions of fitting parameter β 30

2-6. Discrete conditions of fitting parameter sr 30

2-7. Bond strength calculated in design standards (derived from Ametrano, 2011). 35

2-8. Failure modes associated with concrete compressive strength 37

2-9. Bond strength versus concrete strength f_c' 38

2-10. Normalized bond slip versus strength f_c' 39

2-11. Failure mode associated with concrete cover 40

2-12. Normalized bond strength versus c/d_b 41

2-13. Normalized bond slip versus c/d_b 42

2-14. Failure mode associated with embedment length 43

2-15. Normalized bond strength versus l_d/d_b 44

2-16. Bond slip versus l_d 44

2-17. Failure modes associated with bar diameter 45

2-18. Bond strength versus d_b 46

2-19. Two failure modes associated with varying bar surface conditions 47

3-1. General information of GFRP bars used in previous studies: (a) surface treatment and (b) bar diameter (Yan, Lin, and Yang, 2016) 75

3-2. General information of concrete mix and GFRP bars used in previous studies: (a) concrete compressive strength, (b) embedment length, and (c) concrete cover (Yan, Lin, and Yang, 2016) 76

3-3. GFRP bars used in this study 77

3-4. View of the formwork manufactured with different c/db 78

3-5. Demonstration of the freeze-thaw cycling test 80

3-6. Demonstration of dynamic modulus test for (a) transverse mode and (b) longitudinal mode (demonstrated from ASTM C 215) 81

3-7. Schematic demonstration of the (a) pullout specimen and (b) test setup 83

3-8. Typical failure modes for unconditioned and conditioned specimens: (a) splitting and (b) pullout failures 86

3-9. Examples of specimens exposed to different environmental conditions 88

3-10. Weight loss under different environmental conditions 90

3-11. Variations of relative dynamic modulus after 35 and 75 freeze-thaw cycles 92

3-12. Effect of environmental conditions on durability factor 93

3-13. Typical bond stress-slip relationship for unconditioned and conditioned specimens 95

3-14. (a) Bond strength and (b) normalized bond strength 96

3-15. Slip corresponding to bond strength at (a) loaded end and (b) free end 97

3-16. Curve fittings of the typical bond stress-slip relationship 100

4-1. GFRP bars used in previous studies: (a) surface treatment and (b) bar diameter (Yan, Lin, and Yang, 2016) 112

4-2. Concrete size used in previous studies: (a) concrete cover, (b) embedment length (Yan, Lin, and Yang, 2016) 113

4-3. GFRP bars used in this study 114

4-4. Fiber types (a) steel fiber and (b) PVA fiber 115

4-5. Specimen design: (a) GFRP bars in formwork before concrete pouring and (b) specimens after concrete cast 116

4-6. Schematic demonstration of the (a) pullout specimen and (b) test setup 119

4-7. Representative bond stress-slip responses for plain concrete and FRC specimens 123

4-8. Adhesion stress for plain concrete and fiber reinforced concrete specimens 125

4-9. Bond strength and normalized bond strength for the specimens at 70 ℃ 126

4-10. Curve fittings of the typical bond stress-slip relationship 129

4-11. Relationship between relative humidity and correction factor (derived from Dong et al., 2016) 132

4-12. Bond strength retention vs. exposure time in log-log scale: (a)-(e)..... 134

4-13. Master and derivative curves for bond strength retention 136

5-1. BPE model for steel bar 151

5-2. Modified BPE model for FRP bar 151

5-3. Strain equivalence principle (Skrzypek and Ganczarski, 2013) 153

5-4. Demonstration of the bond-slip relation 154

5-5. Finite element modeling for the Losberg arrangement of pullout test..... 157

5-6. Simplified stress-strain relation of concrete 160

5-7. Bond-slip relations of the plain concrete specimens..... 165

5-8. Bond-slip relations of the FRC specimens..... 167

5-9. Bond damage evolutions of the plain concrete specimens 169

5-10. Bond damage evolutions of the FRC specimens 172

5-11. Bond damage comparisons of the plain concrete specimens..... 174

5-12. Comparisons of the critical bond damage and its corresponding slip 175

5-13. Bond damage comparisons of the FRC specimens..... 176

5-14. Critical bond damage comparisons..... 176

6-1. Searching strategy of BPNN..... 186

6-2. Framework of the hybrid modeling strategy..... 187

6-3. Bond failure modes..... 190

6-4. Architecture of the ANN model (7-n-1) 191
6-5. Workflow of information transfer 192
6-6. Demonstration of constituents of chromosomes 196
6-7. Synthesis working principle 196
6-8. Variations of best fitness 203
6-9. Comparisons of ANN-GA and ANN models 205
6-10. Linear regressions of predictions and targets 206
6-11. Bond strength predictions of different modeling methods 207
6-12. Mean absolute errors (MAEs) of different modeling methods 208
6-13. Root mean square errors (RMSEs) of different modeling methods 208
6-14. Pearson's correlation coefficients (R-values) of different modeling methods 209
7-1. Concept of ANN-based anchorage reliability analysis 218
7-2. Influences of design variables on bond strength 221
7-3. Preliminary architecture of the ANN 225
7-4. Synthesis of workflow of the ANN-GA model 226
7-5. Variations of the best fitness 228
7-6. Comparisons between the ANN-GA and ANN models 229
7-7. Regression analyses of data predicted by the ANN-GA model as compared to experimental results 229
7-8. PF calculations 230
7-9. Working principle of single neuron 231
7-10. Development length calculation based on the targeted reliability index 238
7-11. Training and validating of the ANN-GA model 240
7-12. GUI for Development length estimation 244
7-13. GUI for the ANN-based reliability analysis 244

LIST OF ABBREVIATIONS

PMC .....Polymer-Matrix Composite.

GFRP.....Glass Fiber-Reinforced Polymer.

CFRP.....Carbon Fiber-Reinforced Polymer.

AFRP.....Aramid Fiber-Reinforced Polymer.

BFRP.....Basalt Fiber-Reinforced Polymer.

SC.....Sand-coated.

HW.....Hellically-Wrapped.

HWSC.....Hellically-Wrapped and Sand-Coated.

CTE.....Coefficient of Thermal Expansion.

RC .....Reinforced Concrete.

FT.....Freeze-Thaw.

AS .....Alkaline-Saline.

LVDT.....Linear Variable Differential Transformer.

FRC.....Fiber-Reinforced Concrete.

PVA.....Polyvinyl Alcohol.

TSF.....Time Shift Factor.

RH.....Relative Humidity.

ANN.....Artificial Neural Network.

GA.....Genetic Algorithm.

PF .....Performance Function.

LIST OF SYMBOLS

d_b .....Bar Diameter.

l_d .....Development Length of Reinforcing Bar.

c.....Concrete Cover.

f_c' .....Concrete Compressive Strength.

f_u .....Ultimate Tensile Strength of Reinforcing Bar.

ρ .....Transverse Reinforcement Ratio.

P_{max} .....Maximum Tensile Load.

τ_b.....Bond Strength.

τ_b^*.....Normalized Bond Strength.

τ_b^r.....Bond Strength Retention.

τ_{ons}.....Adhesion Stress.

s_b .....Slip Corresponding to Bond Strength.

$s_{b,le}$.....Slip Corresponding to Bond Strength at Loaded End.

$s_{b,fe}$ .....Slip Corresponding to Bond Strength at Free End.

ΔW_n .....Weight Loss in Percentage.

W_0 .....Original Weight in kg.

W_r.....Residual Weight in kg.

DF .....Durability Factor.

E.....Dynamic Modulus of Elasticity.

R_E .....Relative Dynamic Modulus of Elasticity.

V_f .....Fiber Volume Fraction.

1. INTRODUCTION

This dissertation consists of eight chapters. The primary chapters (Chapter 2 to 7) are based on independent academic papers that have been published or are currently under review, and the formatting are constructed using the format guidelines for technical paper writing approved by the Graduate School of North Dakota State University, which intends to benefit and encourage professional publications. For this reason, some critical information presented in those chapters may be repeated, in order to maintain the completeness of each chapter to help comprehensively understand the proposed problems and their related work. Chapter 1 generally presents the background of fiber-reinforced polymer (FRP) bars in civil engineering. The statement of the problem, research significance and objectives, and the organization of this dissertation are covered.

1.1. Background

The corrosion of conventional steel reinforced concrete (RC) structures is a rather troubling problem worldwide for many decades. The reinforcement corrosion is the leading causes of malfunction or even failures of RC structures in the United States, Canada and most European countries (Koch et al., 2002; Nkurunziza et al., 2005; Sastri et al., 2007). Corrosion causes significantly reduction of the effective cross section of the steel bars, which results in substantial decrease in load-carrying capacity of the structural members. Meanwhile, the corrosion build-up such as the rusts and stains attached at the bar surface constantly accumulates and expands as corrosion develops. The volume increase can reach up to 2 to 5 times the original steel. This exerts additional radial tensile stresses to the surrounding concrete, which leads to cracks or even spalling of concrete cover. Moreover, the damaged concrete in turn provides more accesses by which the chemical agents can migrate to the steel reinforcements and cause further

deterioration to the steel. The U.S. Federal Highway Administration (FHWA) released a 2-year report in 2002 on the corrosion-induced costs, which covers nearly every industry field such as the infrastructures, transportation, utilities, government, and production and manufacturing (Koch et al., 2002). The total annual estimated cost due to corrosion in the U.S. is a phenomenal $276 billion, which takes up around 3.1% of the nation's Gross Domestic Product (GDP). In particular, the corrosion cost on the highway bridges is approximately $8.3 billion, accounting for 36.73% within the infrastructure category (see Figure 1-1). Meanwhile, statistical data indicates approximately 15% of the total 583,000 bridges are structurally deficient because of aging problems. This arises up to substantial economic burden on repairs and rehabilitations to maintain and extending the service lifetime of these public projects.

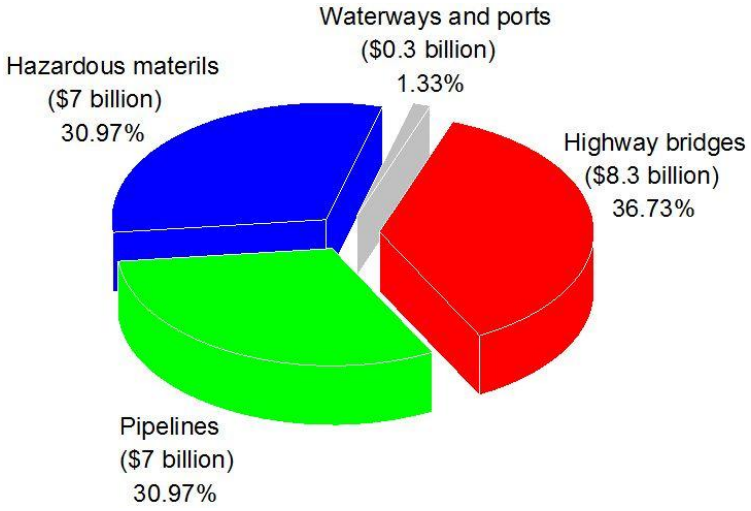

Figure 1-1. Annual corrosion cost in the infrastructure category (derived from Koch et al., 2002)

From the perspective of structural safety, the corrosion-induced damage may lead to heavy casualties especially when the critical members are structurally deficient. Figure 1-2 shows the typical corrosion damage on bridge abutments and piers. Clearly, a large area of spalling of the concrete cover took place in the backwall, bent cap and pier columns. As a result, steel reinforcements were directly exposed to environment without any protection. Significant

reduction in load-carrying capacity of those substructures may cause serious calamities such as unseating of superstructures and collapse of bridge spans. These consequences reveal the urgent need to develop new strategies that can effectively alleviate and prevent steel corrosion due to environmental attack.

Figure 1-2. Typical corrosion-induced damages on (a) abutment and (b) pier (Gergely et al., 1998; Hansson, 1995)

At present, there has been a variety of ways to address the corrosion problem. These measures include coating techniques (fusion-bonded epoxy coatings, and galvanized coatings), plating (electroplating and hot dipping), cathodic protection. In recent decade, the FRP bars have gaining increasing attention due to their superior corrosion resistance that can be exploited toward corrosion-free RC structures.

Basically, FRP is a kind of composite material made of continuous fibers and protective resin matrix. Fibers are utilized as the reinforcing composition to carry loads along the fiber orientation, providing directional stiffness and strength. Commercially available fibers are glass, carbon, and aramid fibers, of which glass fibers take priority over the others because of their low cost. Carbon fibers exhibit the most excellent corrosion resistance whereas demonstrate the premium cost. Aramid fibers hold about 40% lower density than glass fibers. However, they are quite sensitive to environmental conditions and thus require good protection by resin matrix.

Also, their higher cost than glass fibers makes them less common in construction applications. In addition, basalt fibers have emerged in recent years due to their close cost while higher tensile strength compared to the E-glass fibers, and may come to potential alternative of FRP in future. Table 1-1 details the material and physical properties of typical fibers. The resin matrix plays critical role in mainly three aspects: to transfer load between fibers, to clench fibers together, and to protect fibers from environmental attack. Generally, two types of polymer matrices are often used: thermosetting (vinyl ester, polyester, and epoxy, etc.) and thermoplastic polymers (nylon, polyethylene, etc.). Polymers usually display high toughness and plasticity, which can be changed by addition of fibers to increase their elasticity. Table 1-2 summarizes the typical material and physical properties of resin matrix.

Table 1-1. Material and Physical Properties of Fibers (derived from Nanni et al., 2014)

Fiber type	Density (kg/m^3)	Tensile strength (GPa)	Tensile modulus (GPa)	Ultimate tensile strain (%)
E-glass	2501	3.45	72	2.4
S-glass	2501	4.55	86	3.3
AR-glass	2254	1.79 – 3.45	70 – 76	2.0 – 3.3
High-modulus carbon	1952	2.48 – 4.00	350 – 650	0.5
Low-modulus carbon	1750	3.50	240	1.1
Aramid (Kevlar 29)	1440	2.76	62	4.4
Aramid (Kevlar 149)	1440	3.62	124	2.2

Table 1-2. Material and Physical Properties of resin matrix (derived from Nanni et al., 2014)

Fiber type	Density (kg/m^3)	Tensile strength (MPa)	Longitudinal modulus (GPa)	Poisson's ratio (%)	Glass transition temperature ℃
Vinyl ester	1127-1365	3.0 – 8.9	3.00 – 3.45	0.36 – 0.39	70 – 165
Polyester	1187-1424	4.2 – 11.3	2.76 – 4.14	0.38 – 0.40	70 – 100
Epoxy	1187-1424	5.9 – 6.5	2.07 – 3.45	0.35 – 0.39	95 – 175

FRP bars show high strength-to-weight ratio, good fatigue resistance, as well as ease of handling (Nanni et al., 2014). The comparisons between steel and FRP reinforcing bars are detailed in Table 1-3. Cleary, although CFRP bars demonstrate most excellent physical properties, GFRP bars yield good compromise between cost-efficiency and structural performance, and thus have huge market potential for construction industry. Currently, GFRP bars have been permitted by the Canadian highway bridge design code (Canadian Standards Association, 2006). This dissertation mainly focuses on the bond behavior and its durability performance of GFRP bars embedded in concrete.

Table 1-3. Physical Properties of Reinforcing bars (ACI Committee, 2006)

Fiber type	Nominal yield stress (MPa)	Tensile strength (MPa)	Elastic Modulus (GPa)	Yield strain (%)	Rupture strain (%)
Steel	276 – 517	483 – 690	200	0.14 – 0.25	6.0 – 12.0
GFRP	N/A	483 – 1600	35 – 51	N/A	1.2 – 3.1
CFRP	N/A	600 – 3690	120 – 580	N/A	0.5 – 1.7
AFRP	N/A	1720 – 2540	41 – 125	N/A	1.9 – 4.4

Note: Typical values for fiber volume fractions are 50% to 70%.

1.2. Problem Statement

Despite the those aforementioned superiorities over steel material, wide acceptance of GFRP in industry still faces several challenges, and the currently existing problems are yet to be clarified and solved.

1.2.1. Bond Behavior and Its Predictive Models

Bond characteristic of GFRP bars to concrete is the most critical parameter for implementation of this advance material in RC structures. Unlike steel reinforcement, GFRP materials behave anisotropic, non-homogeneous and linear elastic properties, which results in different force transfer mechanism between reinforcement and concrete (Chaallal and

Benmokrane, 1993; Faza and GangaRao, 1991). Primary factors affecting bond behavior (Achillides and Pilakoutas, 2004; Brown and Bartholomew, 1993; Pecce et al., 2001; Yan and Lin, 2016), such as concrete strength, concrete cover, and concrete confinement provided by transverse reinforcement, have been investigated based on either beam test or direct pullout test (Daniali, 1992; DeFreese and Roberts-Wollmann, 2002; Faza and GangaRao, 1991; Lee et al., 2008; Okelo and Yuan, 2005; Shield et al., 1997). Correspondingly, design codes for FRP reinforcement in the U.S., Canada and Japan have stipulated guidelines associated with bond mechanism in terms of both embedment length and bond strength (ACI Committee, 2006; Canadian Standards Association, 2002, 2006; Machida and Uomoto, 1997).

Although much research has showed that different factors respond for the different bond performance of GFRP bars in concrete and accordingly yield the different bond strength, current design codes cannot accurately account for the bond strength with respect to transverse reinforcement. For example, the empirical bond strength equations used in ACI 440.1R-06 (2012) is defined based on Wambeke and Shield (Wambeke and Shield, 2006) database, of which very few of the beam test specimens encompassed transverse reinforcement. On the other hand, several models have been developed to construct the bond stress-slip relations (Masmoudi et al., 2010; Yoo et al., 2015) and each of them may be derived under certain assumptions. So far, no unified model is available that can be applied to general bond behavior of GFRP bar. This necessitates review on existing bond models and their applicability, in order to provide references to civil engineers. Moreover, more advanced models that are capable of predicting the bond strength according to different parameters of GFRP bars and concrete mix need to be developed for more extensive applications.

1.2.2. Bond Durability and Its Predictive Models

It is well established that aqueous solutions with high pH can reduce the tensile strength of bare GFRP bars despite test results showed great differences in previous studies (Benmokrane et al., 2002; Chen et al., 2007; Kim et al., 2008; Micelli and Nanni, 2004). Also, considerable studies have gone into various environmental attacks on the bond strength of GFRP bars. However, the combined effect of the environmental agents including alkaline solution, saline solution, and freeze thaw cycles, remains unsolved or even holds contrary opinions.

Chen et al. used several types of solutions, the tap water, alkaline solutions with respective pH of 12.7 and 13.6, saline solution, and alkaline solution contaminated with chloride ions, to investigate the durability of bare GFRP bars and GFRP-concrete elements. Those specimens also experienced FT cycles and wet-dry cycles before testing. Significant reductions in tensile strength and bond strength were observed for the respective bare and embedded GFRP bars. Alkali attack was stated to be more serious than the FT cycles and wet-dry cycles. Davalos et al. (Davalos et al., 2008) reported bond performance of GFRP bars in concrete subjected to different environmental conditions: tap water at normal temperature and 60 ℃, thermal cycles ranging from 20 to 60 ℃. They reported that there were 0-20% reductions in bond strength being observed for the GFRP bars. Similar results of the bond strength reduction can also be found in (Galati et al., 2006). Fursa et al. (Fursa et al., 2015) conducted experiments on sixteen GFRP-concrete samples subjected to FT cycles. They used the electric response to evaluate the bond strength, and found that the bond strength reduced nearly 50% after 18 FT cycles ranging from 40 to 20 ℃.

On the contrary, Mufti et al. (Mufti et al., 2007) conducted studies on five field GFRP reinforced concrete bridge structures exposed to natural environments for durations of five to

eight years. The environmental conditions encompassed FT cycles, wet-dry cycles, de-icing salts, thermal range from -35 to 35 ℃. The GFRP bars in those selected demonstration structures were all composed of E-glass and vinyl ester resin. The analysis results stated that the structures maintained a good bond at the GFRP bar-concrete interface and no degradation was observed by either optical microscope or Fourier transformed infrared spectroscopy. Robert and Benmokrane (Robert and Benmokrane, 2010) performed experimental investigation on the bond durability of GFRP bars embedded in concrete. The specimens were exposed to tap water at different temperatures (23, 40, 50 ℃) for three immersion durations (60, 120, 180 days). It was concluded that the bond strength decreased as the exposure durations increased whereas minor reductions of the bond strength were observed with increasing the exposure temperature. They also conducted experiments of mortar-wrapped GFRP bar specimens immersed in saline solutions with 50 ℃ for 365 days and 70 ℃ for 120 days (Robert and Benmokrane, 2013). The micrographs showed that no significant damage was captured at the bar-concrete interface. Moreover, the bar-concrete interface and fiber-matrix interface appeared uninfluenced by the moisture absorption and high temperatures. Zhou et al. (Zhou et al., 2011) studied the bond durability of GFRP bars in concrete under different environments, including the tap water, alkaline solution (pH = 13.5), acid solution (pH = 2), and ocean water for different exposure durations (30, 60, and 90 days) at 20 ℃. It was reported that there was no bond degradation under the simulated environments except for the acid solution. Even more, Alves et al. (Alves et al., 2010) conducted experiments on GFRP-concrete elements under sustained and fatigue loading conditions, and stated that the FT cycles enhanced the bond strength between the sand-coated GFRP bar and concrete by approximately 40%.

Clearly, although extensive studies have been carried out on the bond durability of the GFRP bars to concrete, the literature review generally demonstrates large discrepancies. This can be attributed to the different test methods and diversities in the characteristics of those test bars. Also, some laboratory tests considering the extreme environmental conditions may not correspond to field conditions that the structures actually experienced in reality. On the other hand, limited resources dedicated to GFRP reinforced structures exposed to aggressive cold environments including the combined effect of FT cycles, alkaline solution and saline solution. As such, the concrete pore solution that displays highly alkaline would be contaminated with chloride ions from de-icing salts, resulting in bond degradation of structures. Engineers need to comprehensively consider these environmental attacks on the long-term structural performance.

On the other hand, it is desirable for civil engineering structures to maintain the functionality and achieve long-lasting durability over time. Effective evaluation of the long-term (e.g., 75 – 100 years) durability performance of GFRP bars in concrete structures thus will be crucial. Accelerated aging procedures and predictive models based on the Arrhenius concept have been generally developed for assessing service lifetime (Chen et al., 2006; Robert and Benmokrane, 2013). These Arrhenius-base predictive models were mainly used for tensile strength estimates by which bare GFRP bars or mortar-wrapped GFRP bars were exposed to simulated environmental solutions. However, limited resources are available for bond strength estimates of GFRP bars. Moreover, considering that fiber-reinforced concrete (FRC) has emerged as a promising solution not only for enhancement of bond strength but also for the durability performance under aggressive environmental conditions. However, the Arrhenius law is yet to be verified its validity that is applicable for the long-term prediction of GFRP-FRC bond.

1.2.3. Bond Development Associated with Damage Evolution

GFRP bars display different mechanical and physical properties as compared to steel bars, the bond behaviors are quite different, which in turn leads to different bond damage and evolution at the bar-concrete interface (Chaallal and Benmokrane, 1993; Tepfers, 2006; Yan et al., 2016). In addition, GFRP bars usually use sand coatings, fibers and epoxy to create the outer surface, which render the bars non-homogeneous and thus yield different wedging effect as compared to ribs on surfaces of steel bars to concrete. Based on existing experimental and analytical data in the literature, a universal assessment approach has yet to be proposed to demonstrate the interfacial damage evolution. Furthermore, due to complexity of the interfacial contact, limited resources are available to describe this highly nonlinear behavior using the general finite element (FE) packages. This necessitates a general damage assessment approach that can intuitively present the complete bond damage evolution as the slip development at the bar-concrete interface, where the FE packages were utilized to accurately derive the bond-slip relation before the damage assessment.

1.2.4. Reliability Assessment for GFRP-Concrete Anchorage

Anchorage reliability assessment requires a performance function (PF) with respect to a set of design variables, while the PFs are usually implicit in most cases. Although data generated from either numerical simulation or experimental tests are commonly used for determining the PFs (Chiachio et al., 2012; Elhewy et al., 2006). The GFRP bar bond-slip behavior exhibits a highly nonlinear contact feature between GFRP bars and concrete (Akishin et al., 2014), resulting in high variation in modeling (parameter selection and optimization); and b) Limitation of experimental tests. Most laboratory tests, due to limited facilities, time consuming and cost, may be conducted under certain particular conditions, which in turn do not accommodate all

critical design variables (e.g., bar position, bar diameter and concrete cover) commonly experienced in construction. As a result, both numerical simulation and experimental tests neither consider the different characteristics of GFRP materials nor distinguish issues inherent to particular applications to construct the PFs for anchorage reliability analysis. Thus, a new modeling strategy accounting for GFRP-concrete anchorage needs to be developed, which should be capable of not only accurately mapping the strong nonlinear bond behavior but also holding powerful function to solve implicit PFs in terms of the critical factors contributing to the GFRP-concrete bond.

In addition, sufficient development length of reinforcing bars plays an important role in preventing bond premature failure and ultimately ensures the safety of the structures. Anchorage reliability of GFRP bars to concrete therein is one of the most critical indices for implementation of such engineered material to the concrete structures. A reasonable reliability index of the development length must be designated to allow the GFRP bar to yield desirable flexural failure prior to anchorage failure.

1.3. Research Significance

GFRP bars generally demonstrate great potential as an alternative in the implementation of preventive strategy addressing corrosion problems. Their good balance between cost and structural behavior make them more prospects than CFRP and AFRP composites. Although corrosion control and prevention have gained great achievements by various new technologies, more optimal and effective measures still need to be encouraged and promoted, in order to further alleviate economic burden and improve the structural safety.

More extensive acceptance and application of GFRP bars in RC structures requires: (1) fully understanding of the bond mechanism associated with failure mode, bond stress-slip

relationship, and bond strength; (2) a rough estimate on the long-term bond degradation under harsh environmental conditions. Previous bond tests have provided various short-term data, however, those test results generally exhibit large discrepancies and cannot be directly used as design references. Meanwhile, long-term monitoring statistics for the bond durability performance in field conditions are time-consuming whereas the corrosion problems at present need urgent resolution. Conventional accelerating aging tests used to approximate field conditions overestimated environmental effect and thus lead to too conservative estimates. Moreover, the service life predicted based on the short-term data lacks of general applicability when environmental condition changes, such as the temperature and relative humidity. These limitations are believed as major obstructions for the recognition and approval in a broader context of civil infrastructures.

1.4. Research Objectives

This study aims to investigate the GFRP-concrete bond and its durability performance. The research objectives are summarized in the following:

First, the bond mechanism of GFRP bars to concrete is analyzed based on a database of over 680 pullout specimens. Critical factors and their impact on bond strength and failure mode are presented through statistical analysis, which also provide a sound basis for the subsequent experimental preparation for bond test.

Second, an experimental study on the bond durability performance of GFRP bars embedded in plain concrete are performed under various environmental conditions, including alkaline-saline solutions, freezing-thawing cycles, and the coupled effect of the both. Elevated temperatures are used to accelerate the degradation rate of bond strength. The critical indices of durability performance, such as failure mode, weight loss, relative dynamic modulus of elasticity

and durability factor, bond strength and its corresponding slip are studies. Based on the experimental data, analytical models accounting for the bond stress-slip relationship are calibrated by considering environmental effect to better demonstrate GFRP-concrete bond.

Third, the GFRP-FRC bond durability under saline solutions is investigated. The concrete reinforced with steel and PVA fibers are adopted. The experimental data also aid to calibrate the analytical models for GFRP-FRC bond by considering the environmental effects. Also, a detailed procedure using Arrhenius law and time shift factor (TSF) methods is developed to predict the long-term bond degradation under different environmental temperatures and relative humidity.

Fourth, a universal damage assessment approach for GFRP bar-concrete interface is proposed, which can be used to evaluate the bond damage evolution in terms of slip development. A detailed procedure to implement such approach is discussed, and further demonstrated through previous pullout tests for both plain concrete and FRC.

Finally, the intelligent computational techniques of artificial neural network (ANN) and genetic algorithm (GA) are used for bond strength modeling based on the beam test results derived from available literatures. The predictions of bond strength are validated with experimental results to demonstrate its accuracy, meanwhile compared with those calculated by design equations stipulated in the U.S., Canadian, and Japanese design codes, as well as conventional multi-nonlinear regression method to show the superiority. Besides, this modeling strategy is further extended for anchorage reliability assessment for GFRP bars in concrete. Accordingly, a systematic application of graphical user interface toolbox is developed for practical use.

1.5. Organization of the Dissertation

This dissertation is constructed with eight chapters:

Chapter 1 introduces the background and currently existing problems of GFRP bars, and then presents the research significance and objectives, as well as the organization of this dissertation.

Chapter 2 presents a comprehensive literature review on the bond mechanism and bond durability of GFRP bars to concrete. The critical factors associated with bond strength and failure mode are studied based on the statistical analysis, providing a sound basis for the subsequent experimental study. The commonly encountered environmental impacts on bond durability performance are discussed and summarized.

Chapter 3 presents an experimental investigation on the bond durability of GFRP bars in concrete when subjected to harsh environments. The pullout specimens having different concrete covers were designed based on a created database to demonstrate the generality of the current experimental program. The freeze-thaw (FT) cycles, alkaline-saline (AS) solution, and both coupled effects were used to simulate environmental conditions in cold regions. The durability performance in terms of the failure mode, weight loss, relative dynamic modulus of elasticity, durability factor, as well as the bond strength, were measured and investigated accordingly. Moreover, the analytical models: modified Bertero-Eligehausen-Popov (mBPE) model and Cosenza-Manfredi-Realfonzo (CMR) model, were calibrated by considering the environmental influences based on the experimental data to better demonstrate the degradation of GFRP-concrete bond.

Chapter 4 presents the bond durability of GFRP bars to FRC exposed to saline solutions. Total 105 pullout specimens reinforced with steel and PVA fibers were prepared and immersed

in the saline solutions at 50 and 70 ℃ under 30, 45, and 60 days, respectively. Their durability was quantified in terms of failure mode, adhesion stress as well as the bond strength. Besides, the experimental data also aided to calibrate the analytical models, mBPE and CMR models, to better define the GFRP bond to FRC by considering the environmental effects. Also, a detailed procedure using Arrhenius law and time shift factor (TSF) methods was developed to predict the long-term bond degradation under different environmental temperatures and relative humidity.

Chapter 5 presents a bond damage assessment approach for GFRP bar-concrete interface. The damage evolution equations are proposed based on the strain equivalence principle of damage mechanics, where the variations of the secant modulus of the bond-slip curve are utilized to evaluate the interface deterioration against slip. Numerical analyses are conducted with the ANSYS finite element (FE) program to simulate the bond behavior of pullout test. Nonlinear material behaviors of the GFRP composite and concrete matrix with respect to plain concrete and fiber-reinforced concrete (FRC) are implemented using appropriate constitutive models. The interfacial bond-slip behavior is implemented using nonlinear spring elements. Numerical predictions are validated by the experimental results and compared with the widely used analytical models accounting for the FRP-concrete bond. Upon this, the bond damage evolution curves are derived thereafter. Further comparisons of different specimens are performed to investigate the critical factors and their impacts on the damage evolution, as well as those on the critical bond damage corresponding to the bond strength.

Chapter 6 develops an optimized modeling strategy that harnesses the strong nonlinear mapping ability of ANN with the global searching ability of GA for bond strength prediction. The factors that affect the bond strength were identified from the test data of 157 beam-test specimens in the literature, in terms of bar conditions (bar diameter, surface, position and

embedment length), concrete (thickness of concrete cover and concrete compressive strength), and confinement from transverse reinforcements.

Chapter 7 presents the ANN-based reliability assessment GFRP bars to concrete. The new methodology harnesses not only the strong nonlinear mapping ability in the ANN to approximate the performance function (PF) and solve its partial derivatives in terms of the design variables, but also global searching ability in the GA to explore the optimal initial weights and biases of the ANN to avoid falling into local minima during the network training. The ANN-based first order second moment (FOSM) method and Monte Carlo simulation (MCS) method were first derived. Implementation of the proposed hybrid ANN-GA procedures for GFRP bar anchorage reliability analysis were then achieved by the targeted reliability index and development length. Both the ANN-based FOSM and MCS methods were utilized for determining the reliability index and probability of failure of GFRP bar anchorage. The further implementation of the proposed strategy was achieved by a graphical user interface toolbox in Matlab environment for practical use.

Chapter 8 summarizes the primary conclusions, and addresses future research directions.

1.6. References

Achillides, Z., and Pilakoutas, K. (2004). Bond behavior of fiber reinforced polymer bars under direct pullout conditions. Journal of Composites for Construction, 8(2), 173-181.

ACI Committee. (2006). Guide for the design and construction of structural concrete reinforced with FRP bars. ACI 440.1 R, 6.

Akishin, P., Kovalovs, A., Kulakov, V., and Arnautov, A. (2014). Finite element modelling of slipage between FRP rebar and concrete in pull-out test. Paper presented at the The International Scientific Conference „Innovative Materials, Structures and Technologies".

Alves, J., El-Ragaby, A., and El-Salakawy, E. (2010). Durability of GFRP bars' bond to concrete under different loading and environmental conditions. Journal of Composites for Construction.

Benmokrane, B., Wang, P., Ton-That, T. M., Rahman, H., and Robert, J.-F. (2002). Durability of glass fiber-reinforced polymer reinforcing bars in concrete environment. Journal of Composites for Construction, 6(3), 143-153.

Brown, V. L., and Bartholomew, C. L. (1993). FRP reinforcing bars in reinforced concrete members. ACI Materials Journal, 90(1).

Canadian Standards Association. (2002). Design and construction of building components with fibre-reinforced polymers: Canadian Standards Association.

Canadian Standards Association. (2006). Canadian highway bridge design code: Canadian Standards Association.

Chaallal, O., and Benmokrane, B. (1993). Pullout and bond of glass-fibre rods embedded in concrete and cement grout. Materials and Structures, 26(3), 167-175.

Chen, Y., Davalos, J. F., and Ray, I. (2006). Durability prediction for GFRP reinforcing bars using short-term data of accelerated aging tests. Journal of Composites for Construction, 10(4), 279-286.

Chen, Y., Davalos, J. F., Ray, I., and Kim, H.-Y. (2007). Accelerated aging tests for evaluations of durability performance of FRP reinforcing bars for concrete structures. Composite Structures, 78(1), 101-111.

Chiachio, M., Chiachio, J., and Rus, G. (2012). Reliability in composites–A selective review and survey of current development. Composites Part B: Engineering, 43(3), 902-913.

Daniali, S. (1992). Development length for fiber-reinforced plastic bars. Paper presented at the Advanced Composite Materials in Bridges and Structures.

Davalos, J. F., Chen, Y., and Ray, I. (2008). Effect of FRP bar degradation on interface bond with high strength concrete. Cement and Concrete Composites, 30(8), 722-730.

DeFreese, J. M., and Roberts-Wollmann, C. L. (2002). Glass fiber reinforced polymer bars as top mat reinforcement for bridge decks.

Elhewy, A. H., Mesbahi, E., and Pu, Y. (2006). Reliability analysis of structures using neural network method. Probabilistic Engineering Mechanics, 21(1), 44-53.

Faza, S. S., and GangaRao, H. V. (1991). Bending and bond behavior of concrete beams reinforced with plastic rebars. Transportation Research Record(1290).

Fursa, T., Utsyn, G., Korzenok, I., and Petrov, M. (2015). Using electric response to mechanical impact for evaluating the durability of the GFRP-concrete bond during the freeze-thaw process. Composites Part B: Engineering.

Galati, N., Nanni, A., Dharani, L. R., Focacci, F., and Aiello, M. A. (2006). Thermal effects on bond between FRP rebars and concrete. Composites Part A: Applied Science and Manufacturing, 37(8), 1223-1230.

Gergely, I., Pantelides, C. P., Nuismer, R. J., and Reaveley, L. D. (1998). Bridge pier retrofit using fiber-reinforced plastic composites. Journal of Composites for Construction, 2(4), 165-174.

Hansson, C. M. (1995). Concrete: The advanced industrial material of the 21st century. Metallurgical and materials transactions B, 26(3), 417-437.

Kim, H.-Y., Park, Y.-H., You, Y.-J., and Moon, C.-K. (2008). Short-term durability test for GFRP rods under various environmental conditions. Composite Structures, 83(1), 37-47.

Koch, G. H., Brongers, M. P., Thompson, N. G., Virmani, Y. P., and Payer, J. H. (2002). Corrosion cost and preventive strategies in the United States.

Lee, J.-Y., Kim, T.-Y., Kim, T.-J., Yi, C.-K., Park, J.-S., You, Y.-C., et al. (2008). Interfacial bond strength of glass fiber reinforced polymer bars in high-strength concrete. Composites Part B: Engineering, 39(2), 258-270.

Machida, A., and Uomoto, T. (1997). Recommendation for design and construction of concrete structures using continuous fiber reinforcing materials (Vol. 23): Research Committee on Continuous Fiber Reinforcing Materials, Japan Society of Civil Engineers.

Masmoudi, A., Masmoudi, R., and Ouezdou, M. B. (2010). Thermal effects on GFRP rebars: experimental study and analytical analysis. Materials and Structures, 43(6), 775-788.

Micelli, F., and Nanni, A. (2004). Durability of FRP rods for concrete structures. Construction and Building Materials, 18(7), 491-503.

Mufti, A. A., Banthia, N., Benmokrane, B., Boulfiza, M., and Newhook, J. P. (2007). Durability of GFRP composite rods. Concrete International, 29(02), 37-42.

Nanni, A., De Luca, A., and Zadeh, H. J. (2014). Reinforced Concrete with FRP Bars: Mechanics and Design: CRC Press.

Nkurunziza, G., Debaiky, A., Cousin, P., and Benmokrane, B. (2005). Durability of GFRP bars: A critical review of the literature. Progress in structural engineering and materials, 7(4), 194-209.

Okelo, R., and Yuan, R. L. (2005). Bond strength of fiber reinforced polymer rebars in normal strength concrete. Journal of Composites for Construction.

Pecce, M., Manfredi, G., Realfonzo, R., and Cosenza, E. (2001). Experimental and analytical evaluation of bond properties of GFRP bars. Journal of Materials in Civil Engineering, 13(4), 282-290.

Robert, M., and Benmokrane, B. (2010). Effect of aging on bond of GFRP bars embedded in concrete. Cement and Concrete Composites, 32(6), 461-467.

Robert, M., and Benmokrane, B. (2013). Combined effects of saline solution and moist concrete on long-term durability of GFRP reinforcing bars. Construction and Building Materials, 38, 274-284.

Sastri, V. S., Ghali, E., and Elboujdaini, M. (2007). Corrosion prevention and protection: practical solutions: John Wiley & Sons.

Shield, C., French, C., and Retika, A. (1997). Thermal and mechanical fatigue effects on GFRP rebar-concrete bond. Paper presented at the Proceedings of the 3rd international symposium on non-metallic (FRP) reinforcement for concrete structures (FRPRCS-3), Sapporo.

Tepfers, R. (2006). Bond clause proposals for FRP bars/rods in concrete based on CEB/FIP Model Code 90. Part 1: Design bond stress for FRP reinforcing bars. Structural Concrete, 7(2), 47-55.

Wambeke, B. W., and Shield, C. K. (2006). Development length of glass fiber-reinforced polymer bars in concrete. ACI Structural Journal, 103(1).

Yan, F., and Lin, Z. (2016). New strategy for anchorage reliability assessment of GFRP bars to concrete using hybrid artificial neural network with genetic algorithm. Composites Part B: Engineering, 92, 420-433.

Yan, F., Lin, Z., and Yang, M. (2016). Bond mechanism and bond strength of GFRP bars to concrete: A review. Composites Part B: Engineering, 98, 56-69.

Yoo, D.-Y., Kwon, K.-Y., Park, J.-J., and Yoon, Y.-S. (2015). Local bond-slip response of GFRP rebar in ultra-high-performance fiber-reinforced concrete. Composite Structures, 120, 53-64.

Zhou, J., Chen, X., and Chen, S. (2011). Durability and service life prediction of GFRP bars embedded in concrete under acid environment. Nuclear Engineering and Design, 241(10), 4095-4102.

2. LITERATURE REVIEW

2.1. Introduction

Corrosion of steel reinforcing bars in reinforced concrete (RC) structures is a serious problem when they are in exposure to various environments (ACI Committee, 2006). In particular, sodium chloride and calcium chloride based deicers, traditionally used in cold regions for snow and ice removal operations, primarily respond for the initiation of steel corrosion. Corrosion process and its products damage the interface between steel bar and concrete, thus degrade bond strength, and ultimately shorten the service life of the concrete structures. This arises up to substantial economic burden during periodic maintenance, repairs and rehabilitations in the United States, Canada and European countries (Bedard, 1992; French, 2003; Koch et al., 2002). There has been an increasing demand for alternate materials and techniques for reinforcement in RC structures (Ballinger, 1991; A Nanni et al., 1995; Saadatmanesh and Ehsani, 1989). These include coating techniques (fusion bonded epoxy and galvanized coatings) on steel or non-metallic reinforcements (CFTP, GFRP and AFRP). Among them GFRP reinforcing bar has received increasing attention due to its high chemical resistance, high strength-weight ratio, and high cost efficiency, as well as its superior corrosion resistance (Antonio Nanni et al., 2014).

Bond characteristics of GFRP bars in concrete are the most critical parameter for implementation of the material to the concrete structures. Unlike steel reinforcement, GFRP materials behave anisotropic, non-homogeneous and linear elastic properties, which results in different force transfer mechanism between reinforcement and concrete. Primary factors affecting bond behavior (Achillides and Pilakoutas, 2004; Brown and Bartholomew, 1993; Pecce et al., 2001; F. Yan and Z. Lin, 2016), such as concrete strength, concrete cover, and concrete confinement provided by transverse reinforcement, have been investigated based on either beam

test or direct pullout test (Daniali, 1992; DeFreese and Roberts-Wollmann, 2002; Faza and GangaRao, 1991; Lee et al., 2008; Okelo and Yuan, 2005; Shield et al., 1997). Correspondingly, design codes for FRP reinforcement in the U.S., Canada and Japan have stipulated guidelines associated with bond mechanism in terms of both embedment length and bond strength (ACI Committee, 2006; Canadian Standards Association, 2002, 2006; Machida and Uomoto, 1997).

Although much research has showed that different factors respond for the different bond performance of GFRP bars in concrete and accordingly yield the different bond strength, current design codes cannot accurately account for the bond strength with respect to transverse reinforcement. For example, the empirical bond strength equations used in ACI 440.1R-06 (2012) is defined based on Wambeke and Shield (Wambeke and Shield, 2006) database, of which very few of the beam test specimens encompassed transverse reinforcement. On the other hand, several models have been developed to construct the bond stress-slip relations (A. Masmoudi et al., 2010; R. Masmoudi et al., 2011; Yoo et al., 2015) and each of them may be derived under certain assumptions. So far, no unified model is available that can be applied to general bond behavior of GFRP bar. Thus it is necessary to review the existing bond models and their applicability, for assisting engineers to select desirable models.

Moreover, since concrete has a high alkaline with a pH value ranging from 12.7~13.6 (Belarbi and Wang, 2011; Chen et al., 2007), several previous studies demonstrated that GFRP bars embedded in concrete have reduction in both tensile and bond strengths (Charles, 2012; Gonenc, 2003; Micelli and Nanni, 2004; Mijovic, 1985; Tuttle, 1996). Laboratory based tests also revealed that elevated temperature can further accelerate their strength degradation process (Abbasi and Hogg, 2005). Degradation modeling and prediction (e.g., Arrhenius concept) of tensile strength retention has been proposed and been successfully validated (Chen et al., 2007;

Gonenc, 2003). Bond degradation of GFRP bars in concrete, however, in particular under harsh environments, such as extremely thermal cycling, alkaline solutions and other chemical attacks, is more complex, while accordingly existing studies and methods on mechanism and prediction are different and even in contrary opinions in the available literatures (Alves et al., 2010; Koller et al., 2007; Won et al., 2013). Thus, it is important to better understand their bond behavior and mechanism for more widespread applications of GFRP bars in concrete structures.

To maximize the knowledge and experience gained in existing studies and practices in the literature, this study is undertaken to summarize the key issues primarily on bond mechanism in terms of failure modes and bond strength. Both bond stress vs. slip models and primary factors affecting bond behavior are investigated through statistical analysis based on a database created. Meanwhile, comparisons between different design standards regarding bond strength prediction are presented and discussed in this study. Furthermore, bond degradations under environmental conditions, such as freezing-thawing cycling, wet-dry cycling, alkaline solutions and high temperature are presented and analyzed respectively. Future work for both theoretical bond degradation and laboratory test would be performed based on the contribution covered in this study.

2.2. Bond Behavior and Modeling of GFRP Bars to Concrete

2.2.1. Bond Stress-Slip Behavior and Its Modeling

Generally, bond of reinforcing bar to concrete includes: a) Adhesion resistance of the interface, defined as chemical bond; b) Frictional resistance of the interface against slip; and c) Mechanical interlock due to irregularity of the interface (ACI 408 Committee, 2003). GFRP bar has a different bond behavior compared to steel bar, which is mainly attributed to difference in material property and surface texture that lead to different surface toughness and the force

transfer mechanism between reinforcement and concrete (Chaallal and Benmokrane, 1993; Edoardo Cosenza et al., 1997; Faza and GangaRao, 1991; F. Yan and Z. B. Lin, 2016). GFRP reinforcement behaves linearly elastic till failure, whereas conventional steel reinforcement exhibits an obvious plastic stage with large deformation after yielding. GFRP bar usually has different surface texture and treatments, such as ribbed, sand coated and helically wrapped, and thus its bearing force due to mechanical interlock is commonly smaller than that of steel ribbed bar. It is believed that such mechanical interlock of surface texture and surface treatments to concrete matrix accounts for the majority of bond strength of GFRP bar over chemical adhesion or friction (Achillides and Pilakoutas, 2004). However, another contrary opinion holds that chemical adhesion is the primary bond during pullout process, while mechanical interlock and friction are only the secondary contribution (Pepe et al., 2013).

Currently, several analytical models of bond stress vs. slip relations have been developed using the explicit mathematical formula to describe bond behavior of FRP bar to concrete, as addressed in the following sections.

2.2.2. BPE and Modified BPE Models

The BPE model was originally developed to describe bond behavior of steel bar to concrete (Edoardo Cosenza et al., 1997), as shown in Figure 2-1. Consider that the FRP bond has no apparent plateau as steel bar, the model was then modified as Figure 2-2 for FRP material [39]. In this model, the bond-slip curve of the FRP bar in concrete, illustrated in Figure 2-2, is mainly simplified into three stages. In stage I, an ascending function in bond stress corresponds to the chemical adhesion between the bar and concrete, as well as the bearing force. Cracks develop at later this stage. After the bond force increases to a certain value, the bar starts to slide along the lug area. Concrete cracks (or even crushing) occur and the bearing force due to

mechanical interlocking against the concrete diminishes, resulting in a rapid decrease of the bond stress accompanying with an apparent slip as shown in stage II. In stage III, significant cracks formed in the concrete and the bar continues to slide while remaining a certain bond force mainly due to friction.

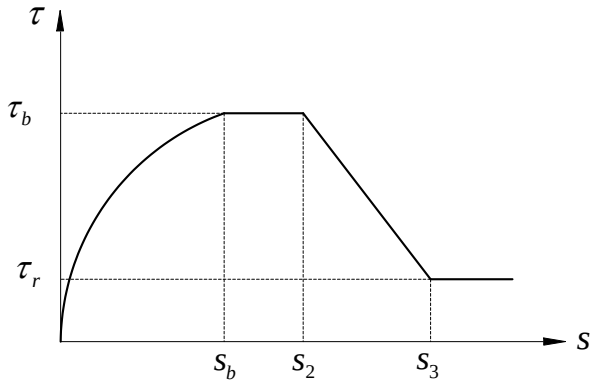

Figure 2-1. BPE model for steel bar

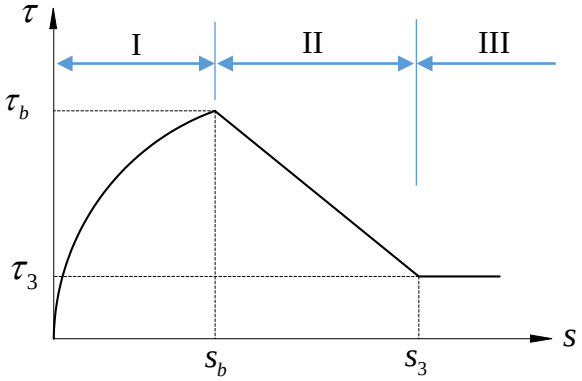

Figure 2-2. Modified BPE model for FRP bar

Thus, the modified BPE (mBPE) bond stress-slip model in Figure 2-2 can be piecewisely expressed as these three stages in Equations (2-1)-(2-3).

$$\frac{\tau}{\tau_b} = (\frac{s}{s_b})^{\alpha} \text{ for } 0 \le s \le s_b, \tag{2-1}$$

$$\frac{\tau}{\tau_b} = 1 - p(\frac{s}{s_b}) \text{ for } s_b \le s \le s_3, \tag{2-2}$$

$$\tau = \tau_3 \text{ for } s \ge s_3, \tag{2-3}$$

where τ and s are defined as the bond stress and the slip, while τ_b and s_b are the maximum bond stress (bond strength) and its corresponding slip; α and p are parameters that can be determined from curve fitting of experimental results. The effect of surface treatment on bond strength is considered in this model (Won et al., 2013). The ascending branch of BPE/mBPE was observed to have larger bond stress than the experimental results in Masmoudi's work. It is worth noting that both fiber type and bar diameter are not taken into account in this model.

2.2.3. Malvar's Model

Rather than use of three piecewise equations in the mBPE model (Won et al., 2013), this model uses a polynomial function (Malvar, 1994) to predict the bond stress-slip behavior, as shown below in Eqn.:

$$\tau = \tau_b \frac{F\left(\frac{s}{s_b}\right)+(G-1)\left(\frac{s}{s_b}\right)^2}{1+(F-2)\frac{s}{s_b}+G\left(\frac{s}{s_b}\right)^2}, \tag{2-4}$$

where,

$$\frac{\tau_b}{f_t} = A + B(1 - e^{-C\sigma_r/f_t}) \text{ and } s_b = D + E\sigma_r, \tag{2-5}$$

in which constants *A*, *B*, *C*, *D*, *E*, *F* and *G* are parameters to be determined from experimental results; σ_r is confining axisymmetric radial pressure while f_t is concrete tensile strength.

In Malvar's study (Malvar, 1994), GFRP bar with four different surface textures were investigated. Note that Malvar's model did not predict the first ascending stage as accurately as the mBPE model (Edoardo Cosenza et al., 1997). Moreover, it is assessed to be less reliable compared to BPE, mBPE and CMR models (Lin and Zhang, 2014). Additionally, impacts of bar diameter on the bond strength were ignored in this model.

2.2.4. CMR Model

To overcome the drawback of the Malvar's model, the CMR model proposed by Cosenza et al. (E Cosenza et al., 1995) was used to better represent ascending function at the first stage of bond stress-slip curve for FRP bar to concrete in form of.

$$\frac{\tau}{\tau_b} = (1 - exp(-\frac{s}{s_r}))^{\beta}, \tag{2-6}$$

where s_r and β are parameters that are derived from curve fitting of experimental data. Since the initial slope in the CMR model is infinite, it may account for impacts of chemical adhesion at the initial stage. It shows a good agreement with experimental results than the BPE model in Masmoudi's study.

2.2.5. Parameters Determined for the Existing Bond-Slip Models

As compared to the mBPE model and the CMR model, Malvar's model requires more parameters to be determined and has been reported to be less comprehensive and lower reliable (Lin and Zhang, 2014). Differently, the mBPE model and CMR model are more concise and convenient for implementation and thus these two models will be mainly discussed herein. Basically, α in the mBPE model in Equation (2-1), and s_r and β in the CMR model in Equation (2-6) are determined using the data-driven curve fitting.

The data reported in (Antonietta Aiello et al., 2007; Baena et al., 2009; B Benmokrane and Tighiouart, 1996; R. Masmoudi et al., 2011; Yoo et al., 2015) were used to demonstrate the distribution state of the fitting parameters. Those test contained the parameters including the bar size, surface treatment, concrete compressive strength, kinds of fibers, kinds of test, operating temperature. Data from literatures in terms of the bar size and surface treatment are plotted in Figure 2-3, in which parameters α, s_r and β are displayed by squares, circles and triangles, respectively. High variation in Figure 2-3 revealed that values of these parameters in the mBPE

and CMR models are highly affected by different rebar conditions, such as rebar diameter and surface treatment (Antonietta Aiello et al., 2007; Baena et al., 2009; B Benmokrane and Tighiouart, 1996; Yoo et al., 2015), and other environmental factors, such as varying operating temperature (R. Masmoudi et al., 2011). For GFRP rebars with a diameter of 12.7 mm and with a surface of helically wrapped and sand coated, α=0.18 was suggested for mBPE model, and s_r=0.0668, and β=0.3691 for CMR model (Baena et al., 2009). Yoo et al. (2015) calibrated parameters in the existing models for GFRP rebar with different diameters. Specifically, for diameter of 12.7 mm, the coefficients of mBPE model has α=0.18; while s_r=0.16, and β=0.50 for CMR model. In addition, Masmoudi et al. (2011) investigated the impacts of elevated temperature on the selection of parameters. Their tests for GFRP rebars with a 16-mm diameter after 4 months thermal exposure showed that the parameter α is likely a constant, with 0.085 at 20 ℃, 0.089 at 40 ℃, 0.087 at 60 ℃ and 0.084 at 80 ℃.

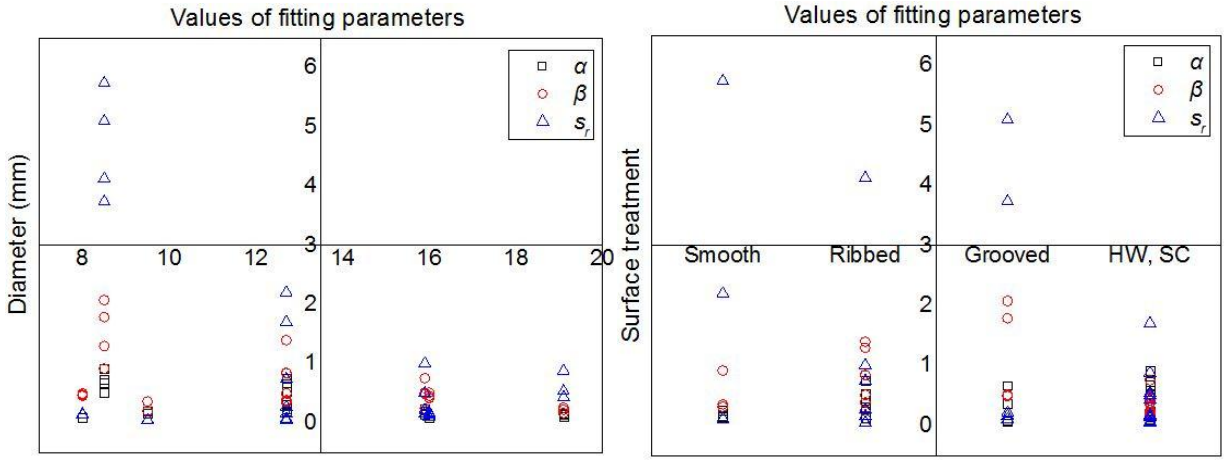

Figure 2-3. Dispersion conditions of fitting parameters β and s_r

The box plots for these three parameters with regard to specific rebar diameter and surface treatment are displayed in Figure 2-4 through 2-6.

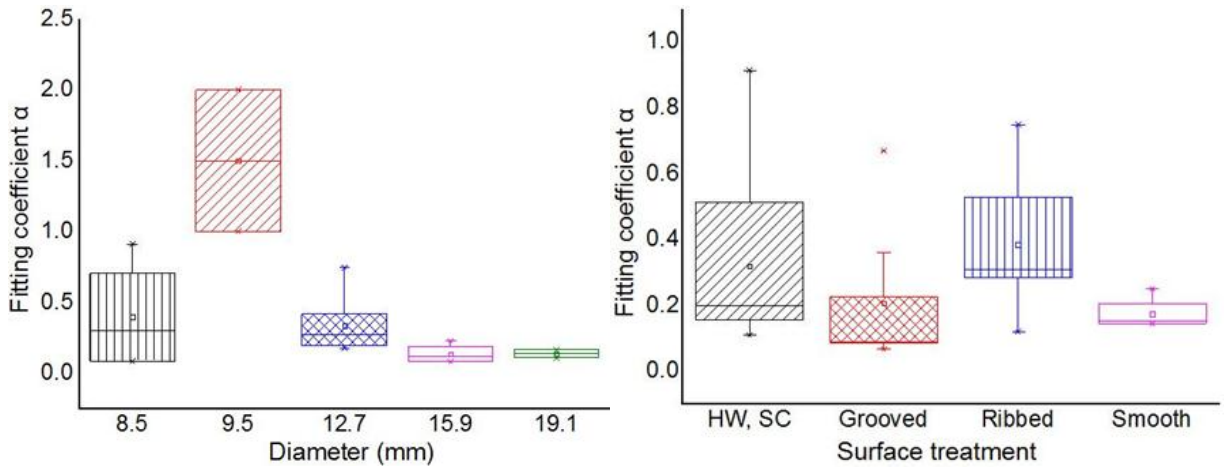

Figure 2-4. Discrete conditions of fitting parameter α

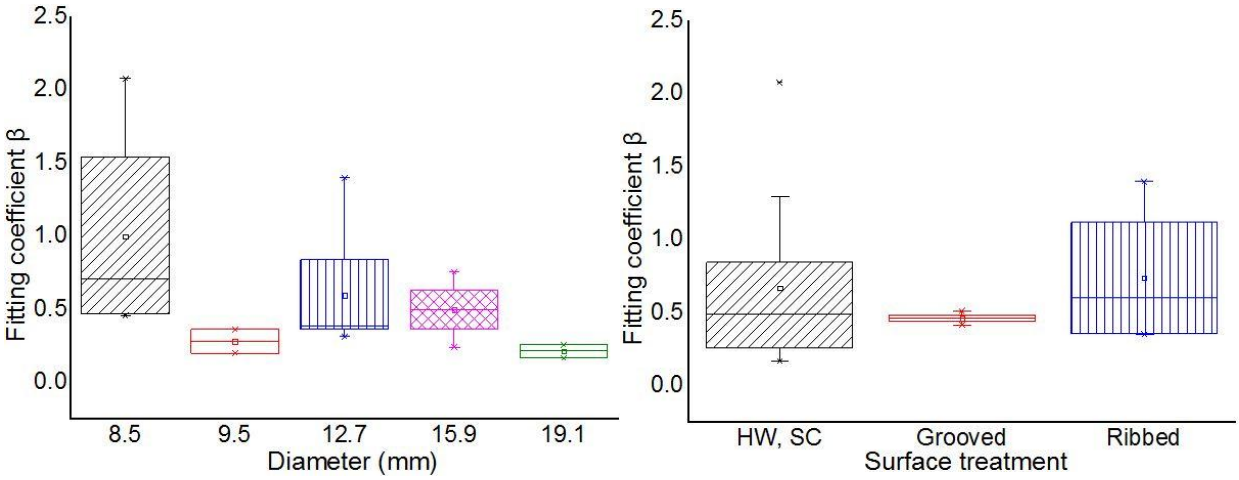

Figure 2-5. Discrete conditions of fitting parameter β

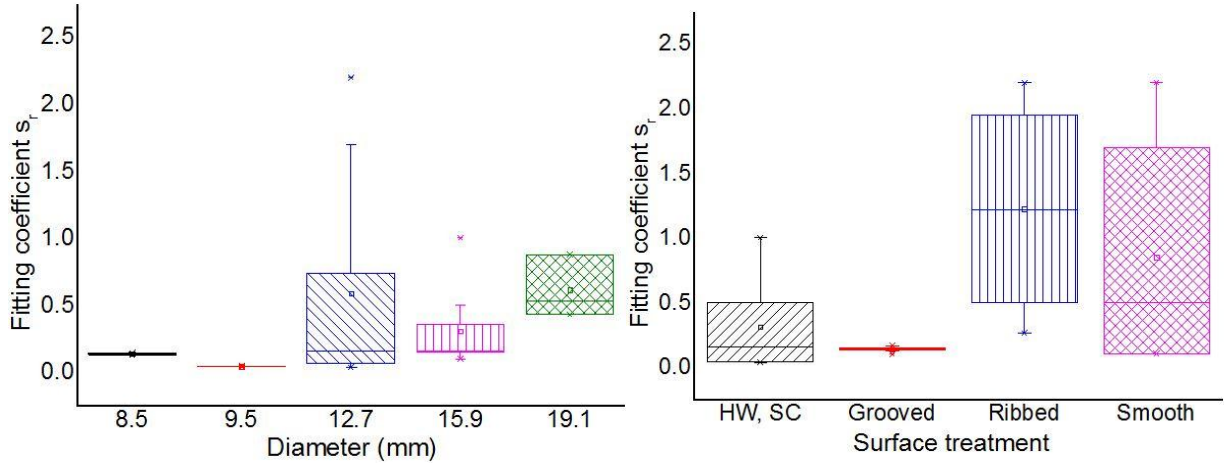

Figure 2-6. Discrete conditions of fitting parameter s_r

The lower and upper limits in these plots can provide a preference of parameters to a certain extent if when experiments are not available. For example, α is supposed to be the median that can be derived from the left boxplot of Figure 2-4, when diameter is equal to 12.7 mm, α is found to be 0.2715, and similarity to β and s_r. With the obtained parameters for either the mBPE or CMR, the bond-slip model of GFRP rebar to concrete will be available.

2.2.6. Bond Strength Specified in Existing Design Provisions

2.2.6.1. ACI 440.1R-06

Bond strength of FRP bar to concrete is specified in ACI 440.1R-06 (ACI Committee, 2006), a linear regression of normalized average bond stress ($\tau_b/\sqrt{f_c'}$) is described by the normalized concrete cover (c/d_b) and embedment length (l_d/d_b):

$$\frac{\tau_b}{0.083\sqrt{f_c'}} = 4.0 + 0.3\frac{c}{d_b} + 100\frac{d_b}{l_d}, \tag{2-7}$$

where τ_b is the bond strength (MPa); f_c' is the concrete compressive strength (MPa) at 28-day age; c is the lesser of the cover to the center of the bar or one-half of the center-on-center spacing of the bars being developed; d_b is bar diameter; l_d is embedded length in concrete. This equation was developed from a comprehensive study by Wambeke and Shield (Wambeke and Shield, 2006) through the 269 bond tests. The tests built up a valuable database, widely covering beam-end tests, notch-beam tests, and splice tests, while GFRP bars were used as the major reinforcement (by 240 out of total number of 269). Bar surfaces included sand coated, spiral wrap and helical lug, including with and without confining reinforcements. The diameter of the bar ranged from 13 to 29 mm. The concrete compressive strength ranged from 28 to 45 MPa. Out of 240 GFRP specimens, 75 failed by concrete splitting, 94 by pullout failure and 71 by bar tensile fracture failure. In the Wambeke and Shield database, the bar surface did not appear to influence the test results. Meanwhile, no explicit expression was presented to the transverse

reinforcement, however it was claimed that the confinement influence needs to be further investigated.

2.2.6.2. Canadian standards association

Canadian Standards Association (CSA S806-02) (Canadian Standards Association, 2002) specifies the following equation for the average bond strength of FRP bars to concrete:

$$\tau_b = \frac{d_{cs}\sqrt{f_c'}}{1.15(K_1K_2K_3K_4K_5)\pi d_b}, \tag{2-8}$$

where d_{cs} is the smallest of the distance from the closest concrete surface to the center of the bar being developed or two-thirds the center-on-center spacing of the bars being developed (mm); K_1 is bar location factor (1.3 for horizontal reinforcement placed more than 300 mm of fresh concrete is cast below the bar, 1.0 for all other cases); K_2 is concrete density factor (1.3 for structural low-density concrete, 1.2 for structural semi-low-density concrete, 1.0 for normal-density concrete); K_3 is bar size factor (0.8 for $A_b \leq 300$ mm^2, 1.0 for $A_b > 300$ mm^2); K_4 is bar fiber factor (1.0 for CFRP and GFRP, 1.25 for AFRP); K_5 is bar surface profile factor (1.0 for surface roughened or sand coated or braided surfaces, 1.05 for spiral pattern surfaces or ribbed surfaces, 1.8 for indented surfaces). Thus, it can be observed that the proposed bond strength in Equation (2-8) corresponds to concrete cover, concrete strength, concrete density, bar diameter, bar surface conditions, bar location, and fiber type.

2.2.6.3. Canadian highway bridge design code

Canadian highway bridge design code (CSA S6-06) (Canadian Standards Association, 2006) recommends the bond strength of FRP bars to concrete in the following:

$$\tau_b = \frac{f_{cr}(d_{cs}+K_{tr}E_{FRP}/E_s)}{0.45\pi d_b k_1 k_4}, \tag{2-9}$$

where f_{cr} is the cracking strength of concrete (MPa); K_{tr} is transverse reinforcement index (mm) which is defined as $\frac{A_{tr}f_y}{10.5sn}$, where A_{tr} is the area of transverse reinforcement normal to the plane of splitting through the bars (mm^2), f_y is the yield strength of transverse reinforcement (MPa), *s* is the distance of center to center spacing of the transverse reinforcement (mm), *n* is the number of bars being developed along the plane of splitting; E_{FRP} is the modulus of elasticity of FRP bar (MPa); E_s is the modulus of elasticity of steel (MPa); k_1 is the bar location factor; k_4 is the bar surface profile factor. Thus, CSA S6-06 describes the bond strength as the function of concrete cover, concrete strength, concrete confinement provided by transverse reinforcement, bar diameter and bar surface conditions.

2.2.6.4. Japanese design code

The Japanese design code (JSCE) (Machida and Uomoto, 1997) derives the bond strength of FRP bars to concrete, mainly from the modification of the expression for steel bars, which is limited to splitting failure as given by Equation (2-7) in ACI 440.1R-06:

$$\tau_b = f_{bod}/\alpha_1, \tag{2-10}$$

where α_1 is a confinement modification factor defined in the following:

$\alpha_1 = 1.0$ for $k_c \leq 1.0$;

$\alpha_1 = 0.9$ for $1.0 < k_c \leq 1.5$;

$\alpha_1 = 0.8$ for $1.5 < k_c \leq 2.0$; (2-11)

$\alpha_1 = 0.7$ for $2.0 < k_c \leq 2.5$;

$\alpha_1 = 0.6$ for $k_c > 2.5$.

$$k_c = \frac{c}{d_b} + \frac{15A_t}{sd_b}\frac{E_t}{E_s}, \tag{2-12}$$

$$f_{bod} = \frac{0.28\alpha_2 f_c'^{2/3}}{1.3} \leq 3.2\ N/mm^2, \tag{2-13}$$

where c is the smaller of the bottom clear cover of the main reinforcement or half of the clear space between reinforcement being developed; A_t is the area of transverse reinforcement; s is the spacing of transverse reinforcement; E_t is the modulus of elasticity for the transverse reinforcement; E_s is the modulus of elasticity for the steel. f_{bod} is the designed bond strength of concrete; α_2 is the modification factor for bond strength (1.0 where bond strength is equal to or greater than that of deformed steel bars; otherwise value shall be reduced according to test results). It is clear that the bond strength of FRP bars defined in Japanese design code is a function of the concrete strength, the concrete cover, the concrete confinement provided by transverse reinforcement and the bar location.

2.2.6.5. Comparisons of national and international design specifications

National and international design specifications associated with the bond strength of GFRP bars to concrete have been discussed through Section 2.2.6. A comparison among these codes is summarized and listed in Table 2-1 to better understand the standardized language in bond strength, the factors that affect bond strength considered in the design standards, and their applicability.

It is clear that key factors such as, concrete strength, bar diameter, concrete cover and bar location are taken into account for all these standards. Embedment length is considered only in ACI 440.1R-06 standard for bond strength calculation. It is worth noting that the bar surface profile (spiral wrapped vs. helical lugged) did not appear to influence the bond strength, and it is necessary to be further investigated. Differently, more additional information for determination of bond strength, including fiber type used in reinforcement, and confinement provided by transverse reinforcement, is used in the Canadian or Japanese Codes, which is ignored in ACI 440.1R-06.

Table 2-1. Factors for determining bond strength in the national and international design codes

Design standards	Concrete strength	Bar diameter	Concrete cover	Bar location	Embedded length	Bar surface	Transverse confinement	Fiber type
ACI 440.1R-06	√	√	√	√	√	√	×	×
CSA S806-02	√	√	√	√	×	√	×	√
CSA S6-06	√	√	√	√	×	√	√	√
JSCE	√	√	√	√	×	×	√	×

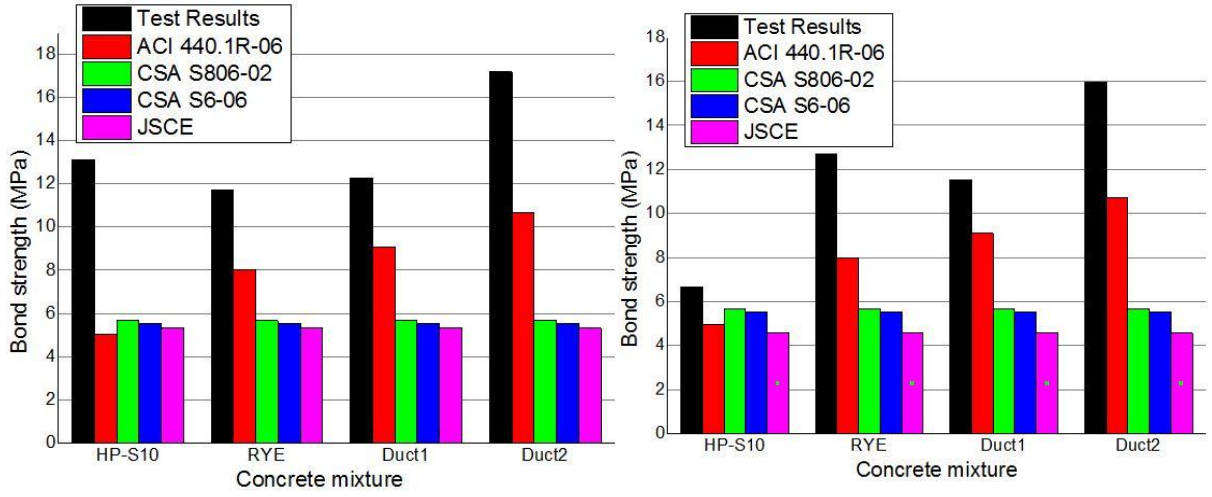

(a) d_b=15.9 mm (b) d_b=19.1 mm

Figure 2-7. Bond strength calculated in design standards (derived from Ametrano, 2011).

Further valuable information of these design codes, ACI 440.1R-06, CSA S806-02, CSA S6-06 and JSCE, for bond strength prediction was reported in (Ametrano, 2011), where the beam test was used. He documented his investigation on the bond strength of GFRP bars with two different bar sizes with diameters db =15.9 and 19.1 mm, and to four different concrete mixes, labeled as HP-S10, RYE, Duct1 and Duct2, with compression strength of 71.2, 115 (~130 MPa), 147.8 and 174.5 MPa, respectively. As clearly illustrated in Figure 2-7(a) and 2-7(b), bond strengths obtained from the tests are higher than those predicted through the four design standards, indicating that the codes is conservative, and the development length provided is sufficient for FRP bars to reach their ultimate stress prior to bond failure. Furthermore, the bond

strength predicted by ACI 440.1R-06 is closer to the test results. For another, the bond strength predicted by CSA S806-02, CSA S6-06 and JSCE differ little from each other.

2.3. Critical Factors and Their Impacts on Failure Modes and Bond Strength of GFRP Bars to Concrete

A data-driven parametric study was carried out for over 680 pullout-test specimens that were collected from available literatures. This database was valuable information for determining the critical factors that affect the bond behavior of GFRP bars to concrete and their corresponding failure modes and bond strength. The review demonstrated that GFRP bars to concrete commonly displays several bond failure modes, including pullout failure, splitting failure, anchorage failure, rebar fracture and peeling off of resin, while these bond failures and the bond strength are majorly associated with: concrete compressive strength, bar size, concrete cover, embedment length, bar spacing, and transverse reinforcements, as discussed in more detail below.

2.3.1. Failure Mode and Bond Strength Associated with Concrete Compressive Strength

2.3.1.1. Failure mode

Figure 2-8 was plotted to describe the relationship of the failure modes with respect to the concrete compressive strength. It is clear that both pullout and splitting failures are overwhelmingly dominant, accounting for over 80% of all the failure modes regardless of concrete strength. Specifically, pullout failure vs. concrete compressive strength displays an approximate normal distribution with a mean value of the concrete compressive strength ranging from 40 to 50 MPa. Splitting failure primarily falls into the range of the concrete compressive strength between 30 and 50 MPa. Differently, anchorage failure occurred when concrete has a higher compressive strength over 30 MPa. Rebar fracture was observed from about 32 cases that

compressive strength was at 30 MPa and 50 MPa, while 42 specimens failed by peeling off of resin at higher concrete strength at levels of 50 to 60 MPa.

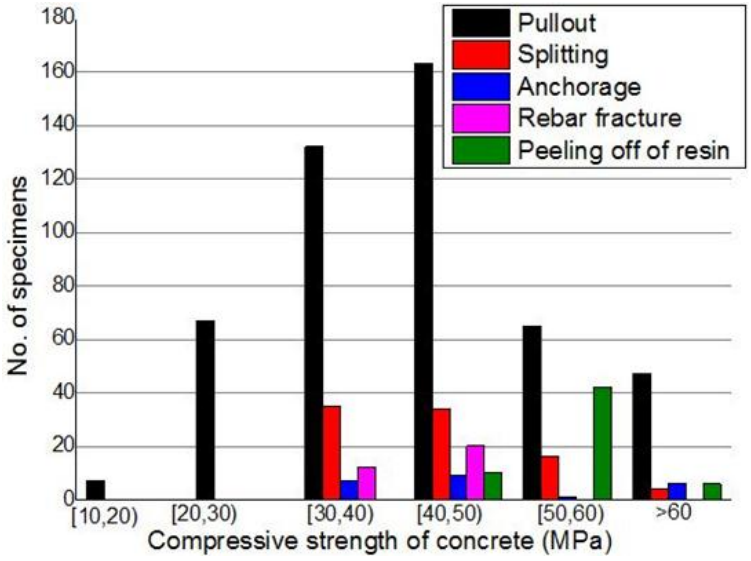

Figure 2-8. Failure modes associated with concrete compressive strength

2.3.1.2. Bond strength

The pullout and splitting failures are two major dominant failure modes, as stated in Section 3.11. Thus, the data mining from the literature mainly aligns with these two failures. Figure 2-9 displays the bond strength vs. the concrete compressive strength (in terms of $\sqrt{f_c'}$) curves of both pullout and concrete splitting, in which τ_b is the bond strength between concrete and GFRP bar, and f_c' refers to the concrete compressive strength at 28 days.

Clearly, large scatter data at both pullout and splitting failure still display the increase trendline with the increase of the concrete compressive strength, by certain proportionality to $\sqrt{f_c'}$, as observed in the literature (B Benmokrane and Tighiouart, 1996; Makitani et al., 1993; Okelo and Yuan, 2005; Tighiouart et al., 1998). It is usually GFRP bar is implemented in concrete products with a compressive strength below 55 MPa (8,000 psi) (Darwin et al., 1992;

Esfahani and Rangan, 1998; Orangun et al., 1977; Tepfers, 1973), which is confirmed by heavy data points falling within 27 to 55 MPa shown in Figure 2-9.

Davalos et al. (Davalos et al., 2012) summarized the relationship between the bond strength and $\sqrt{f_c'}$. Their findings indicated that the bond strengths predicted by design codes CSA-S806 and JSCE in Section 2.2.6.3 and 2.2.6.4 are conservative, whereas ACI 440 may not be conservative when concrete compressive strength is relatively low. By using the high-strength concrete over 55 MPa (8,000 psi), the bond strength predicted by ACI is more conservative than other design codes.

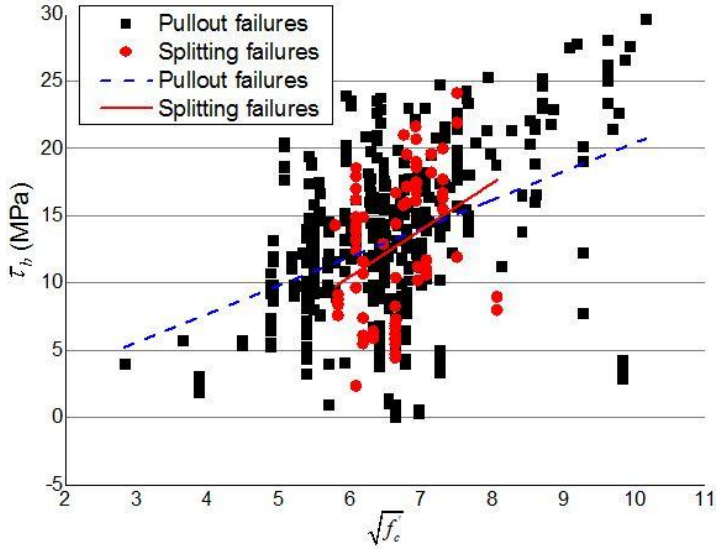

Figure 2-9. Bond strength versus concrete strength $\sqrt{f_c'}$

Note that the ratio of the bond strength to concrete strength, $\tau_b/\sqrt{f_c'}$, starts to decrease with the increase of the compressive strength after beyond 55 MPa (8,000 psi) (Azizinamini et al., 1993; Zuo, 1999; Zuo and Darwin, 2000). It is partly because higher concrete strength demands higher threshold for pulling out a bar, while the feature of high brittle for high strength concrete thus makes concrete more vulnerable to fail by coupled pullout with splitting failures. As a result, full capacity of pullout failures are less observed for high strength concrete. To

clarify this statement, the bond slip, s_b, associate with the testing data in the literature is plotted against the concrete strength $\sqrt{f_c'}$, as shown in Figure 2-10, where y axis is the normalized slip by s_b/l_d and l_d is the embedded length of a bar to concrete. With the increase of the compressive strength, particularly over 55 MPa (8,000 psi) shown in Figure 2-10, there is a significant drop in bond slip, suggesting that tests were mainly terminated by more sudden failures when concrete had a relative higher strength.

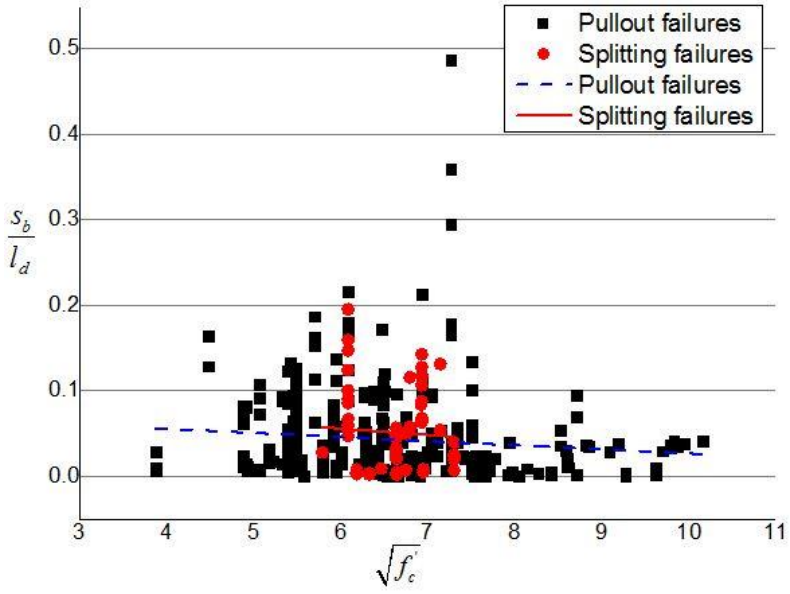

Figure 2-10. Normalized bond slip versus strength $\sqrt{f_c'}$

2.3.2. Failure Mode and Bond Strength Associated with Concrete Cover

2.3.2.1. Failure mode

Concrete cover is another critical factor that affects failure modes, bond strength and the durability of GFRP bar to concrete. Ehsani et al. (Ehsani et al., 1993) tested 48 GFRP bar reinforced concrete beams. Their test results indicated that specimens had splitting failures when concrete cover, c, is one time of the bar diameter ($c = 1.0d_b$), while pullout failures or even bar fracture were observed when concrete cover has at least twice of the bar diameter. Alves et al. (Alves et al., 2010) investigated bond characteristics of GFRP bars to concrete when subjected to

environmental and loading conditions. Two different bar diameter (15.9 and 18.9 mm) and three concrete covers ($1.5d_b$, $2.0d_b$ and $2.5d_b$) were included in their study. The findings showed that failure modes switched from typical splitting failure to pullout failure, with the increase of concrete cover. Moreover, the study confirmed that the clear concrete cover having the value of $2.0d_b$ ensure the pullout failure for 15.9-mm bar, while $2.5d_b$ for the 18.9-mm bar. It implied that increasing concrete cover leads to higher confinement pressure (bearing effect) on the GFRP bars, thereby reducing the possibility of developing more cracks in the concrete surrounding the bars and thus delaying the splitting failure.

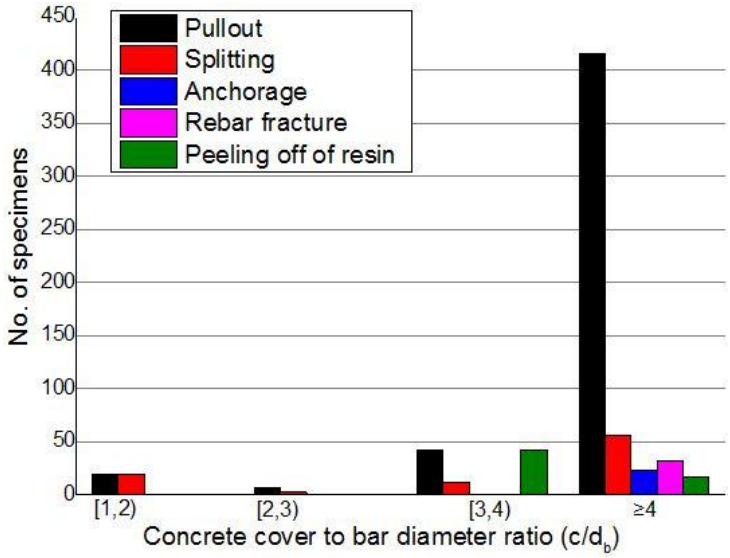

Figure 2-11. Failure mode associated with concrete cover

The summary of the data in the literature of concrete cover to failure modes of GFRP bar is plotted in Figure 2-11, in which x axis is defined by the normalized concrete cover, c/db, by bar diameter db. As clearly illustrated in Figure 2-11, particularly when the ratio of concrete cover to bar diameter is equal to or greater than four, over 400 specimens were failed by pulling out, reaching up to 60% of all over the database. Therefore, it implies that larger concrete cover provides higher confinement to the bar, thereby resulting in the more dominant pullout failure.

Otherwise, splitting failure occurs prior to pullout failure when concrete cover is not sufficient to apply adequate confinement to reinforcing bars.

2.3.2.2. Bond strength

Figure 2-12 shows the relationship of the bond strength (normalized by $\tau_b/\sqrt{f_c'}$) with concrete cover (c/d_b). High scatter data points account for high variation during tests, including varying specimen preparation, test conditions, methods and operational variation. There is still a basic increasing trendline with the increase of concrete cover, as illustrated in Figure 2-12. This trend is more clearly observed if test data are more comparable. For example, Aly et al. (Aly, 2007) tested six full-scale beams reinforced with GFRP bars to investigate the effects of concrete cover on their bond strength, and they observed that the specimens had a increase in bond strength by approximately 27%, as concrete cover increased from one to four times of the bar diameter. Clearly, sufficient concrete cover confines GFRP bar and allows the bar to develop higher bearing force, thereby resulting in the higher bond strength to concrete.

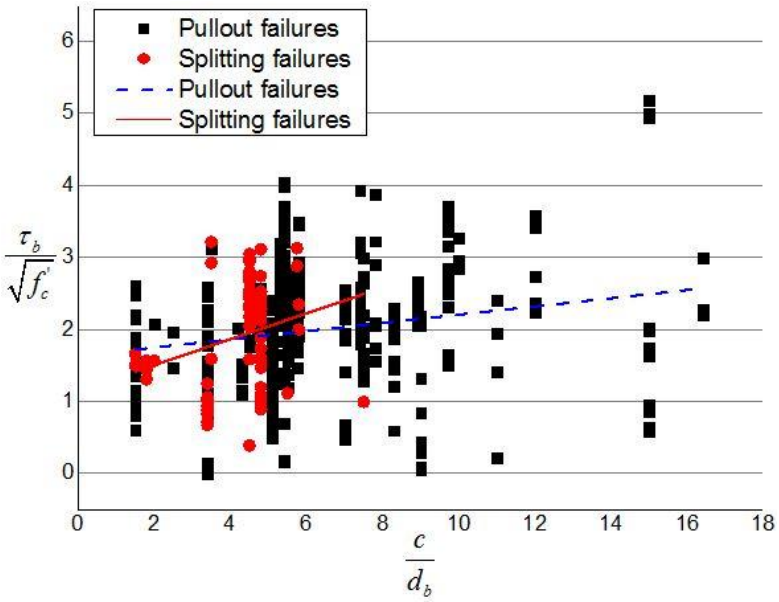

Figure 2-12. Normalized bond strength versus c/d_b

In addition, further information is gained from the correlation between the bond slip (s_b/l_d) and concrete cover (c/d_b), as shown in Figure 2-13. The slip decreased when concrete cover increased as expected. Also, the trendline of splitting failure (in solid lines) has a higher gradient than that of pullout failure, indicating that increasing concrete cover provide higher confinement, which prevents development of slip movement, and thus more likely fails by a sudden energy release.

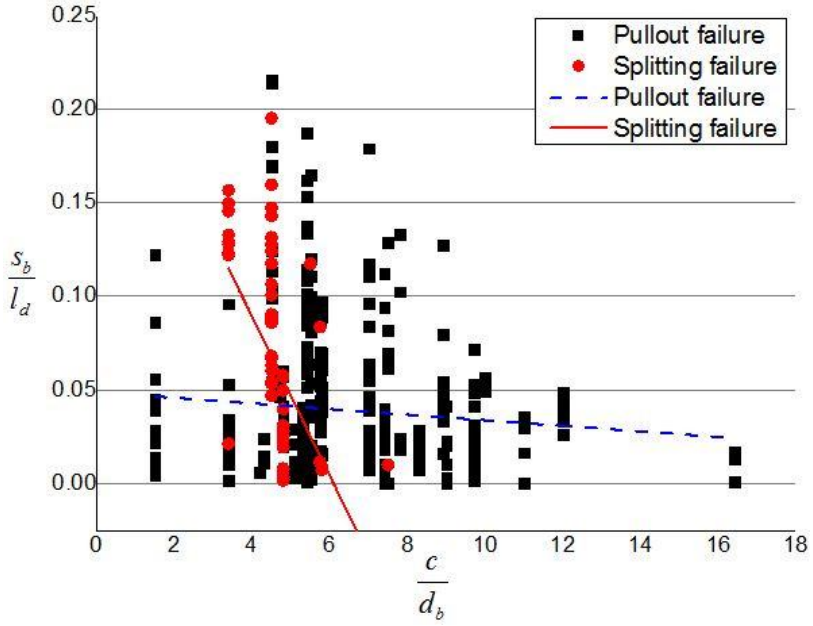

Figure 2-13. Normalized bond slip versus c/d_b

2.3.3. Failure Mode and Bond Strength Associated with Embedment Length

2.3.3.1. Failure mode

Similar to concrete cover, embedment length, l_d, is one of critical parameters that influence the bond strength of FRP bar to concrete. Figure 2-14 is plotted for the testing data associated with both pullout and splitting failures. Pullout failure dominates the failure modes, while approximately yielding a normal distribution with a mean value ranging from 5 to 6 (times of l_d/d_b). Such embedment (5 to 6 times of bar size d_b) responds for total amount of 256 specimens failed by pulling out, 54% of overall failure modes. It also implies that the

embedment length having five times of bar diameter enables to provide desirable bond pullout failure for GFRP bar to concrete.

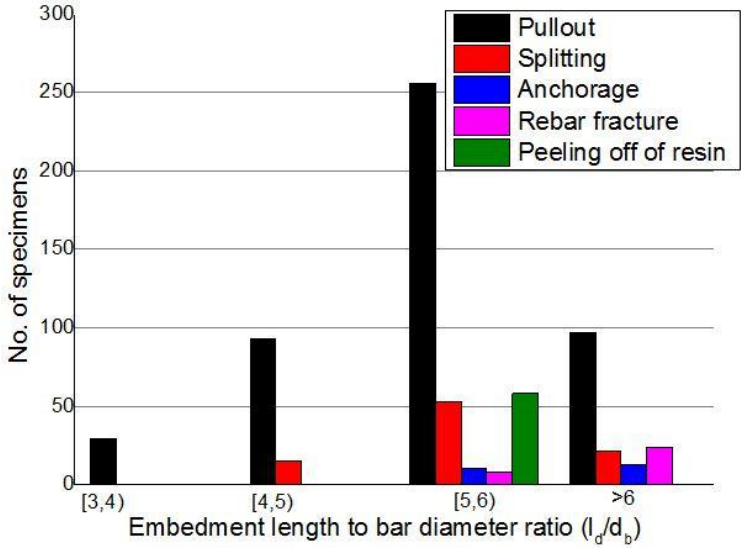

Figure 2-14. Failure mode associated with embedment length

2.3.3.2. Bond strength

Figure 2-15 plots the normalized bond strength vs. the normalized embedment length (l_d/d_b) under both pullout and splitting failures. The maximum average bond stress of GFRP bars to concrete, illustrated in Figure 2-15, decreases as the embedment length increases, similar to the previous observations for steel bars (Achillides and Pilakoutas, 2004; B Benmokrane and Tighiouart, 1996; Fava et al., 2016; Makitani et al., 1993; A Nanni et al., 1995; Tighiouart et al., 1998). It is mainly due to a nonlinear distribution of the bond stress along the reinforcing bar, as schematically shown in an inserted plot in Figure 2-15. As the embedment length increases, the stress yields the high unevenly distributed over a longer length, thereby resulting in the decrease in average bond stress. The identical conclusion can be drawn from the ACI 440 1R-06 in Section 2.2.1 and also most single cases confirm this observation. For example, Achillides et al. (Achillides and Pilakoutas, 2004) reported that the increase of the embedment length not only leads to the decrease of the maximum average developed bond stress of FRP bars, but also yields

the lower initial bond stiffness accordingly, which responds for high nonlinearly non-uniform distribution of the bond stress along the longer bar.

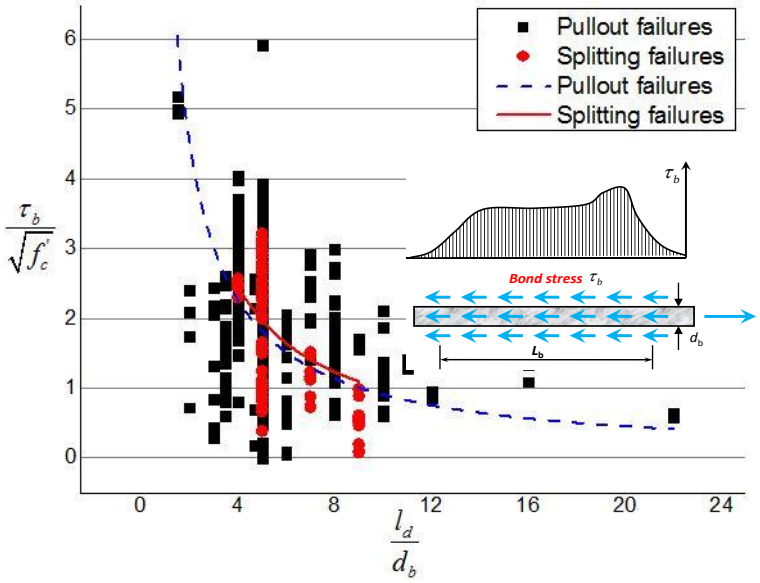

Figure 2-15. Normalized bond strength versus l_d/d_b

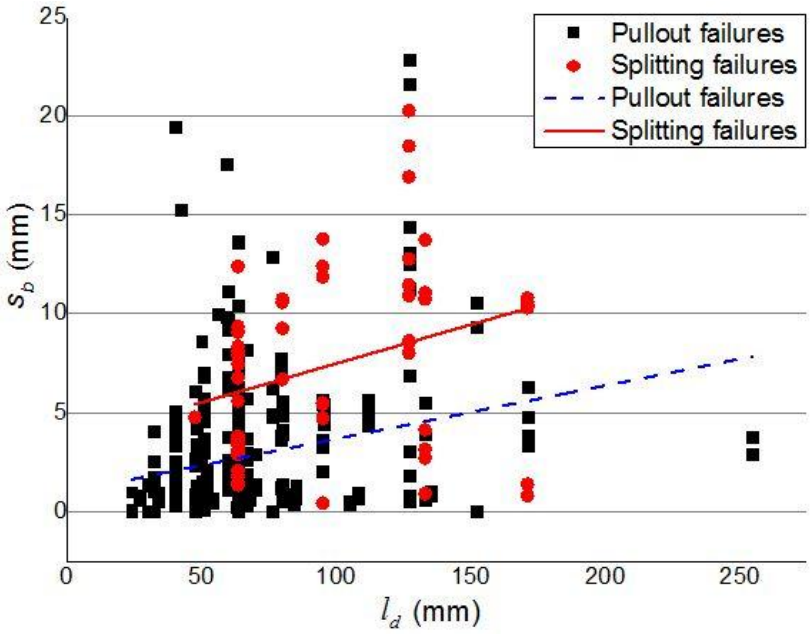

Figure 2-16. Bond slip versus l_d

On the other hand, the bond slip increased as the embedment increased, as shown in Figure 2-16. The longer embedded length yields relatively higher applied force, while the longer

length provides the longer "strain" length to develop deformation when subjected to higher applied force, and thus failure frequently occurs at the larger slip.

2.3.4. Failure Mode and Bond Strength Associated with Bar Diameter

2.3.4.1. Failure mode

Figure 2-17 presents the failure types with respect to the bar diameter. Even though there is no clear correlation between bar size and failure modes, pullout and splitting failures are still major failures through different bar size. Pullout failures respond for 500 out of 682 cases, in particular at bar diameter of 12 to 14 mm. It seems that there are increasing splitting failures as the increase of bar diameter, while other three failure modes were observed far less frequently, with 23 specimens for anchorage failure; 32 specimens for rebar fracture and 53 specimens for peeling off of resin.

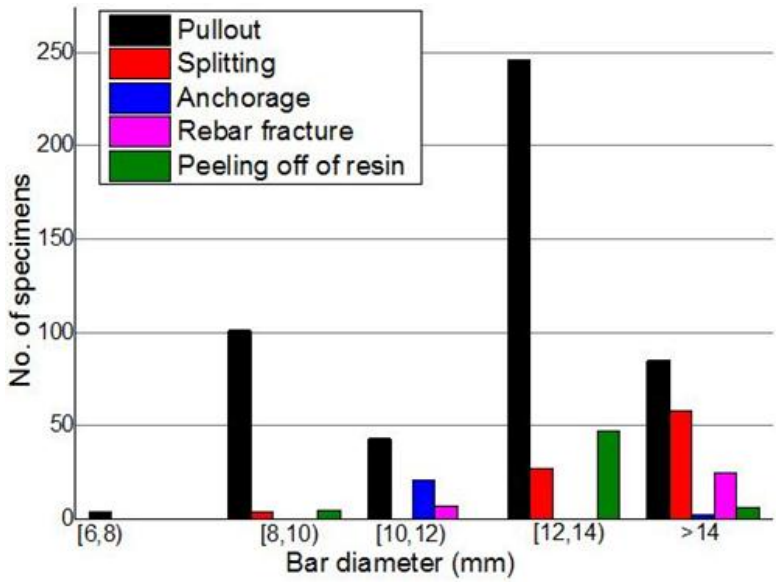

Figure 2-17. Failure modes associated with bar diameter

2.3.4.2. Bond strength

Figure 2-18 shows the relationship of bond strength (τ_b) with bar diameter (d_b). It is clear that the bond strength decreased as the bar diameter increased for both pullout and splitting

failures. It is partially because the increased bar diameter leads to the increased contact area with concrete, while naturally trap the void or other defects at the interface during concrete cast and construction (Alves et al., 2010; De Larrard et al., 1993; Quayyum, 2010), thereby statistically causing the higher possibility to form weak interface between the bar and concrete, and ultimately reducing to the lower average bond strength.

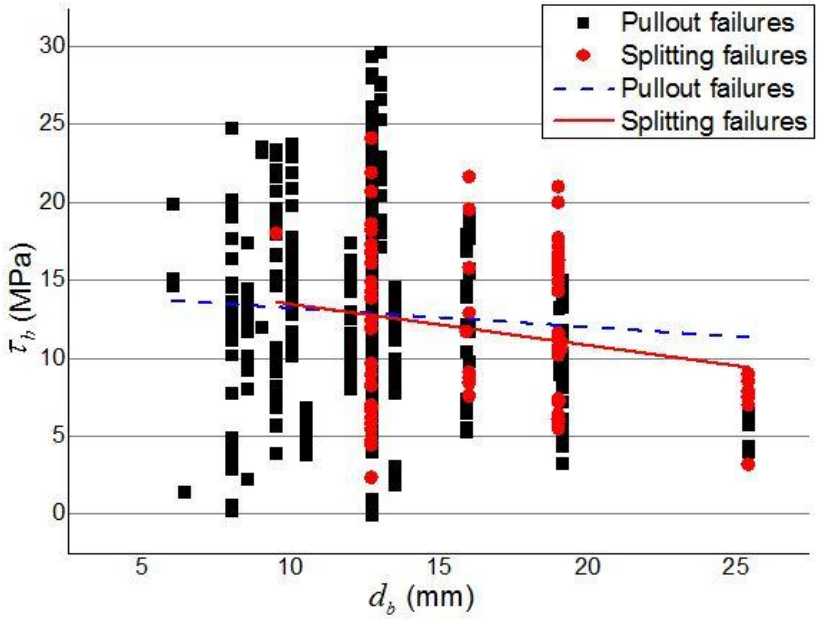

Figure 2-18. Bond strength versus d_b

2.3.5. Failure Mode and Bond Strength Associated with Bar Surface Conditions

2.3.5.1. Failure mode

Bar surface conditions in terms of ribbed, helically wrapped, sand coated, helically wrapped or sand coated are commonly used in direct pullout tests. Smooth surface is normally taken as a reference to quantify the effects of various surface treatments on bond behavior and failure modes. Figure 2-19 demonstrates the relationships between surface conditions and failure modes. Failure modes and surface conditions are assigned with the legends, as shown in Figure 2-19. For simplicity, the first term of the legends used represents the failure modes, while the

second term is for surface conditions: a) R = ribbed; b) HW = helically wrapped; c) SC = sand coated; d) HWSC = helically wrapped and sand coated; e) SW = spirally wrapped.

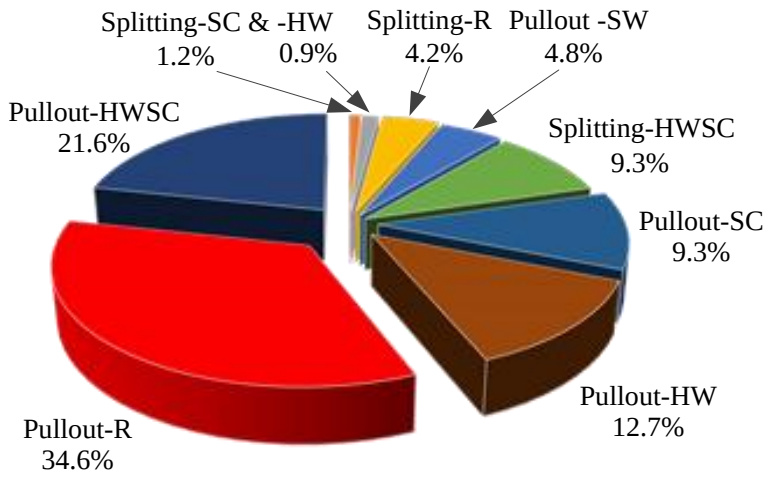

Figure 2-19. Two failure modes associated with varying bar surface conditions

Clearly, the pullout failure mode are over 84% of all cases, while the ribbed FRP bars (Pullout-R) occupied the largest proportion among all surface treatments, with about 35% of total failures. Helically wrapped and sand coated surface of GFRP bar (P-HW-SC) and P-HW are the second and third better surfaces to allow desirable mechanical interlocking, taking up about 22% and 13%, respectively. There are only 16% splitting failures, while similarly to its counterpart, helically wrapped and sand coated or ribbed surfaces are the major treatments. These surface conditions provide higher mechanically interlocking, which leads to relatively higher hoop stress and hence results in splitting failures.

2.3.5.2. Bond strength

FRP bar is manufactured to different deformed surface patterns, such as ribbed/lugged, indented, sand coated and spirally wrapped. The ACI 440.1R-06 states that surface textures of the FRP bar plays an important role in bond mechanism to concrete, even though no specific variable is included in the existing ACI code to account for the contribution. The CSA S806-02 specifies a coefficient factor (i.e., 1.0 for surface roughed or sand coated or braided surface; 1.05

for spiral pattern surfaces or ribbed surfaces; 1.8 for indented surfaces) for different bar surfaces for determining the development length of FRP bars.

Till now, there still remain opposite opinions about the effects of bar surfaces on the bond strength, as reported by different researchers. Wambeke et al. (Wambeke and Shield, 2006) summarized tests of 269 beam-type specimens, and concluded that bar surfaces have no effects on the bond strength of FRP bars to concrete. This was agreed with Mosley et al. (Mosley et al., 2008) who reported the identical conclusions based upon their beam splice tests for bond behaviors of both GFRP and AFRP bars. Differently, Baena et al. (Baena et al., 2009) performed 88 direct pullout tests for FRP bars, suggesting that surface treatments appear to influence the bond strength significantly. Also, Hao et al. (Hao et al., 2009) studied the ribbed GFRP bars with different rib height and spacing. Their findings showed that the surface macrotexture has high impact on the bond behavior, failure modes and the bond strength of GFRP bars to concrete.

2.3.6. Failure Mode and Bond Strength Associated with Enhancement of Concrete from Transverse Reinforcement

2.3.6.1. Enhancement from transverse reinforcement confinement

Transverse reinforcement provides confinement to concrete, which not only delays the splitting cracking but also changes the failure modes and bond-slip relationship by relatively higher ductile performance, thus increasing the bond strength and bond slip of reinforcing bars to concrete. With the help of the transverse reinforcement, as stated in the ACI 408R-06, the concrete is confined to prevent or delay a splitting failure, and thus it will develop higher bond stress to the bar and likely fail by bar pulling out.

On the other hand, some researchers, including Wambeke et al. (Wambeke and Shield, 2006), pointed out that such confinement from transversal reinforcement may not increase the

average bond stress of FRP bar effectively. Steel bar has apparent ribs and thus the transverse reinforcement can effectively apply higher bearing force on the steel ribs to develop the higher bond strength. However, the argument for FRP bar lies in the fact that a relative lower rib area in FRP bar may lead to relatively weaker bearing force, even though there is transverse reinforcement.

2.3.6.2. Enhancement from fiber-reinforced concrete matrix

Discrete fibers are usually used to mix in concrete, referred to fiber reinforced concrete, to enhance concrete tensile strength and toughness. Recently, fiber reinforced concrete has been accepted to improve bond behavior in FRP bar to concrete (Dancygier et al., 2010; Ding et al., 2014; Harajli et al., 2002; B. Kim et al., 2013; Plizzari, 1999; H. Wang and Belarbi, 2011, 2013; Won, Park, et al., 2008; Yang et al., 2012). Plizzari (Plizzari, 1999) and Harajli et al. (Harajli et al., 2002) reported that fibers increased the splitting bond strength and improved the ductility of bond failure as compared to plain concrete. Wang and Belarbi (H. Wang and Belarbi, 2011, 2013) investigated bond strength of GFRP and CFRP bars in both plain and fiber reinforced concrete when exposed to aggressive environments, including freeze-thaw cycles, and salt solutions. They found that the polypropylene fibers in concrete matrix significantly improved the bond capacity and their durability. The fiber-reinforce concrete specimens after environmental exposure only had a 6% reduction in ultimate bond strength, as compared to 28% reduction for plain concrete counterparts. Enhancement of the bond behavior and bond strength in fiber reinforced concretes are attributed to the restriction effects of polypropylene fibers to prevent and delay the crack development and propagation at both environmental exposure and direct pullout tests. Kim et al. (B. Kim et al., 2013) investigated 63 cubic fiber-reinforced-concrete specimens with GFRP bars embedded in them and concluded that with fiber addition (steel, PP and PVA fibers) in concrete,

both bond strength and crack development are significantly enhanced. Ding et al. (Ding et al., 2014) reported that the bond capacity of GFRP bars in concrete reinforced by hybrid fibers (both steel fibers and polypropylene fibers), was appeared to show equivalent or better performance than that of steel bars in concrete. Furthermore, the hybrid use of different fibers demonstrated significant influence on the post-peak bond behavior of GFRP bars in concrete matrix.

2.3.7. Failure Mode and Bond Strength Associated with Bar Casting Position

ACI 440.1R-06 states that bond strength of horizontal FRP bar, in particular at top location, may experience a high decrease in bond strength and thus a modification factor is stipulated for accounting for the location, similar to the identical requirements for determining the development length of reinforcing steel bar (in ACI 318-14). Previous tests from the literature (Ehsani et al., 1993) revealed that the top-cast bars had an approximately 66% decrease in bond strength as compared to that of the bottom-cast bars. Chaallal and Benmokrane (Chaallal and Benmokrane, 1993) investigated three bar diameters (No. 4-6) and recommended that the top-cast bar modification factor ranged from 1.08 to 1.38 for normal-strength concrete, while 1.11 to 1.22 for high-strength concrete. This modification factor was further revised through more tests by Wambeke and Shield (Wambeke and Shield, 2006), and use 1.5 for top-cast bars in ACI 440.1R-06, while 1.3 given in CSA S806-02.

2.4. Environmental Conditions and Their Impacts on Bond Behavior and Bond Strength of FRP Bars

2.4.1. Freeze-Thaw Cycles

Damage in concrete due to freeze-thaw cycles relies on the saturation of concrete. Freezing-thaw cycles have minimum adverse effects on dry concrete, even under a relative humidity to 75 ~ 80% (ACI Committee 201, 1977). Experience shows that accumulated damage

in concrete are frequently observed (Fursa et al., 2015; Yun, 2013), however, when the concrete is partially or fully saturated with freezing water or deicing chemicals. There still remain opposite opinions about the impacts of freeze-thaw cycles on FRP bar bond strength. Mashima et al. (Makitani et al., 1993) investigated bond behavior of CFRP, GFRP and AFRP bars to concrete when subjected to freeze-thaw cycles. The pullout test, they found that CFRP and GFRP bars performed well after the freezing and thawing cycle, without obvious reduction in bond capacity. However, the AFRP bar specimens lost about 40% bond strength after 600 freezing and thawing cycles. Micelli and Nanni (Micelli and Nanni, 2004) studied CFRP and GFRP bars to concrete exposed to 200 freeze-thaw cycles. They found that freeze-thaw cycles combined with humidity did not degrade the specimens. Similar conclusions were also observed from other researchers (Koller et al., 2007). Uomoto et al. (Uomoto et al., 2002) studied the effect of freezing and thawing on FRP bars by immersing FRP bars in a freeze-thaw water chamber over 300 cycles, indicating that the effects of freeze-thaw cycles are only limited to the surface of FRP material. Strength reduction of FRP bars was only within 8%.

On the other hand, Won and Park (Won et al., 2013) documented their study on GFRP bars to concrete under 300 freeze-thaw cycles. Their results stated that approximately 20% reduction in bond resistance was observed. The reason is that the water permeates through the voids (or new developed microcracks) in concrete matrix, while the growth of ice crystals during repeated freezing process generate high pressure to concrete, thus leading to microcracks in concrete. As a result, this will break down the interface between concrete and GFRP bar. Presence of concrete cracks also yields a low confinement to GFRP bar and thus causes less bond strength. Moreover, accumulated micro-/macro-cracks in concrete during the freezing and thawing cycles may allow other chemical solution to easily penetrate to concrete matrix, and

even easily degrade GFRP bar when penetrating through the interface, ultimately resulting in bar strength loss and the bond strength reduction.

It is clear that the freeze-thaw damage to concrete may be affected by complex interaction of numerous factors, including concrete permeability, temperature gradient, and air void systems. Alves et al. (Alves et al., 2010) tested GFRP bars embedded in concrete under sustained and fatigue loading conditions. Their results even supported that freeze-thaw cycles enhanced the bond strength between sand-coated GFRP bar and concrete by approximately 40%.

2.4.2. Wet-Dry Cycles

Wet-dry cycles are usually related to freeze-thaw cycles or solution conditions (Micelli and Nanni, 2004). Sen et al. (Sen et al., 1993) investigated durability of S-2 glass/epoxy pretensioned beams exposed to wet-dry cycles in a 15% salt solution. They reported that GFRP bars lost their effectiveness after 6 months for the precracked beams and 15 months for the uncracked beams.

Almusallam et al. (Almusallam and Al-Salloum, 2006) carried out experiment tests of concrete beams reinforced with GFRP bars when subjected to different certain stress levels. After wet-dry conditioning, there were significant loss in tensile strength of GFRP bars when subjected to sustained loads of 20-25% ultimate strength, about 27~29% after 4 months, 37~47% after 8 months and 47~55% after 16 months. Ahmed et al. (Ahmed et al., 2008) tested 90 concrete specimens with sand-coated GFRP reinforcing bars, which were subjected to 25 wet-dry cycles. The test results indicated that the bond strength and anchorage capacity of GFRP bars reduced over time when exposed to wet-dry cycles, which was also confirmed to the prediction by ACI-349-85.

2.4.3. Alkaline Solutions

Concrete has a high alkalinity with a pH value ranging from 10.5 to 13.5, while GFRP reinforcements embedded in concrete tend to degrade under high alkaline environment (Al-Salloum et al., 2013; Won, Lee, et al., 2008). Studies about effect of alkaline environment on FRP materials can be traced back to 1990's. Cowley and Robertson (Cowley and Robertson, 1991) studied the effect of the pH and temperature on GFRP composite in sodium hypochlorite solutions. The results showed that GFRP bar degraded proportionally with the increase of temperature over time after 4-month exposure to solutions with variable pH values (7 to 7.75, 8 to 8.85, 9 to 9.5, 10 to 10.5 and 11 to 11.5) under the temperature 99 ℃. Tannous and Saadatmanesh (Tannous and Saadatmanesh, 1999) tested 160 bar samples and 10 concrete beams to evaluate the durability of AR glass bars. The specimens were exposed to solutions with the pH of 12 at temperature of 25 and 60 ℃, respectively. Significant loss of strength of AR glass bars was observed, indicating AR glass did not improve resistance in alkaline concrete environment. Also, similar studies related to alkali attack to GFRP bars were conducted by many researchers (Abbasi and Hogg, 2005; Brahim Benmokrane et al., 2002; H.-Y. Kim et al., 2008; Micelli and Nanni, 2004; Nkurunziza et al., 2005; Zhou et al., 2012). Chen et al. (Chen et al., 2007) conducted five types of solutions to simulate environmental conditions for both bare FRP (GFRP and CFRP) bars and FRP-concrete elements. Solution 1 was tap water to simulate high humidity. Solution 2 was made with a pH value of 13.6 to simulate the pore solution of normal concrete, while solution 3 with a pH value of 12.7 was aimed for high-performance concrete. Solution 4 consisted of sodium chloride (NaCI) and sodium sulfate (Na2SO4) was to simulate ocean water. Solution 5 included sodium chloride (NaCI) and potassium hydroxide (KOH) with a pH value of 13, and was to simulate concrete pore solution with chloride from deicing salts. In addition,

elevated temperatures of 40 and 60 ℃ were employed to accelerate the test process. The results showed that GFRP bars failed with separation of fibers and rupture of fiber bundle. A reduction of 4% for CFRP bars and 36% for GFRP bars in tensile strength were observed in solution 2 at 60 ℃. Furthermore, bond strength of GFRP bars to concrete decreased by approximately 12%. Alkali attacks to GFRP bars may have more severe adverse effects on the GFRP bar reinforced concrete durability, as compared to the impacts of wet-dry and freeze-thaw cycles.

On the other hand, the work undertaken by ISIS Canada (ISIS Canada. ISIS Canada, 2001) on the long-term full size tests of RC structures over ten years claimed that the GFRP flexural tension reinforcing bars are durable and highly compatible with concrete material in field structures (A Mufti et al., 2005; Aftab Mufti et al., 2005; Mufti et al., 2001). Those engineering structures were exposed to natural environmental conditions including de-icing salt, freeze-thaw and wet-dry cycles, thermal range from -35 ℃ to 35 ℃ for a duration of five to eight years. A set of analytical approaches such as Scanning Electron Microscopy (SEM), Energy Dispersive X-ray (EDX), Optical Microscopy (OM), Fourier Transformed Infrared Spectroscopy, were used to monitor and detect the degradation state of GFRP material. Different from laboratory test conclusions, there was no obvious degradation of the GFRP reinforcements. Particularly, the manufacturing process in terms of the curing ratio (96 percent or above) is of central importance to ensure the resin system to resist the chemical attack and avoid moisture absorption.

2.4.4. High Temperatures

The Coefficient of thermal expansion (CTE) of steel bars in concrete is similar to surrounding concrete. Thus, there are negligible stresses built up in the interface between steel and concrete, when subjected to thermal loading. However, GFRP reinforcements (with resins)

have much larger CTE, as compared to concrete. Accordingly, when ambient temperature vibrates, GFRP bar reinforced concrete may experience high thermal stresses, ultimately resulting in splitting cracks (Galati et al., 2006; R. Masmoudi et al., 2005).

Glass fibers have high reliable mechanical properties under high temperature up to 250 ℃ (Yamasaki et al., 1993). Polymer resins (e.g., vinyl ester and polyester resins) in GFRP bar may, however, turn soft with high viscoelasticity, but with decreasing mechanical performance (strength and stiffness), if ambient temperature reaches up to or even over the glass transition temperature (Fried, 2014). Also the resins may experience failures, such as matrix hardening, microcracking and fiber-matrix debonding when exposed to sub-zero temperature (Karbhari et al., 2003). Kumahara et al. (Kumahara et al., 1993) conducted high-temperature tests of FRP bars and reported that there was a reduction of about 20% in the tensile strength for CFRP and GFRP bars at a temperature of 250 ℃, and about 60% for AFRP bars. It was expected that failure may occur firstly in resin matrix rather than fibers. Similar conclusions of tensile strength loss was also observed by Alsayed et al (Alsayed et al., 2012).

Katz et al. (A Katz, 1999; Ammon Katz et al., 1999) investigated the GFRP bar bond behavior in concrete in terms of bond strength, pre-peak and post-peak performance under the temperature ranging from 20 to 250 ℃. It appeared to have an 80-90% reduction in bond strength. The load-slip curve exhibited two different stages. At the first stage prior to pre-peak, the load-slip curve has a gradually decreasing slope as temperature increased. It implied that the GFRP bar stiffness decrease with the increase of the temperature. At the second stage (post-peak), the slope decreased moderately at elevated temperature (200~250 ℃) than that at room temperature (20 ℃). It mainly because of a weakened wedging effect of GFRP bar to concrete at

elevated temperature (A Katz, 1999; Ammon Katz et al., 1999). Identical results were observed by Wang et al. (Y. Wang et al., 2007) and Carvelli et al. (Carvelli et al., 2013).

By use of this thermal feature in GFRP bar, high temperature is often implemented as accelerated testing to predict long-term (75- to 100-year) durability of FRP bar reinforced concrete (Belarbi and Wang, 2011; Chen et al., 2007; Gonenc, 2003; Robert and Benmokrane, 2010).

2.5. Conclusions

This section presented an overall review of bond behavior of GFRP bar to concrete, and the associated durability. Some conclusions can be drawn as follows:

1. There are still no universal analytical models that can be applicable to general bond-slip behavior of GFRP bar to concrete. BPE modified model and CMR model have relatively simple form and reliable results that can be applied to investigate bond stress-slip process. The fitting parameters, α, β and s_r, specified in these two models are generated based on the literature, and the suggested values are classified based on different bar diameters and surface treatments, if tests data are not available.

2. Bond strength of GFRP to concrete has been specified in the national and international design codes and is summarized to ensure engineers to better understand their applicability. Comparisons between different design standards regarding bond strength prediction show that four key factors, including concrete strength, bar diameter, concrete cover and bar location, are taken into account in all these standards. Embedment length is considered only in ACI 440 standard for bond strength calculation. Differently, more information (bar surface profile, fiber type used in reinforcement, and confinement provided by transverse reinforcement) is considered in the Canadian or Japanese Codes, which is ignored in ACI 440. Moreover, the equations

regarding bond strength provided in ACI 440 is specific to splitting failure and hence, formula for pullout failure needs to be developed for general purpose.

3. Over 600 pullout-test specimens were mined from the literature and presented a comprehensive parametric study from a statistical point of view. All data supported that pullout and splitting failures are overwhelmingly dominant over all of the failure modes. Factors that affect the bond behavior, failure modes and bond strength of GFRP bar to concrete are identified and quantitatively plotted for ensuring engineers to fully understand their impacts. Specifically, bond strength has linear relationships with critical factors: a) concrete compressive strength; b) concrete cover; and c) bar size. There is a nonlinear relationship between the bond strength and embedment length. Moreover, discrete fiber or transverse reinforcement is accepted as an effective solution to increase the bond strength of GFRP bar to concrete.

4. Bond degradations under environmental conditions, such as freezing-thawing cycling, wet-dry cycling, alkaline solutions and high temperature are summarized. Environmental damage to concrete may be affected by complex interaction of numerous factors. Thus, there still remain opposite opinions in the effects of environmental conditions, such as freeze-thaw and wet-dry cycles, on the bond strength. Some studies revealed that alkaline solution or high temperature leads to significant loss of both tensile and bond strength. Future studies are required to determine the combined environmental effects.

2.6. References

Abbasi, A., and Hogg, P. J. (2005). Temperature and environmental effects on glass fibre rebar: modulus, strength and interfacial bond strength with concrete. Composites Part B: Engineering, 36(5), 394-404.

Achillides, Z., and Pilakoutas, K. (2004). Bond behavior of fiber reinforced polymer bars under direct pullout conditions. Journal of Composites for Construction, 8(2), 173-181.

ACI 408 Committee. (2003). Bond and Development of Straight Reinforcing Bars in Tension (ACI 408R-03). American Concrete Institute, Detroit, Michigan, US.

ACI Committee 201. (1977). Guide to Durable Concrete. Paper presented at the ACI Journal Proceedings.

ACI Committee. (2006). Guide for the design and construction of structural concrete reinforced with FRP bars. ACI 440.1 R, 6.

Ahmed, E. A., El-Salakawy, E. F., and Benmokrane, B. (2008). Tensile capacity of GFRP postinstalled adhesive anchors in concrete. Journal of Composites for Construction, 12(6), 596-607.

Al-Salloum, Y. A., El-Gamal, S., Almusallam, T. H., Alsayed, S. H., and Aqel, M. (2013). Effect of harsh environmental conditions on the tensile properties of GFRP bars. Composites Part B: Engineering, 45(1), 835-844.

Almusallam, T. H., and Al-Salloum, Y. A. (2006). Durability of GFRP rebars in concrete beams under sustained loads at severe environments. Journal of Composite Materials, 40(7), 623-637.

Alsayed, S., Al-Salloum, Y., Almusallam, T., El-Gamal, S., and Aqel, M. (2012). Performance of glass fiber reinforced polymer bars under elevated temperatures. Composites Part B: Engineering, 43(5), 2265-2271.

Alves, J., El-Ragaby, A., and El-Salakawy, E. (2010). Durability of GFRP bars' bond to concrete under different loading and environmental conditions. Journal of Composites for Construction.

Aly, R. (2007). Stress along tensile lap-spliced fibre reinforced polymer reinforcing bars in concrete. Canadian Journal of Civil Engineering, 34(9), 1149-1158.

Ametrano, D. (2011). Bond characteristics of glass fibre reinforced polymer bars embedded in high performance and ultra-high performance concrete. Ryerson University, Toronto, Ontario, Canada, 1-132.

Antonietta Aiello, M., Leone, M., and Pecce, M. (2007). Bond performances of FRP rebars-reinforced concrete. Journal of Materials in Civil Engineering, 19(3), 205-213.

Azizinamini, A., Stark, M., Roller, J. J., and Ghosh, S. (1993). Bond performance of reinforcing bars embedded in high-strength concrete. ACI Structural Journal, 90(5).

Baena, M., Torres, L., Turon, A., and Barris, C. (2009). Experimental study of bond behaviour between concrete and FRP bars using a pull-out test. Composites Part B: Engineering, 40(8), 784-797.

Ballinger, C. A. (1991). Development of composites for civil engineering. Paper presented at the Advanced Composites Materials in Civil Engineering Structures.

Bedard, C. (1992). Composite reinforcing bars: assessing their use in construction. Concrete International, 14(1), 55-59.

Belarbi, A., and Wang, H. (2011). Bond durability of FRP bars embedded in fiber-reinforced concrete. Journal of Composites for Construction, 16(4), 371-380.

Benmokrane, B., and Tighiouart, B. (1996). Bond strength and load distribution of composite GFRP reinforcing bars in concrete. ACI Materials Journal, 93(3).

Benmokrane, B., Wang, P., Ton-That, T. M., Rahman, H., and Robert, J.-F. (2002). Durability of glass fiber-reinforced polymer reinforcing bars in concrete environment. Journal of Composites for Construction, 6(3), 143-153.

Brown, V. L., and Bartholomew, C. L. (1993). FRP reinforcing bars in reinforced concrete members. ACI Materials Journal, 90(1).

Canadian Standards Association. (2002). Design and construction of building components with fibre-reinforced polymers: Canadian Standards Association.

Canadian Standards Association. (2006). Canadian highway bridge design code: Canadian Standards Association.

Carvelli, V., Pisani, M. A., and Poggi, C. (2013). High temperature effects on concrete members reinforced with GFRP rebars. Composites Part B: Engineering, 54, 125-132.

Chaallal, O., and Benmokrane, B. (1993). Pullout and bond of glass-fibre rods embedded in concrete and cement grout. Materials and Structures, 26(3), 167-175.

Charles, R. (2012). The strength of silicate glasses and some crystalline oxides. Paper presented at the ICF0, Swampscott-MA (USA) 1959.

Chen, Y., Davalos, J. F., Ray, I., and Kim, H.-Y. (2007). Accelerated aging tests for evaluations of durability performance of FRP reinforcing bars for concrete structures. Composite Structures, 78(1), 101-111.

Cosenza, E., Manfredi, G., and Realfonzo, R. (1995). Analytical modelling of bond between FRP reinforcing bars and concrete. Paper presented at the Non-Metallic (FRP) Reinforcement for Concrete Structures: Proceedings of the Second International RILEM Symposium.

Cosenza, E., Manfredi, G., and Realfonzo, R. (1997). Behavior and modeling of bond of FRP rebars to concrete. Journal of Composites for Construction, 1(2), 40-51.

Cowley, T., and Robertson, M. (1991). Effect of pH and temperature on fiberglass-reinforced composites in sodium hypochlorite solutions. Materials performance, 30(7), 46-49.

Dancygier, A. N., Katz, A., and Wexler, U. (2010). Bond between deformed reinforcement and normal and high-strength concrete with and without fibers. Materials and Structures, 43(6), 839-856.

Daniali, S. (1992). Development length for fiber-reinforced plastic bars. Paper presented at the Advanced Composite Materials in Bridges and Structures.

Darwin, D., McCabe, S. L., Idun, E. K., and Schoenekase, S. P. (1992). Development length criteria: bars not confined by transverse reinforcement. ACI Structural Journal, 89(6).

Davalos, J. F., Chen, Y., and Ray, I. (2012). Long-term durability prediction models for GFRP bars in concrete environment. Journal of Composite Materials, 46(16), 1899-1914.

De Larrard, F., Shaller, I., and Fuchs, J. (1993). Effect of the bar diameter on the bond strength of passive reinforcement in high-performance concrete. ACI Materials Journal, 90(4).

DeFreese, J. M., and Roberts-Wollmann, C. L. (2002). Glass fiber reinforced polymer bars as top mat reinforcement for bridge decks.

Ding, Y., Ning, X., Zhang, Y., Pacheco-Torgal, F., and Aguiar, J. (2014). Fibres for enhancing of the bond capacity between GFRP rebar and concrete. Construction and Building Materials, 51, 303-312.

Ehsani, M., Saadatmanesh, H., and Tao, S. (1993). Bond of GFRP rebars to ordinary-strength concrete. ACI Special Publication, 138.

Esfahani, M. R., and Rangan, B. V. (1998). Local bond strength of reinforcing bars in normal strength and high-strength concrete (HSC). ACI Structural Journal, 95(2).

Fava, G., Carvelli, V., and Pisani, M. A. (2016). Remarks on bond of GFRP rebars and concrete. Composites Part B: Engineering, 93, 210-220.

Faza, S. S., and GangaRao, H. V. (1991). Bending and bond behavior of concrete beams reinforced with plastic rebars. Transportation Research Record(1290).

French, C. (2003). Durability of concrete structures. Structural Concrete, 4(3), 101-107.

Fried, J. R. (2014). Polymer science and technology: Pearson Education.

Fursa, T., Utsyn, G., Korzenok, I., and Petrov, M. (2015). Using electric response to mechanical impact for evaluating the durability of the GFRP-concrete bond during the freeze-thaw process. Composites Part B: Engineering.

Galati, N., Nanni, A., Dharani, L. R., Focacci, F., and Aiello, M. A. (2006). Thermal effects on bond between FRP rebars and concrete. Composites Part A: Applied Science and Manufacturing, 37(8), 1223-1230.

Gonenc, O. (2003). Durability and service life prediction of concrete reinforcing materials. University of Wisconsin-Madison.

Hao, Q., Wang, Y., He, Z., and Ou, J. (2009). Bond strength of glass fiber reinforced polymer ribbed rebars in normal strength concrete. Construction and Building Materials, 23(2), 865-871.

Harajli, M., Hamad, B., and Karam, K. (2002). Bond-slip response of reinforcing bars embedded in plain and fiber concrete. Journal of Materials in Civil Engineering, 14(6), 503-511.

ISIS Canada. ISIS Canada, D. M. N. (2001). Strengthening reinforcing concrete structures with externally bonded fiber reinforced polymers. Canadian Network of Centers of Excellence on Intelligent Sensing for Innovative Structures, ISIS Canada Corporation, Winnipeg, Manitoba, Canada.

Karbhari, V., Chin, J., Hunston, D., Benmokrane, B., Juska, T., Morgan, R., et al. (2003). Durability gap analysis for fiber-reinforced polymer composites in civil infrastructure. Journal of Composites for Construction, 7(3), 238-247.

Katz, A. (1999). Bond mechanism of FRP rebars to concrete. Materials and Structures, 32(10), 761-768.

Katz, A., Berman, N., and Bank, L. C. (1999). Effect of high temperature on bond strength of FRP rebars. Journal of Composites for Construction, 3(2), 73-81.

Kim, B., Doh, J.-H., Yi, C.-K., and Lee, J.-Y. (2013). Effects of structural fibers on bonding mechanism changes in interface between GFRP bar and concrete. Composites Part B: Engineering, 45(1), 768-779.

Kim, H.-Y., Park, Y.-H., You, Y.-J., and Moon, C.-K. (2008). Short-term durability test for GFRP rods under various environmental conditions. Composite Structures, 83(1), 37-47.

Koch, G. H., Brongers, M. P., Thompson, N. G., Virmani, Y. P., and Payer, J. H. (2002). Corrosion cost and preventive strategies in the United States.

Koller, R., Chang, S., and Xi, Y. (2007). Fiber-reinforced polymer bars under freeze-thaw cycles and different loading rates. Journal of Composite Materials, 41(1), 5-25.

Kumahara, S., Masuda, Y., Tanano, H., and Shimizu, A. (1993). Tensile strength of continuous fiber bar under high temperature. ACI Special Publication, 138.

Lee, J.-Y., Kim, T.-Y., Kim, T.-J., Yi, C.-K., Park, J.-S., You, Y.-C., et al. (2008). Interfacial bond strength of glass fiber reinforced polymer bars in high-strength concrete. Composites Part B: Engineering, 39(2), 258-270.

Lin, X., and Zhang, Y. (2014). Evaluation of bond stress-slip models for FRP reinforcing bars in concrete. Composite Structures, 107, 131-141.

Machida, A., and Uomoto, T. (1997). Recommendation for design and construction of concrete structures using continuous fiber reinforcing materials (Vol. 23): Research Committee on Continuous Fiber Reinforcing Materials, Japan Society of Civil Engineers.

Makitani, E., Irisawa, I., and Nishiura, N. (1993). Investigation of bond in concrete member with fiber reinforced plastic bars. ACI Special Publication, 138.

Malvar, L. J. (1994). Bond stress-slip characteristics of FRP rebars: DTIC Document.

Masmoudi, A., Masmoudi, R., and Ouezdou, M. B. (2010). Thermal effects on GFRP rebars: experimental study and analytical analysis. Materials and Structures, 43(6), 775-788.

Masmoudi, R., Masmoudi, A., Ouezdou, M. B., and Daoud, A. (2011). Long-term bond performance of GFRP bars in concrete under temperature ranging from 20 C to 80 C. Construction and Building Materials, 25(2), 486-493.

Masmoudi, R., Zaidi, A., and Gérard, P. (2005). Transverse thermal expansion of FRP bars embedded in concrete. Journal of Composites for Construction, 9(5), 377-387.

Micelli, F., and Nanni, A. (2004). Durability of FRP rods for concrete structures. Construction and Building Materials, 18(7), 491-503.

Mijovic, J. (1985). Interplay of physical and chemical aging in graphite/epoxy composites. Journal of Composite Materials, 19(2), 178-191.

Mosley, C. P., Tureyen, A. K., and Frosch, R. J. (2008). Bond strength of nonmetallic reinforcing bars. ACI Structural Journal, 105(5).

Mufti, A., Benmokrane, B., Boulfiza, M., Bakht, B., and Breyy, P. (2005). Field study on durability of GFRP reinforcement. Paper presented at the International Bridge Deck Workshop, Winnipeg, Manitoba, Canada.

Mufti, A., Onofrei, M., Benmokrane, B., Banthia, N., Boulfiza, M., Newhook, J., et al. (2005). Durability of GFRP reinforced concrete in field structures. Paper presented at the Proceedings of the 7th International Symposium on Fiber-Reinforced Polymer Reinforcement for Reinforced Concrete Structures (FRPRCS-7), Kansas City, Mo.

Mufti, A. A., Rizkalla, S., and Canada, I. (2001). Reinforcing Concrete Structures with Fibre Reinforced Polymers [computer File]: ISIS Canada.

Nanni, A., Al-Zaharani, M., Al-Dulaijan, S., Bakis, C., and Boothby, I. (1995). Bond of FRP reinforcement to concrete-experimental results. Paper presented at the Non-Metallic (FRP) Reinforcement for Concrete Structures: Proceedings of the Second International RILEM Symposium.

Nanni, A., De Luca, A., and Zadeh, H. J. (2014). Reinforced Concrete with FRP Bars: Mechanics and Design: CRC Press.

Nkurunziza, G., Debaiky, A., Cousin, P., and Benmokrane, B. (2005). Durability of GFRP bars: A critical review of the literature. Progress in structural engineering and materials, 7(4), 194-209.

Okelo, R., and Yuan, R. L. (2005). Bond strength of fiber reinforced polymer rebars in normal strength concrete. Journal of Composites for Construction.

Orangun, C., Jirsa, J., and Breen, J. (1977). A reevaulation of test data on development length and splices. Paper presented at the ACI Journal Proceedings.

Pecce, M., Manfredi, G., Realfonzo, R., and Cosenza, E. (2001). Experimental and analytical evaluation of bond properties of GFRP bars. Journal of Materials in Civil Engineering, 13(4), 282-290.

Pepe, M., Mazaheripour, H., Barros, J., Sena-Cruz, J., and Martinelli, E. (2013). Numerical calibration of bond law for GFRP bars embedded in steel fibre-reinforced self-compacting concrete. Composites Part B: Engineering, 50, 403-412.

Plizzari, G. (1999). Bond and splitting crack development in normal and high strength fiber reinforced concrete. Paper presented at the 13th Engrg mechanics division conference—EMD99, Baltimore (MD, USA), on CD.

Quayyum, S. (2010). Bond behaviour of fibre reinforced polymer (FRP) rebars in concrete.

Robert, M., and Benmokrane, B. (2010). Effect of aging on bond of GFRP bars embedded in concrete. Cement and Concrete Composites, 32(6), 461-467.

Saadatmanesh, H., and Ehsani, M. R. (1989). Application of fiber-composites in Civil Engineering. Paper presented at the Structural materials.

Sen, R., Mariscal, D., and Shahawy, M. (1993). Durability of fiberglass pretensioned beams. ACI Structural Journal, 90(5).

Shield, C., French, C., and Retika, A. (1997). Thermal and mechanical fatigue effects on GFRP rebar-concrete bond. Paper presented at the Proceedings of the 3rd international symposium on non-metallic (FRP) reinforcement for concrete structures (FRPRCS-3), Sapporo.

Tannous, F. E., and Saadatmanesh, H. (1999). Durability of AR glass fiber reinforced plastic bars. Journal of Composites for Construction, 3(1), 12-19.

Tepfers, R. (1973). A theory of bond applied to overlapped tensile reinforcement splices for deformed bars: Chalmers University of Technology Goteborg.

Tighiouart, B., Benmokrane, B., and Gao, D. (1998). Investigation of bond in concrete member with fibre reinforced polymer (FRP) bars. Construction and Building Materials, 12(8), 453-462.

Tuttle, M. (1996). A framework for long-term durability predictions of polymeric composites. Progress in Durability Analysis of Composite Systems. Rotterdam, 196-176.

Uomoto, T., Mutsuyoshi, H., Katsuki, F., and Misra, S. (2002). Use of fiber reinforced polymer composites as reinforcing material for concrete. Journal of Materials in Civil Engineering, 14(3), 191-209.

Wambeke, B. W., and Shield, C. K. (2006). Development length of glass fiber-reinforced polymer bars in concrete. ACI Structural Journal, 103(1).

Wang, H., and Belarbi, A. (2011). Ductility characteristics of fiber-reinforced-concrete beams reinforced with FRP rebars. Construction and Building Materials, 25(5), 2391-2401.

Wang, H., and Belarbi, A. (2013). Flexural durability of FRP bars embedded in fiber-reinforced-concrete. Construction and Building Materials, 44, 541-550.

Wang, Y., Wong, P., and Kodur, V. (2007). An experimental study of the mechanical properties of fibre reinforced polymer (FRP) and steel reinforcing bars at elevated temperatures. Composite Structures, 80(1), 131-140.

Won, J.-P., Lee, S.-J., Kim, Y.-J., Jang, C.-I., and Lee, S.-W. (2008). The effect of exposure to alkaline solution and water on the strength–porosity relationship of GFRP rebar. Composites Part B: Engineering, 39(5), 764-772.

Won, J.-P., Park, C.-G., Kim, H.-H., Lee, S.-W., and Jang, C.-I. (2008). Effect of fibers on the bonds between FRP reinforcing bars and high-strength concrete. Composites Part B: Engineering, 39(5), 747-755.

Won, J.-P., Park, C.-G., Lee, S.-J., and Hong, B.-T. (2013). Durability of hybrid FRP reinforcing bars in concrete structures exposed to marine environments. International Journal of Structural Engineering, 4(1-2), 63-74.

Yamasaki, Y., Masuda, Y., Tanano, H., and Shimizu, A. (1993). Fundamental properties of continuous fiber bars. ACI Special Publication, 138.

Yan, F., and Lin, Z. (2016). New strategy for anchorage reliability assessment of GFRP bars to concrete using hybrid artificial neural network with genetic algorithm. Composites Part B: Engineering, 92, 420-433.

Yan, F., and Lin, Z. B. (2016). Bond durability assessment and long-term degradation prediction for GFRP bars to fiber-reinforced concrete under saline solutions. Composite Structures.

Yang, J.-M., Min, K.-H., Shin, H.-O., and Yoon, Y.-S. (2012). Effect of steel and synthetic fibers on flexural behavior of high-strength concrete beams reinforced with FRP bars. Composites Part B: Engineering, 43(3), 1077-1086.

Yoo, D.-Y., Kwon, K.-Y., Park, J.-J., and Yoon, Y.-S. (2015). Local bond-slip response of GFRP rebar in ultra-high-performance fiber-reinforced concrete. Composite Structures, 120, 53-64.

Yun, H.-D. (2013). Effect of accelerated freeze–thaw cycling on mechanical properties of hybrid PVA and PE fiber-reinforced strain-hardening cement-based composites (SHCCs). Composites Part B: Engineering, 52, 11-20.

Zhou, J., Chen, X., and Chen, S. (2012). Effect of different environments on bond strength of glass fiber-reinforced polymer and steel reinforcing bars. KSCE Journal of Civil Engineering, 16(6), 994-1002.

Zuo, J. (1999). Bond strength of high relative rib area reinforcing bars.

Zuo, J., and Darwin, D. (2000). Splice strength of conventional and high relative rib area bars in normal and high-strength concrete. ACI Structural Journal, 97(4).

3. EXPERIMENTAL STUDY ON BOND DURABILITY OF GFRP BARS IN CONCRETE EXPOSED TO HARSH ENVIRONMENTAL AGENTS: FREEZE-THAW CYCLES AND ALKALINE-SALINE SOLUTIONS

3.1. Introduction

Bond degradation mechanism is a complex process that normally initiates from the bar surface. The two constituents of GFRP bars, glass fibers and resin matrix, tend to deteriorate in strength when exposed to wet alkaline environments. Considering that concrete presents highly alkaline with a pH of about 12.5 to 13.5, this may not only deteriorate the resin matrix due to hydrolysis of the ester group and hydroxide ions, but also damage the glass fibers due to leaching and etching (Chen et al., 2007). Thus, it requires that the resin should be fully cured to provide appropriate protection to fibers. On the other hand, moisture could diffuse through the resin up to the fiber-matrix interphase or even to the fibers, resulting in hydrolysis and plasticization of the resin, as well as a bond loss of the fiber-matrix interphase. As the major load-carrying component of GFRP composites, glass fibers may even deteriorate in properties due to the moisture extracting ions from the fibers (Karbhari et al., 2003). Moreover, bond degradation of GFRP bars to the surrounding concrete become more serious in the presence of moisture containing chloride ions (Altalmas et al., 2015; Ceroni et al., 2006). Such phenomenon is inevitably encountered for structures in cold regions, where the concrete pore solution may be contaminated with chloride ions as normally found in de-icing salts (Tannous and Saadatmanesh, 1998). In addition, FT cycles, another environmental agent, also need to be considered for those structures. Damage in concrete due to FT cycles depends on the saturation of concrete. The water can permeate through the voids (or new developed microcracks) in concrete matrix, while the growth of ice crystals during repeated freezing process generates high pressure to concrete, thus

leading to microcracks in concrete. As a result, this will break down the bar-concrete interface. Also, presence of concrete cracks also yields a low confinement to GFRP bar and thus causes less bond strength.

Therefore, this chapter aims to investigate the bond durability of GFRP bars to concrete, especially in cold regions. In order to simulate and approximate field conditions that the structures normally experience in service-life stage, GFRP bars embedded in concrete were designed and exposed to different weathering: a) FT cycles, b) alkaline solution contaminated with chloride ions were considered; and (c) elevated temperature to accelerate the degradation rate. Some critical indices associated with the environmental conditioning, such as the weight loss, the relative dynamic modulus of elasticity and durability factor, and the bond strength reduction, were measured to evaluate the durability performance of the GFRP-concrete elements. Moreover, the analytical models were integrated with experimental data to better demonstrate the degradation of GFRP-concrete bond.

3.2. Background and Research to Date

3.2.1. Bond Durability

It is well established that aqueous solutions with high pH can reduce the tensile strength of bare GFRP bars despite test results showed great differences in (Benmokrane et al., 2002; Chen et al., 2006; Kim et al., 2008; Micelli and Nanni, 2004; Yan, Lin, Wang, et al., 2016; F. Yan and Z. B. Lin, 2016). Also, considerable studies have gone into various environmental attacks on the bond strength of GFRP bars. However, the combined effect of the environmental agents including alkaline solution, saline solution, and freeze thaw cycles, remains unsolved or even holds contrary opinions.

Chen et al. (Chen et al., 2007) used several types of solutions, the tap water, alkaline solutions with respective pH of 12.7 and 13.6, saline solution, and alkaline solution contaminated with chloride ions, to investigate the durability of bare GFRP bars and GFRP-concrete elements. Those specimens also experienced FT cycles and wet-dry cycles before testing. Significant reductions in tensile strength and bond strength were observed for the respective bare and embedded GFRP bars. Alkali attack was stated to be more serious than the FT cycles and wet-dry cycles. Davalos et al. (Davalos et al., 2008) reported bond performance of GFRP bars in concrete subjected to different environmental conditions: tap water at normal temperature and 60 ℃, thermal cycles ranging from 20 to 60 ℃. They reported that there were 0-20% reductions in bond strength being observed for the GFRP bars. Similar results of the bond strength reduction can also be found in (Galati et al., 2006). Fursa et al. (Fursa et al., 2015) conducted experiments on sixteen GFRP-concrete samples subjected to FT cycles. They used the electric response to evaluate the bond strength, and found that the bond strength reduced nearly 50% after 18 FT cycles ranging from −40 to 20 ℃.

On the contrary, Mufti et al. (A. Mufti et al., 2005; A. A. Mufti et al., 2007) conducted studies on five field GFRP reinforced concrete bridge structures exposed to natural environments for durations of five to eight years. The environmental conditions encompassed FT cycles, wet-dry cycles, de-icing salts, thermal range from −35 to 35 ℃. The GFRP bars in those selected demonstration structures were all composed of E-glass and vinyl ester resin. The analysis results stated that the structures maintained a good bond at the GFRP bar-concrete interface and no degradation was observed by either optical microscope or Fourier transformed infrared spectroscopy. Robert and Benmokrane (Robert and Benmokrane, 2010) performed experimental investigation on the bond durability of GFRP bars embedded in concrete. The specimens were

exposed to tap water at different temperatures (23, 40, 50 ℃) for three immersion durations (60, 120, 180 days). It was concluded that the bond strength decreased as the exposure durations increased whereas minor reductions of the bond strength were observed with increasing the exposure temperature. They also conducted experiments of mortar-wrapped GFRP bar specimens immersed in saline solutions with 50 ℃ for 365 days and 70 ℃ for 120 days (Robert and Benmokrane, 2013). The micrographs showed that no significant damage was captured at the bar-concrete interface. Moreover, the bar-concrete interface and fiber-matrix interface appeared uninfluenced by the moisture absorption and high temperatures. Zhou et al. (Zhou et al., 2012) studied the bond durability of GFRP bars in concrete under different environments, including the tap water, alkaline solution (pH=13.5), acid solution (pH=2), and ocean water for different exposure durations (30, 60, and 90 days) at 20 ℃. It was reported that there was no bond degradation under the simulated environments except for the acid solution. Even more, Alves et al. (Alves et al., 2010) conducted experiments on GFRP-concrete elements under sustained and fatigue loading conditions, and stated that the FT cycles enhanced the bond strength between the sand-coated GFRP bar and concrete by approximately 40%.

3.2.2. Statement of the Problem

Clearly, although extensive studies have been carried out on the bond durability of the GFRP bars to concrete, the literature review generally demonstrates large discrepancies. This can be attributed to the different test methods and diversities in the characteristics of those test bars. Also, some laboratory tests considering the extreme environmental conditions may not correspond to field conditions that the structures actually experienced in reality. On the other hand, limited resources dedicated to GFRP reinforced structures exposed to aggressive cold environments including the combined effect of FT cycles, alkaline solution and saline solution.

As such, the concrete pore solution that displays highly alkaline would be contaminated with chloride ions from de-icing salts, resulting in bond degradation of structures. Engineers need to comprehensively consider these environmental attacks on the long-term structural performance. Based on this, the objective of this study is to present an experimental study on the durability performance of the GFRP-concrete element, providing a reference and supplement to the current and future database for engineers and researchers.

3.3. Experimental Study

3.3.1. Sample Design

3.3.1.1. Material selection and sample size determination

The sample design was on the basis of a database generated in early work (Yan, Lin, and Yang, 2016). The database consisted of over 680 pullout specimens of GFRP bars in the literature. The critical information with reference to both GFRP bars and concrete mix can provide a sound basis for material selection and sample size determination.

Figure 3-1 (a) and (b) show the surface treatment and diameter of GFRP bars used in previous studies. Failure modes and surface conditions are assigned with the legends. For simplicity, the first term of the legends used represents the failure modes, while the second term is for surface conditions: a) R = ribbed; b) HW = helically wrapped; c) SC = sand coated; d) HWSC = helically wrapped and sand coated; e) SW = spirally wrapped. Clearly, the ribbed surface, and helically wrapped and sand coated surface, both associated with pullout failure take up a large proportion among all surface types. Also, the bar diameter (d_b) ranging from 12 to 14 mm were mostly found in those pullout tests. Therefore, the GFRP bars having a nominal diameter of 12.7 mm and helically wrapped and sand-coated surface can be selected without loss of generality.

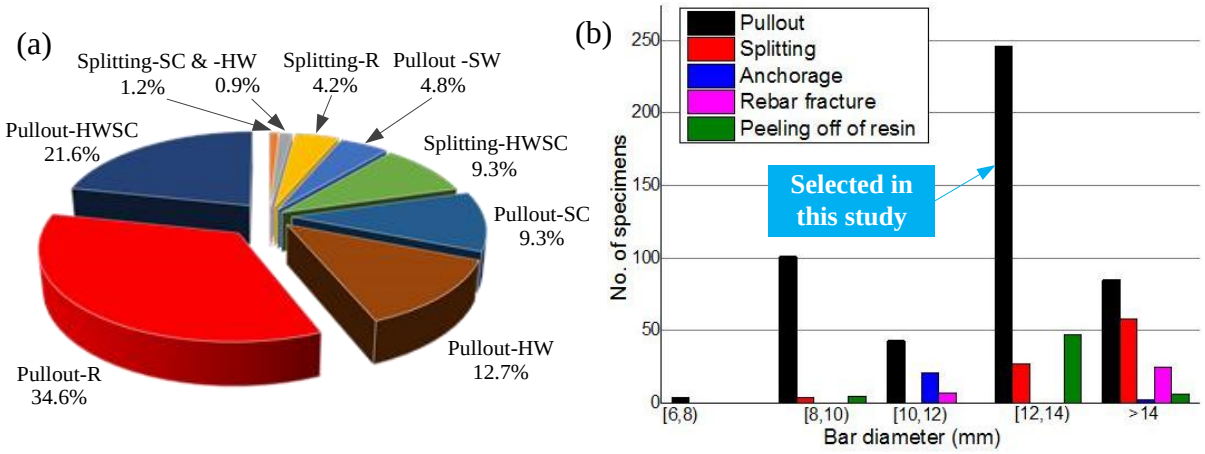

Figure 3-1. General information of GFRP bars used in previous studies: (a) surface treatment and (b) bar diameter (Yan, Lin, and Yang, 2016)

On the other hand, Figure 3-2 (a)–(c) demonstrate the critical statistics for pullout specimen design in terms of concrete compressive strength (f_c'), bar embedment length (l_d) and concrete cover (c). First, Figure 3-2 (a) indicates that the concrete compressive strength of about 40 to 50 MPa associated with pullout failure was the most of previous cases. Accordingly, the concrete compressive strength was reasonably designed to fall into the interval of [40, 50] MPa with appropriate mix proportions. Second, Figure 3-2 (b) illustrates that the embedment length to bar diameter ratio ranging from 5 to 6 is the most used parameter in the previous studies. Thus, the embedment length of GFRP bars was determined to be $l_d = 5d_b$, which is also in accordance with the pullout testing of FRP bars bonded to concrete stipulated in ASTM D 7913/D 7913M (ASTM D7913/D7913M, 2014). Finally, Figure 3-2 (c) reveals that $c/d_b \geq 4$ associated with pullout failure accounts for the majority over other scenarios. This also conforms to the limit of 3.5 specified in ACI 440.1R-06 bond equation (ACI Committee, 2006) when pullout failure is predicted. Upon this, the ratios of c/d_b with 1.5, 3.0 and 4.5 can be designed to allow different failure mode occurring.

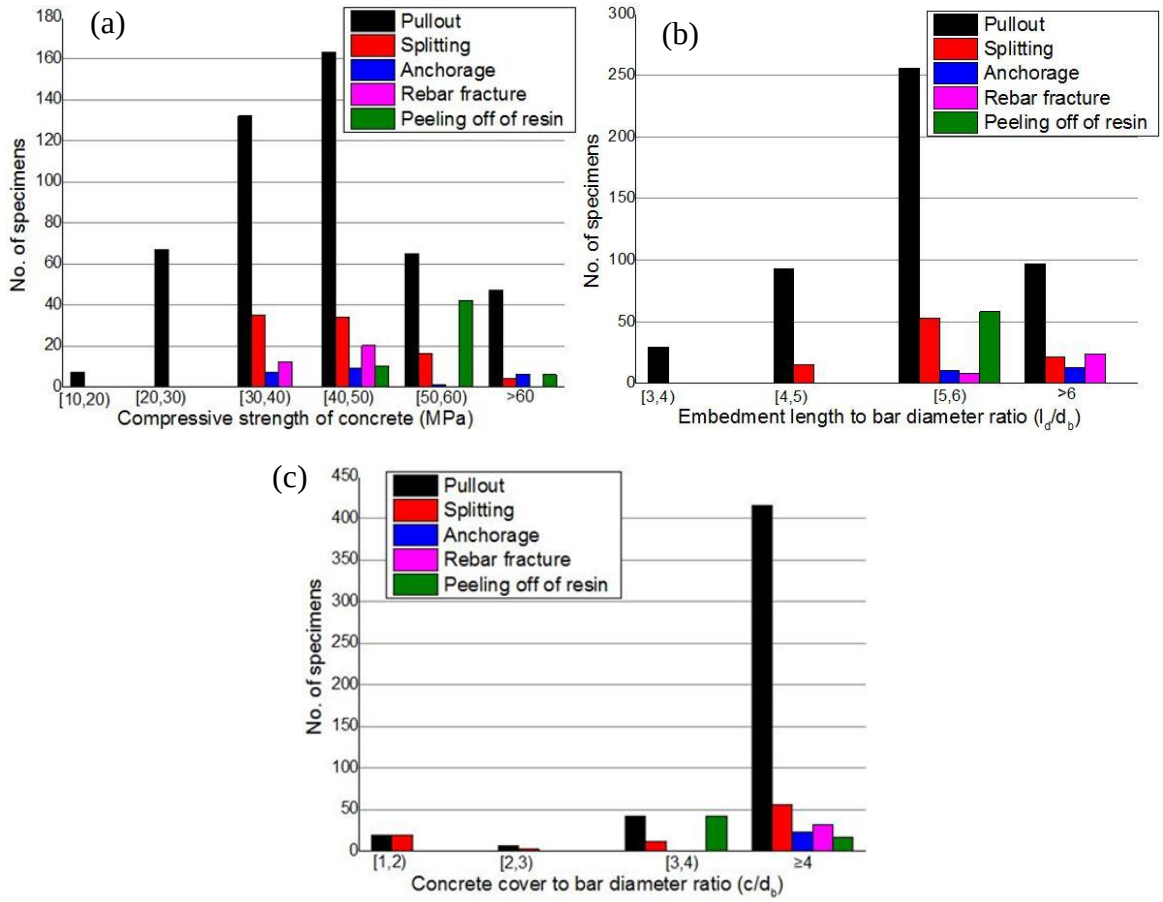

Figure 3-2. General information of concrete mix and GFRP bars used in previous studies: (a) concrete compressive strength, (b) embedment length, and (c) concrete cover (Yan, Lin, and Yang, 2016)

3.3.1.2. Material properties

(1) GFRP bars

The brand Aslan 100 series GFRP bars were used in this study. The surface of the GFRP bars is helically wrapped with fiber strands to create indentations along the bar, and sand particles are coated on the surface to enhance the bond strength, as shown in Figure 3-3. All the bars are made of continuous longitudinal E-glass fibers impregnated in a thermosetting vinyl ester resin, and are manufactured using the pultrusion process. The nominal diameter of the bars is 12.7 mm. The tensile strength reduction from ambient at -40 ℃ is less than 5% according to ASTM D 7205 (ASTM D7205 / D7205M-06, 2011), and tensile strength retention due to the

exposure to 12.8 pH solution for 90 days at 60 ℃ is greater than 80% according to ASTM D 7205 (ASTM D7205 / D7205M-06, 2011). The 24 hour moisture absorption at 50 ℃ is less than or equal to 0.25% according to ASTM D 570 (ASTM D570, 2010). The detailed mechanical and physical properties as reported by the manufacturer are summarized in Table 3-1.

Figure 3-3. GFRP bars used in this study

Table 3-1. Material properties of 12.7 mm diameter GFRP bars (as reported by manufacturer)

	Item	Unit	Value
Mechanical properties	Guaranteed tensile strength	MPa	758
	Tensile modulus of elasticity	GPa	46
	Ultimate strain	%	1.64
	Strength retention due to alkali resistance	%	> 80
	Strength reduction at cold temperature	%	< 5
	Transition temperature of Resin	℃	> 110
Physical properties	Moisture absorption	%	≤ 0.25
	Glass fiber content by weight	%	> 70

(2) Concrete

Since the bar diameter of 12.7 mm was selected, the concrete prism in terms of the concrete cover should allow both splitting failure and pullout failure to take place. The sample size of $127 \times 127 \times 177.8$ mm was implemented by a set of formwork constructed out of plywood, as shown in Figure 3-4. Prior to casting, the GFRP bars with bond breakers made of plastic tubes were deployed with different c/d_b of 1.5, 3.0 and 4.5, respectively. The embedment

length was determined to be $5d_b = 63.5$ mm, which was generally assumed to be capable of representing the local bond behavior of the GFRP bar-concrete interface.

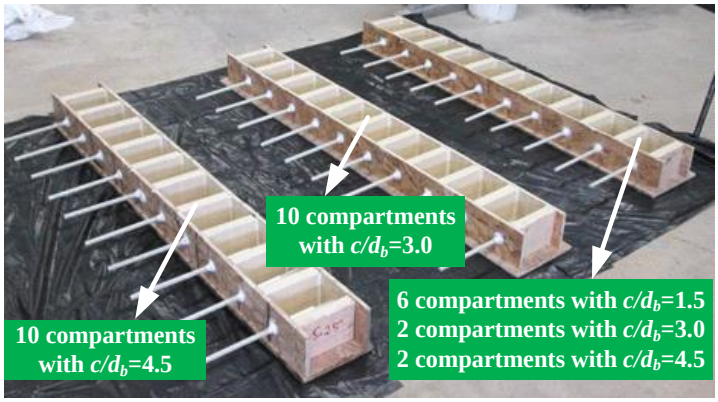

Figure 3-4. View of the formwork manufactured with different c/d_b

The concrete was prepared in the laboratory, with detailed mix proportions as presented in Table 3-2. Type I Portland cement was used for concrete mixing. The nominal maximum size of the coarse aggregate was 12.7 mm, and the fine aggregate size ranged from 0 to 4.75 mm. The concrete was mixed in a concrete mixer with an capacity of 0.03 m^3. In order to ensure mixing quality, totally three batches of concrete were used, of which the volume of each batch was less than 0.02 m^3. The coarse and fine aggregates were first mixed. Then the cement was added and thoroughly mixed. Finally, the water was added and the mixture was continuously mixed until the concrete exhibited uniform in appearance. The concrete was cast with GFRP bars in the horizontal position. After molding, all the samples were immediately covered with a plastic sheet to prevent moisture loss for 24 h, and then removed from the molds and cured in water at room temperature of 25 ℃ for 28 days. The mean concrete compressive strength of the specimens used in the test was determined according to ASTM C 39/C 39 M (C39M, 2016), where three 150×300 mm cylinders were used for each batch, as presented in Table 3-3.

Table 3-2. Composition and characteristics of concrete

Item	Unit	Value
Water (W)	kg/m^3	186
Cement (C)	kg/m^3	503
W/C	—	0.38
Coarse aggregate	kg/m^3	910
Fine aggregate	kg/m^3	717
Air-entraining agent	mL/m^3	312
28-day compressive strength	MPa	34 ± 1
Air content	%	5.2

3.3.2. Environmental Aging Design

3.3.2.1. Freeze-thaw cycles

The rapid FT cabinet (model G-118-H-3185B) was used to implement the repeated FT cycles on the test specimens in water. The original system is designed to accommodate up to eighteen $76 \times 102 \times 406$ mm concrete prism specimens simultaneously, with one being a control. Consider the specimen size used in this study, the container of each compartment needs to be redesigned for its capacity. A container with internal space of $198 \times 165 \times 508$ mm was determined to be capable of accommodating two $127 \times 127 \times 177.8$ mm GFRP-concrete specimens with sufficient water coverage according to ASTM C 666/ C 666M (ASTM C666 / C666M, 2015). The deployment of the total six compartments in the cabinet is shown in Figure 3-5.

The FT cycles were carried out according to ASTM C 666/C 666M Procedure A. The minimum and maximum core temperature of each specimen was set to be -18 ± 2 ℃ and 4 ± 2 ℃. The control specimen was used to monitor and accurately record the complete temperature variations throughout the testing period. Each FT cycle was found to accomplish in approximately 5 hours, and 40% of the time was used for thawing within each cycle. The

specimens were immersed in water for at least 24 hours before placing into the FT cabinet, and were taken out at the half and the end of the testing cycle in thawing condition for measurements. The weights of all the specimens before and after 75 FT cycles were measured to investigate the damage to concrete. The fundamental transverse and longitudinal frequencies of the concrete prism were measured at 0, 35 and 75 FT cycles for the purpose of calculating the dynamic modulus of elasticity according to ASTM C 215 (C215, 2014), where the forced resonance method was used.

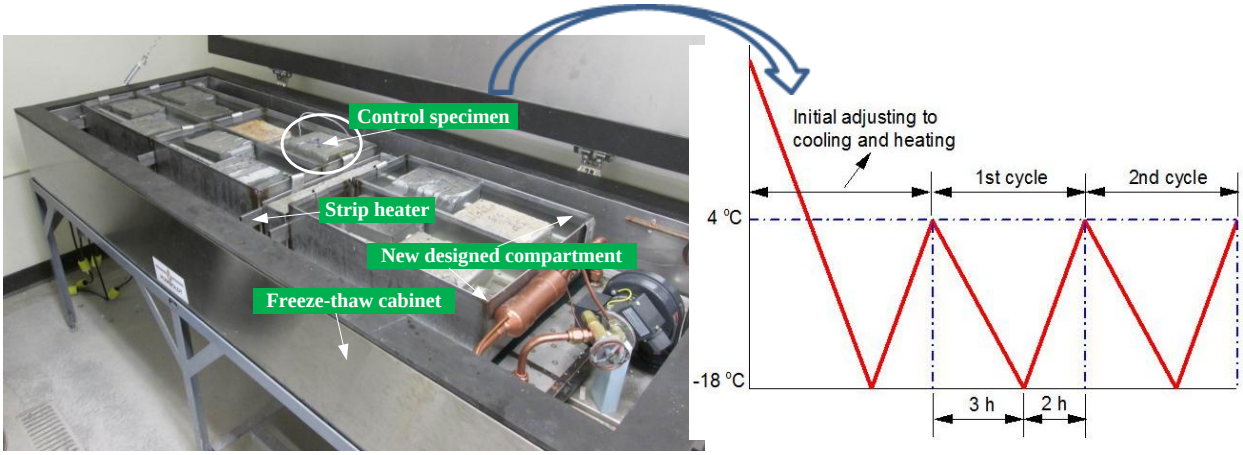

Figure 3-5. Demonstration of the freeze-thaw cycling test

In this study, the test apparatus Humboldt H-3175 sonometer utilizing a phono-type cartridge as a pickup was adopted to determine changes in resonance frequency of the concrete specimens. The driver and pickup are mounted on portable stands, which allows for greater flexibility in testing. The basic testing schematic is to vibrate the supported specimen using a driving unit with varying frequencies and record the response using a lightweight pickup unit. The value of frequency was recorded as the resonance frequency when the measured response reaches the maximum amplitude.

Figure 3-6 (a) demonstrates the test setup for the specimen that is able to vibrate freely in transverse mode. The specimen is supported at $0.224L$ from the edges, and the driving unit is

placed at the center of one surface, producing mechanical vibrations and imparting these vibrations to the test specimen. Meanwhile, a lightweight pickup unit is set at the middle along the width of the specimen. Figure 3-6 (b) shows the test setup for the longitudinal mode, where the specimen is supported at the middle span, and the driving unit is placed approximately at the center of one end surface to produce longitudinal excitation to the concrete prism. For both testing procedures, the frequency of vibrations can be controlled ranging from 400 to 12,000 cycles per second with an accuracy of better than $\pm 2\%$. The driving frequency is adjusted gradually until a maximum response is captured and displayed on a built-in digital counter, which is the resonant frequency of the specimen.

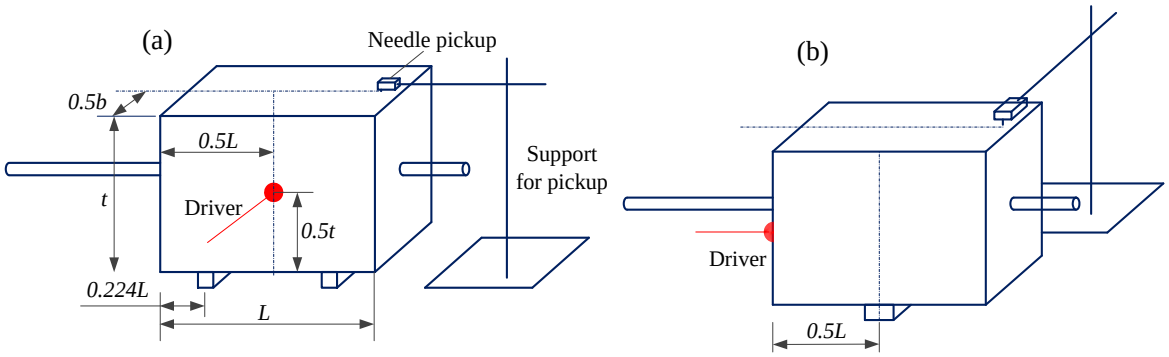

Figure 3-6. Demonstration of dynamic modulus test for (a) transverse mode and (b) longitudinal mode (demonstrated from ASTM C 215)

The dynamic modulus can be calculated based on the respective fundamental frequencies as shown in Equations (3-1) and (3-2),

$$E = CMn^2, \tag{3-1}$$

$$\text{or } E = DM(n')^2, \tag{3-2}$$

where E is the dynamic modulus of elasticity; $C = 0.9464(TL^3/bt^3)$, T is the correction factor and calculated to be 3.58 according to ASTM C 215 (C215, 2014), M is the mass of the specimen in kg; $D = 4(L/bt)$, n' is the fundamental longitudinal frequency in Hz.

3.3.2.2. Alkaline-saline solutions

The alkaline-saline (AS) solution was considered to simulate the concrete pore solution contaminated with chloride ions from de-icing salts. The alkaline solution with a pH = 12.5 was prepared with a mix of sodium hydroxide (NaOH), calcium hydroxide ($Ca(OH)_2$) and potassium hydroxide (KOH) in the ratio of 2.4:2:19.6 *g/L*, respectively (Altalmas et al., 2015). The 3% concentration sodium chloride (NaCI) was added into the alkaline solution to implement the AS solution (Kim et al., 2008; Robert and Benmokrane, 2013). In addition to the room temperature (25 ℃), the elevated temperature of 90 ℃ was used to accelerate the degradation rate of GFRP-concrete elements for duration of 90 days before testing.

3.3.3. Pullout Test Design

The pullout tests were performed using the universal testing machine that is capable of handling loads up to 1000 *kN*. The GFRP-concrete specimens were sheathed with thick-wall hollow steel pipes at the free portion of the GFRP bar, as shown in Figure 3-7 (a). The pipes were 203 mm in length and 19.05 mm in inside diameter, which were further processed with internal threaded along the length to increase the roughness of anchorage. The pipes were filled with a commercial epoxy to adhere the bar for at least 24 hours to take effect before testing. The schematic demonstration of the test setup is shown in Figure 3-7 (b). The sample encased in a steel reaction frame was instrumented with three linear variable differential transformers (LVDTs) to record the elongation of the bar. All the tests were conducted using displacement control at a rate of 0.02 mm/s, thus the post peak behavior of the bond-slip relationship can be obtained. The load was measured with the electronic loading cell of the machine, and the slips at both loaded end and free end were measure with the LVDTs. All measurements, including the

pullout load and displacements, were recorded synchronously by an automatic data-acquisition system at a rate of 2 data/s.

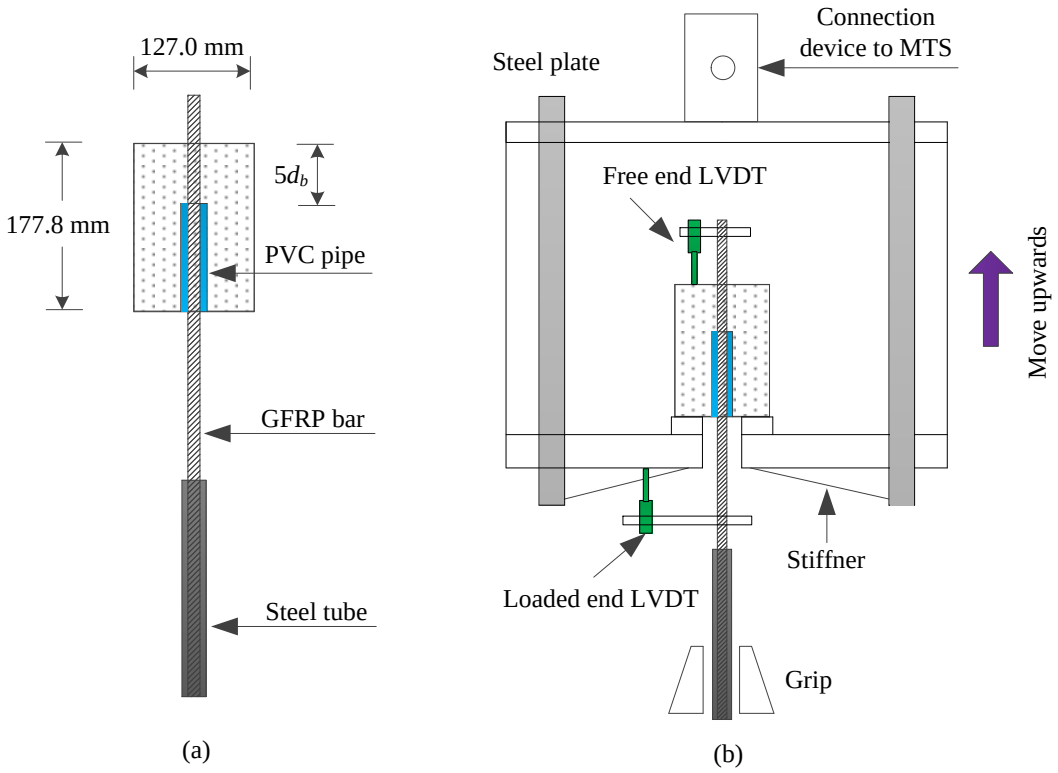

Figure 3-7. Schematic demonstration of the (a) pullout specimen and (b) test setup

3.4. Experimental Results and Discussion

A total of 26 GFRP-concrete specimens were considered in this test, including 3 specimens with $c/d_b = 1.5$, 11 specimens with $c/d_b = 3.0$, and 12 specimens with $c/d_b = 4.5$ to investigate the bond durability under different environmental conditions. The specimen identification is in the form: M-G-C-N, where M denotes the batch of the concrete mix, G denotes the specimen group, C denotes the concrete cover to bar diameter ratio, and N denotes the specimen number. For example, M3-D-4.5-2 indicates that the specimen No.2 with $c/d_b = 4.5$ was derived from concrete mix batch No.3, and was conditioned with the coupled FT cycles

and AS solution. In the pullout test, the stress along the embedment length is not constantly distributed and hence, the average bond stress is defined as:

$$\tau = \frac{P}{\pi d_b l_d}, \tag{3-3}$$

Table 3-3. Pullout test results of GFRP-concrete specimens exposed to different environmental conditions

Specimen	f_c' (MPa)	P_{max} (kN)	τ_b (MPa)	$\tau_b{}^a$ (MPa)	$s_{b,le}$ (mm)	$s_{b,le}{}^a$ (mm)	$s_{b,fe}$ (mm)	$s_{b,fe}{}^a$ (mm)	τ_b^* ($MPa^{0.5}$)	$\tau_b^{r\,a}$ (%)	Failure mode[b]
Unconditioned (control) specimens: Group A											
M1-A-1.5-1	44.22	29.11	11.49	13.03	0.39	0.50	N/A	0.15	1.73	100	S
M1-A-1.5-2	44.22	37.42	14.77		0.62		0.13		2.22		S
M1-A-1.5-3	44.22	32.48	12.82		0.48		0.17		1.93		S
M2-A-3.0-1	43.09	43.73	17.26	17.30	1.78	1.71	1.22	1.26	2.63	100	PO
M2-A-3.0-2	43.09	45.71	18.04		1.69		1.40		2.75		PO
M2-A-3.0-3	43.09	42.03	16.59		1.67		1.15		2.53		PO
M3-A-4.5-1	46.73	48.42	19.11	18.86	1.53	1.42	0.67	0.65	2.80	100	PO
M3-A-4.5-2	46.73	47.05	18.57		1.32		0.65		2.72		PO
M3-A-4.5-3	46.73	47.86	18.89		1.41		0.64		2.76		PO
Specimens conditioned with freeze-thaw cycles: Group B											
M2-B-3.0-1	43.09	40.38	15.94	15.31	2.13	1.99	1.44	1.41	2.43	88	S
M2-B-3.0-2	43.09	37.19	14.68		1.85		1.38		2.24		S
M3-B-4.5-1	46.73	45.78	18.07	18.27	1.75	1.72	1.15	1.17	2.64	97	PO
M3-B-4.5-2	46.73	46.64	18.41		1.79		1.22		2.69		PO
M3-B-4.5-3	46.73	46.44	18.33		1.61		1.14		2.68		PO
Specimens conditioned with alkaline-saline solution: Group C											
M2-C-3.0-1	43.09	44.34	17.50	17.17	1.95	1.92	1.54	1.53	2.67	99	PO
M2-C-3.0-2	43.09	43.60	17.21		1.89		1.48		2.62		PO
M2-C-3.0-3	43.09	42.54	16.79		1.91		1.57		2.56		PO
M3-C-4.5-1	46.73	44.89	18.72	18.58	1.67	1.67	0.62	0.62	2.59	94	PO
M3-C-4.5-2	46.73	45.81	18.68		1.61		0.59		2.64		PO
M3-C-4.5-3	46.73	43.91	18.33		1.72		0.66		2.54		PO
Specimens conditioned with both freeze-thaw cycles and alkaline-saline solution: Group D											
M2-D-3.0-1	43.09	37.62	14.85	14.87	2.03	1.95	1.74	1.69	2.26	86	S
M2-D-3.0-2	43.09	38.26	15.10		1.97		1.69		2.30		S
M2-D-3.0-3	43.09	37.14	14.66		1.86		1.64		2.23		S
M3-D-4.5-1	46.73	43.37	17.12	17.34	1.81	1.78	1.35	1.38	2.50	93	PO
M3-D-4.5-2	46.73	44.49	17.56		1.89		1.38		2.57		PO
M3-D-4.5-3	46.73	43.96	17.35		1.65		1.40		2.54		PO

[a] Mean value for nominally identical specimens.
[b] PO = pullout failure; S = splitting failure.

where P is the tensile load. The experimental results obtained from the pullout test were detailed in Table 3-3, where P_{max} is the maximum tensile load, τ_b is the bond strength, τ_b^r is the bond strength retention, $s_{b,le}$ and $s_{b,fe}$ are the slips corresponding to bond strength at the loaded end and free end, respectively. The mean values of the bond strength and corresponding slips of nominally identical specimens are also listed. Meanwhile, the normalized bond strength τ_b^* is used to account for the influence of concrete compressive strength, which is defined as:

$$\tau_b^* = \frac{\tau_b}{\sqrt{f_c'}}. \tag{3-4}$$

3.4.1. Mode of Failure

Table 3-3 details the mode of failure of unconditioned and conditioned pullout specimens. Splitting failure took place in all the control specimens with concrete cover $c = 1.5d_b$, whereas pullout failure occurred in the other control specimens with $c = 3.0d_b$ and $c = 4.5d_b$. Thus, the conditioned specimens that exposed to individual FT cycles and AS solutions, as well as the coupled effect of the both, considered these two types of concrete covers to investigate the environmental attack on the failure mode.

Figure 3-8 (a) shows the typical splitting failure and its corresponding interface between the GFRP bar and concrete for both unconditioned and conditioned specimens. This failure mode demonstrates obvious cracks that initiated from the GFRP-concrete interface and further developed up to the concrete outer surface, leading to brittle failure during the pullout process. The conditioned specimens with $c = 3.0d_b$ experienced to individual FT cycles and coupled FT cycles and AS solution all failed by concrete splitting rather than by pullout of the bar. Such change of failure mode indicates the concrete cover $c = 3.0d_b$ is not capable of resisting attacks of environmental agents including FT cycles, whereas transverse reinforcements are required to provide additional constraint to concrete. This conclusion also confirms the limit of $c = 3.5d_b$

term stipulated in ACI design codes (ACI Committee, 2006) when the pullout failure is usually predicted. The GFRP bars in these specimens exhibited minor scratches on the bar surface along the embedment length (e.g., specimen M2-D-3.0-1). The sands and fiber strands remained intact and closely adhere to the bar surface. On the contrary, the specimens conditioned with individual AS solutions all failed by pullout of the bars for both $c = 3.0d_b$ and $c = 4.5d_b$. The individual AS solution did not change the failure mode. Thus, the FT cycles play more significant influence on the bond durability of GFRP-concrete element, which may result in brittle failure when the concrete cover is not sufficient to hold reinforcements.

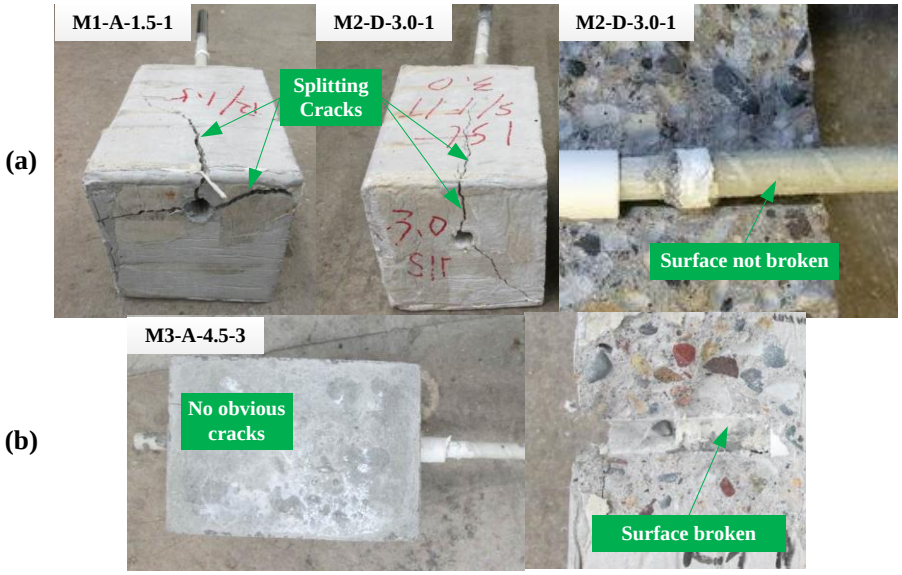

Figure 3-8. Typical failure modes for unconditioned and conditioned specimens: (a) splitting and (b) pullout failures

On the other hand, the specimens failed by pullout failure displayed similar conditions at the bar-concrete interface, as shown in Figure 3-8 (b). The sand particles and wrapped strands significantly peeled off due to the friction and sliding of pulling, with residues being observed at the concrete interface along the embedment length (e.g., specimen M3-A-4.5-3). The conditioned specimens showed similar phenomenon as that presented in the unconditioned specimen. There

were no trace of chemical attack in terms of abnormal color and corrosive substances being observed except for the stripping of sand residues on the concrete interface or removal of the resin. The specimens with concrete cover $c = 4.5d_b$ all failed by pullout failure in those conditioned with individual FT cycles, AS solution, and coupled effect of both, indicating that $c = 4.5d_b$ is capable of preventing brittle failure under those environmental attacks.

3.4.2. Weight Loss

Scaling is a degradation phenomenon of hardened concrete, of which a local peeling or flaking of a finished surface takes place due to environmental attacks. The deterioration of concrete structures is usually related to surface scaling, especially when they are subjected to FT cycles. It usually initiates from localized small patches that may further extend to expose large areas. The mortar and paste strip from the concrete surface or the alkali-silica reacts with the alkali-reactive aggregate inside the concrete mix, leading to loosening of the coarse aggregates and ultimate strength reduction of concrete structures.

Figure 3-9 shows the surface conditions of the specimens exposed to individual environment of FT cycles, AS solution, and coupled effect of the both. The control specimen M3-A-4.5-1 displayed intact surface in contrast to the conditioned specimens. The specimen M3-C-4.5-1 that was conditioned with AS solution exhibited yellowish white color and rough mortar surface whereas no obvious peeling of patches and cracks were observed. The specimens conditioned with respective FT cycles and coupled FT cycles and AS solution demonstrated different degrees of surface scaling. The specimen M3-B-4.5-3 showed peeling of the surface mortar at the edge of the prism especially near the arris of the outer surface whereas no obvious aggregates exposed. The specimen M3-D-4.5-2 clearly displayed the coarse aggregate with

distinct loss of the surface mortar, indicating the couple environments of FT cycles and AS solution may lead to more severe deterioration to concrete integrity.

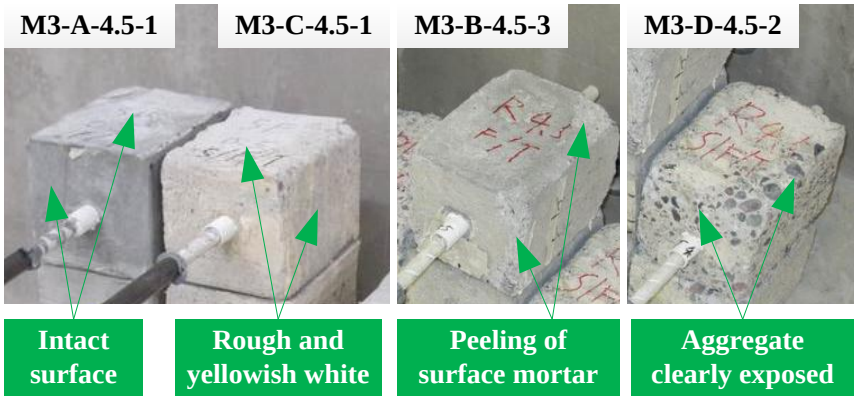

Figure 3-9. Examples of specimens exposed to different environmental conditions

The weight loss of all the conditioned specimens was measured using Equation (3-5),

$$\Delta W_n = \frac{W_0 - W_r}{W_r} \times 100, \tag{3-5}$$

where ΔW_n is the weight loss after n FT cycles, W_0 and W_r are the original weight and residual weight of the specimen before and after conditioning, respectively. More detailed information is summarized in Table 3-4 and plotted in Figure 3-10, where characters located before and after the hyphen denote the environmental conditions and concrete cover to bar diameter ratio, respectively. For example, FT+AS-3.0 indicates the specimen with $c = 3.0d_b$ was experienced coupled environments of FT cycles and AS solution. The specimens exposed to AS solutions showed the smallest weight loss among other environments. The mean weight losses were 0.24 percent and 0.21 percent for the specimens with $c = 3.0d_b$ and $c = 4.5d_b$, respectively. The specimens subjected to FT cycles lost less than 1 percent of their original weight, with 0.70 percent and 0.72 percent for the specimens with $c = 3.0d_b$ and $c = 4.5d_b$, respectively. This indicates that the air-entrained concrete performed well according to ASTM C 666/ C 666M Procedure A (ASTM C666 / C666M, 2015). However, when the specimens were experienced

with coupled environments of FT cycles and AS solutions, the weight loss increased to 1.23 percent and 1.34 percent for specimens with $c = 3.0d_b$ and $c = 4.5d_b$, respectively. The coupled environments resulted in the largest weight loss of the GFRP-concrete specimens among all the environmental conditions.

Table 3-4. Weight loss of conditioned specimens

Specimen	Original weight (g)	Residual weight (g)	Weight loss (%)	Mean (%)	Standard deviation (%)
Freeze thaw cycles					
M2-B-3.0-1	6706.2	6669.3	0.55	0.70	0.14
M2-B-3.0-2	6710.0	6654.3	0.83		
M3-B-4.5-1	6415.2	6363.9	0.80	0.72	0.09
M3-B-4.5-2	6566.3	6518.4	0.73		
M3-B-4.5-3	6670.5	6629.1	0.62		
Alkaline-saline solution					
M2-C-3.0-1	6608.6	6592.1	0.25	0.24	0.09
M2-C-3.0-2	6559.7	6550.5	0.14		
M2-C-3.0-3	6616.2	6594.4	0.33		
M3-C-4.5-1	6600.3	6590.4	0.15	0.21	0.05
M3-C-4.5-2	6679.8	6663.1	0.25		
M3-C-4.5-3	6547.0	6531.9	0.23		
Coupled freeze-thaw cycles & alkaline-saline solution					
M2-D-3.0-1	6686.7	6604.5	1.23	1.23	0.20
M2-D-3.0-2	6702.1	6606.3	1.43		
M2-D-3.0-3	6627.6	6559.3	1.03		
M3-D-4.5-1	6558.5	6477.2	1.24	1.34	0.12
M3-D-4.5-2	6563.8	6477.8	1.31		
M3-D-4.5-3	6560.4	6464.6	1.46		

Considering that field concrete structures in cold regions inevitably experience the concrete pore solution contaminated with de-icing salts and freeze-thaw cycles due to climate change. Thus, the conclusions drawn from the simulated environmental conditions reveal that the coupled FT cycles and AS solution may be more hazardous than the individual FT cycles despite the results obtained in the laboratory test may be more severe due to higher cycling rate or deviations with the practical situation.

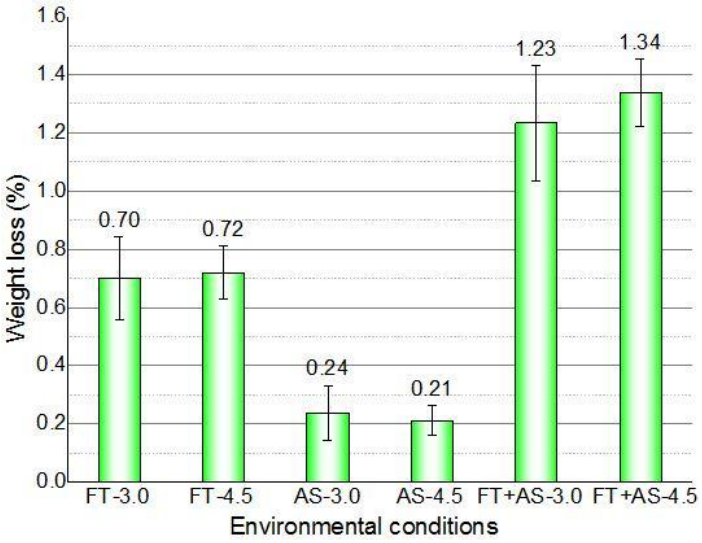

Figure 3-10. Weight loss under different environmental conditions

3.4.3. Relative Dynamic Modulus of Elasticity and Durability Factor

The specimens were measured after 35 and 75 FT cycles respectively to investigate the potentially deteriorating influences. Considering that the dynamic modulus of different specimens may vary from each other due to different mix batch or aggregate distribution. Thus, the relative dynamic modulus of elasticity is defined in the following according to ASTM C 666/C 666M (ASTM C666 / C666M, 2015):

$$R_E = \frac{E_n}{E_0} \times 100, \tag{3-6}$$

where R_E is the relative dynamic modulus of elasticity, E_0 and E_n are the dynamic modulus of elasticity at 0 and n FT cycles. It aims to facilitate the comparisons among different individuals, eliminating the influences caused by the diversity of the test specimens. Table 3-5 details the dynamic modulus of elasticity calculated based on respective transverse and longitudinal vibration modes. Generally, the dynamic modulus calculated using the transverse vibration mode was slightly smaller than that using the longitudinal vibration mode, which is consistent with the observation in (Popovics et al., 2008). The maximum error of the dynamic modulus using

different vibration modes was 3.94 percent, indicating the forced resonance method performed in this study yielded good accuracy.

Table 3-5. Relative dynamic modulus of elasticity

Specimen	Transverse vibration mode				Longitudinal vibration mode				
	E (GPa)	R_E (%)	Mean (%)	Standard deviation (%)	E (GPa)	R_E (%)	Mean (%)	Standard deviation (%)	Error[a] (%)
Before conditioned									
M2-B-3.0-1	71.32	100	100	0	72.11	100	100	0	1.11
M2-B-3.0-2	75.36	100			76.13	100			1.02
M3-B-4.5-1	65.89	100	100	0	66.22	100	100	0	0.50
M3-B-4.5-2	64.81	100			65.58	100			1.19
M3-B-4.5-3	69.19	100			70.67	100			2.14
M2-D-3.0-1	72.44	100	100	0	73.08	100	100	0	0.88
M2-D-3.0-2	74.69	100			75.45	100			1.02
M2-D-3.0-3	76.18	100			77.02	100			1.10
M3-D-4.5-1	69.02	100	100	0	69.88	100	100	0	1.25
M3-D-4.5-2	64.51	100			65.46	100			1.47
M3-D-4.5-3	67.67	100			68.39	100			1.06
After 35 freeze thaw cycles									
M2-B-3.0-1	67.26	94.31	93.70	0.86	69.01	95.70	94.84	1.22	2.60
M2-B-3.0-2	70.15	93.09			71.54	93.97			1.98
M3-B-4.5-1	55.36	84.02	83.28	0.75	57.03	86.12	83.96	1.87	3.02
M3-B-4.5-2	53.48	82.52			54.28	82.77			1.50
M3-B-4.5-3	57.63	83.29			58.65	82.99			1.77
After 35 freeze-thaw cycles & alkaline-saline solution									
M2-D-3.0-1	63.58	87.77	84.17	3.13	64.37	88.08	74.16	0.56	1.24
M2-D-3.0-2	61.72	82.63			62.49	82.82			1.25
M2-D-3.0-3	62.55	82.11			63.35	82.25			1.28
M3-D-4.5-1	51.64	74.82	78.54	4.31	52.58	75.24	70.10	1.63	1.82
M3-D-4.5-2	53.71	83.26			54.61	83.42			1.68
M3-D-4.5-3	52.48	77.55			53.70	78.52			2.32
After 75 freeze thaw cycles									
M2-B-3.0-1	52.98	74.28	73.80	0.69	53.76	74.55	84.38	3.21	1.47
M2-B-3.0-2	55.25	73.31			56.15	73.76			1.63
M3-B-4.5-1	46.78	71.00	69.68	1.26	47.66	71.97	79.06	4.12	1.88
M3-B-4.5-2	44.39	68.49			45.22	68.95			1.87
M3-B-4.5-3	48.12	69.55			49.03	69.38			1.89
After 75 freeze-thaw cycles & alkaline-saline solution									
M2-D-3.0-1	47.83	66.03	58.32	7.47	48.72	66.67	58.89	7.56	1.86
M2-D-3.0-2	43.17	57.80			44.08	58.42			2.11
M2-D-3.0-3	38.94	51.12			39.73	51.58			2.03
M3-D-4.5-1	40.16	58.19	61.48	3.00	41.02	58.70	62.36	3.17	2.14
M3-D-4.5-2	41.33	64.07			42.16	64.41			2.01
M3-D-4.5-3	42.08	62.18			43.74	63.96			3.94

[a] Error is defined as the absolute difference between the *E* calculated using transverse and longitudinal modes divided by the *E* using the transverse mode.

Figure 3-11 shows the comparisons of the relative dynamic modulus of elasticity after 35 and 75 FT cycles. Taking the examples based on the transverse vibration mode, in general, the specimens experienced coupled FT cycles and AS solution displayed smaller relative dynamic modulus of elasticity than those experienced individual FT cycles. The R_E of the specimens M2-B-3.0, M3-B-4.5 decreased to the respective percent of 93.70 and 83.28 after 35 FT cycles, and further decreased to the respective percent of 73.80 and 69.68 after 75 FT cycles.

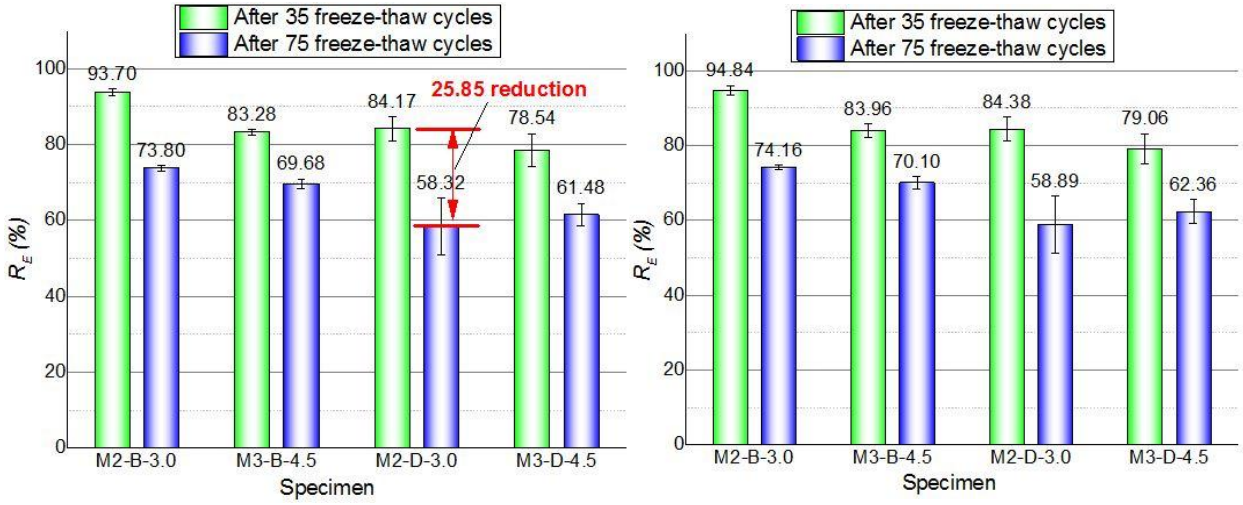

(a) Transverse vibration mode (b) Longitudinal vibration mode

Figure 3-11. Variations of relative dynamic modulus after 35 and 75 freeze-thaw cycles

On the other hand, the R_E of the specimens M2-D-3.0 and M3-D-4.5 decreased to the respective percent of 84.17 and 78.54 after 35 FT cycles combined with AS solution, and further decreased to the respective percent of 58.32 and 61.48 after 75 FT cycles combined with AS solution. In particular, the largest reduction in R_E, 25.85 percent between 35 FT cycles combined with AS solution and 75 FT cycles combined with AS solution, was observed in the specimen M2-D-3.0 among all scenarios, indicating that smaller concrete cover may suffer from more potentially deteriorating influences as the number of FT cycles increases. Such phenomenon is consistent with the splitting failure observed in the specimens M2-B-3.0-1, M2-B-3.0-2, M2-D-

3.0-1, M2-D-3.0-2, and M2-D-3.0-3, of which the smaller concrete cover resulted in weaker FT resistance.

In addition, the durability factor is defined according to ASTM C 666/ C 666M (ASTM C666 / C666M, 2015),

$$DF = R_{E,n} \cdot n/m, \tag{3-7}$$

where DF is the durability factor of the test specimen; $R_{E,n}$ is the relative dynamic modulus of elasticity at n cycles in %, and the transverse vibration mode is used herein; and m is the specified number of cycles at which the exposure is to be terminated, which is 75 since the FT cycles was conducted to 75 cycles in this study.

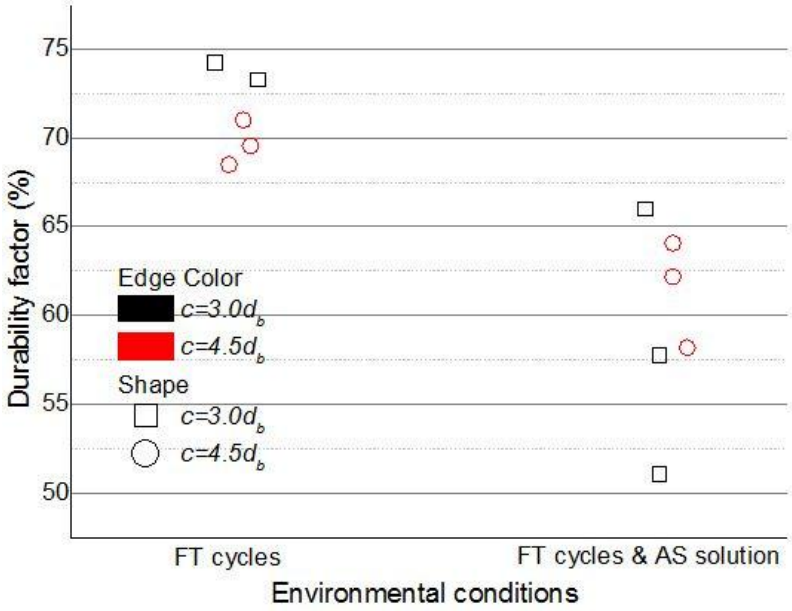

Figure 3-12. Effect of environmental conditions on durability factor

Figure 3-12 demonstrates the impact of environmental conditions on the durability factor, where the specimens experienced individual 75 FT cycles and coupled 75 FT cycles and AS solution were used. It is clear that larger reductions in durability factor were observed when the specimens were subjected to the coupled environment rather than the individual environment. The durability factor of all specimens experienced FT cycles were larger than 40 percent while

smaller than 85 percent, indicating the medium FT resistance of the test specimens (Wang et al., 2009).

3.4.4. Bond Behavior and Durability

3.4.4.1. Bond stress-slip response

The bond stress-slip relationship at the loaded end and free end are shown in Figure 3-13, where the representative of the control specimens and environmental conditioned specimens with different concrete covers are presented. Generally, the ascending branches of all the bond-slip curves at the free end displayed apparent lag effect compared to those at the loaded end, which conform to the fact that the slip development at the free end lags behind that at the loaded end. The descending branches associated with the conditioned specimens failed by concrete splitting (e.g., specimen M2-D-3.0-1) showed shorter segment compared with the specimens failed by the pullout of the bars (e.g., specimen M3-D-4.5-3). For the typical specimens M2-A-3.0-2, M2-B-3.0-1, M2-C-3.0-1, and M2-D-3.0-1, the complete bond-slip curves at both loaded end and free end of the conditioned specimens located below the bond-slip curves of the control specimens. This indicates that the specimens having smaller concrete cover $c = 3.0d_b$, may have lower bond resistance to environmental attacks at both pre-peak stage and post-peak stage of the bond development. On the other hand, for the typical specimens M3-A-4.5-2, M3-B-4.5-1, M3-C-4.5-1, M3-D-4.5-3, the ascending branches exhibited minor difference between the control specimen and conditioned specimens, whereas the descending branches presented obvious reduction in bond stress. This suggests that increasing the concrete cover may have great contribution in enhancing the pre-peak bond resistance to the environmental attacks in terms of AS solution, FT cycles and coupled influences of the both.

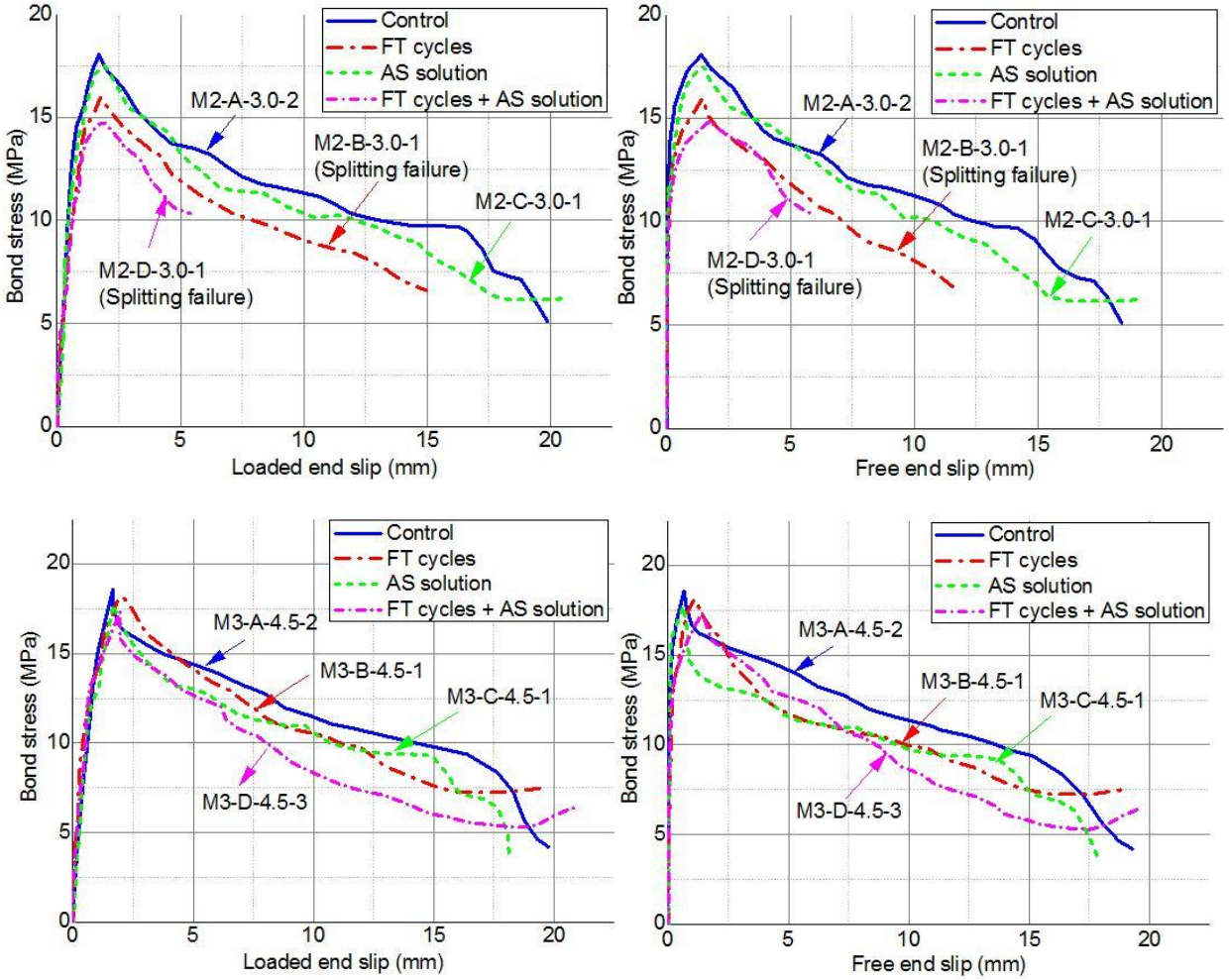

Figure 3-13. Typical bond stress-slip relationship for unconditioned and conditioned specimens

Compared to the control specimens, it can be noticed that the conditioned specimens associated with the coupled FT cycles and AS solution exhibited larger reductions in the bond stresses than those associated with the individual environmental agent. In particular, the specimens conditioned with the AS solution presented the smallest reduction among all the environmental scenarios, as demonstrated in the green dash lines of all the figures. Moreover, the impact of the individual FT cycles on the specimens having larger concrete cover mainly reflected in the post-peak bond behavior, as illustrated in the bond-slip curves of the specimen M3-B-4.5-1. Referring to the bond toughness introduced in (Ding et al., 2014), this indicates that

the capacity of the post-peak energy absorption may decrease more obviously than the capacity of the pre-peak energy absorption when subjected to FT cycles.

3.4.4.2. Bond strength and its corresponding slip

The bond strengths of the specimens under different environmental conditions are displayed in Figure 3-13 (a). In order to eliminate the influence of different concrete mix on the test results, the normalized values with respect to the square root of concrete compressive strength were presented in Figure 3-13 (b).

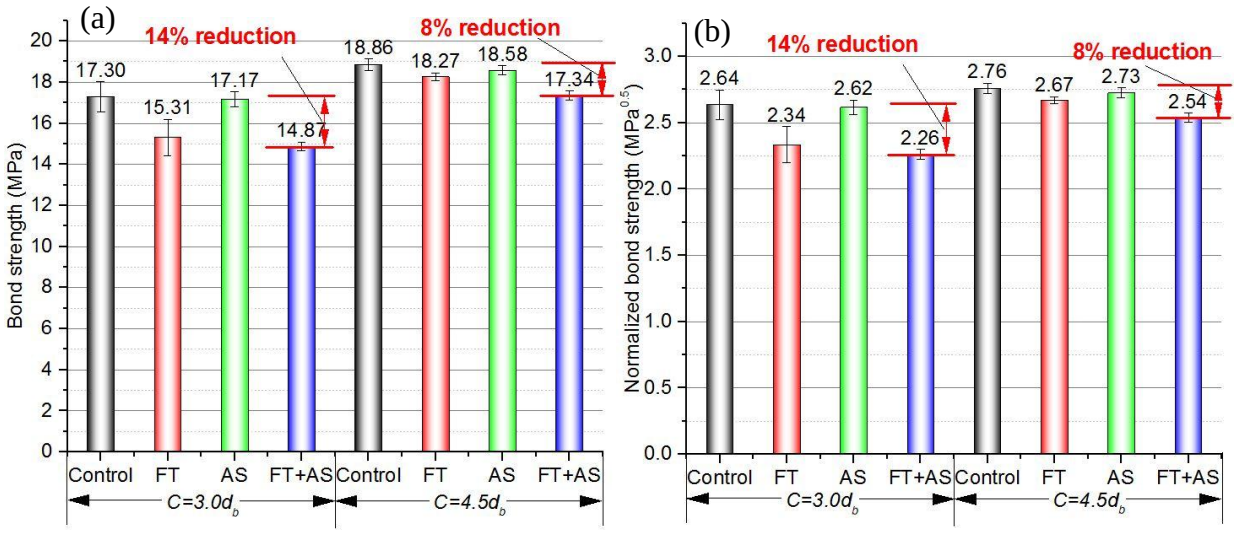

Figure 3-14. (a) Bond strength and (b) normalized bond strength

Generally, it is noticed that that all the conditioned specimens showed deterioration in their bond strength. For the specimens having smaller concrete cover $c = 3.0d_b$, the environmental conditions including FT cycles exhibited more detrimental impact on the bond strength whereas the AS solution demonstrated minor influence. In particular, the coupled conditioning and individual FT cycles resulted in 14 percent and 12 percent reductions in both bond strength and normalized bond strength, respectively. While for the specimens having larger concrete cover $c = 4.5d_b$, the FT resistance was significantly improved accordingly. The bond strength reduction was reduced to 8 percent under the coupled conditioning, and 3 percent under

the individual FT cycles. The normalized bond strength of all the conditioned specimens exhibited the similar patterns to the bond strength observation. It is worth noting that the coupled environment was the worst case regardless of the concrete cover.

The slips corresponding to the bond strength at the loaded end and free end are presented in Figure 3-15. The results reveal that the specimens having larger concrete cover exhibited smaller slip at both loaded end and free end compared to those having smaller concrete cover. The conditioned specimens generally showed larger slip than the unconditioned specimens despite the discrepancy occurred due to the random effect of individual test results, which was consistent with the observations in (Belarbi and Wang, 2011). In particular, the loaded end slip has more significance in practice. The slip associated with the FT cycles decreased from 1.99 to 1.72 mm when the concrete cover increased from $c = 3.0d_b$ to $c = 4.5d_b$, with approximately 14% reduction due to the enhanced confinement to the GFRP bars. Such test results were consistent with the failure mode observed in these two different concrete covers. Moreover, the slip of the specimens ($c = 4.5d_b$) conditioned with the coupled environment was 1.78 mm with approximately 20% increase compared with the control specimen.

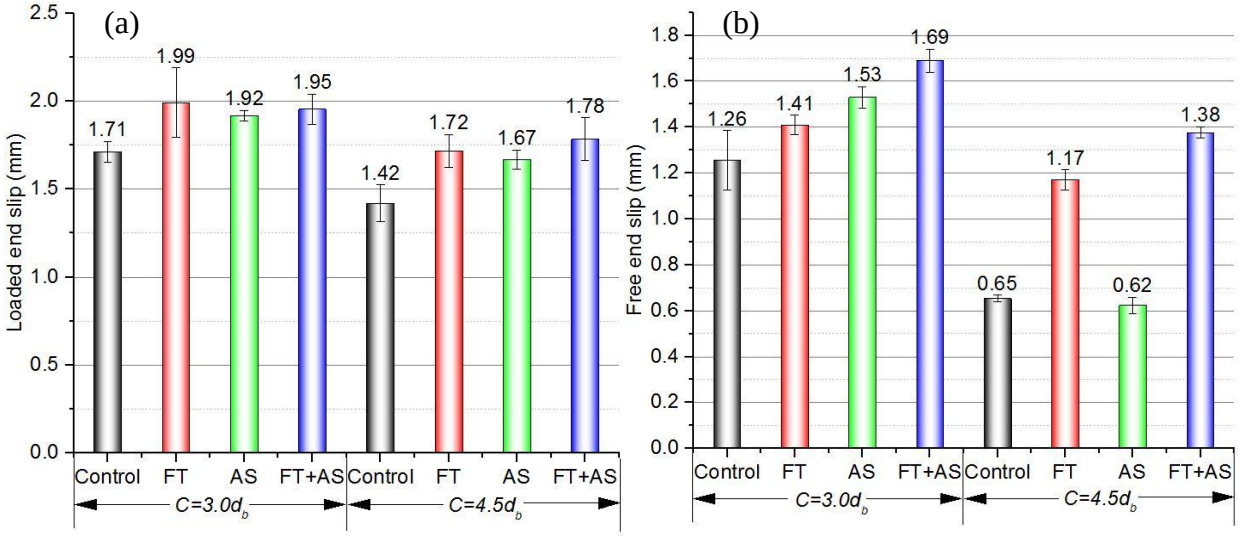

Figure 3-15. Slip corresponding to bond strength at (a) loaded end and (b) free end

3.5. Calibration of Analytical Models Considering Environmental Effects

Currently, the FRP-concrete bond under pullout loads can be demonstrated through several available analytical models, which use a set of explicit expressions to depict the development of the bond stress against slip (E Cosenza et al., 1995; Malvar, 1994; Rossetti et al., 1995). The model proposed by Malvar (Malvar, 1994) uses a polynomial function in terms of seven curve-fitting parameters to describe the bond-slip relationship. Nevertheless, the ascending branch was later evaluated to be less reliable for FRP material (Edoardo Cosenza et al., 1997). The BPE model developed by Eligehausen et al. (Eligehausen et al., 1982) was originally used to illustrate the steel-concrete bond, and then applied to FRP bars by recalibrating those parameters (Antonietta Aiello et al., 2007; E Cosenza et al., 1995; Rossetti et al., 1995). Cosenza et al. (E Cosenza et al., 1995) and Rossetti et al. (Rossetti et al., 1995) conducted experiments of FRP bars with different surface treatments. However, their test results were too scattered to determine the parameters. More detailed comparisons among those analytical models can be found in (Lin and Zhang, 2014) and (F. Yan and Z. Lin, 2016). This study adopted another two widely used analytical models viz., modified Bertero-Eligehausen-Popov (mBPE) model and Cosenza-Manfredi-Realfonzo (CMR) model for the bond-slip prediction. Moreover, considering that the calibrated models in previous studies did not consider the environmental impact on the bond performance and hence, it is necessary to provide a more accurate calibration involving the environmental influence to better demonstrate the GFRP- concrete bond behavior.

(I) mBPE model

The bond-slip relationship of the mBPE model can be expressed as a piecewise function in Equation (3-8),

$$\frac{\tau}{\tau_b} = \begin{cases} (\frac{s}{s_b})^{\alpha} & (0 \le s \le s_b) \\ 1 - p\left(\frac{s}{s_b} - 1\right) & (s_b \le s \le s_3), \\ \frac{\tau_3}{\tau_b} & (s \ge s_3) \end{cases} \quad (3\text{-}8)$$

where τ_b and s_b are the peak bond stress (bond strength) and its corresponding slip; α and p are parameters that can be determined from curve fitting of experimental results.

II) CMR model

To overcome the drawback of the Malvar's model, the CMR model proposed by Cosenza et al. (E Cosenza et al., 1995) was used to better represent the ascending branch of bond-slip curve for FRP-concrete bond:

$$\frac{\tau}{\tau_b} = (1 - exp(-\frac{s}{s_r}))^{\beta} \qquad (0 \le s \le s_b), \quad (3\text{-}9)$$

where s_r and β are parameters that are derived from curve fitting of experimental data. Since the CMR model is only for the ascending part, it is worth noting that it may be applicable to the bond at serviceability state level, while not capable of describing the complete bond behavior of structures till failure (Lin and Zhang, 2014).

Figure 3-16 displays the bond-slip relationship at the loaded end using the respective mBPE model and CMR model, of which the parameters of these models were determined from the curve fittings of the test results and summarized in Table 3-6. Since the descending branch of the mBPE model uses a linear expression to describe the post-peak bond behavior, the deviations were legitimately larger for those curves having larger fluctuations, as shown in the green dash dot lines in Figure 3-16. The coefficient of determination (R^2) were 0.8864, 0.8090, 0.7706 and 0.6675 for the respective control specimen and conditioned specimens, indicating rough accuracy of the predictions. On the contrary, all the results predicted by the ascending branch of the mBPE model and CMR model matched well with the test results, as shown in the red solid

lines and blue short dash dot lines in Figure 3-16. Furthermore, the ascending branches of the bond-slip curves predicted by the CMR model performed better than those predicted by the mBPE model. The R^2 of the CMR model for all the specimens were greater than 0.98, yielding good accuracy.

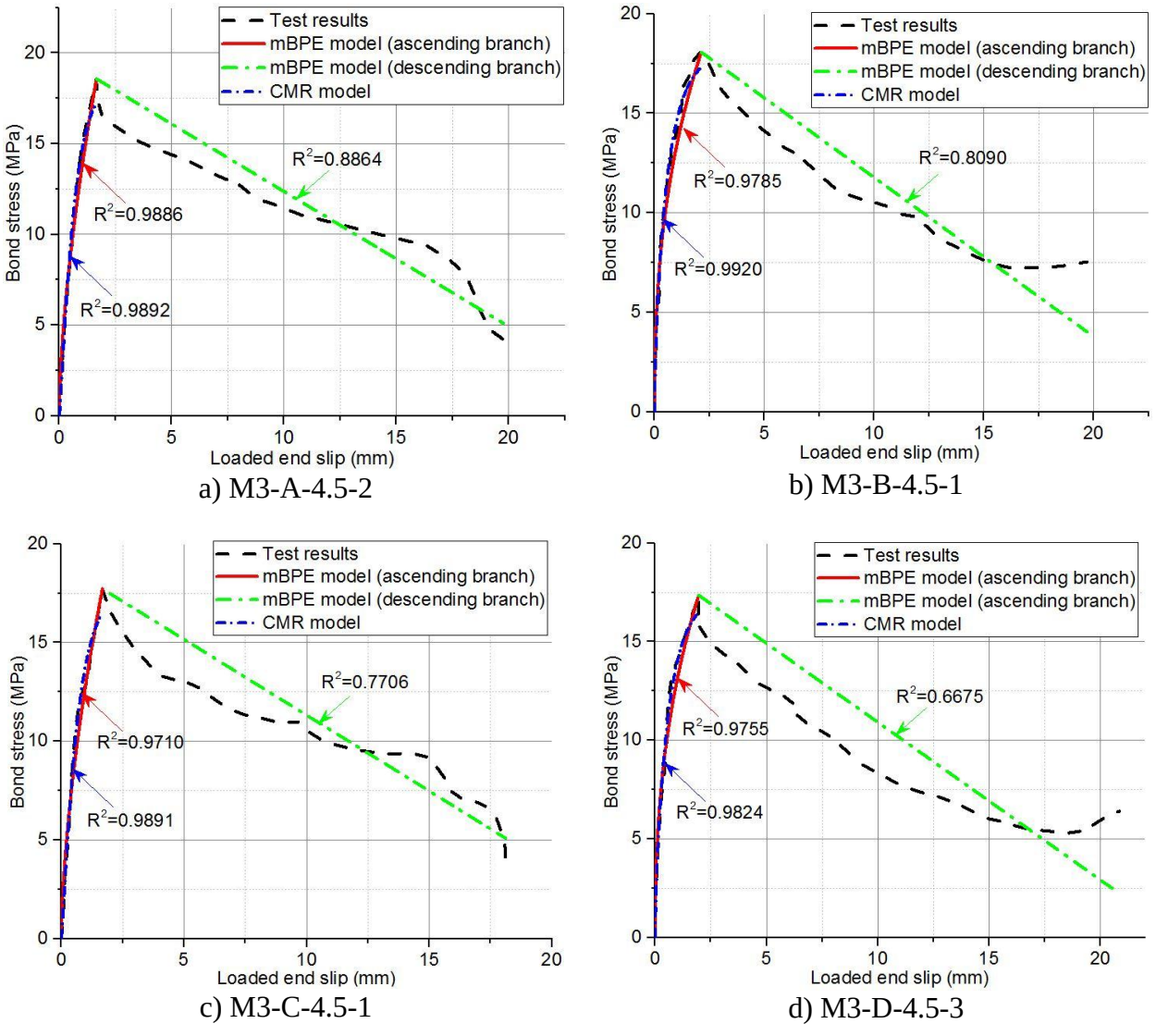

a) M3-A-4.5-2 b) M3-B-4.5-1

c) M3-C-4.5-1 d) M3-D-4.5-3

Figure 3-16. Curve fittings of the typical bond stress-slip relationship

Table 3-6. Fitting parameters of the mBPE model and CMR model

Specimen	τ_b (MPa)	s_b (mm)	mBPE model		CMR model	
			α	p	s_r	β
M3-A-4.5-2	18.8898	1.4070	0.6136	0.0664	0.5777	1.2459
M3-B-4.5-1	18.0655	1.7512	0.4011	0.0940	0.7630	0.6768
M3-C-4.5-1	18.7163	1.6730	0.6087	0.0725	0.5911	1.1783
M3-D-4.5-3	17.3500	1.6537	0.4150	0.0900	0.7318	0.7219

For the unconditioned specimen, the calibrated parameters α and p, s_r and β were 0.6136, 0.0664, 0.5777 and 1.2459 for the double branch of the mBPE model and CMR model, respectively. Consider the most adverse case, the coupled FT cycles and AS solution, these calibrated parameters were changed to 0.4150, 0.0900, 0.7318 and 0.7219 for the mBPE model and CMR model, respectively. It is worth noting that these calibrated parameters determined from the experimental data were also dependent on the bond strength and its corresponding slip. The GFRP bars used in this study only consider the surface treatment of sand coated and helically wrapped. For different types of surface conditions, the calibrated parameters may vary accordingly and should be determined additionally.

Table 3-7 shows the calibrated average values for both mBPE model and CMR model considering different environmental conditions, and the values for unconditioned specimens are also listed. Based on the test results, α and p of mBPE model were suggested to be 0.6211 and 0.0675 for unconditioned scenario, 0.4166 and 0.0879 for FT cycles, 0.6009 and 0.0846 for AS solution, 0.4064 and 0.0897 for coupled FT cycles and AS solution. Also, s_r and β of CMR model were recommended to be 0.0613 and 1.2438 for unconditioned scenario, 0.7642 and 0.6800 for FT cycles, 0.6005 and 1.1722 for AS solution, 0.7365 and 0.7266 for coupled environment. The most detrimental environment attack on the bond behavior was encountered when the GFRP-concrete specimens were subjected to the coupled environmental conditions and

thus, safe design values for the calibrated parameters are recommended as the values chosen from the coupled scenario.

Table 3-7. Mean values of the parameters considering different environmental conditions

Environments	τ_b (MPa)	s_b (mm)	mBPE model		CMR model	
			α	p	s_r	β
Unconditioned	18.86	1.42	0.6211	0.0675	0.6013	1.2438
FT cycles	18.27	1.72	0.4166	0.0879	0.7642	0.6800
AS solution	18.58	1.67	0.6009	0.0846	0.6005	1.1722
Coupled FT cycles and AS solution	17.34	1.78	0.4064	0.0897	0.7365	0.7226

3.6. Conclusions

This chapter presented a detailed experimental-analytical investigation on the bond durability of GFRP bars in concrete when exposed to simulated weathering. Totally 26 pullout samples with three different concrete covers were designed and exposed to different environmental conditions in terms of FT cycles, AS solution and the coupled both effects. The durability of the GFRP-concrete specimens under weathering were assessed through the failure mode, weight loss, relative dynamic modulus of elasticity and durability factor, as well as the bond strength reduction. With the obtained experimental data, the analytical models were then calibrated by considering environmental influences for more widespread applications. Specifically, several conclusions can be drawn in the following:

(1) The failure mode of the pullout specimens having concrete cover $c = 3.0d_b$ changed from pullout of the bars to concrete splitting when exposed to 75 FT cycles with temperatures ranging from -18 ± 2 ℃ and 4 ± 2 ℃, while pullout failure was observed in all the specimens having concrete cover $c = 4.5d_b$. Such observations were consistent with the stipulations of ACI

440.1R-06, of which the bond equation accounts for pullout failure by limiting c/d_b to 3.5. From the perspective of design, concrete cover with sufficient resistance to prevent brittle failure of concrete splitting needs to be addressed especially for the weathering, such as FT effects.

(2) The surface scaling of the specimens subjected to the coupled FT cycles and AS solution was obvious, where the flaking of the surface mortar and exposure of the coarse aggregate were clearly observed. Also, the weight loss of those coupled conditioned specimens was the largest among all scenarios, with 1.23 percent and 1.34 percent for the specimens having $c = 3.0d_b$ and $c = 4.5d_b$, respectively. On the contrary, the specimens conditioned with AS solution exhibited minor weight losses, with 0.24 percent and 0.21 percent for the specimens having $c = 3.0d_b$ and $c = 4.5d_b$, respectively.

(3) The specimens having $c = 3.0d_b$ suffered from approximately 26 percent reduction in the relative dynamic modulus of elasticity under the coupled FT cycles and AS solution. Accordingly, the durability factors of the pullout specimens conditioned with coupled environments were generally smaller than those conditioned with individual FT cycles. The smallest durability factor was 51.21 percent, which was observed in the specimen with $c = 3.0d_b$ under the coupled environment. Furthermore, the durability factors of all the FT conditioned specimens fell into the interval between 40 percent and 85 percent, indicating the medium FT resistance.

(4) The bond-slip relationship reveals that increasing concrete cover may have great contribution in enhancing the pre-peak bond resistance to the environmental attacks in terms of FT cycles, AS solution, and coupled influences of the both. By increasing the concrete cover from $c = 3.0d_b$ to $c = 4.5d_b$, the bond strength reductions were reduced from 14 percent to 8 percent under the coupled conditioning, and from 12 percent to 3 percent under the individual FT

cycles. Similar patterns were also observed in the normalized bond strength, indicating that larger concrete cover can effectively improve the FT resistance of the GFRP-concrete element. In addition, the individual AS solution was found to have minor impact on the bond strength of the pullout specimens.

(5) The calibrated analytical models considering the environmental effect matched well with the experimental results for the bond-slip prediction in terms of the ascending branch. In particular, the CMR model performed better than the mBPE model. The R^2 of the CMR model for all bond-slip curve-fittings were greater than 0.98, indicating rather close predictions to the test results. The average values of the unconditioned and conditioned specimens were summarized. Considering the worst case, the coupled conditioning, α and p of mBPE model were suggested to be 0.4064 and 0.0897, and s_r and β of CMR model were recommended to be 0.7365 and 0.7266, respectively.

3.7. References

ACI Committee. (2006). Guide for the design and construction of structural concrete reinforced with FRP bars. ACI 440.1 R, 6.

Altalmas, A., El Refai, A., and Abed, F. (2015). Bond degradation of basalt fiber-reinforced polymer (BFRP) bars exposed to accelerated aging conditions. Construction and Building Materials, 81, 162-171.

Alves, J., El-Ragaby, A., and El-Salakawy, E. (2010). Durability of GFRP bars' bond to concrete under different loading and environmental conditions. Journal of Composites for Construction.

Antonietta Aiello, M., Leone, M., and Pecce, M. (2007). Bond performances of FRP rebars-reinforced concrete. Journal of Materials in Civil Engineering, 19(3), 205-213.

ASTM C666 / C666M. (2015). Standard Test Method for Resistance of Concrete to Rapid Freezing and Thawing. ASTM International, West Conshohocken, PA.

ASTM D570. (2010). Standard Test Method for Water Absorption of Plastics. ASTM International, West Conshohocken, PA.

ASTM D7205 / D7205M-06. (2011). Standard Test Method for Tensile Properties of Fiber Reinforced Polymer Matrix Composite Bars. ASTM International, West Conshohocken, PA.

ASTM D7913/D7913M. (2014). Standard Test Method for Bond Strength of Fiber-Reinforced Polymer Matrix Composite Bars to Concrete by Pullout Testing. ASTM International, West Conshohocken, PA.

Belarbi, A., and Wang, H. (2011). Bond durability of FRP bars embedded in fiber-reinforced concrete. Journal of Composites for Construction, 16(4), 371-380.

Benmokrane, B., Wang, P., Ton-That, T. M., Rahman, H., and Robert, J.-F. (2002). Durability of glass fiber-reinforced polymer reinforcing bars in concrete environment. Journal of Composites for Construction, 6(3), 143-153.

C39M, A. C. (2016). Standard Test Method for Compressive Strength of Cylindrical Concrete Specimens. ASTM International, West Conshohocken, PA.

C215, A. (2014). Standard Test Method for Fundamental Transverse, Longitudinal, and Torsional Resonant Frequencies of Concrete Specimens. ASTM International, West Conshohocken, PA.

Ceroni, F., Cosenza, E., Gaetano, M., and Pecce, M. (2006). Durability issues of FRP rebars in reinforced concrete members. Cement and Concrete Composites, 28(10), 857-868.

Chen, Y., Davalos, J. F., and Ray, I. (2006). Durability prediction for GFRP reinforcing bars using short-term data of accelerated aging tests. Journal of Composites for Construction, 10(4), 279-286.

Chen, Y., Davalos, J. F., Ray, I., and Kim, H.-Y. (2007). Accelerated aging tests for evaluations of durability performance of FRP reinforcing bars for concrete structures. Composite Structures, 78(1), 101-111.

Cosenza, E., Manfredi, G., and Realfonzo, R. (1995). Analytical modelling of bond between FRP reinforcing bars and concrete. Paper presented at the Non-Metallic (FRP) Reinforcement for Concrete Structures: Proceedings of the Second International RILEM Symposium.

Cosenza, E., Manfredi, G., and Realfonzo, R. (1997). Behavior and modeling of bond of FRP rebars to concrete. Journal of Composites for Construction, 1(2), 40-51.

Davalos, J. F., Chen, Y., and Ray, I. (2008). Effect of FRP bar degradation on interface bond with high strength concrete. Cement and Concrete Composites, 30(8), 722-730.

Ding, Y., Ning, X., Zhang, Y., Pacheco-Torgal, F., and Aguiar, J. (2014). Fibres for enhancing of the bond capacity between GFRP rebar and concrete. Construction and Building Materials, 51, 303-312.

Eligehausen, R., Popov, E. P., and Bertero, V. V. (1982). Local bond stress-slip relationships of deformed bars under generalized excitations.

Fursa, T., Utsyn, G., Korzenok, I., and Petrov, M. (2015). Using electric response to mechanical impact for evaluating the durability of the GFRP-concrete bond during the freeze-thaw process. Composites Part B: Engineering.

Galati, N., Nanni, A., Dharani, L. R., Focacci, F., and Aiello, M. A. (2006). Thermal effects on bond between FRP rebars and concrete. Composites Part A: Applied Science and Manufacturing, 37(8), 1223-1230.

Karbhari, V., Chin, J., Hunston, D., Benmokrane, B., Juska, T., Morgan, R., et al. (2003). Durability gap analysis for fiber-reinforced polymer composites in civil infrastructure. Journal of Composites for Construction, 7(3), 238-247.

Kim, H.-Y., Park, Y.-H., You, Y.-J., and Moon, C.-K. (2008). Short-term durability test for GFRP rods under various environmental conditions. Composite Structures, 83(1), 37-47.

Lin, X., and Zhang, Y. (2014). Evaluation of bond stress-slip models for FRP reinforcing bars in concrete. Composite Structures, 107, 131-141.

Malvar, L. J. (1994). Bond stress-slip characteristics of FRP rebars: DTIC Document.

Micelli, F., and Nanni, A. (2004). Durability of FRP rods for concrete structures. Construction and Building Materials, 18(7), 491-503.

Mufti, A., Onofrei, M., Benmokrane, B., Banthia, N., Boulfiza, M., Newhook, J., et al. (2005). Durability of GFRP reinforced concrete in field structures. Paper presented at the Proceedings of the 7th International Symposium on Fiber-Reinforced Polymer Reinforcement for Reinforced Concrete Structures (FRPRCS-7), Kansas City, Mo.

Mufti, A. A., Banthia, N., Benmokrane, B., Boulfiza, M., and Newhook, J. P. (2007). Durability of GFRP composite rods. Concrete International, 29(02), 37-42.

Popovics, J., Zemajtis, J., and Shkolnik, I. (2008). A study of static and dynamic modulus of elasticity of concrete. ACI-CRC Final Report.

Robert, M., and Benmokrane, B. (2010). Effect of aging on bond of GFRP bars embedded in concrete. Cement and Concrete Composites, 32(6), 461-467.

Robert, M., and Benmokrane, B. (2013). Combined effects of saline solution and moist concrete on long-term durability of GFRP reinforcing bars. Construction and Building Materials, 38, 274-284.

Rossetti, V. A., Galeota, D., and Giammatteo, M. (1995). Local bond stress-slip relationships of glass fibre reinforced plastic bars embedded in concrete. Materials and Structures, 28(6), 340-344.

Tannous, F. E., and Saadatmanesh, H. (1998). Environmental effects on the mechanical properties of E-glass FRP rebars. Materials Journal, 95(2), 87-100.

Wang, K., Lomboy, G., and Steffes, R. (2009). Investigation into freezing-thawing durability of low-permeability concrete with and without air entraining agent.

Yan, F., and Lin, Z. (2016). Bond behavior of GFRP bar-concrete interface: Damage evolution assessment and FE simulation implementations. Composite Structures, 155, 63-76.

Yan, F., Lin, Z., Wang, X., Azarmi, F., and Sobolev, K. (2016). Evaluation and prediction of bond strength of GFRP-bar reinforced concrete using artificial neural network optimized with genetic algorithm. Composite Structures.

Yan, F., Lin, Z., and Yang, M. (2016). Bond mechanism and bond strength of GFRP bars to concrete: A review. Composites Part B: Engineering, 98, 56-69.

Yan, F., and Lin, Z. B. (2016). Bond durability assessment and long-term degradation prediction for GFRP bars to fiber-reinforced concrete under saline solutions. Composite Structures.

Zhou, J., Chen, X., and Chen, S. (2012). Effect of different environments on bond strength of glass fiber-reinforced polymer and steel reinforcing bars. KSCE Journal of Civil Engineering, 16(6), 994-1002.

4. BOND DURABILITY ASSESSMENT AND LONG-TERM DEGRADATION PREDICTION FOR GFRP BARS TO FIBER-REINFORCED CONCRETE UNDER SALINE SOLUTIONS

4.1. Introduction

To achieve long-term durable performance over 75 years or more, understanding of bond mechanism of GFRP bars to concrete over time and long-term degradation of GFRP materials under harsh environments is in high demand for their more widespread applications in civil engineering structures.

As stated in (Achillides and Pilakoutas, 2004; Baena et al., 2009; Okelo and Yuan, 2005; Yan and Lin, 2016), bond mechanism of GFRP bars to concrete is different to that of conventional steel reinforcements due to different material and mechanical properties. It is well established that concrete matrix shows significant influence on GFRP bond to concrete. In particular, use of discrete fiber in concrete enables increase in both bond strength and ductility capacity due to fiber bridging mechanism in cement matrix (Ding et al., 2014; B. Kim et al., 2013). Kim et al. (B. Kim et al., 2013) conducted pullout tests of sand-coated and helically-wrapped GFRP bars embedded in concrete reinforced with hooked-end steel fiber, polypropylene (PP) fiber, and PVA fiber, respectively. They observed that pullout failure of the GFRP bars in FRC was significantly delayed with maintaining high residual strength and toughness due to effective confinement to crack development. Belarbi and Wang (Belarbi and Wang, 2011) investigated sand-coated and helically-wrapped GFRP bars in PP fiber reinforced concrete specimens under different environmental conditioning, including deicing salt solutions, elevated temperatures, and freeze-thaw cycles. They found that bond strength reduction was 6% in the FRC in contrast to 28% in the plain concrete when exposed to environmental aging over 200

cycles. Clearly, GFRP bars to FRC system exhibits advanced structural performance and superior corrosion resistance as compared to those in plain concrete.

Considering concrete presents a highly alkaline (12.5 to 13.5 pH) which may degrade the GFRP material, many studies addressed efforts on assessing the long-term performance under alkaline solutions. However, it has been reported that traditional accelerated aging techniques by using either high alkaline solutions or bare bars directly immersing in solutions overestimated the degradation level of GFRP bars, which in turn led to unrealistic predictions with too conservative estimates (Robert and Benmokrane, 2013; Robert et al., 2009; Yan, Lin, Zhang, et al., 2016). Robert and Benmokrane (Robert and Benmokrane, 2013) reported their experiments of mortar-wrapped GFRP bar specimens immersed in saline solutions at 50 ℃ for 365 days and 70 ℃ for 120 days. The later micrograph analysis demonstrated that no significant damage was captured at the bar-concrete interface. Such experimental results were consistent with field studies. Mufti et al. (Mufti et al., 2005) further confirmed that the GFRP bars are durable and highly compatible with concrete based on the field investigations on five GFRP reinforced concrete bridge structures exposed to natural environments over five to eight years. Their analysis supported that the structures maintained good bond at the GFRP bar-concrete interface and no significant degradation due to alkalinity of concrete was observed by both optical microscope and Fourier transformed infrared spectroscopy. Thus, it is more reasonable to predict the long-term performance of GFRP bar to concrete by embedding bars to concrete in saline solutions, to more accurately simulate actual situations in field, whereas there is not direct immersion of the bars in solutions.

It is desirable for civil engineering structures to maintain the functionality and achieve long-lasting durability over time. Effective evaluation of the long-term (e.g., 75-100 years)

durability performance of GFRP bars in concrete structures thus will be crucial. Accelerated aging procedures and predictive models based on the Arrhenius concept have been generally developed for assessing service lifetime (Chen et al., 2006; Robert and Benmokrane, 2013). Zhou et al. (Zhou et al., 2011) developed a predictive model using Arrhenius relation and time shift factor (TSF) method to account for the effects of acid rain on the bond strength of GFRP bars to concrete. They predicted that the bond strength retention of GFRP bars after 34 years was about 84% when exposed to the level of the acid environment in the southeastern China. Similar prediction method was also adopted in (Dong et al., 2016) for determining long-term bond strength of basalt fiber-reinforced polymer (BFRP) bars under seawater conditions. Although applications of the Arrhenius-based methods have been in either tensile strength or bond strength prediction of FRP bars to plain concrete, the methodology has not been explored so far for the GFRP to FRC elements, and its applicability is yet to be verified.

Thus, this chapter mainly aims at durability assessment and long-term degradation prediction of the GFRP bar bond to FRC elements. The commonly used steel and PVA fibers with different fiber volume fractions were used herein. The environmental conditionings included the effect of saline solutions, which are often encountered in marine environment or deicing salts used in cold regions. GFRP bars embedded in concrete were designed and exposed to the simulated solutions at different elevated temperatures under different durations of time. Some critical indices associated with the weathering, such as the failure mode, adhesion stress and bond strength, were measured to evaluate the durability performance of the GFRP-FRC elements. Moreover, the analytical models were integrated with the experimental data to better explore their applications to the bond development over time. Besides, a detailed procedure based on Arrhenius relation and TSF method was first developed and verified for the long-term

degradation prediction of bond strength, and then applied in different environmental aging under representative average annual temperatures and relative humidity.

4.2. Experimental Program

4.2.1. Specimen Design

4.2.1.1. Statistical data

The samples herein were designed in accordance with a database of over 680 pullout GFRP specimens summarized from the literature, which was recently reported by Yan et al. (Yan, Lin, and Yang, 2016). The critical information pertaining to both GFRP bars and concrete matrix, as well as structural fibers, provides a sound basis to select materials widely accepted in previous studies.

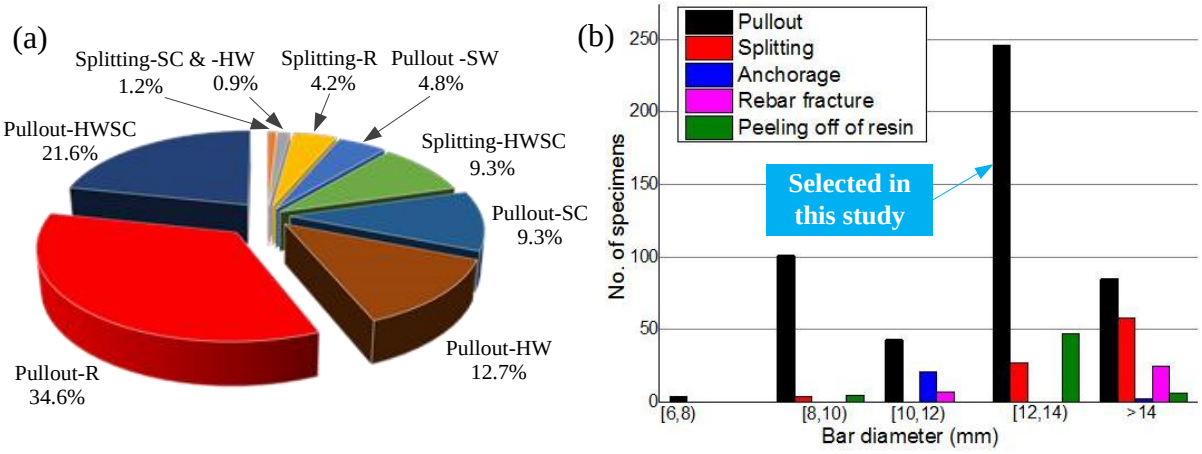

Figure 4-1. GFRP bars used in previous studies: (a) surface treatment and (b) bar diameter (Yan, Lin, and Yang, 2016)

Figure 4-1 (a) and 1 (b) show the key parameters of the GFRP bars. Observed failure modes and surface treatment are assigned with the legends. For simplicity, the first term of the legends denotes the failure mode, the second term denotes the surface treatment: a) R = ribbed; b) HW = helically wrapped; c) SC = sand coated; d) HWSC = helically wrapped and sand coated; e) SW = spirally wrapped. Clearly, the ribbed surface, helically wrapped and sand coated surface

are associated with pullout as the majority of failure modes. Also, the bar diameter (d_b) ranging from 12 to 14 mm are mostly found in those pullout tests. Hence, the GFRP bars with a nominal diameter of 12.7 mm and helically wrapped and sand-coated surface can be selected without loss of generality.

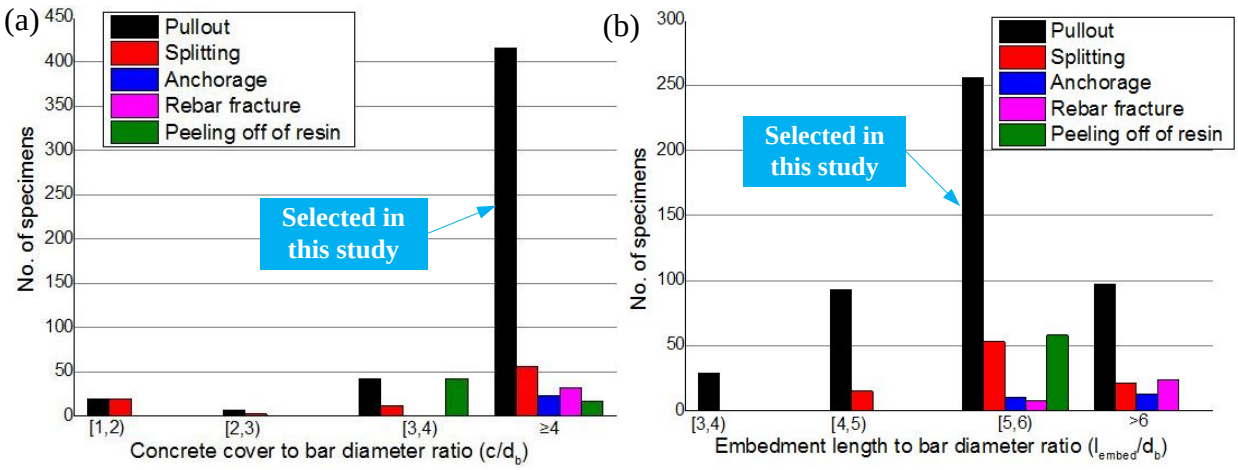

Figure 4-2. Concrete size used in previous studies: (a) concrete cover, (b) embedment length (Yan, Lin, and Yang, 2016)

Figure 4-2 (a) and 2 (b) demonstrate the critical statistics for the pullout concrete specimens in terms of concrete cover (c) and bar embedment length (l_d). Figure 4-2 (a) indicates that the scenarios of $c/d_b \geq 4$ associated with pullout failure account for the majority over other scenarios. This conforms to the stipulations of ACI 440.1R-06, of which the bond equation accounts for pullout failure by limiting c/d_b to 3.5 (ACI Committee, 2006). Therefore, the ratio of $c/d_b = 4.5$ can be designed to probably prevent splitting failure. Figure 4-2 (b) reveals that the embedment length to bar diameter ratio ranging from 5 to 6 is mostly used in the previous studies. Thus, the embedment length of GFRP bars was determined to be $l_d = 5d_b$, which is also in accordance with the embedment length stipulated in ASTM D 7913/D 7913M (ASTM D7913/D7913M, 2014).

Enhanced structural performance of FRC using the commonly used fibers have been reported in previous studies (Ding et al., 2014; Ding et al., 2012; B. Kim et al., 2013; Wang and Belarbi, 2011, 2013), and summarized in (Yan, Lin, and Yang, 2016), including the favorable characteristics in improvement of workability, splitting, bending and shear behaviors, as well as the beneficial interfacial bond to concrete matrix. Among those types of fibers, steel and PVA fibers exhibit considerable improvement on the bond behavior of GFRP bars to concrete and hence, they were selected to be added into the concrete mixture. In addition, the two different fiber volume fractions (V_f), 0.5 and 1.0% by volume, were used to investigate their influences on the bond performance, respectively.

4.2.1.2. Materials

(I) GFRP bars

Figure 4-3. GFRP bars used in this study

The brand Aslan 100 series GFRP bars with helically-wrapped and sand-coated surface treatment were used, as shown in Figure 4-3. All of the bars are made of E-glass fibers and thermosetting vinyl ester resin, and have the nominal diameter of 12.7 mm. The glass content by weight is greater than 70%. The guaranteed tensile strength in accordance with manufacturer is 758 MPa, and elastic modulus was 46 GPa. The tensile strength retention is greater than 80% according to the ASTM D 7205 (ASTM D7205 / D7205M-06, 2011) when exposed to 12.8 pH solution at 60 ℃ over 90 days. The 24-hour moisture absorption at 50 ℃ is less than or equal to

0.25% according to the ASTM D 570 (ASTM D570, 2010). Table 4-1 summarizes the detailed mechanical and physical properties, as reported by the manufacturer.

Table 4-1. Material properties of 12.7 mm diameter GFRP bars (as reported by manufacturer)

	Item	Unit	Value
Mechanical properties	Guaranteed tensile strength	MPa	758
	Tensile modulus of elasticity	GPa	46
	Ultimate strain	%	1.64
	Strength retention due to alkali resistance	%	> 80
Physical properties	Transition temperature of Resin	℃	> 110
	Moisture absorption	%	≤ 0.25
	Glass fiber content by weight	%	> 70

(I) Fibers and concrete

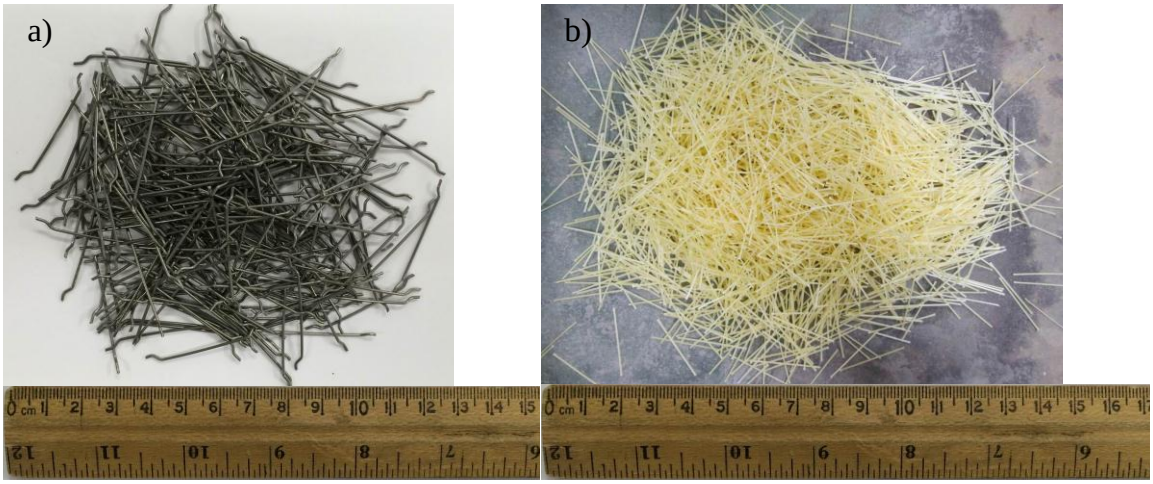

Figure 4-4. Fiber types (a) steel fiber and (b) PVA fiber

Structural fibers were used to investigate their enhancement on the bond durability for GFRP bars. Figure 4-4 shows the hooked-end steel and PVA fibers used in this study, and Table 4-2. presents their material properties, respectively. The pullout specimens were determined to be $127 \times 127 \times 177.8$ mm, of which all the GFRP bars were embedded in the center of the

cross section to make $c/d_b = 4.5$. The embedment length was $l_d = 5d_b = 63.5$ mm, which is regarded to be capable of describing the local GFRP-concrete bond. Accordingly, a set of formwork was constructed out of plywood. Prior to casting, the GFRP bars with bond breakers made of plastic tubes were deployed in the formwork, as shown in Figure 4-5.

Table 4-2. Fiber properties

Fiber type	Fiber length (mm)	Diameter (μm)	Aspect ratio	Density (g/cm^3)	Tensile strength (MPa)	Elastic modulus (GPa)	Surface structure
Steel	30	560	54	7.8	1100	200	Hook end
PVA	50	660	45	1.3	800	29	Monofilament

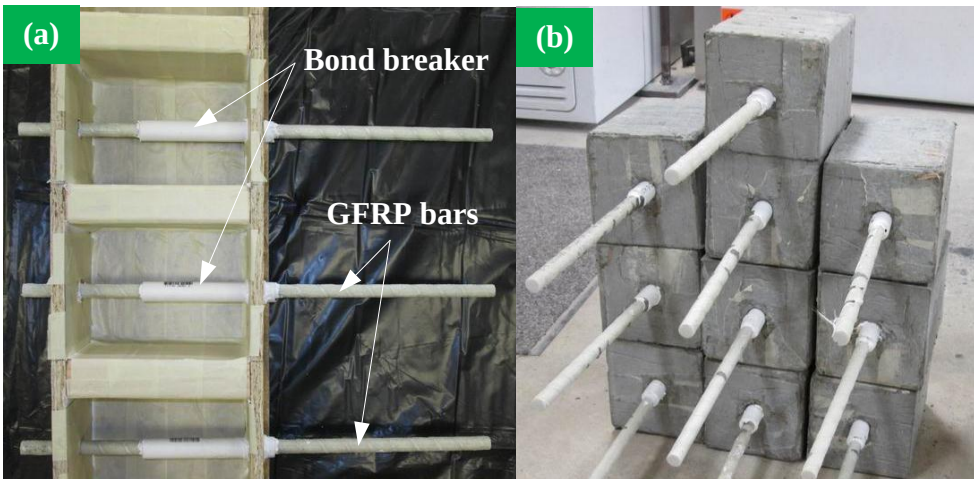

Figure 4-5. Specimen design: (a) GFRP bars in formwork before concrete pouring and (b) specimens after concrete cast

Table 4-3 details the mix design for both plain concrete and FRC with different fiber contents. Type I Portland cement was used for concrete mixture. The nominal maximum size of the coarse aggregate was 12.7 mm, and the fine aggregate size was about 0 to 4.75 mm. The concrete was mixed in a concrete mixer with a capacity of 0.17 m^3. To ensure mixing quality, totally five batches of concrete were used, of which the volume of each batch was less than 0.10 m^3. The mixing procedure used the following steps: first, the coarse and fine aggregates were

dry-mixed, and cement was added and thoroughly dry-mixed thereafter. Then water was added and the mixture was continuously mixed. Finally, fibers and super-plasticizer were slowly added into the mix until the concrete exhibited uniform in appearance. The concrete was cast in horizontal position. After molding, all the specimens were immediately covered with a plastic sheet to prevent moisture loss at 24 hours, and then removed from the molds and cured in water at room temperature of 23 ℃ at 28 days. The mean concrete compressive strength of the specimens used in the test was determined according to ASTM C 39/C 39 M (C39M, 2016), where three 150×300 mm cylinders were used for each batch, as presented in Table 4-4.

Table 4-3. Composition of concrete mix

Mix type	Fiber type	Fiber volume fraction V_f (%)	Water (kg/m^3)	Cement (kg/m^3)	Coarse aggregate (kg/m^3)	Fine aggregate (kg/m^3)	Super-plasticizer (kg/m^3)
PC	0	0	186	503	910	717	0.89
Steel0.5	0.5	0.5	186	503	910	717	0.89
Steel1.0	1.0	1.0	186	503	910	717	1.95
PVA0.5	0.5	0.5	186	503	910	717	0.89
PVA1.0	1.0	1.0	186	503	910	717	1.95

4.2.2. Environmental Aging Design

As stated early, the traditional accelerated aging using high alkaline environment may overestimate the solutions as supposed in actual situation, and thus lead to unrealistic estimation. The alkaline effect was considered by which the pH of the solution surrounding GFRP bars resulted from the concrete absorbing water, thereby releasing alkaline ions from the concrete itself directly surrounding to the bars. On the other hand, the saline solution was implemented by 3% concentration sodium chloride (NaCI) (H.-Y. Kim et al., 2008; Robert and Benmokrane, 2013), which was used to simulate the marine environment in warm regions or use of deicing

salts in cold regions. Referring to the method suggested in (Robert and Benmokrane, 2013), the aging specimens were placed in several plastic containers. The covers were sealed to inhibit excessive evaporation of watering during the period of conditioning. Moreover, the water level was maintained to retain the constant pH level. The immersion of specimens was performed under two different temperatures (50 and 70 ℃, respectively) implemented by a temperature control room through three different durations (30, 45, and 60 days, respectively). At the end of each period of time, three specimens were removed from the saline solution and dried in air for 24 hours before they were subjected to pullout testing for determining their bond strengths.

4.2.3. Pullout Test Design

The pullout tests of the samples were performed using the 1000-kN capacity universal testing machine at NDSU. The test specimens were sheathed with thick-wall hollow steel pipes at the free portion of the GFRP bar, as shown in Figure 4-6 (a). The pipes were 203 mm in length and 19.05 mm in inside diameter, which were further processed with internal threaded along the length to increase the roughness for anchorage. The pipes were filled with a commercial epoxy to adhere the bar for at least 24 hours to take effect before testing. The schematic demonstration of the test setup is shown in Figure 4-6 (b). The sample encased in a steel reaction frame was instrumented with three linear variable differential transformers (LVDTs) to record the elongation of the bar. All the tests were conducted using displacement control at a rate of 0.02 mm/s, thus the post peak behavior of the bond-slip relationship can be obtained. The load was measured with the electronic loading cell of the machine, and the slips at both loaded and free ends were measured with the LVDTs. All measurements, including the pullout load and displacements, were recorded synchronously by an automatic data-acquisition system at a rate of 2 data/s.

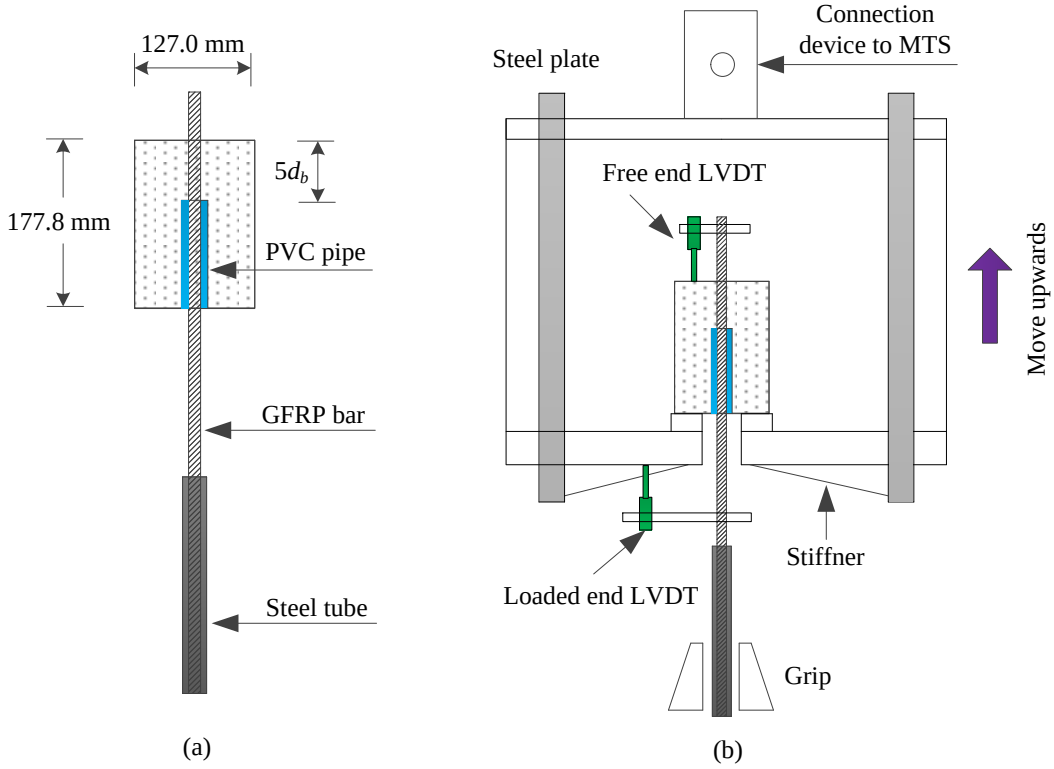

Figure 4-6. Schematic demonstration of the (a) pullout specimen and (b) test setup

4.3. Experimental Results and Discussion

A total of 105 prism specimens were prepared and tested, including 15 control specimens and 90 conditioned specimens. The conditioned specimens are labeled in the following order: concrete mix type, immersion temperature, immersion time in days, and specimen number in each set. For example, specimen Steel1.0-50-45-3 refers to a steel FRC specimen with fiber volume fraction of 1.0%, and was immersed in the saline solution at 50 ℃ for 45 days. The digit (3) refers to the third specimen in its set. In the pullout test, the stress is not constantly distributed along the embedment length and hence, the average bond stress is defined as:

$$\tau = \frac{P}{\pi d_b l_d}, \tag{4-1}$$

where P is the tensile load.

Table 4-4. Pullout test results for both plain concrete and FRC specimens

Specimen	f_c' (MPa)	τ_b (MPa)			$\tau_b{}^a$ (MPa)	St. (%)	τ_b^{*a} (MPa$^{0.5}$)	$\tau_{ons}{}^a$ (MPa)	τ_b^{ra} (%)	Failure mode[b]
		No. 1	No. 2	No. 3						
Control specimens										
PC0.0-Control-1,2,3	46.58	15.68	16.11	15.09	15.63	0.51	2.29	0.69	100	PO-1,2,3
Steel0.5-Control-1,2,3	45.27	19.15	18.23	18.87	18.75	0.47	2.79	0.57	100	PO-1,2,3
Steel1.0-Control-1,2,3	46.72	21.26	22.44	21.96	21.89	0.59	3.20	0.42	100	PO-1,2,3
PVA0.5-Control-1,2,3	44.93	15.63	17.50	16.94	16.69	0.96	2.49	0.60	100	PO-1,2,3
PVA1.0-Control-1,2,3	45.32	16.32	17.16	18.69	17.39	1.20	2.58	0.36	100	PO-1,2,3
Conditioned plain concrete specimens										
PC0.0-50-30-1,2,3	46.58	15.18	14.22	15.41	14.94	0.63	2.19	0.73	95.59	PO-1,2,3
PC0.0-50-45-1,2,3		13.89	14.66	14.93	14.49	0.54	2.12	0.81	92.71	PO-1,2,3
PC0.0-50-60-1,2,3		13.91	14.95	13.68	14.18	0.68	2.08	0.65	90.72	PO-1,2,3
PC0.0-70-30-1,2,3		14.36	15.39	13.92	14.56	0.75	2.13	0.84	93.15	PO-1,2,3
PC0.0-70-45-1,2,3		14.25	13.54	14.06	13.95	0.37	2.04	0.77	89.25	PO-1,2,3
PC0.0-70-60-1,2,3		14.11	13.38	10.06	13.75[c]	2.16	2.01	0.63	87.97	PO-1,2; S-3
Conditioned steel fiber reinforced concrete specimens										
Steel0.5-50-30-1,2,3	45.27	18.39	16.95	18.69	18.01	0.93	2.68	0.62	96.05	PO-1,2,3
Steel0.5-50-45-1,2,3		17.82	17.06	17.80	17.56	0.43	2.61	0.68	93.65	PO-1,2,3
Steel0.5-50-60-1,2,3		16.64	17.05	17.90	17.20	0.64	2.56	0.61	91.73	PO-1,2,3
Steel0.5-70-30-1,2,3		18.17	18.01	16.29	17.49	1.04	2.60	0.69	93.28	PO-1,2,3
Steel0.5-70-45-1,2,3		15.99	16.76	18.00	16.92	1.01	2.51	0.72	90.24	PO-1,2,3
Steel0.5-70-60-1,2,3		16.28	17.44	16.49	16.74	0.62	2.49	0.65	89.28	PO-1,2,3
Steel1.0-50-30-1,2,3	46.72	21.33	20.75	21.79	21.29	0.52	3.11	0.52	97.26	PO-1,2,3
Steel1.0-50-45-1,2,3		21.42	19.38	21.97	20.92	1.36	3.06	0.58	95.57	PO-1,2,3
Steel1.0-50-60-1,2,3		19.25	20.02	22.08	20.45	1.46	2.99	0.55	93.42	PO-1,2,3
Steel1.0-70-30-1,2,3		21.01	20.55	20.73	20.76	0.23	3.04	0.55	94.84	PO-1,2,3
Steel1.0-70-45-1,2,3		19.38	21.44	19.85	20.22	1.08	2.96	0.63	92.37	PO-1,2,3
Steel1.0-70-60-1,2,3		18.75	19.92	20.63	19.77	0.95	2.89	0.59	90.32	PO-1,2,3
Conditioned PVA fiber reinforced concrete specimens										
PVA0.5-50-30-1,2,3	44.93	15.99	16.09	15.79	15.96	0.15	2.38	0.65	95.63	PO-1,2,3
PVA0.5-50-45-1,2,3		16.58	14.91	15.02	15.50	0.93	2.31	0.66	92.87	PO-1,2,3
PVA0.5-50-60-1,2,3		15.33	15.75	14.41	15.16	0.69	2.26	0.59	90.83	PO-1,2,3
PVA0.5-70-30-1,2,3		15.57	16.08	15.17	15.61	0.46	2.33	0.74	93.53	PO-1,2,3
PVA0.5-70-45-1,2,3		16.04	14.88	13.71	14.88	1.17	2.22	0.68	89.16	PO-1,2,3
PVA0.5-70-60-1,2,3		15.24	14.00	11.20	14.62	2.07	2.18	0.57	87.60	PO-1,2,3
PVA1.0-50-30-1,2,3	45.32	18.16	18.00	17.75	16.72	0.21	2.48	0.42	96.15	PO-1,2,3
PVA1.0-50-45-1,2,3		16.93	17.88	17.72	16.29	0.51	2.42	0.49	93.67	PO-1,2,3
PVA1.0-50-60-1,2,3		17.35	17.20	16.93	15.97	0.21	2.37	0.32	91.83	PO-1,2,3
PVA1.0-70-30-1,2,3		16.78	17.88	18.11	16.37	0.71	2.43	0.48	94.13	PO-1,2,3
PVA1.0-70-45-1,2,3		17.41	16.04	18.30	16.05	1.14	2.38	0.51	92.29	PO-1,2,3
PVA1.0-70-60-1,2,3		17.16	16.09	12.68	15.52	2.34	2.31	0.29	89.25	PO-1,2,3

[a] Mean value for nominally identical specimens.
[b] PO = pullout failure; S = splitting failure.
[c] Mean value excluding splitting failure.

The experimental results obtained from the pullout test were detailed in Table 4-4, where τ_b is the bond strength, τ_b^r is the bond strength retention in percentage, and St. is the standard deviation. The mean values of the bond strength of nominally identical specimens are also listed. Meanwhile, the normalized bond strength τ_b^* is used to account for the influence of concrete compressive strength, which is defined as:

$$\tau_b^* = \frac{\tau_b}{\sqrt{f_c'}} \quad (4\text{-}2)$$

Referring to the method used in (Altalmas et al., 2015), the adhesion stress τ_{ons} was determined as the stress at the onset of slip at the loaded end, indicating the stress at which the adhesion breaks between GFRP bars and surrounding concrete.

4.3.1. Mode of Failure

Table 4-4 details the failure modes of unconditioned and conditioned pullout specimens. Generally, for both plain concrete and FRC, most specimens failed by pullout of the bars except for specimen PC0.0-70-60-3 failed by concrete splitting. It was observed that the splitting failure occurred due to the imperfection of the bar eccentricity that caused radial tension to the surrounding concrete. The main crack went throughout the cross section of the specimen, leading to a brittle failure along with an abrupt splitting boom during the pullout test. Referring to the limit of $c = 3.5d_b$ term specified in ACI code [30] for pullout failure being probably predicted, the concrete cover $c = 4.5d_b$ used in this study confirms the stipulation of the design standards, and coincide with the aforementioned statistical analysis results. In particular, considering steel and PVA fibers additionally provide confining pressure to the surrounding concrete compared with plain concrete, the statistically designed concrete cover $c = 4.5d_b$ is expected to be sufficient to prevent abrupt splitting failure for reinforced concrete structures under the simulated saline environment.

4.3.2. Bond Stress-Slip Response

Figure 4-7 displays the typical bond stress vs. slip curves of both plain concrete and FRC concrete specimens, where the most severe conditions (at 70 ℃ over 60 days) were selected for the plots, in order to present test results more intuitively. In general, the ascending branches of the bond-slip curves at the free end show evident lag effect compared to those at the loaded end. This phenomenon is in accordance with the fact that the slip development at the free end lags behind that at the loaded end. The bond-slip curves display a sharp increase in bond stress over a small range of slip first, and thereafter develop along with a gradual reduction in bond stress over a large range of slip. Similar experimental results were previously reported in (Baena et al., 2009) for GFRP bars with deformed surface, where a gradually decayed slope was predominant in the post-peak bond development. On the contrary, GFRP bars with sand-coated surface were reported to have an abrupt decay for either plain concrete (Baena et al., 2009) or FRC (B. Kim et al., 2013). Such different post-peak bond behavior can be attributed to different governing bond mechanism due to surface treatment. It is known that the major load transfer mechanism for non-deformed (e.g., sand-coated) bars is known to be the friction developed at the bar-concrete interface, which is highly dependent on the transverse confinement or pressure (Baena et al., 2009). Unlike individual sand-coated surface, the surface of helically-wrapped fiber strands combined with sand particles can enhance the bond by which the bearing forces acting on the deformed surface contribute to the bond development as the bar is mobilized. At the early stage of pre-peak bond development, bearing force and chemical adhesion contribute to the majority of bond stress. When the bond force increases to a certain value, the bar starts sliding along the lug area. Concrete cracks (or even crushing) occur and the bearing force due to mechanical interlocking against the concrete diminishes, resulting in a gradual decay in the bond stress

accompanying with an apparent slip. Finally, the residual wedging action of the bar deformations on the surrounding concrete governs the bond mechanism of the post-peak branch.

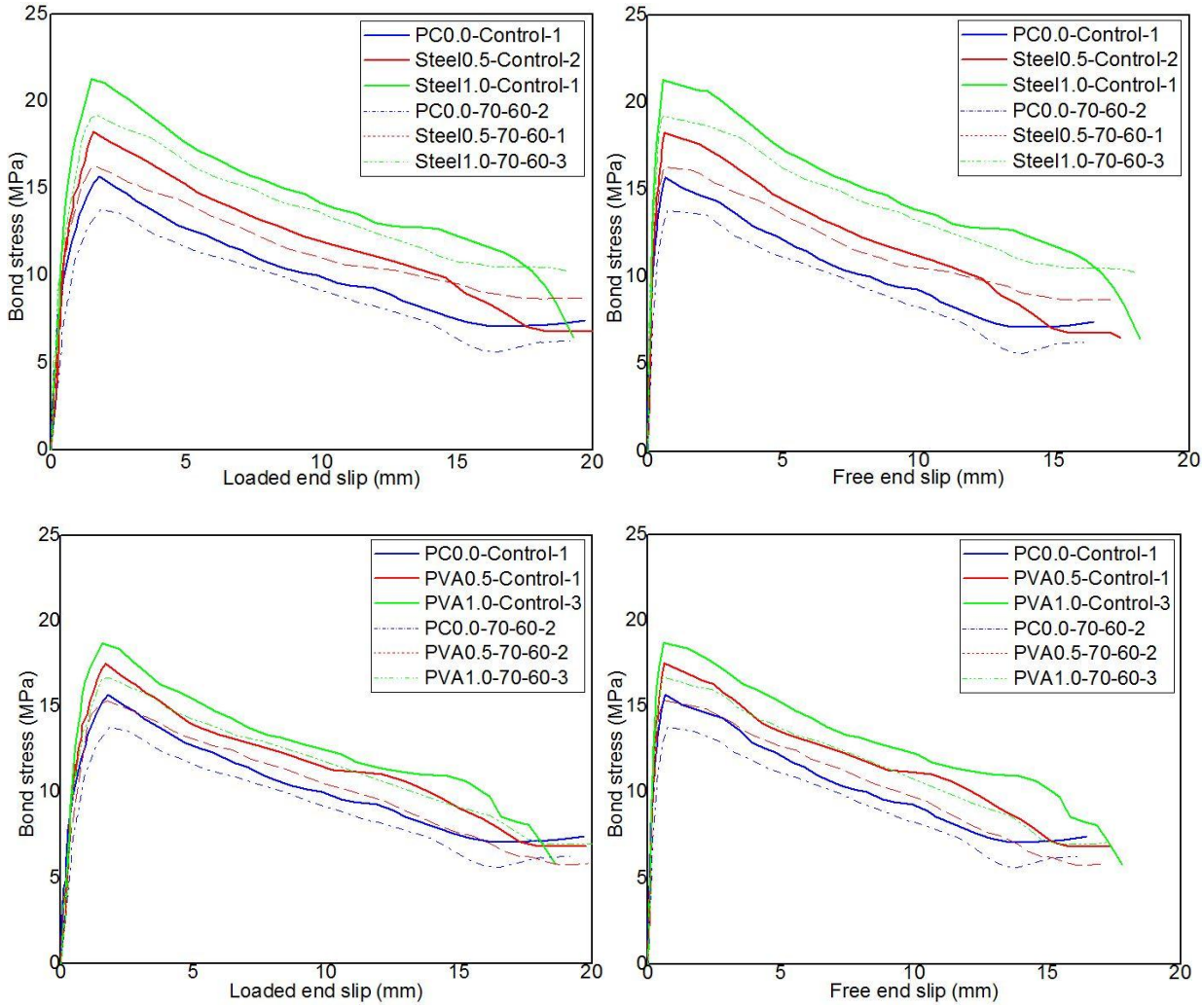

Figure 4-7. Representative bond stress-slip responses for plain concrete and FRC specimens

The control and conditioned FRC specimens (outlined in green and red lines) showed larger bond stress as slip developed compared to the corresponding plain concrete specimens (outlined in blue lines), indicating the improvement of bond performance by adding structural fibers into concrete matrix. This agrees with the experimental results previously reported in (B. Kim et al., 2013), which stated that the addition of hooked-end steel and PVA fibers significantly enhanced the bond stress, as well as the residual stress. With the same fiber content, steel FRC

specimens (e.g., Steel0.5-Control-2, Steel1.0-Control-1, Steel0.5-70-60-1, and Steel1.0-70-60-3) demonstrated more remarkable enhancement in bond stress compared to PVA FRC specimens (e.g., PVA0.5-Control-1, PVA1.0-Control-3, PVA0.5-70-60-2, and PVA0.5-70-60-3). In particular, the steel FRC specimens with fiber volume fraction of 1.0% clearly demonstrated the largest capacity of energy absorption because of the larger area under the post-peak branch.

4.3.3. Adhesion Stress

Adhesion is the major component accounting for GFRP-concrete bond at the initial stage of loading. The adhesion stress was determined as the stress at the onset of slip at the loaded end, indicating the stress at which the adhesion breaks at the bar-concrete interface. In this study, referring to the method used in (Altalmas et al., 2015), the adhesion stress was derived from the bond-slip curves at the point where the slope of the ascending branch exhibited sharp change that implies the destruction of adhesion.

Figure 4-8 shows the average adhesion stress for both control and conditioned specimens exposed to different temperatures for different durations of time. Two general trends were observed. First, the plain concrete specimens demonstrated larger adhesion stress compared to the FRC specimens. Second, the adhesion stresses of both plain concrete and FRC specimens increased at the early stage of exposure, and then decreased over continuous immersion. In detail, both the plain concrete and FRC specimens exhibited an increasing trend after 30 days of exposure, which can be attributed to the swelling of the bars exerting a tightening force between the bar and concrete. The adhesion stress decreased after 45 days of exposure under a temperature of 50 ℃ whereas decreased after 45 days under 70 ℃. This can be explained by that the rate of dissipation of solution agents tended to diminish over time, and the bond degradation due to environmental conditions also counteracted a portion of the initial increase. Moreover,

when the adhesion degradation due to environments is larger than its increase due to swelling, reduction was observed accordingly. Such shift process can be accelerated under higher temperatures. Thus, the reduction of adhesion stress occurred earlier under 45 ℃ than that under 70 ℃. In addition, a discrepancy was noticed in the PVA FRC specimens with fiber contents of 1.0% under 70 ℃ because of the random deterioration of GFRP bars.

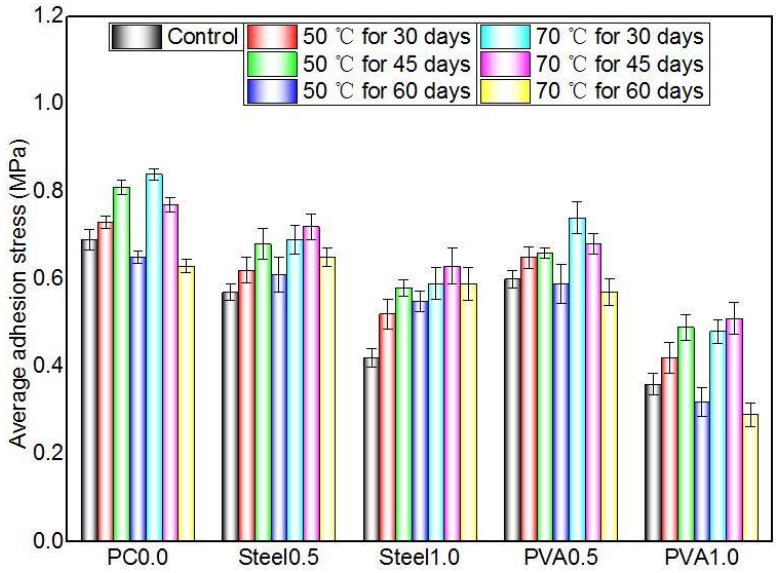

Figure 4-8. Adhesion stress for plain concrete and fiber reinforced concrete specimens

4.3.4. Bond Strength

The conditioned specimens exposed to saline solutions at higher temperatures are expected to suffer from more severe degradation and hence, their bond strengths were selected as representative scenarios as plotted in Figure 4-9 (a). Also, the normalized bond strengths specified in Equation (4-2) were also presented in Figure 4-9 (b) to eliminate the influence of concrete mix on test results.

Clearly, both steel and PVA FRC specimens exhibited improved bond strengths as compared to the plain concrete ones. Especially, steel fibers demonstrated the more noticeable reinforcing effect on bond strength than PVA fibers when the same fiber volume fraction was

used. All the conditioned specimens display deterioration in their bond strengths. The steel FRC specimens with 1.0% of fiber volume fraction maintained a 19.77 MPa of bond strength retention (approximately 10% reduction compared to the corresponding control FRC specimens) after 60 days, whereas maintained a 13.75 MPa for plain concrete specimens (approximately 12% reduction compared to the corresponding control plain concrete specimens) after 60 days. This representative phenomenon indicates better bond durability for GFRP bars in FRC under the marine environment or the use of deicing salts in cold regions. Since the bond mechanism is a combination of the bearing force, chemical adhesion and friction between the bar and concrete. Since adhesion accounted for a small portion of the total bond and hence, it can be probably concluded that the bearing force due to surface deformation and the friction due to surface roughness play a leading role in bond mechanism for the helically-wrapped and sand-coated bars. This also agrees with the findings reported in (Baena et al., 2009). In addition, the normalized bond strength presented similar patterns to the average bond strength.

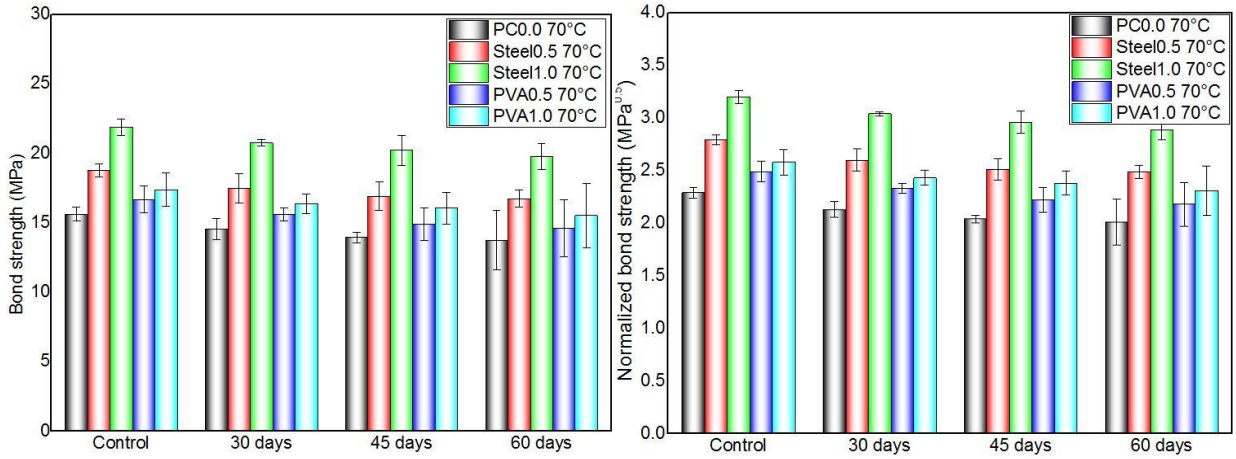

Figure 4-9. Bond strength and normalized bond strength for the specimens at 70 ℃

4.4. Calibration of Analytical Models Considering Environmental Effect

At present, FRP-concrete bond under pullout loads can be demonstrated through several available analytical models, which employ a set of explicit expressions to describe the development of the bond stress against slip (E Cosenza et al., 1995; Malvar, 1994; Rossetti et al., 1995). The model proposed by Malvar (Malvar, 1994) uses a polynomial function in terms of seven curve-fitting parameters to describe the bond-slip relationship. Nevertheless, the ascending branch was later evaluated to be less reliable for FRP material (Edoardo Cosenza et al., 1997). The BPE model developed by Eligehausen et al. (Eligehausen et al., 1982) was originally used to illustrate the steel-concrete bond, and then applied to FRP bars by recalibrating those parameters (Antonietta Aiello et al., 2007; E Cosenza et al., 1995; Rossetti et al., 1995). Cosenza et al. (E Cosenza et al., 1995) and Rossetti et al. (Rossetti et al., 1995) conducted experiments of FRP bars with different surface treatments. However, their test results were too scattered to determine the parameters. More detailed comparisons among those analytical models can be found in (Lin and Zhang, 2014) and (Yan and Lin, 2016). This study adopted another two widely used analytical models viz., modified BPE (mBPE) model and CMR model for the bond-slip prediction. Moreover, since the calibrated models in previous studies did not consider the environmental impact on the bond development, this necessitates a more accurate calibration involving the environmental effect to better demonstrate the GFRP-concrete bond.

(I) mBPE model

The bond-slip relationship of mBPE model can be expressed using a piecewise function in Equation (4-3),

$$\frac{\tau}{\tau_b} = \begin{cases} (\frac{s}{s_b})^{\alpha} & (0 \le s \le s_b) \\ 1 - p\left(\frac{s}{s_b} - 1\right) & (s_b \le s \le s_3), \\ \frac{\tau_3}{\tau_b} & (s \ge s_3) \end{cases} \quad (4\text{-}3)$$

where τ_b and s_b are the peak bond stress (bond strength) and its corresponding slip; α and p are parameters that can be determined from curve fitting of experimental data.

(I) CMR model

The CMR model proposed by Cosenza et al. (E Cosenza et al., 1995) was used to better represent the ascending branch of the bond-slip curve:

$$\frac{\tau}{\tau_b} = (1 - exp(-\frac{s}{s_r}))^{\beta} \qquad (0 \le s \le s_b), \quad (4\text{-}4)$$

where s_r and β are parameters that are derived from curve fitting of experimental data. Since the CMR model is only for the ascending part, the model may be applicable to the bond at serviceability state level, while not capable of describing the complete bond behavior of structures till failure (Lin and Zhang, 2014).

Figure 4-10 displays the bond-slip plots predicted by the mBPE and CMR models respectively. The representative specimens of plain concrete and FRC exposed to the most severe environments (under 70 ℃ through an exposure time of 60 days) are selected for demonstration. The parameters of these models were derived from the curve fittings of the test results and summarized in Table 4-5. Generally, all the curve-fittings yield high accuracy using the analytical models, where the coefficients of determination (R^2) were close to one, indicating the predictions matched well with test results. Also, the ascending branches of the bond-slip curves predicted by the CMR model performed better than those predicted by the mBPE model. The R^2 values of the CMR model for all the specimens were greater than 0.98, while those of the mBPE model presented a certain degree of discrepancy ranging from 0.91 to 0.99.

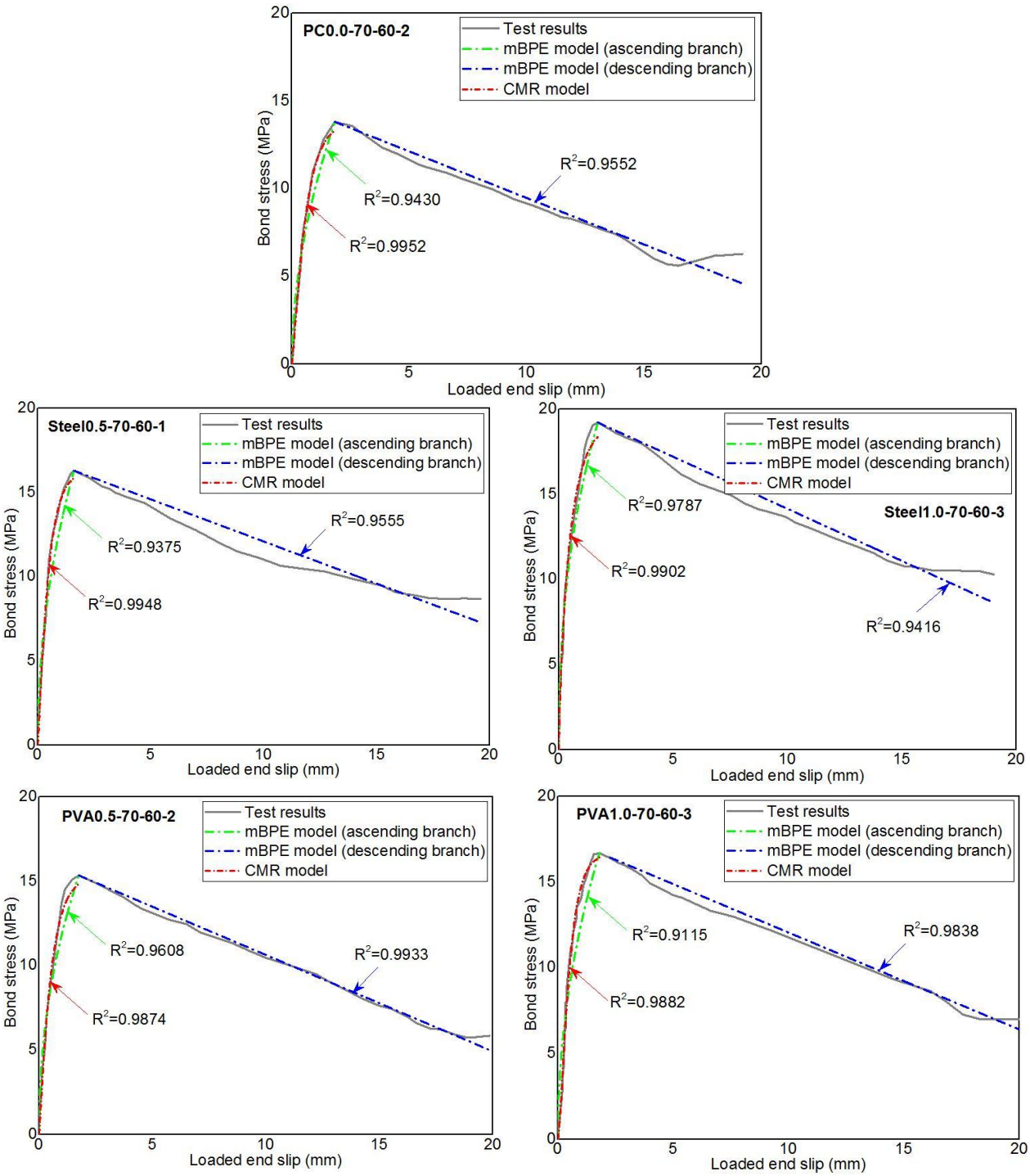

Figure 4-10. Curve fittings of the typical bond stress-slip relationship

Table 4-5. Fitting parameters of the mBPE model and CMR model

Specimen	τ_b (MPa)	s_b (mm)	mBPE model		CMR model	
			α	p	s_r	β
PC0.0-70-60-2	13.7900	1.8321	0.5265	0.0705	0.5102	1.3127
Steel0.5-70-60-1	16.2800	1.6057	0.4821	0.0494	0.4198	1.2098
Steel1.0-70-60-3	19.20165	1.69915	0.4219	0.0541	0.5998	0.7408
PVA0.5-70-60-2	15.3276	1.7513	0.4630	0.0652	0.5010	1.0969
PVA1.0-70-60-3	16.6774	1.7954	0.4913	0.0608	0.3894	1.5778

Table 4-6. Mean values of the parameters with and without considering alkaline-saline environment

Concrete mix type	Temperature	τ_b	s_b	mBPE model		CMR model	
	(℃)	(MPa)	(mm)	α	p	s_r	β
Unconditioned specimens							
Plain concrete	23	15.63	1.78	0.4126	0.0586	0.4000	1.1636
Steel fibers with 0.5% of V_f	23	18.75	1.56	0.3978	0.0458	0.3621	1.0452
Steel fibers with 1.0% of V_f	23	21.89	1.49	0.3972	0.0428	0.5484	0.6337
PVA fibers with 0.5% of V_f	23	16.69	1.69	0.3752	0.0613	0.4660	1.0047
PVA fibers with 1.0% of V_f	23	17.39	1.56	0.4425	0.0541	0.3525	1.4686
Conditioned specimens							
Plain concrete	50	14.18	1.80	0.4678	0.0614	0.4368	1.2292
Steel fibers with 0.5% of V_f	50	17.20	1.58	0.4466	0.0424	0.3948	1.0995
Steel fibers with 1.0% of V_f	50	20.45	1.68	0.4037	0.0480	0.5507	0.6263
PVA fibers with 0.5% of V_f	50	15.16	1.72	0.4046	0.0611	0.4439	0.9346
PVA fibers with 1.0% of V_f	50	15.97	1.73	0.4460	0.0527	0.3560	1.4338
Plain concrete	70	13.79	1.83	0.5310	0.0722	0.5115	1.3133
Steel fibers with 0.5% of V_f	70	16.28	1.61	0.4833	0.0488	0.4205	1.2069
Steel fibers with 1.0% of V_f	70	19.20	1.70	0.4379	0.0536	0.5954	0.7317
PVA fibers with 0.5% of V_f	70	15.33	1.75	0.4598	0.0664	0.5027	1.0944
PVA fibers with 1.0% of V_f	70	16.68	1.80	0.4906	0.0612	0.3882	1.5791

Table 4-6 details the calibrated average mean values of the analytical models after 60 days of exposure time considering the effect of saline environment, where the values of

unconditioned specimens are also listed for comparisons. For plain concrete specimens, α and p of the mBPE model were suggested to be 0.4678 and 0.0614 at 50 ℃ while 0.4833 and 0.0488 at 70 ℃; s_r and β of the CMR model were recommended to be 0.4368 and 1.2292 at 50 ℃ while 0.5115 and 1.3133 at 70 ℃. For steel FRC specimens with 1.0% of fiber volume fraction, which demonstrates the best bond performance, α and p decrease to 0.4037 and 0.0480 at 50 ℃ while 0.4379 and 0.0536 at 70 ℃; s_r and β decreased to 0.5507 and 0.6263 at 50 ℃ while 0.5954 and 0.7317 at 70 ℃.

4.5. Prediction of Long-Term Bond Strength Degradation under Saline Environment

4.5.1. Arrhenius Relation and Time Shift Factor Method

Bond degradation is a complicated process associated with many accelerated factors such as the temperature, pH, surrounding solution media, and moisture (Robert et al., 2009). This necessitates a simplified method by which the long-term performance can be evaluated, in order to establish a 50- to 75-year life-cycle durability performance for the GFRP reinforced concrete structures. Predictive models based on Arrhenius law have been extensively studies and implemented. The degradation rate in Arrhenius relation is expressed as (Nelson, 2009):

$$k = A \cdot exp(\frac{-E_a}{RT}), \tag{4-5}$$

where k = degradation rate (1/time); A = constant of the material and degradation process; E_a = activation energy; R = universal gas constant; and T = Kelvin temperature. The Arrhenius relation yields the primary assumption that elevated temperatures will not change the single governing degradation mechanism or introduce other degradation mechanisms during the exposure whereas degradation rate will be expedited. In this study, the environmental impact on the GFRP-concrete bond was considered by which the surrounding concrete will release alkali ions in the presence of the salt solutions including chloride ions. Besides, since the capillary

water and absorbed water can be removed from concrete as the environmental relative humidity (RH) decreases, leading to the change of hydroxide alkalinity surrounding the bars (Huang and Aboutaha, 2010). Thus, referring to the method used in (Dong et al., 2016), a correction factor β was introduced herein to account for the effect of RH variation, and was assumed to be equal to the ratio of the capillary water and absorbed water in concrete, as demonstrated in Figure 4-11. It assumes that the bond degradation mechanism does not change with temperature and humidity but the degradation rate can be accelerated by them.

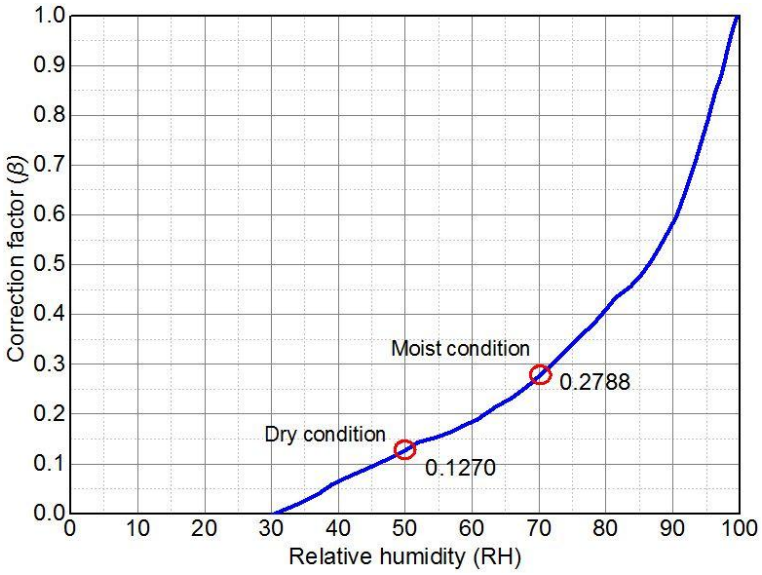

Figure 4-11. Relationship between relative humidity and correction factor (derived from Dong et al., 2016)

In addition, Dejke and Tepfers (Dejke and Tepfers, 1997) proposed another method to predict the service life of GFRP bars, which used a time shift factor (TSF) to relate the accelerated and non-accelerated exposures. The TSF value between the reference temperature and selected temperature can be calculated using Equation (4-6),

$$TSF = exp(\frac{B}{T_1+273.15} - \frac{B}{T_2+273.15}), \quad (4\text{-}6)$$

where $B = E_a/R$ is a constant that can be determined from two experimental curves with known temperatures ($T_1 < T_2$). The TSF method requires only two experimental aging data sets at

different temperatures. The TSF value can be calculated by taking the ratio of time required for the specific strength reduction from two different temperatures, and then substituting it into Equation (4-6) to further derive the constant B. The detailed implementation is demonstrated in the following.

4.5.2. Prediction Procedure

4.5.2.1. Evaluation of validity for the predictive models

The first step is to verify the applicability of the predictive models. The bond strength retention (τ_{max}^{r}) vs. exposure time (t) at 50 and 70 ℃ were linearly fitted in logarithmic scale, as shown in Figure 4-12 (a)-(e). Clearly, the regression lines corresponding to the two temperatures were approximately parallel to each other, of which the R^2 values in Figure 4-12 (a)-(e) were all greater than 0.88. This indicates the fundamental assumptions are applicable to the predictive models. Also, the explicit linear regression functions for these temperatures were derived, which were used to calculate the constant B in the following step.

Table 4-7 summarizes the long-term prediction of the bond strength retention according to the fitted functions at 50 and 70 ℃, respectively. Clearly, the FRC specimens demonstrate larger bond strength retention compared to the plain concrete specimens. In particular, the steel FRC with 1.0% of fiber volume fraction will have the largest bond strength retention after 75 years of service lifetime, which are 67.02 and 65.20 % under 50 and 70 ℃, respectively. The enhancements are approximately 24.96 and 25.41 % compared to the corresponding plain concrete specimens under 50 and 70 ℃, respectively. Moreover, when steel and PVA fibers with the same fiber volume fraction are used, steel fibers exhibit more remarkable improvement on the long-term bond strength retention than PVA fibers.

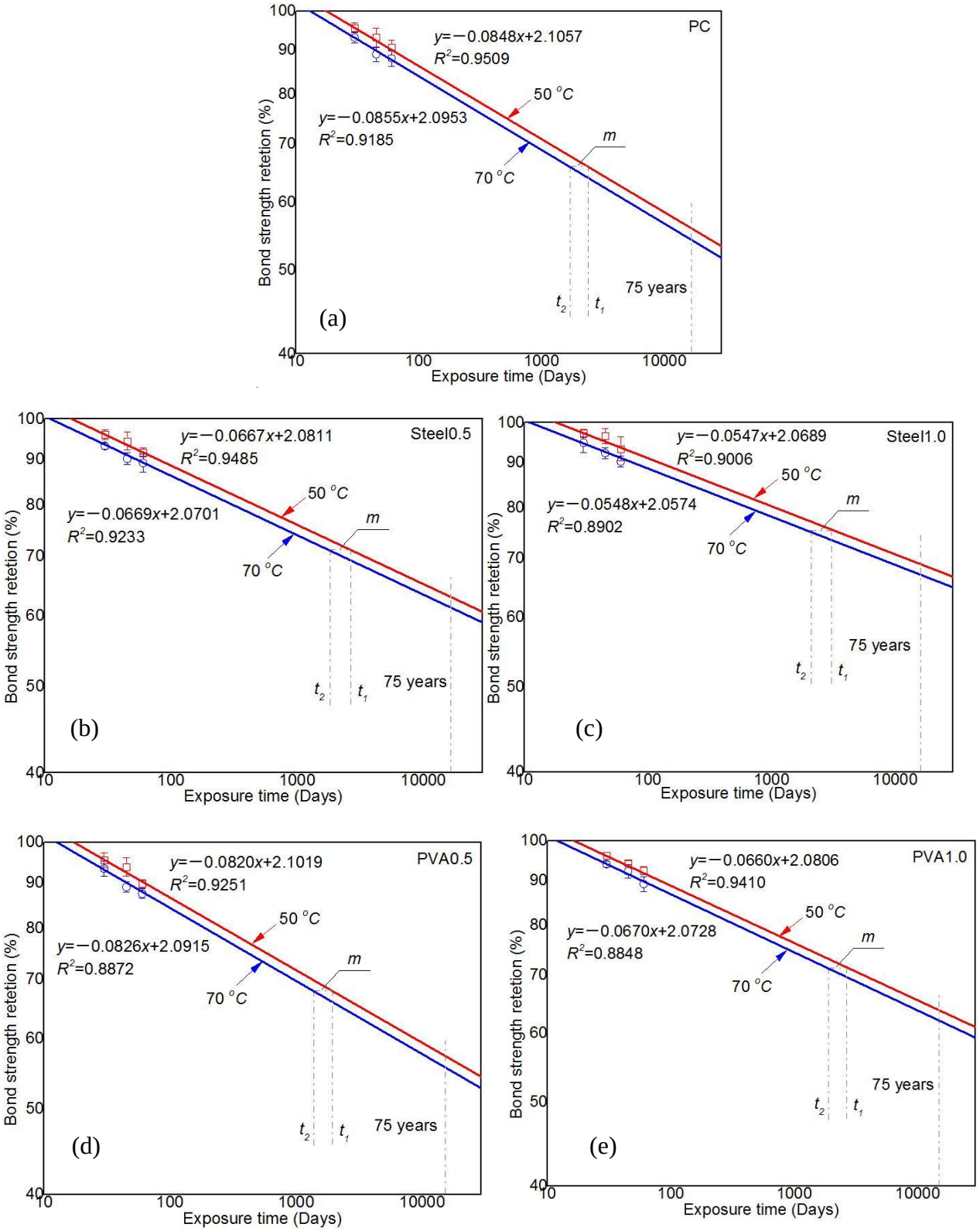

Figure 4-12. Bond strength retention vs. exposure time in log-log scale: (a)-(e)

Table 4-7. Bond strength retention over 75-year service lifetime

Concrete mix type	Bond strength retention τ_{max}^{r} (%)		Enhancement (%)	
	50 ℃	70 ℃	50 ℃	70 ℃
Plain concrete	53.63	51.99	-	
Steel fibers with 0.5% of V_f	60.97	59.33	13.69	14.11
Steel fibers with 1.0% of V_f	67.02	65.20	24.96	25.41
PVA fibers with 0.5% of V_f	54.71	53.09	2.01	2.11
PVA fibers with 1.0% of V_f	61.34	59.63	14.37	14.71

4.5.2.2. Derivation of the time shift factor formula

The next step is to determine the TSF formula, by which the bond strength retention at other specified temperatures can be determined based on the results obtained at the reference temperature. From the linear regression lines plotted in the log-log scale, the horizontal distance m can be calculated using Equation (4-7),

$$m = lg(t_1) - lg(t_2) = lg(t_1/t_2), \tag{4-7}$$

where t_1 and t_2 are the time required for the bond strength to reach a same give value at temperatures of T_1 and T_2, respectively. The TSF value with respect to the known temperatures T_1 and T_2 can be calculated as follows,

$$TSF = \frac{t_1}{t_2} = 10^m. \tag{4-8}$$

After that, by substituting the TSF value, as well as $T_1 = 50$ ℃ and $T_2 = 70$ ℃ into Equation (4-6), the constant B can be obtained accordingly. Table 4-8 details these critical parameters, where B value varies with different concrete mix types. Upon this, if taking 50 ℃ as the reference temperature ($T_2 = 50$ ℃), the TSF formulas in terms of a specified unknown temperature (T) can be derived, as shown in Equation (9):

$$TSF = exp(\frac{B}{T+273.15} - \frac{B}{50+273.15}). \tag{4-9}$$

Table 4-8. Critical parameters using the time shift factor method

Concrete mix type	m	TSF	B
Plain concrete	0.1468	1.4022	3748
Steel fibers with 0.5% of V_f	0.1750	1.4962	4468
Steel fibers with 1.0% of V_f	0.2173	1.6493	5548
PVA fibers with 0.5% of V_f	0.1487	1.4083	3797
PVA fibers with 1.0% of V_f	0.1697	1.4781	4333

4.5.2.3. Prediction of long-term bond strength retention

The master curve at the reference temperature 50 ℃ is shown in Figure 4-13. Considering the primary assumption of the predictive models is that the bond degradation mechanism will not change with temperature and humidity. Thus, the derivative curves for different temperatures and relative humidity can be obtained by parallelly shifting the master curve successively, in order to meet different field conditions.

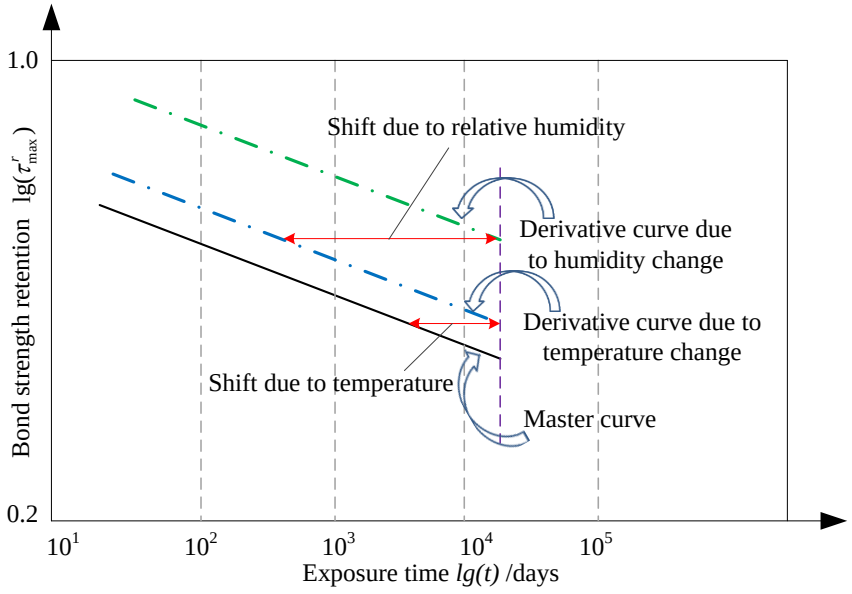

Figure 4-13. Master and derivative curves for bond strength retention

(1) Shift due to temperature

In this step, the bond strength retention at a specified unknown temperature is predicted based on the developed TSF formulas for different concrete mix types. Herein the temperature of 10 ℃ is used to represent the mean annual temperature of the northern parts. For example, the TSF formula of the steel FRC with fiber volume fraction of 0.5% can be obtained by using the corresponding constant B in Equation (4-9), and substituting $T = 10$ ℃, we have:

$$TSF = exp\left(\frac{4468}{10+273.15} - \frac{4468}{50+273.15}\right) = 7.0514. \quad (4\text{-}10)$$

Thus, the shift due to temperature is $lg(7.0514) = 0.8483$. Accordingly, the formula of the bond strength retention at $T = 10$ ℃ is:

$$y = -0.0548(x - 0.8483) + 2.0574, \quad (4\text{-}11)$$

where $y = lg(\tau_{max}^{r})$, and $x = lg(t)$. By substituting the exposure time $t = 75\ (years) = 27375\ (days)$ into Equation (4-11), the bond strength retention τ_{max}^{r} can be calculated to be 77.33%.

(2) Shift due to relative humidity

The experimental data used herein was based on the test specimens fully immersed in solution, that is, the environment is moist with 100% RH. Considering three representative cities in the northern states viz., Bismarck, Fargo, and Minneapolis, the average RH is around 70% moist environment. According to the assumption demonstrated in Figure 4-13, the correction factor β is 0.2788. Thus, the corrected bond strength retention is:

$$\tau_{max}^{r}(\text{RH} = 70\%) = 100\% - \beta \cdot [100\% - \tau_{max}^{r}(\text{RH} = 100\%)]. \quad (4\text{-}12)$$

By substituting $\beta = 0.2788$ and $\tau_{max}^{r}(\text{RH} = 100\%) = 77.33\%$ into Equation (4-12), the corrected bond strength is $\tau_{max}^{r}(\text{RH} = 70\%) = 93.68$ after 75 years of service lifetime.

4.5.3. Application in Representative Cold and Warm Regions

In addition to the mean annual temperature 10 ℃ used for cold regions, referring to (Robert and Benmokrane, 2013), the temperature 40 ℃ is used to exacerbate the combined effect of the mean annual temperature and marine environment for warm regions such as Middle East, Caribbean, and Florida . Besides, different RH values corresponding to dry, moist and saturated conditions are used to account for the circumstance of concrete in contact with seawater or deicing salts. The 75-year bond strength retention considering these critical factors are summarized in Table 4-9 following the aforementioned procedure.

Table 4-9. Prediction of bond strength retention under different environmental conditions

Concrete mix type	Temperature	Relative humidity		
		Dry (RH = 50%)	Moist (RH = 70%)	Saturated (RH = 100%)
Plain concrete	Cold regions (10 ℃)	94.90	88.79	59.81
	Warm regions (40 ℃)	94.11	87.08	53.66
Steel fibers with 0.5% of V_f	Cold regions (10 ℃)	95.89	90.97	67.61
	Warm regions (40 ℃)	95.06	89.16	61.10
Steel fibers with 1.0% of V_f	Cold regions (10 ℃)	96.76	92.88	74.47
	Warm regions (40 ℃)	95.83	90.85	67.19
PVA fibers with 0.5% of V_f	Cold regions (10 ℃)	95.03	89.09	60.89
	Warm regions (40 ℃)	94.25	87.39	54.76
PVA fibers with 1.0% of V_f	Cold regions (10 ℃)	95.90	91.00	67.70
	Warm regions (40 ℃)	95.09	89.23	61.37

Clearly, the bond strength retention decreases as the RH increases for both cold and warm regions. The FRC exhibits better bond durability performance compared to the plain concrete. Especially, steel FRC with fiber volume fraction of 1.0% exhibits the largest bond strength retentions after 75 years of exposure in saline environments. In the cold regions of 10 ℃, the bond strengths are expected to be 96.76, 92.88, and 74.47% for the dry, moist, and saturated conditions, respectively; while in the warm regions under 40 ℃, those values would decrease to

95.83, 90.85, and 67.19%, respectively. Moreover, the predictions reveal that the RH has significant impact on the bond durability performance. Taking the plain concrete under 10 ℃ as an example, the 75-year reduction in bond strength due to moist increase RH from 50 to 100% is approximately 36.98%.

4.6. Conclusions

This chapter presented a detailed experimental-analytical investigation on the bond durability of GFRP bars to FRC when exposed to saline solutions. The elevated temperatures at 50 and 70 ℃ were used to accelerate degradation rate. The bond durability of the test specimens under weathering was assessed through the failure mode, adhesion stress, as well as the bond strength. With the obtained experimental data, the analytical models were then calibrated by considering environmental effects for more widespread applications. Besides, a systematic procedure for long-term prediction of the bond strength was developed based on the Arrhenius relation and TSF method. Specifically, several conclusions can be drawn in the following:

(1) Most test specimens (104 out of 105) were failed by bar pullout, except for one specimens failed by concrete splitting due to bar eccentricity that resulted in radial tension to surrounding concrete. These findings were noticed for both unconditioned and conditioned specimens regardless the FRC and plain concrete. The statistically designed concrete cover $c/d_b = 4.5$ provided sufficient resistance to likely prevent brittle concrete splitting failure under the simulated weathering of saline environment. Such observations are consistent with the stipulations of ACI 440.1R-06, of which the bond equation accounts for pullout failure by limiting c/d_b to 3.5.

(2) Adhesion of both FRC and plain concrete increased at the early stage of immersion due to swelling of the bars, and then decreased over exposure time due to combined effects of

environment-induced degradation and diminished dissipation of solution molecules. Such shift process was accelerated at the higher temperature (70 ℃) as compared to the lower one (50 ℃).

(3) The FRC specimens exhibited the better bond durability than the plain concrete specimens under saline solutions. When the same fiber volume fraction was used, steel fibers displayed the larger enhancement on the bond performance than the PVA fibers. The reduction of bond strength due to weathering was about 10% for the steel FRC specimens with fiber contents of 1.0% as compared to 12% for the plain concrete specimens.

(4) The analytical models of bond-slip development were calibrated by considering environmental effect and matched well with the experimental results for both FRC and plain concrete specimens. The curve-fittings using the CMR model performed better than those using the mBPE model. The R^2 values fitted with the CMR model were all greater than 0.98, indicating rather close predictions to the test results. Moreover, the average values of the unconditioned and conditioned specimens were summarized. Considering the worst case of 70 ℃, for plain concrete, α and p of the mBPE model were suggested to be 0.5310 and 0.0722, and s_r and β of CMR model were recommended to be 0.5115 and 1.3133, respectively; while for steel FRC with 1.0% of fiber volume fraction, these parameters are suggested to be 0.4379 and 0.0536 for mBPE model, and 0.5954 and 0.7317 for CMR model, respectively.

(5) A detailed procedure for the long-term bond strength degradation prediction was presented based on the Arrhenius relation and the TSF method. In order to use the Arrhenius law, we assume that the degradation mechanism stay the same whereas the degradation rate can be accelerated by aging in terms of the temperature and humidity. As a case study, the developed systematic procedure was applied in predicting the bond strength retention in both cold and warm regions with different annual average temperatures and RH. According to the predictions

of 75 years of service, the FRC demonstrates distinct superiority on the bond durability over the plain concrete. Especially, the steel FRC with 1.0% of fiber content will have largest bond strength retention. In cold regions with a temperature of 10 ℃, the 75-year bond strength retentions will be 96.76, 92.88, and 74.47% for the dry, moist, and saturated humidity conditions, respectively; while in warm regions under 40 ℃, these predictions will decreased to 95.83, 90.85, and 67.19 %, respectively.

4.7. References

Achillides, Z., and Pilakoutas, K. (2004). Bond behavior of fiber reinforced polymer bars under direct pullout conditions. Journal of Composites for Construction, 8(2), 173-181.

ACI Committee. (2006). Guide for the design and construction of structural concrete reinforced with FRP bars. ACI 440.1 R, 6.

Altalmas, A., El Refai, A., and Abed, F. (2015). Bond degradation of basalt fiber-reinforced polymer (BFRP) bars exposed to accelerated aging conditions. Construction and Building Materials, 81, 162-171.

Antonietta Aiello, M., Leone, M., and Pecce, M. (2007). Bond performances of FRP rebars-reinforced concrete. Journal of Materials in Civil Engineering, 19(3), 205-213.

ASTM D570. (2010). Standard Test Method for Water Absorption of Plastics. ASTM International, West Conshohocken, PA.

ASTM D7205 / D7205M-06. (2011). Standard Test Method for Tensile Properties of Fiber Reinforced Polymer Matrix Composite Bars. ASTM International, West Conshohocken, PA.

ASTM D7913/D7913M. (2014). Standard Test Method for Bond Strength of Fiber-Reinforced Polymer Matrix Composite Bars to Concrete by Pullout Testing. ASTM International, West Conshohocken, PA.

Baena, M., Torres, L., Turon, A., and Barris, C. (2009). Experimental study of bond behaviour between concrete and FRP bars using a pull-out test. Composites Part B: Engineering, 40(8), 784-797.

Belarbi, A., and Wang, H. (2011). Bond durability of FRP bars embedded in fiber-reinforced concrete. Journal of Composites for Construction, 16(4), 371-380.

C39M, A. C. (2016). Standard Test Method for Compressive Strength of Cylindrical Concrete Specimens. ASTM International, West Conshohocken, PA.

Chen, Y., Davalos, J. F., and Ray, I. (2006). Durability prediction for GFRP reinforcing bars using short-term data of accelerated aging tests. Journal of Composites for Construction, 10(4), 279-286.

Cosenza, E., Manfredi, G., and Realfonzo, R. (1995). Analytical modelling of bond between FRP reinforcing bars and concrete. Paper presented at the Non-Metallic (FRP) Reinforcement for Concrete Structures: Proceedings of the Second International RILEM Symposium.

Cosenza, E., Manfredi, G., and Realfonzo, R. (1997). Behavior and modeling of bond of FRP rebars to concrete. Journal of Composites for Construction, 1(2), 40-51.

Dejke, V., and Tepfers, R. (1997). Durability and service life prediction of GFRP for concrete reinforcement. Proceedings of FRPRCS, 5, 505-514.

Ding, Y., Ning, X., Zhang, Y., Pacheco-Torgal, F., and Aguiar, J. (2014). Fibres for enhancing of the bond capacity between GFRP rebar and concrete. Construction and Building Materials, 51, 303-312.

Ding, Y., Zhang, F., Torgal, F., and Zhang, Y. (2012). Shear behaviour of steel fibre reinforced self-consolidating concrete beams based on the modified compression field theory. Composite Structures, 94(8), 2440-2449.

Dong, Z., Wu, G., Xu, B., Wang, X., and Taerwe, L. (2016). Bond durability of BFRP bars embedded in concrete under seawater conditions and the long-term bond strength prediction. Materials & Design, 92, 552-562.

Eligehausen, R., Popov, E. P., and Bertero, V. V. (1982). Local bond stress-slip relationships of deformed bars under generalized excitations.

Huang, J., and Aboutaha, R. (2010). Environmental reduction factors for GFRP bars used as concrete reinforcement: New scientific approach. Journal of Composites for Construction, 14(5), 479-486.

Kim, B., Doh, J.-H., Yi, C.-K., and Lee, J.-Y. (2013). Effects of structural fibers on bonding mechanism changes in interface between GFRP bar and concrete. Composites Part B: Engineering, 45(1), 768-779.

Kim, H.-Y., Park, Y.-H., You, Y.-J., and Moon, C.-K. (2008). Short-term durability test for GFRP rods under various environmental conditions. Composite Structures, 83(1), 37-47.

Lin, X., and Zhang, Y. (2014). Evaluation of bond stress-slip models for FRP reinforcing bars in concrete. Composite Structures, 107, 131-141.

Malvar, L. J. (1994). Bond stress-slip characteristics of FRP rebars: DTIC Document.

Mufti, A., Onofrei, M., Benmokrane, B., Banthia, N., Boulfiza, M., Newhook, J., et al. (2005). Durability of GFRP reinforced concrete in field structures. Paper presented at the Proceedings of the 7th International Symposium on Fiber-Reinforced Polymer Reinforcement for Reinforced Concrete Structures (FRPRCS-7), Kansas City, Mo.

Nelson, W. B. (2009). Accelerated testing: statistical models, test plans, and data analysis (Vol. 344): John Wiley & Sons.

Okelo, R., and Yuan, R. L. (2005). Bond strength of fiber reinforced polymer rebars in normal strength concrete. Journal of Composites for Construction.

Robert, M., and Benmokrane, B. (2013). Combined effects of saline solution and moist concrete on long-term durability of GFRP reinforcing bars. Construction and Building Materials, 38, 274-284.

Robert, M., Cousin, P., and Benmokrane, B. (2009). Durability of GFRP reinforcing bars embedded in moist concrete. Journal of Composites for Construction, 13(2), 66-73.

Rossetti, V. A., Galeota, D., and Giammatteo, M. (1995). Local bond stress-slip relationships of glass fibre reinforced plastic bars embedded in concrete. Materials and Structures, 28(6), 340-344.

Wang, H., and Belarbi, A. (2011). Ductility characteristics of fiber-reinforced-concrete beams reinforced with FRP rebars. Construction and Building Materials, 25(5), 2391-2401.

Wang, H., and Belarbi, A. (2013). Flexural durability of FRP bars embedded in fiber-reinforced-concrete. Construction and Building Materials, 44, 541-550.

Yan, F., and Lin, Z. (2016). Bond behavior of GFRP bar-concrete interface: Damage evolution assessment and FE simulation implementations. Composite Structures, 155, 63-76.

Yan, F., Lin, Z., and Yang, M. (2016). Bond mechanism and bond strength of GFRP bars to concrete: A review. Composites Part B: Engineering, 98, 56-69.

Yan, F., Lin, Z., Zhang, D., Gao, Z., and Li, M. (2016). Experimental study on bond durability of glass fiber reinforced polymer bars in concrete exposed to harsh environmental agents: Freeze-thaw cycles and alkaline-saline solution. Composites Part B: Engineering.

Zhou, J., Chen, X., and Chen, S. (2011). Durability and service life prediction of GFRP bars embedded in concrete under acid environment. Nuclear Engineering and Design, 241(10), 4095-4102.

5. BOND BEHAVIOR OF GFRP BAR-CONCRETE INTERFACE: DAMAGE EVOLUTION ASSESSMENT AND FE SIMULATION IMPLEMENTATIONS

5.1. Introduction

Understanding of bond performance of the FRP bar-concrete interface is crucial in implementing this advanced engineered material toward corrosion-free RC structures. Much research (Ceroni et al., 2006; Chen et al., 2007; Davalos et al., 2008; Robert and Benmokrane, 2010; Y. Wang et al., 2007) has been conducted for determination and understanding of bond characteristics through experimental, analytical and numerical studies. Experiments (Mazaheripour et al., 2013; Okelo and Yuan, 2005; Yan and Lin, 2016; Yoo et al., 2015) have been conducted to gain critical information for determining bond strength at the interface. Accordingly, several analytical models, such as the modified mBPE and CMR models, have been developed for predicting global GFRP bar-concrete bond-slip relation (Baena et al., 2009; E Cosenza et al., 1995; Edoardo Cosenza et al., 1997; Lin and Zhang, 2014; Malvar, 1994). Besides these findings to the GFRP bond behavior, key interfacial damage features are crucial to reveal GFRP bar-concrete bond damage process under a wide range of deformation conditions and are also highly in demand for better GFRP reinforced structural design and implementation.

Damage feature, from the continuum damage mechanics point of view (Lasar Kachanov, 2013), consists of damage mechanism, damage evolution law and its process. By introducing the scalar internal damage evolution variable, D ($0 \leq D \leq 1$), based on Lemaitre-based damage model (Lemaitre, 2012), the damage evolution is defined by using equivalent stress in the constitutive equation of material:

$$\tilde{\sigma} = \frac{\sigma}{(1-D)}, \tag{5-1a}$$

$$D = \frac{A_D}{A_0}, \tag{5-1b}$$

where, σ and $\tilde{\sigma}$ are the stress at undamaged material and modified effective stress under certain damage level, respectively; A_{D} and A_0 are the areas of damaged and undamaged states, respectively. Also, the scale damage evolution variable D is defined by a linear law of the relative change in Young's modulus at initial state, E_0, over modulus under damaged state, E_i:

$$D = 1 - \frac{E_i}{E_0}. \tag{5-1c}$$

As stated in the literature (Polanco-Loria and Sørensen, 1994; Tang et al., 2016; Zhang and Jivkov, 2014), much research has been conducted to extend the damage evolution law and process in the fields of quasit-brittle type concrete and also ductile materials under uniaxial tensile/compressive states.

There are apparent different descriptions to bond damage and its damage evolution process as compared to compression or tensile damage evolution described above. Damage frequently initiates from defects along the interface and further develops to vicinal layer of adjacent materials as bond stress develops. Interfacial damage failure usually responds for sharp drops in loading. Few studies are available to describe the bond damage mechanisms and its evolution process corresponding to the bond-slip relation. Soh *et al.* proposed an orthotropic damage model to demonstrate the nonlinear bond behavior between steel bar and concrete (C. Soh et al., 1999). The normal and tangential damage factors were defined to describe the evolution equations based on damage mechanics. The bond-slip curves under different normal pressures were derived from the proposed damage model, and agreed well with experimental results. Soh *et al.* (C. K. Soh et al., 2003) extended their work on the bond damage evolution of steel bar to concrete under transversal confinements. Their findings further revealed that the developed damage evolution equations could help engineers to capture the bond failure process. Consider that GFRP bars display different mechanical and physical properties as compared to

steel bars, the bond behaviors are quite different, which in turn leads to different bond damage and evolution at the bar-concrete interface (Chaallal and Benmokrane, 1993; Tepfers, 2006; Yan et al., 2016 (Under review)). In addition, GFRP bars usually use sand coatings, fibers and epoxy to create the outer surface, which render the bars non-homogeneous and thus yield different wedging effect as compared to ribs on surfaces of steel bars to concrete.

Based on existing experimental and analytical data in the literature, a universal assessment approach has yet to be proposed to demonstrate the interfacial damage evolution. Furthermore, due to complexity of the interfacial contact, limited resources are available to describe this highly nonlinear behavior using the general finite element (FE) packages. Therefore, the objective of this study is to propose a damage assessment approach that can intuitively present the complete bond damage evolution as the slip development at the bar-concrete interface, where the FE packages were utilized to accurately derive the bond-slip relation before the damage assessment.

Beyond the lack of damage assessment progress, the accurate simulation of the bond behavior based on general FE packages faces two challenges. First, the nonlinear material behavior of concrete is usually considered by involving the damage criterion in numerical analysis, bringing about difficulty in iterative convergence. Second, the bar-concrete interface lies on a nonlinear contact status subjected to changes with concrete cracks or even crush. The bearing force due to mechanical interlocking against concrete is difficult to be captured over this ever-changing state. Presently, several simplified approaches were reported to simulate the bond behavior. The first approach assumes a perfect bonding on the interface, where the bar and concrete share the same node points at the interface (Kabir and Islam, 2014). The drawback of this approach is that it cannot simulate the sliding process between the bar and concrete and thus

cannot appropriately predict bond behavior. The second approach is to use contact pairs, such as the CONTA174 and TARGE170 provided by ANSYS FE program, to simulate the surface-to-surface extrusion and friction (De Nardin et al., 2005; Wei-ping, 2011). The contact status can be implemented with alternative bond models, such as the rough bond (infinite friction coefficient) and no separation (sliding permitted). It appears that a high dependence on the geometry modeling accuracy of the bar surface is addressed in this method. Meanwhile, it is worth noting that the bond stress may keep increasing for the lug/grooved surface when concrete crush is not considered. The third approach is to use three-dimensional nonlinear spring elements to connect the bar and concrete (Liu et al., 2007; Y.-q. WANG and WANG, 2006). The spring is defined as a zero-length element with two node points coinciding together. The force-slip curve of the element is predefined according to the test results, describing the variations of the bond force against slip. Wang *et al.* adopted the COMBIN39 element in ANSYS to simulate the bond-slip relation between steel bars and concrete (Y.-q. WANG and WANG, 2006). Predicted results matched well with the bond-slip empirical formula.

Therefore, upon the consideration of utilizing the general FE packages, this chapter addresses efforts in developing a damage evolution assessment approach that can be implemented by ANSYS program. First, the damage evolution equations accounting for the interface deterioration are proposed based on the strain equivalence principle of damage mechanics. Second, the FE simulations of the GFRP bar-concrete bond are implemented, detailing in geometry modeling and material modeling, respectively. The nonlinear spring elements (COMBIN39) are used to predict the bond-slip relation between bar and concrete. Analysis results are validated by the experimental results, and compared with the predictions

using the analytical models. Finally, bond damage evolution curves are derived, and further used to investigate the critical factors and their impacts on the interface damage.

5.2. Bond Damage Evolution at the Bar-Concrete Interface

5.2.1. Analytical Models Accounting for FRP-Concrete Bond

Currently, several analytical models demonstrating the FRP-concrete bond under pullout loads have been proposed, focusing on developing an explicit expression to describe the relation of bond stress against slip [11, 12, 30]. The model proposed by Malvar [12] uses a polynomial function in terms of seven parameters that can be determined from experimental results. Nevertheless, the ascending branch was later evaluated to be less reliable for FRP material [10]. The BPE model developed by Eligehausen et al. [31] was originally used to illustrate the bond behavior of steel bars and concrete, and then applied to FRP bars by recalibrating those parameters [11, 30, 32]. Cosenza et al. [11] and Rossetti et al. [30] conducted experiments of FRP bars with different surface treatments. However, their test results were too scattered to determine the parameters. More detailed comparisons among those analytical models can be found in [14]. This study adopted another two widely used analytical models viz., mBPE model and CMR model for the bond-slip prediction.

(I) mBPE model

Figure 5-1 shows the diagram of the BPE model for steel-concrete bond. Consider that FRP-concrete bond has no apparent plateau, the model was then modified to comply with FRP material (Edoardo Cosenza et al., 1997), as demonstrated in Figure 5-2. The mBPE model is mainly simplified into three stages. Stage I uses an ascending branch to represent the chemical adhesion and bearing force against slip. Sliding takes place at the bar-concrete interface after the bond force increases to a certain value. Cracks develop at late this stage. The bond stress loses

part of the contribution from the bearing force when concrete crush occurs and cracks further propagate, resulting in a rapid decrease of the bond stress accompanying with an apparent slip as shown in stage II. In stage III, cracks are obvious in the concrete and the bond stress remains a certain value mainly due to friction.

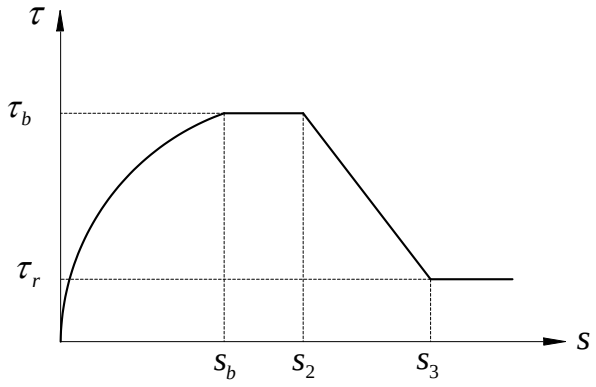

Figure 5-1. BPE model for steel bar

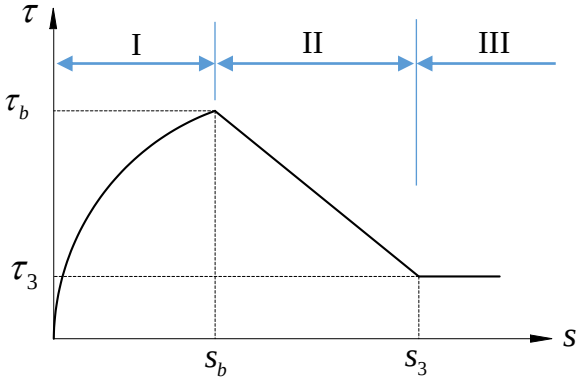

Figure 5-2. Modified BPE model for FRP bar

The bond-slip relationship of mBPE model can be expressed using a piecewise function in Equation (5-2),

$$\frac{\tau}{\tau_b} = \begin{cases} \left(\frac{s}{s_b}\right)^{\alpha} & (0 \le s \le s_b) \\ 1 - p\left(\frac{s}{s_b} - 1\right) & (s_b \le s \le s_3), \\ \frac{\tau_3}{\tau_b} & (s \ge s_3) \end{cases} \tag{5-2}$$

where τ_b and s_b are the peak bond stress (bond strength) and its corresponding slip; α and p are parameters that can be determined from curve fitting of experimental results.

(I) CMR model

To overcome the drawback of the Malvar's model, the CMR model proposed by Cosenza et al. (E Cosenza et al., 1995) was used to better represent the ascending branch of bond-slip curve for FRP-concrete bond:

$$\frac{\tau}{\tau_b} = (1 - exp(-\frac{s}{s_r}))^{\beta} \qquad (0 \leq s \leq s_b), \tag{5-3}$$

where s_r and β are parameters that are derived from curve fitting of experimental data. Since the CMR model is only for the ascending part, it is worth noting that it may be applicable to the bond at serviceability state level, while not capable of describing the complete bond behavior of structures till failure (Lin and Zhang, 2014).

5.2.2. Bond Damage Evolution Equations

Material damage under stress state can be attributed to reduction of effective load-carrying area (LM Kachanov, 1958). However, damage area detection is not convenient and hence, the principle of strain equivalence based on damage mechanics is utilized for damage assessment. This concept was originally proposed to evaluate the concrete damage state, as shown in Figure 5-3, where σ is the applied stress; $\tilde{\sigma}$ is the effective stress; $\tilde{E}$ is the effective elastic modulus associated with damaged state; E is the elastic modulus associated with undamaged state.

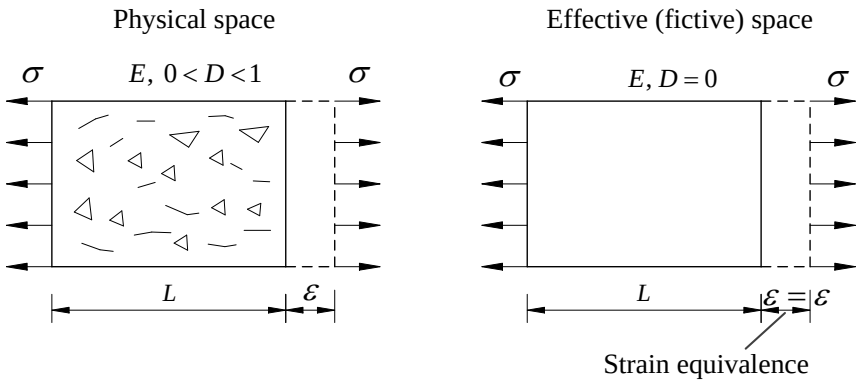

Figure 5-3. Strain equivalence principle (Skrzypek and Ganczarski, 2013)

It is assumed that the strain resulted from the applied stress in a damaged state is equivalent to the strain resulted from the effective stress in an undamaged state (Skrzypek and Ganczarski, 2013). By defining a scalar damage model $D = 1 - \tilde{E}/E$ as stated in Eqn. (1c), the strain equivalence principle can be expressed in Equation (5-4), where $D = 0$ denotes no damage, and D = 1 denotes the limit state of damage (i.e. complete failure). Upon this, the damage occurred in the physical space is converted into the effective space. Furthermore, damage evolution can be demonstrated through the reduction of elastic modulus, solving the inconvenience of measuring effective area in experiments.

$$\varepsilon = \frac{\sigma}{\tilde{E}} = \frac{\tilde{\sigma}}{E} = \frac{\sigma}{(1-D)\cdot E}. \tag{5-4}$$

In order to take advantage of this concept for the bond damage assessment, it is assumed that the slip associated with the damaged interface under the actual bond stress is equal to the slip associated with the undamaged state under the effective bond stress. With reference to the strain equivalence principle used in concrete damage assessment, the relation between bond stress and slip is defined in the form:

$$s = \frac{\tau}{\tilde{\emptyset}} = \frac{\tilde{\tau}}{\emptyset} = \frac{\tau}{(1-D)\cdot \emptyset'}, \tag{5-5}$$

where τ and $\tilde{\tau}$ are the actual bond stress and effective bond stress, respectively; s is the relative slip between bar and concrete. Consider that the secant modulus decreases as the slip increases, as shown in Figure 5-4. It is reasonable to use the secant modulus to represent the bond damage evolution at the interface.

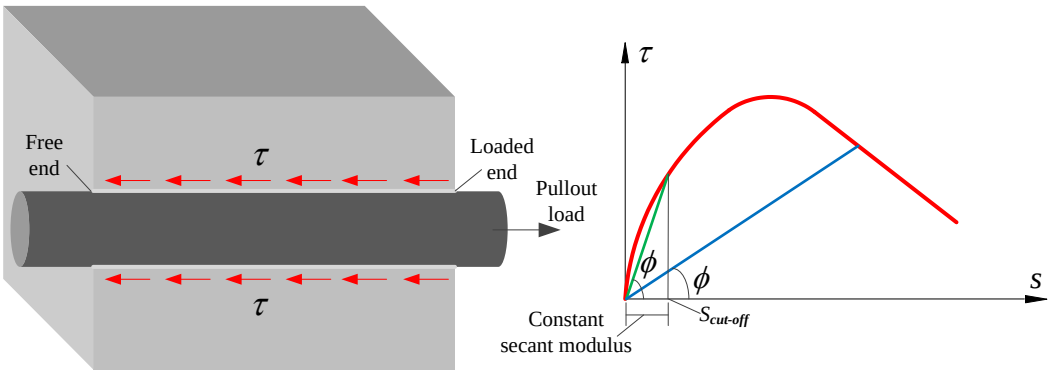

Figure 5-4. Demonstration of the bond-slip relation

On the other hand, note that the initial secant modulus tends to be infinite when the slip is rather small. Here defines a cut-off limiting slip $s_{cut-off}$, representing that the damage will not develop (i.e. $D = 0$) when the slip is smaller than this value. A constant secant modulus $\emptyset$ is used within this interval. Beyond this interval, the effective secant modulus $\widetilde{\emptyset}$ is used.

Therefore, the damage evolution with respect to the slip can be derived from Equation (5-4), as expressed in Equation (5-6),

$$D = \begin{cases} 0 & (0 \le s \le s_{cut-off}) \\ 1 - \frac{1}{\emptyset} \cdot \frac{\tau}{s} & (s > s_{cut-off}) \end{cases}. \tag{5-6}$$

Based on this, it is convenient to derive the bond damage evolution curve from the known bond-slip curve.

5.3. Finite Element Modeling

With the purpose of ultimately assessing the bond damage evolution, the ANSYS FE program is employed to simulate the bond behavior of pullout test, and to predict the bond-slip

relation between the bar and concrete. The bond stress τ is calculated according to Equation (5-7),

$$\tau = \frac{P}{\pi d_b l_d}, \tag{5-7}$$

where P is the pullout force at the end of each loading step during the analysis; d_b is the nominal bar diameter; l_d is the embedment length of the GFRP bar. Consider that the slip at the free end lags behind the slip at the loaded end, the latter one exhibiting faster development is used to derive the bond-slip curve.

5.3.1. Experimental Program Overview

The pullout tests reported in literatures (Baena et al., 2009) and (Ding et al., 2014) were used for the FE modeling with respect to plain concrete matrix and fiber-reinforced concrete (FRC) matrix, respectively. The parameters considered in these tests included the bar diameter, bar surface treatment, concrete compressive strength and fiber types.

Table 5-1. Material properties of the specimens used in the pullout tests

Specimen	GFRP bars					Concrete
	Nominal diameter		Surface treatment	Elastic modulus	Tensile strength	Compressive strength
	mm	in.		GPa	MPa	MPa
B-G/R4 (#4-2-C1)		#4	HW-SC	40.8	690	28.3
B-G/R4 (#5-1-C1)		#5	HW-SC	40.8	655	30.0
B-G/R4 (#4-3-C2)		#4	HW-SC	40.8	690	49.6
B-G/R4 (#5-2-C2)		#5	HW-SC	40.8	655	49.6
C-G/R5 (12-2-C1)	12		Grooved	60.0	1000	29.3
C-G/R5 (12-1-C2)	12		Grooved	60.0	1000	50.5
PC	12		Deformed	47.0	1150	43.2
SF30	12		Deformed	47.0	1150	44.9
PPA2	12		Deformed	47.0	1150	43.4
SF30PPA2	12		Deformed	47.0	1150	48.8

In this study, the nominal bar diameters of #4, #5, and 12 mm were selected to investigate the influence of the diameter on bond damage evolution. The bar surface treatment used helical wrapped and sand coated (HW-SC), grooved, and deformed. The plain concrete involved two different compressive strengths, C1 (with the mean value of 28.63 MPa) and C2 (with the mean value of 52.19 MPa). The macro fibers encompassed steel fibers, polypropylene fibers and the hybrid use of them. Their respective dosages were 30 kg/m^3 for steel fibers (SF30), 2 kg/m^3 for polypropylene fibers (PPA2), and the mixture of SF30 and PPA2 (SF30PPA2). Table 5-1 details the material properties corresponding to those used in the original references.

In addition, the pullout tests adopted in (Baena et al., 2009) and (Ding et al., 2014) were the RILEM/CEB/FIP (1978) (RILEM/CEB/FIP, 1978) and Losberg (1963) (Losberg, 1963) arrangements, respectively. The concrete blocks were 200 mm and 150 mm cubes, respectively. The bonded lengths of the GFRP bars were $5d_b$ for both.

5.3.2. Geometry Modeling

5.3.2.1. Finite element modeling simplifications

The pullout test is usually associated with different failure modes, such as pullout failure, splitting failure, anchorage failure, and bar fracture, of which the first two failures accounts for the majority among others (Yan et al., 2016 (Under review)). To investigate the bond behavior at the interface, pullout failure is desirable, while other failure modes can be effectively avoided by some preventive measures in advance. For example, the splitting failure can be prevented by increasing the concrete cover to bar diameter ratio, and the anchorage failure can be avoided by providing sufficient anchorage length at the loaded end. Therefore, a 150 mm concrete cube commonly allows pullout failure occurring in most cases based on past pullout tests (Achillides and Pilakoutas, 2004; Davalos et al., 2008; Katz and Berman, 2000). Moreover, consider that

only the layer adjacent to the interface contributes to the interfacial behavior, it is reasonable to assume that the bond behavior is independent of the concrete dimensions (Godat et al., 2013). Therefore, the FE model adopting a 150 mm concrete cube is capable of simulating the interfacial behavior and covering the most pullout test scenarios.

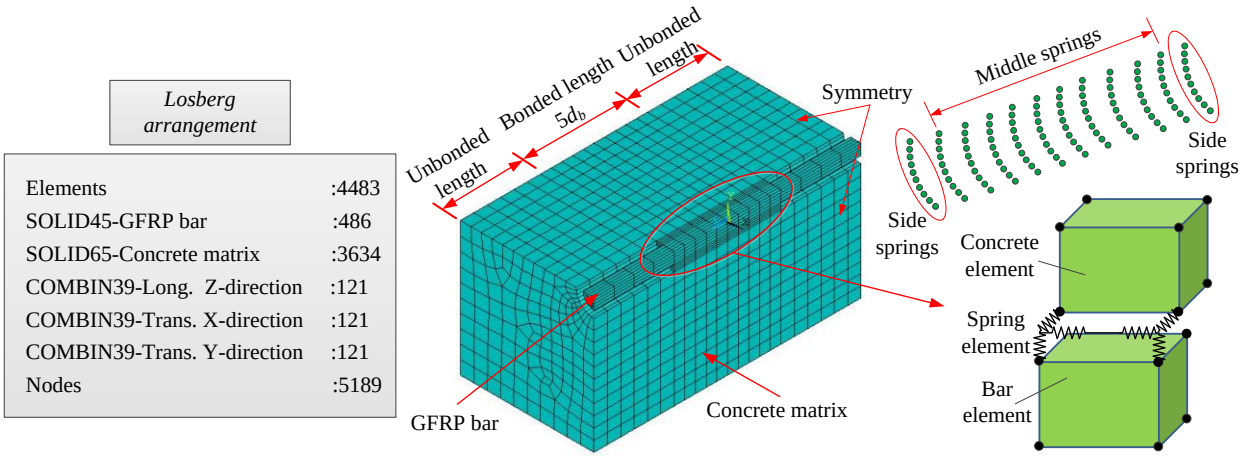

Figure 5-5. Finite element modeling for the Losberg arrangement of pullout test

On the other hand, a test using either RILEM/CEB/FIP or Losberg arrangement was found to have no influence on the numerical predictions of the interfacial responses, as well as the bar diameter. The interfacial elements (i.e. spring elements) play the crucial role in determining the numerical outcomes. Therefore, the Losberg arrangement was adopted, and the diameter of 12 mm is used for the GFRP bar modeling. A quarter of the pullout-test model was set up because of the symmetry. The meshing approach used hexahedrons to ensure the quality and reduce the total number of nodes. Figure 5-5 illustrates the overall information of the FE model. The total numbers of elements were 4483, of which 486 were the GFRP bar elements, 3634 were the concrete elements, and $121 \times 3 = 363$ were the spring elements. In particular, the nonlinear spring elements were used to simulate the extrusion and friction between the bar and concrete, and the side springs and middle springs had different mechanical relations due to different effective spacing as demonstrated in Equation (5-13), where the effective spacing of the

side springs is half of that of the middle springs. More information is detailed in the following sections.

5.3.2.2. GFRP bar and concrete matrix

The GFRP bar and the concrete matrix were modeled using the SOLID45 element and SOLID65 element, respectively. These two types of elements are both defined by eight nodes, of which each node has three translational degrees of freedom (DOFs). The concrete elements adjacent to the bonded interface were finely meshed with 6 mm along the axial direction and 1 mm along the radial direction, which is capable of capturing the interfacial responses. Beyond that, a coarse mesh size with 12 mm along the axial direction and 6 mm along the other two orthogonal directions was proved to guarantee the analysis accuracy.

5.3.2.3. Bar-concrete interface

The unidirectional nonlinear spring element COMBIN39 was used to build connections between the bar and concrete. This element is defined by two node points and a generalized force-slip (*F*-*S*) curve (Release, 2012). The real constant allows users to input up to 20 points to describe the *F*-*S* curve, and the number of points can be further doubled by using the reflective function. The uniaxial tension-compression option with only one translational DOF at each node is activated. As schematically illustrated in Figure 5-5, the node associated with the bar element and the node associated with the concrete element used three spring elements to simulate the tangential and normal stiffness, representing the extrusion and friction between the bar and concrete. These information in the 3-D nonlinear spring elements is derived from the experimental data, as detailed in Section 5.3.3.

5.3.3. Material Modeling

The effectiveness of the simulation of bond damage depends on proper definition of material constitutive equations to describe: a) nonlinear material behavior of concrete and b) nonlinear bar-to-concrete interfacial behavior due to mechanical interlocking, chemical adhesion and friction. Material behavior of concrete is a key to accurately capture the bond behavior of GFRP bar to concrete. Modeling of cracking initiation locally and propagation for concrete is a tough task. Although discrete cracking modeling, such as the extended finite element method (X-FEM) (Dolbow and Belytschko, 1999), has been accepted as a powerful numerical procedure for the analysis of concrete crack problems, it will be really cost and sometimes may not help to capture global bond damage behavior if the 3-D interfacial behavior in the model is not defined correctly. Instead, the bond damage behavior in this study is achieved through implementing bond-slip law in the FE simulation using the 3-D nonlinear spring elements in Section 3.3.3. The bond stress-slip relation in the 3-D nonlinear spring elements is derived from the experimental data, and thus the damage effects or strength degradation at bar-concrete interface have accounted for the impacts of the presence of concrete cracks in the concrete matrix (tension) and the corresponding decreasing confinement and concrete crushing at bar-concrete interface (compression). Besides that, concrete matrix is defined as a nonlinear constitutive relation in Section 3.3.2 that is capable of simulating cracking in tension and crushing in compression of quasi-brittle materials. Also, shear transfer coefficients are defined to effectively describe the loading transfer through cracks for both plain concrete and fiber-reinforced concrete, once there are presence of cracks. Detailed definition of the material properties are present below.

5.3.3.1. GFPR bar

GFRP bars behave linear elastic up to failure without plastic stage and thus the linear isotropic model was used to represent for the GFRP bars. A rupture point on the stress-strain diagram is defined as the maximum stress and its corresponding strain of the GFRP bars.

5.3.3.2. Concrete matrix

The nonlinear material behavior of concrete is crucial to describe concrete cracks in tension and crushing in compression. The constitutive equations for concrete, illustrated in Figure 5-6, is utilized in the SOLID65 element, which is capable of simulating cracking in tension and crushing in compression of quasi-brittle materials. In particular, its treatment of nonlinear material properties is suitable to simulate the concrete behavior, while helps the convergence of analysis.

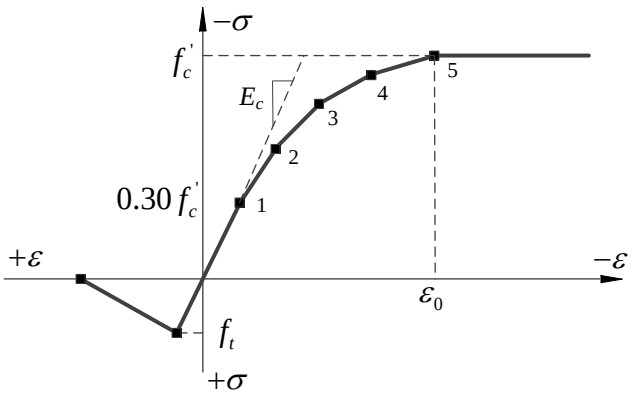

Figure 5-6. Simplified stress-strain relation of concrete

Figure 5-6 shows the simplified stress-strain diagram of the concrete using the multilinear model in compression while linear tension softening in tension. The nonlinear compression behavior of concrete using multilinear model has been successfully used in the FRP composites (Akishin et al., 2014), while linear tension softening is usually defined for concrete softening for cracks (Khalaf et al., 2016), in which f_c' and f_t are the concrete compressive strength and tensile

strength, respectively. The stress-strain relation is calculated according to Equation (5-8), which was proposed by MacGregor et al. (MacGregor et al., 1997):

$$f = \frac{E_c \varepsilon}{1+(\varepsilon/\varepsilon_0)^2}, \tag{5-8}$$

where f is the stress at any strain ε; ε_0 is strain at the ultimate compressive strength, and $\varepsilon_0 = 2f_c'/E_c$; E_c is the concrete elastic modulus. For the numerical analysis, the concrete tensile strength f_t is consistent with the relevant experimental data. When such data are not given, they would be approximated by Equation (5-9) specified in ACI code (Committee et al., 2008),

$$f_t = 0.62\sqrt{f_c'}. \tag{5-9}$$

The failure criterion for concrete adopted Willam and Warnke five-parameter model (William and Warnke, 1975), of which the most important four parameters are open shear transfer coefficient, closed shear transfer coefficient, uniaxial cracking stress, and uniaxial crushing stress. The failure criterion under a multiaxial stress state is demonstrated in Equation (5-10),

$$\frac{F}{f_c'} - S \geq 0, \tag{5-10}$$

where F is a function of the principle stress state; S is the failure surface expressed in terms of the principles stresses. Cracking takes place when the principle stress in any direction lies outside the failure surface. Crushing takes place when all principle stresses are compressive and lie outside the failure surface (Kohnke, 1999). It was found that the FE model failed prematurely when the concrete crushing option is on. Crushing first occurred at the direct loading positions, and then rapidly extended to adjacent elements. The local stiffness reduced significantly and hence, the solution ended in failure associated with a large displacement. Therefore, it was suggested to close the crushing option during the analysis (Hawileh et al., 2010; Jianjing, 2003). On the other hand, the shear transfer coefficient ranging from 0.0 to 1.0 represents a smooth

crack (complete loss of shear transfer) and a rough crack (no loss of shear transfer), respectively. It was found that the open and closed shear transfer coefficients had no apparent impact on the interfacial response whereas directly influenced the convergence of analysis. Thus, with reference to the suggestions in (Damian et al., 2001; Islam et al., 2014; Ru-deng, 2008), the open and closed shear transfer coefficients used 0.5 and 0.9 for plain concrete, and 0.7 and 0.9 for FRC. The simplified concrete model in terms of cracking, as well as those aforementioned key options, were tested to be have minor influence on the bond response at the bar-concrete interface whereas significantly influence the convergence of the numerical simulations. The FE models of the GFRP bar and concrete primarily provide a location where the spring elements can be attached to. The bond damage effect is considered and implemented through introducing the damaged spring elements in the following.

5.3.3.3. Bar-concrete interface

As stated early, the proposed bond damage evolution process is built on the basis of the bond-slip law from the experimental data, where the damage effects with respect to the concrete matrix, GFRP bars, and the bar-concrete interface due to the pullout of the bars have been accounted for. As expected, since the bond stress-slip relation is derived from the experimental data and thus the results in terms of damage are directly related to impacts of concrete cracks in tension and crushing in compression, the defined nonlinear constitutive relation of concrete has minor impact on the bond damage state and evolution. This is confirmed by later comparison of the bond-slip curves predicted by FE simulation with experimental ones in Figs. 7 and 8. The extrusion and friction between the GFRP bar and concrete used respective *F-S* relations based on different mechanical models as follows:

(I) Normal spring elements

The normal stiffness K_n of the spring elements was determined with reference to that adopted in the steel-concrete bond (Y.-q. WANG and WANG, 2006), as demonstrated in Equation (5-11),

$$K_n = \frac{E_{FRP} b_n l}{b}, \tag{5-11}$$

where E_{FRP} is the elastic modulus of FPR composite; b_n is the net width of the girder; b is the girder width, it is assumed that $b_n/b = 1$; and l is the axial spacing of the spring elements. Thus, the *F-S* relation of the normal spring elements can be determined according to Equation (5-12),

$$F_n = K_n \cdot s_n = E_{FRP} \cdot l \cdot s_n. \tag{5-12}$$

where F_n is the normal force due to extrusion s_n.

(II) Tangential spring elements

The *F-S* relation of the tangential spring elements complies with the bond-slip relation of the test results, as demonstrated in Equation (5-13),

$$F_t = \tau \cdot (\pi d l) \cdot s, \tag{5-13}$$

where F_t is the tangential force due to slip s. It is worth mentioning that l needs to take half spacing for the side spring elements.

5.3.4. Boundary Conditions and Loading Conditions

The symmetric boundary conditions were applied on the symmetry areas as shown in Figure 5-5. Consider that the pullout test setup uses the displacement control, where the loaded end of the bar anchored in the steel pipe is gripped with a mechanical jaw, and the loading frame holding the specimen is moving toward the free end of the bar. In the FE analysis, the nodes associated with the GFRP bar at the loaded end were fixed along all directions, and the nodes associated with concrete at the loaded end were applied on the displacement. The ultimate

displacement was implemented through a certain number of loading steps. To ensure the convergence, each loading step was further divided into a set of sub-steps, and the loads were applied in the ramped form for each sub-step.

5.3.5. Modeling Validation

Generally, the bond-slip relation between the GFRP bar and concrete was predicted and validated in two aspects: first, by comparing with the experimental results to demonstrate the accuracy of the FE model; second, by comparing with the analytical models to demonstrate the superiority of the FE model.

5.3.5.1. Bond-slip relation in plain concrete

The bond-slip relation in plain concrete was first predicted. Note that the maximum slip of the pullout test was approximately 25 mm, the ultimate displacement applied on the FE model was determined to be 25 mm to comply with the test conditions. Meanwhile, the number of the loading steps was set to be 25, and each loading step was further divided into 50 substeps. The bond stress at the end of each step was calculated according to Eqn. (7), and its corresponding slip at the loaded end was derived from the spring-element output. In addition, the parameters of the mBPE model and CMR model were determined from the curve fittings of the experimental data, as summarized in Table 5-2.

Table 5-2. Fitting parameters of the mBPE model and CMR model for plain concrete specimens

Specimen	τ_b (MPa)	s_b (mm)	α	p	s_r	β
B-G/R4 (#4-2-C1)	9.6923	6.7829	0.3204	0.3224	0.9312	1.3138
B-G/R4 (#5-1-C1)	10.3269	3.3132	0.4669	0.1257	0.7147	1.5397
B-G/R4 (#4-3-C2)	18.0765	2.1572	0.6487	0.0874	0.6650	1.6355
B-G/R4 (#5-2-C2)	16.8462	8.2279	0.2434	0.3933	1.0716	0.9186
C-G/R5 (12-2-C1)	14.6544	1.4920	0.7889	0.0705	0.3917	2.7015
C-G/R5 (12-1-C2)	7.9934	1.4390	0.5585	0.0832	0.2686	3.0628

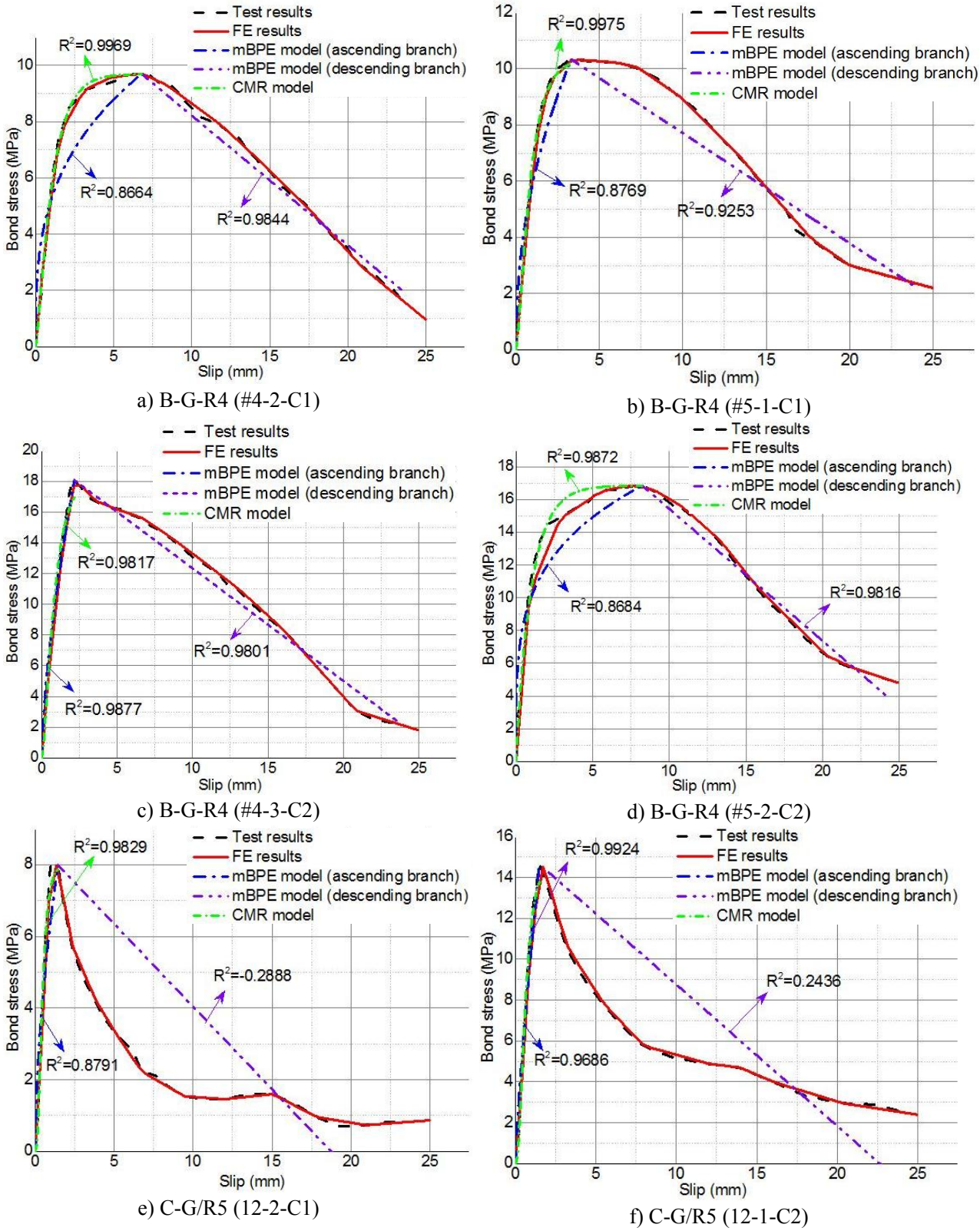

a) B-G-R4 (#4-2-C1)

b) B-G-R4 (#5-1-C1)

c) B-G-R4 (#4-3-C2)

d) B-G-R4 (#5-2-C2)

e) C-G/R5 (12-2-C1)

f) C-G/R5 (12-1-C2)

Figure 5-7. Bond-slip relations of the plain concrete specimens

Figure 5-7 displays the bond-slip predictions using the FE models and the analytical models, respectively. Clearly, all the results predicted by the FE models matched well with the test results, yielding good accuracy. The ascending branches of the bond-slip curves predicted by the CMR model performed better than those predicted by the mBPE model. The coefficient of determination (R^2) of the CMR model for all the specimens were greater than 0.98, indicating that the predicted bond-slip relation were rather close to the test results.

In addition, the double branches of the mBPE model show that the derivations increased as the curvature of the bond-slip curve increased, and vice versa. Since the descending branch of the mBPE model uses a linear expression to represent the post-peak bond behavior, the derivations were legitimately larger for those curves having larger fluctuations, as shown in the specimens of C-G/R5 (12-2-C1) and C-G/R5 (12-1-C2). Therefore, the FE models have obvious advantages in terms of generalization ability over the analytical models.

5.3.5.2. Bond-slip relation in fiber-reinforced concrete

Note that the maximum slip recorded in the pullout test was 8 mm, the ultimate displacement applied on the FE model was determined to be 10 mm. The total number of the loading steps was set to be 10, and each loading step was further divided into 50 substeps. The parameters of the mBPE model and CMR model were derived from the curve fittings of the test results, as detailed in Table 5-3.

Table 5-3. Fitting parameters of the mBPE model and CMR model for FRC specimens

Specimen	τ_b (MPa)	s_b (mm)	α	p	s_r	β
PC	12.2195	2.3014	0.5744	0.2801	0.7218	1.3259
SF30	13.9801	2.4411	0.4472	0.2878	0.7443	0.9841
PPA2	14.6763	2.4429	0.4401	0.2893	0.7611	0.9342
SF30PPA2	17.5569	2.6301	0.3980	0.2195	0.4939	1.5042

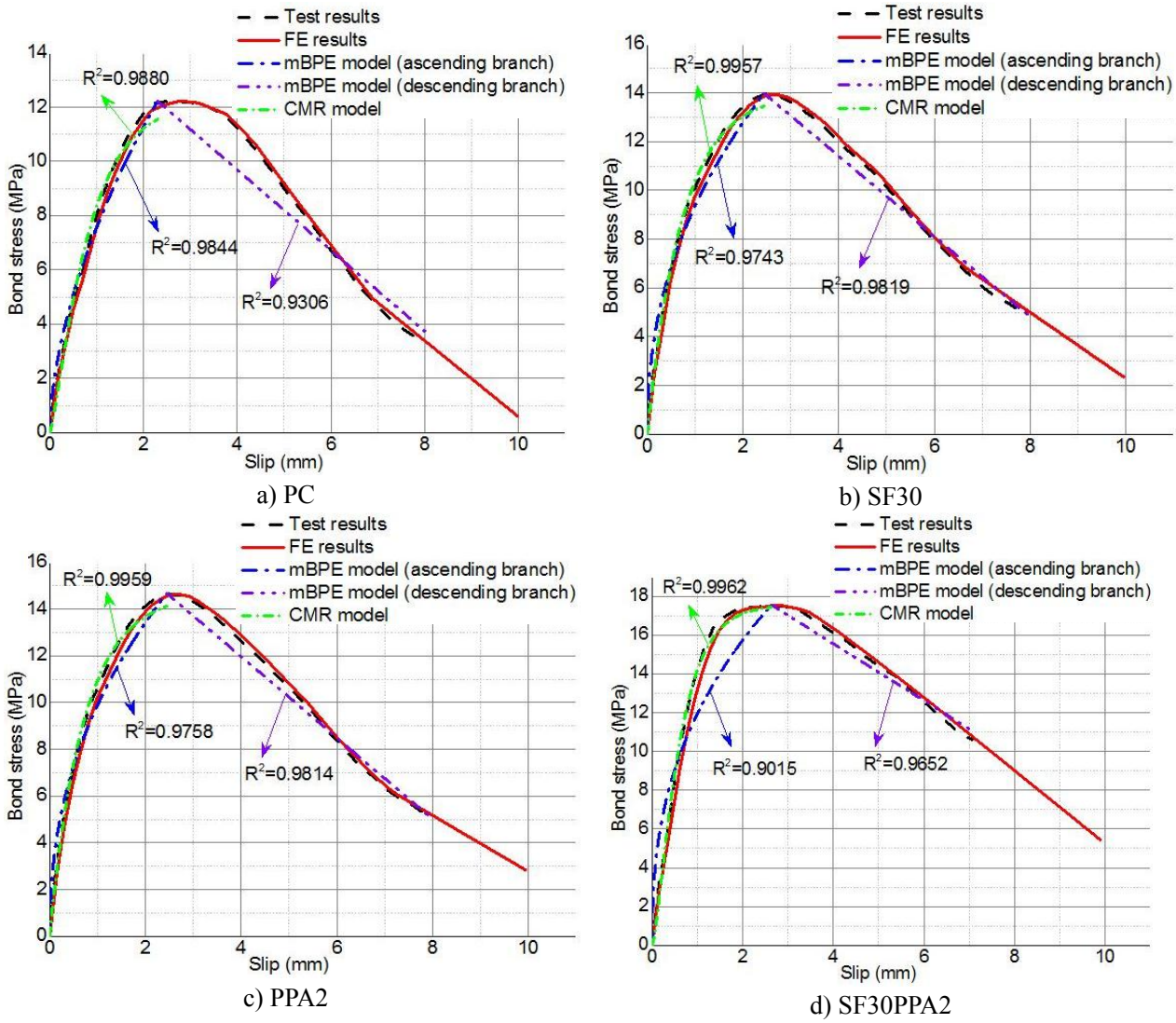

Figure 5-8. Bond-slip relations of the FRC specimens

Figure 5-8 shows the bond-slip predictions using different approaches. First, the bond-slip curves of the FRC specimens seemed relatively gentler at the segment close to the peak bond stress compared to those displayed in the plain concrete specimens, such as C-G/R5 (12-2-C1) and C-G/R5 (12-1-C2). This indicates better energy-dissipating capacity due to the fiber mixture. Second, the results predicted by the FE models agreed well with the test results, and yielded higher accuracy over the analytical models. In addition, similar to the performance shown in the plain concrete specimens, the results predicted by the CMR model for the ascending branches

generally performed better than those predicted by the mBPE model. The R^2 of both analytical models were close to one, indicating good match with the test results.

Therefore, these comparisons among different models and the validations by the experimental results further confirm that the bond-slip relation predicted by the FE model is viable with applications to the subsequent bond damage assessment.

5.4. Bond Damage Assessment

5.4.1. Damage Evolution Patterns

The bond-slip curves predicted by the FE models are used to derive the bond damage evolution curves herein. Meanwhile, two types of distribution patterns viz., the lognormal distribution and Weibull distribution, are used to fit the damage evolution points, as demonstrated in Equations. (5-14) and (5-15), respectively,

$$F_D(s) = \frac{1}{2} + \frac{1}{2} erf\left(\frac{lns - \mu}{\sqrt{2}\sigma}\right), \tag{5-14}$$

$$F_D(s) \begin{cases} 1 - exp(-(s/\lambda)^k) & s \geq 0 \\ 0 & s < 0 \end{cases}, \tag{5-15}$$

where F_D is the cumulative distribution function; μ and σ are the curve fitting parameters of the lognormal distribution; λ and k are the curve fitting parameters of the Weibull distribution. In addition, consider that $s_{cut-off}$ refers to the beginning of the damage evolution, it is assumed that $s_{cut-off}$ is equal to $0.08\% \cdot s_b$. This indicates the bond damage is assumed to be zero before the slip reaches the cut-off limiting slip. Such small segment of the bond-slip curve will not influence the overall assessment of the bond damage evolution.

5.4.1.1. Plain concrete specimens

Figure 5-9 shows the bond damage evolution patterns for the plain concrete specimens. The bond damage calculated using Equation (5-6) was denoted by dots, where the bond-slip relation used the FE predictions.

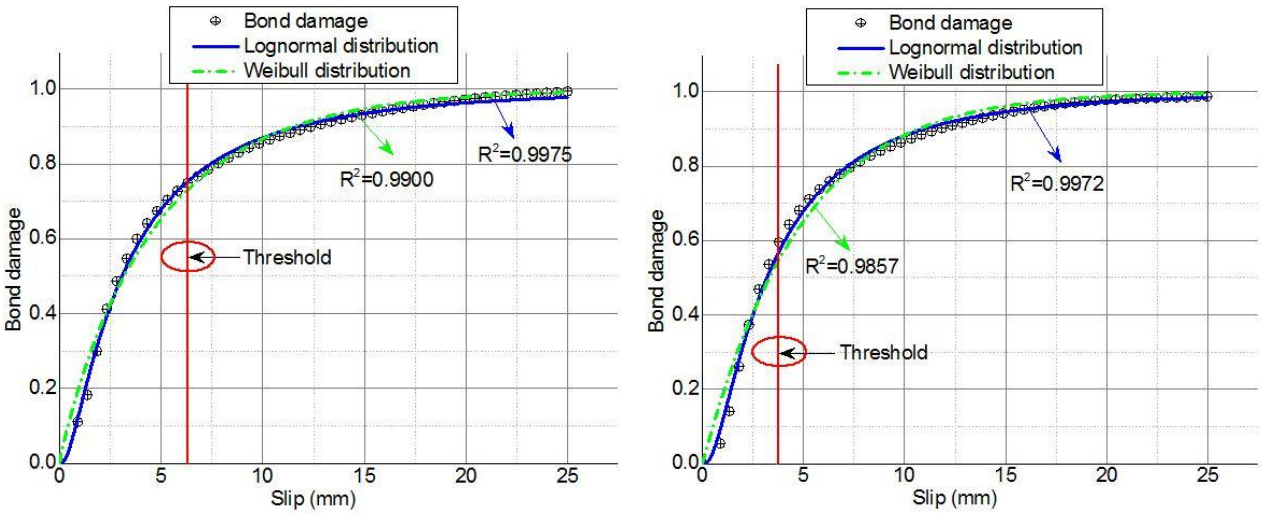

a) B-G-R4-#4-2-C1

b) B-G-R4-#5-1-C1

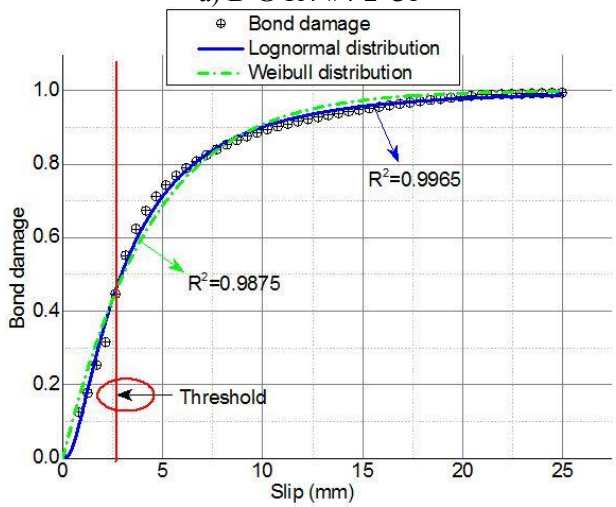

c) B-G-R4-#4-3-C2

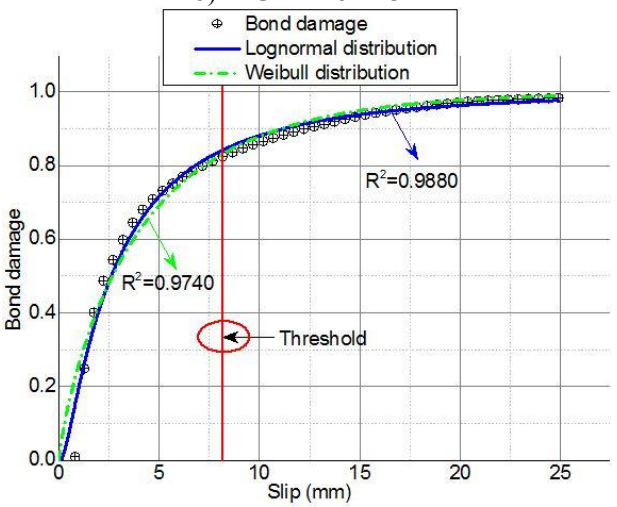

d) B-G-R4-#5-2-C2

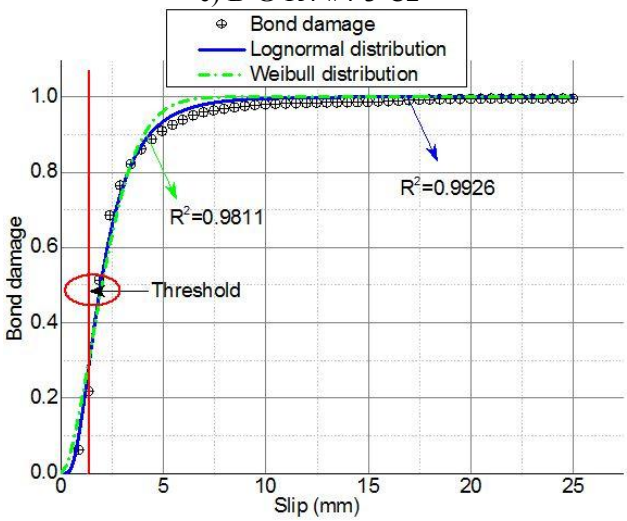

e) C-G/R5 (12-2-C1)

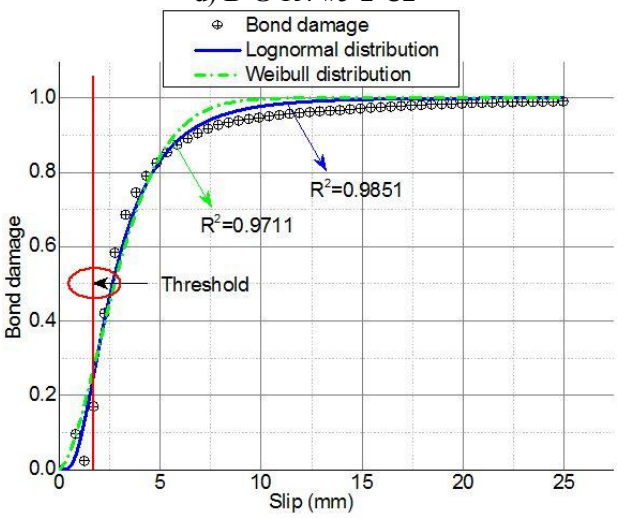

f) C-G/R5 (12-1-C2)

Figure 5-9. Bond damage evolutions of the plain concrete specimens

The damage evolutions fitted with the lognormal distribution and Weibull distribution were displayed in solid curves and short dash dot curves, respectively. In particular, a threshold was marked on the damage evolution curve to represent the critical bond damage associated with the bond strength, distinguishing the damage evolution with respect to the pre-peak bond stage and post-peak bond stage. In addition, Table 5-4 lists the curve fitting parameters of the two distributions using Equations (5-14) and (5-15).

In general, it is clear that the damage evolution patterns strictly followed the lognormal distribution or Weibull distribution, where the R^2 of all fitting curves were approximately equal to one. The R^2 of the lognormal distributions were equal to 0.9975, 0.9972, 0.9965, 0.9880, 0.9926 and 0.9851, respectively. The R^2 of the Weibull distributions were equal to 0.9900, 0.9857, 0.9875, 0.9740, 0.9811 and 0.9711, respectively. The overall performance of the lognormal distribution was better than that of the Weibull distribution whereas such differences were very small. In addition, the shapes of the evolution patterns changed with different factors in terms of the bar diameter, surface treatment and concrete compressive strength, indicating different evolution speed against slip development.

Table 5-4. Fitting parameters of the lognormal distribution and Weibull distribution

Specimen	μ	σ	λ	k
B-G/R4 (#4-2-C1)	1.1252	1.0463	4.7085	0.9334
B-G/R4 (#5-1-C1)	1.1632	0.9617	4.7467	1.0260
B-G/R4 (#4-3-C2)	1.0766	0.9522	4.3273	1.0371
B-G/R4 (#5-2-C2)	0.9630	1.1343	4.1318	0.8458
C-G/R5 (12-2-C1)	0.6604	0.6264	2.4863	1.7063
C-G/R5 (12-1-C2)	0.9732	0.6637	3.4364	1.6356

On the other hand, the damage evolution curves revealed different governing factors at different bond stages distinguished by the threshold. First, for the specimens with HW-SC

surface, at the pre-peak bond stage, the bond damage increased significantly as the slip increased small, indicating that the damage governed the failure progress. At the post-peak bond stage, the slip increased significantly whereas the damage increased a little, indicating that the displacement governed the failure progress. It is worth mentioning that the large displacement usually takes place suddenly and results in brittle failure regardless of the remaining damage that the interface can further sustain. Second, for the specimens with grooved surface, the damage governed the failure progress at the initial segment of the post-peak bond stage, of which the damage kept increasing apparently whereas the slip increased small. This can be explained by that the remaining bearing force due to mechanical interlocking against concrete can still provide a certain degree of resistance against slip. When the concrete crush further deteriorates, large slip occurs and displacement becomes the governing factor at the subsequent bond stage.

5.4.1.2. Fiber-reinforced concrete specimens

Figure 5-10 displays the bond damage evolution patterns for the FRC specimens, where the dots and curve style denoted the same implications as those used in the plain concrete specimens. Table 5-5 lists the curve fitting parameters of the lognormal distribution and Weibull distribution.

Generally, same as the plain concrete specimens, the damage evolution patterns of the FRC specimens strictly followed the lognormal distribution or Weibull distribution as well, where the R^2 of all the fitting curves were approximately equal to one. The R^2 of the lognormal distributions were equal to 0.9709, 0.9894, 0.9898 and 0.9942, respectively. The R^2 of the Weibull distributions were equal to 0.9924, 0.9988, 0.9983 and 0.9975, respectively. The overall performance of the Weibull distribution is better than that of the lognormal distribution whereas such differences were very small. On the other hand, the shapes of the evolution curves were

similar to each other since the factors in terms of the bar diameter, surface treatment stayed the same and the concrete compressive strength differed little for different FRC matrices.

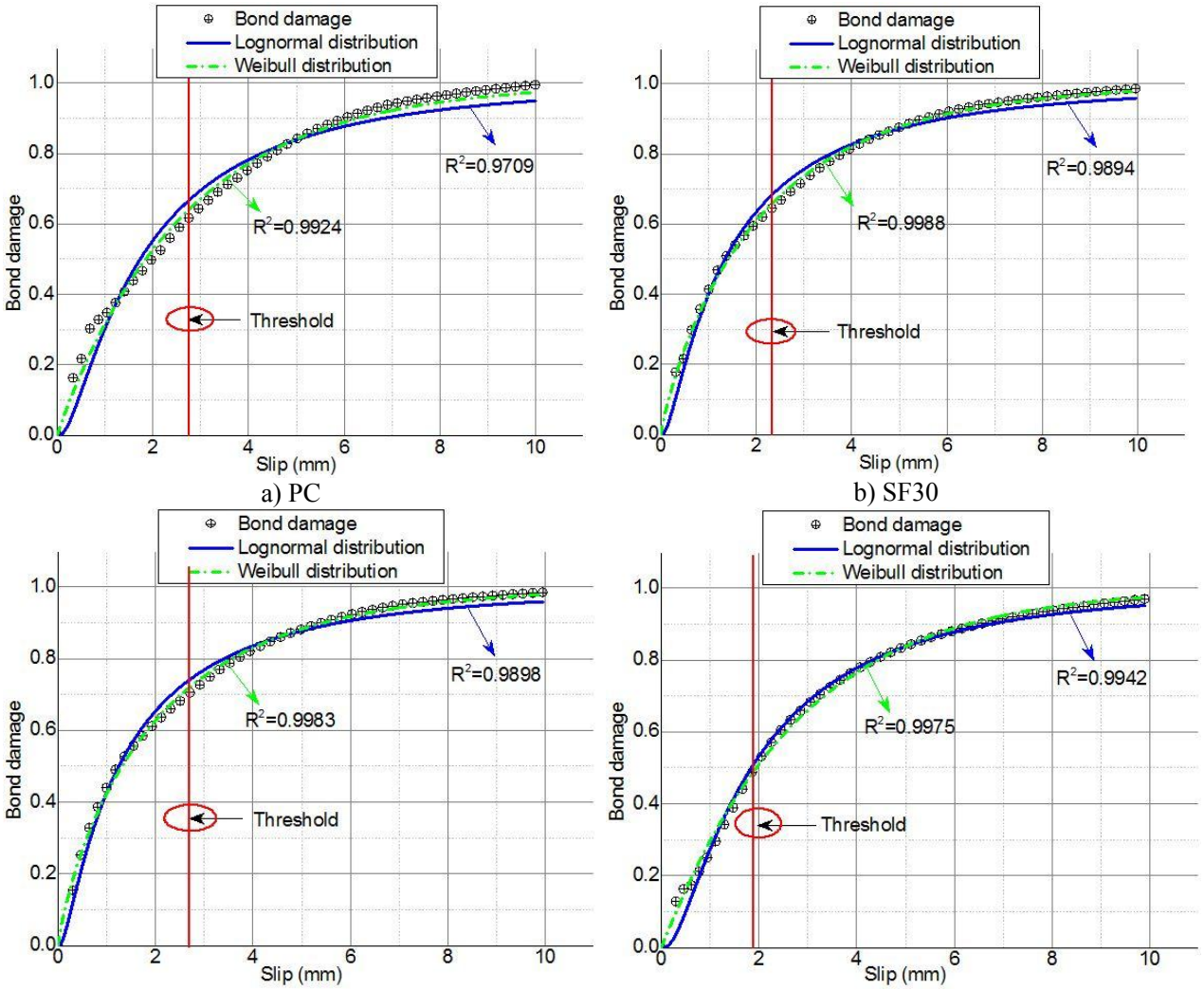

Figure 5-10. Bond damage evolutions of the FRC specimens

Table 5-5. Fitting parameters of the lognormal distribution and Weibull distribution

Specimen	μ	σ	λ	k
PC	0.1251	1.0327	1.6847	0.9817
SF30	0.2215	1.1950	2.0290	0.9133
PPA2	0.4295	1.1580	2.3153	0.9153
SF30PPA2	0.7133	1.0125	2.7854	1.0123

In addition, the governing factors of the failure progress showed similar behavior as the plain concrete specimens, where the damage governed the failure progress at the pre-peak bond stage and the slip governed the failure progress at the post-peak bond stage.

5.4.2. Critical Factors and Their Impacts on Damage Evolutions

The critical factors and their influences on the bond damage evolution, as well as the critical bond damage and corresponding slip, are analyzed according to the fitted damage patterns using the lognormal distribution and Weibull distribution.

5.4.2.1. Palin concrete specimens

Figure 5-11 displays the comparisons of the plain concrete specimens. It is clear that the damage evolution curves with the same surface treatment in terms of HW-SC differed little when the bar diameter and concrete compressive strength changed, as demonstrated in the curves with respect to B-G-R4-#4-2-C1, B-G-R4-#5-1-C1, B-G-R4-#4-3-C2, and B-G-R4-#5-2-C2. While the damage evolution curves exhibited obvious differences when the surface treatment changed, as demonstrated in the curves with respect to C-G/R5 (12-2-C1), C-G/R5 (12-1-C2) among others. The specimens with the HW-SC surface showed larger bond damage than those with the grooved surface under the same slip. This can be explained by the wedging effect of the grooved surface is more evident than that of the HW-SC surface. The concrete crush due to the bearing force acting on the lug interface would be more serious for the grooved surface, leading to more obvious reduction of the effective secant modulus. Therefore, it can be concluded that the most distinct factor contributing to the bond damage refers to the surface treatment of the GFRP bar.

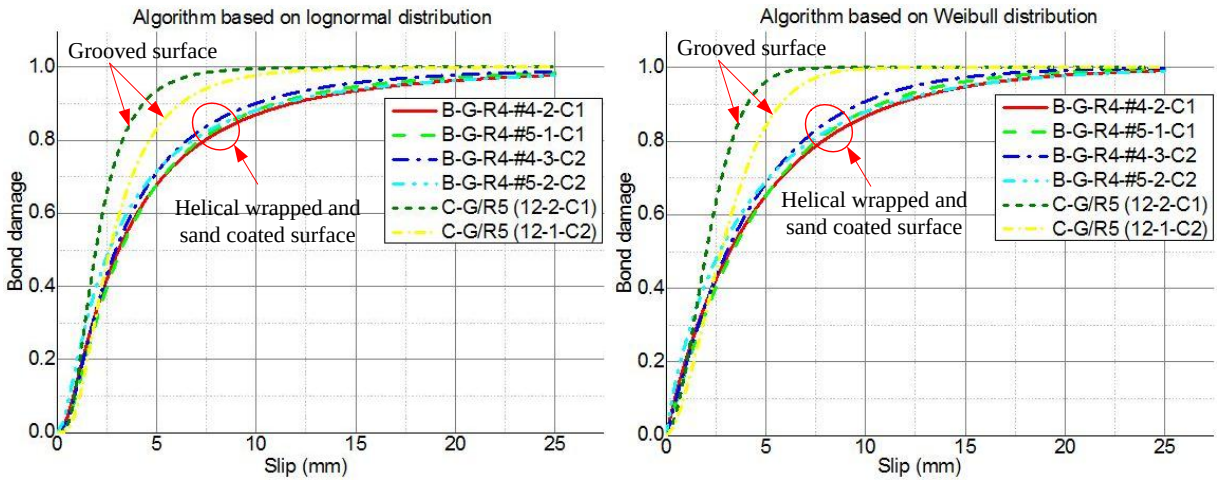

Figure 5-11. Bond damage comparisons of the plain concrete specimens

For another, Figure 5-12 displays the comparisons of the critical bond damage and its corresponding slip for different specimens. It can be seen that the critical damage with respect to the grooved surface was much smaller than that with respect to the HW-SC surface. Specifically, the critical damages of the C-G/R5 (#12-2-C1) and C-G/R5 (#12-1-C2) were equal to 0.2810 and 0.1705, respectively, while those of the other specimens were all greater than 0.4. This can be attributed to the smaller slip developed when the specimen reached the critical bond damage. The lug surface significantly prevented the pullout of the GFRP bar at the pre-peak bond stage, resulting in smaller slip development. On the other hand, the GFRP bar suffered from less resistance due to smaller roughness provided by the HW-SC surface, legitimately resulting in larger slip development. Furthermore, since the aforementioned features regarding the governing factors, the specimens with grooved surface are capable of further sustain a certain degree of the bond damage due to the damage governing features at the initial segment of the post-peak bond stage, whereas the specimens with HW-SC surface may fail suddenly due to the slip governing features at the post-peak bond stage.

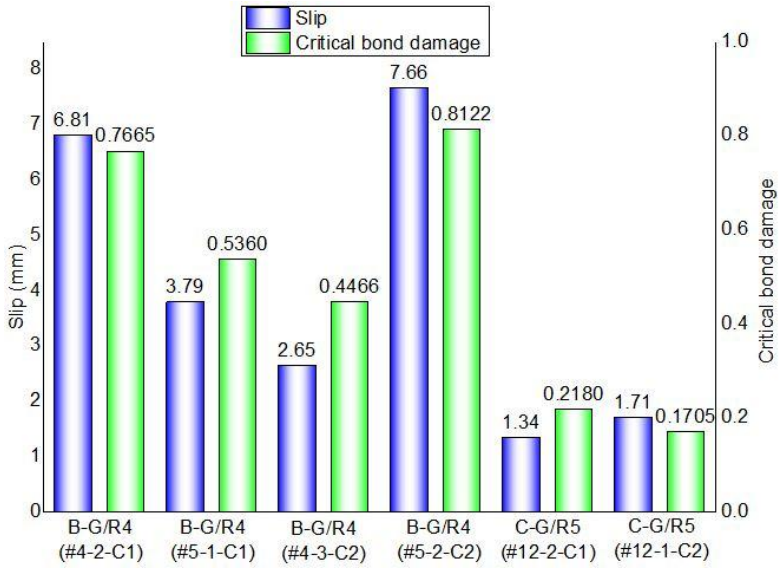

Figure 5-12. Comparisons of the critical bond damage and its corresponding slip

5.4.2.2. Fiber-reinforced concrete specimens

Figure 5-13 shows the damage evolution curves of the FRC specimens. Generally, the curves of the FRC specimens were located below that of the plain concrete specimen, indicating that the fiber mixture contributes to ameliorate the damage development at the interface. In addition, the damage degree of the SF30PPA2 is the smallest among the FRC specimens under the same slip. Therefore, it can be concluded that mixing fibers into concrete matrix helps to decrease and slow down the bond damage evolution at the bar-concrete interface.

In addition, Figure 5-14 compares the critical bond damages and their corresponding slips of different specimens. It can be seen that SF30PPA2 showed the smallest critical bond damage and slip among others, which were equal to 0.4719 and 1.89 mm, respectively. While the PC displayed the largest critical bond damage and slip, which were equal to 0.8016 and 2.76 mm. Therefore, concrete matrix mixing with macro fibers effectively decreased the critical bond damage and its slip.

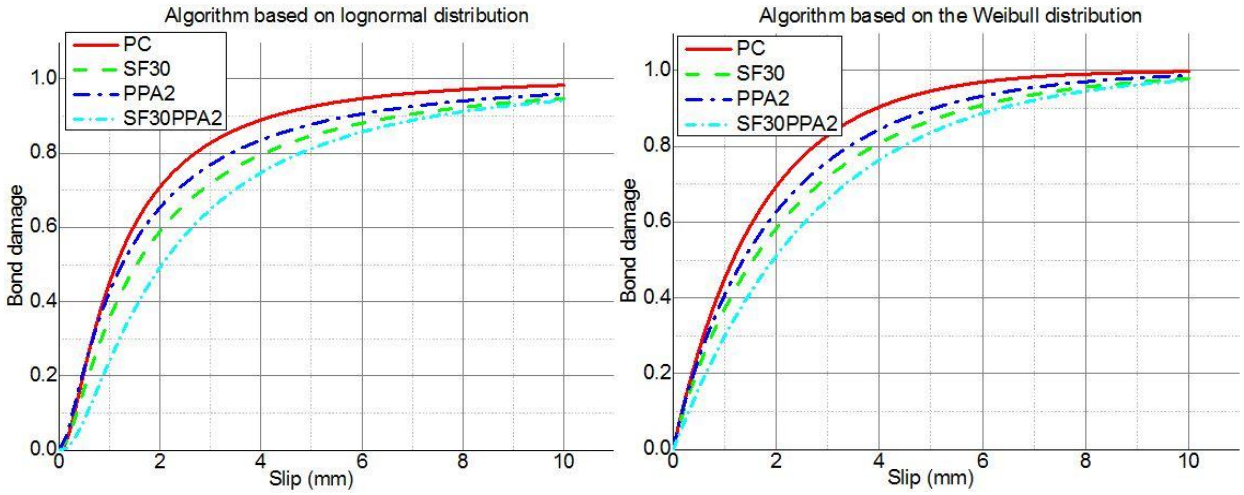

Figure 5-13. Bond damage comparisons of the FRC specimens

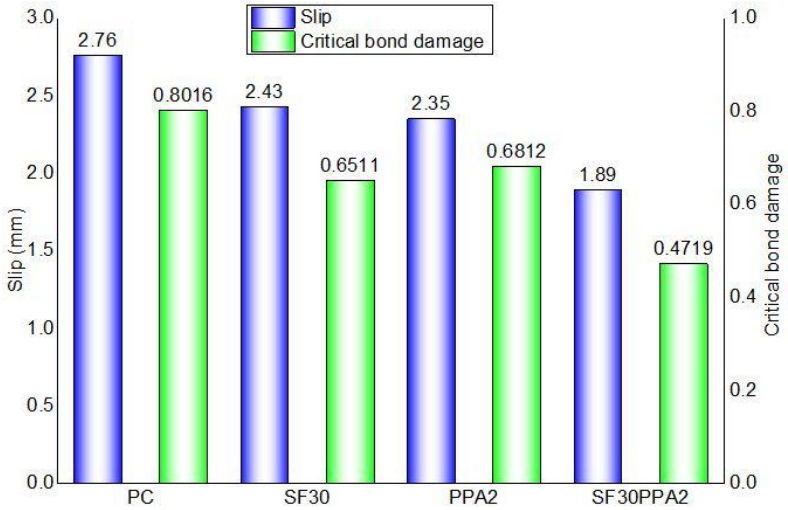

Figure 5-14. Critical bond damage comparisons

5.5. Conclusions

This chapter presented a bond damage assessment approach for the GFRP bar-concrete interface. The damage evolution equations were derived grounded on the concept of strain equivalence principle. The FE models were used to predict the bond-slip relations with respect to plain concrete and FRC, covering both geometry modeling and material modeling. The numerical predictions were validated through the experimental data of the literatures, and further compared with two widely used analytical models. Based on this, the damage evolution curves

were derived, and fitted with two distribution patterns. Specifically, several conclusions can be drawn in the following:

(1) The nonlinear spring elements of the FE models enable to accurately capturing the interfacial responses. The bond-slip curves predicted by the FE models matched well with experimental results, and yielded higher accuracy over the analytical models. The mBPE model exhibited larger deviations when the curvature of the bond-slip curve was relatively larger whereas the CMR model performed better for the ascending branch. Therefore, with consideration of complete bond-slip modeling, the FE model shows obvious advantages in the generalization capacity over the analytical models.

(2) The damage evolution patterns derived from the bond-slip relations strictly followed the lognormal distribution or Weibull distribution for both plain concrete specimens and FRC specimens, of which the coefficient of determination (R^2) were approximately equal to one. Moreover, the proposed critical bond damage associated with the bond strength distinguished the damage evolution into different bond stages. Damage governed the failure progress at the pre-peak bond stage whereas displacement governed the failure progress at the post-peak bond stage. Especially, considering the abrupt features of the bond-slip relation in terms of the descending branch, large displacement usually takes place in the form of brittle failure regardless of the remaining damage that the interface can further sustain.

(3) The comparisons of those bond damage evolution curves revealed that the surface treatment was the most distinct factor contributing to the damage evolution. The plain concrete specimens with grooved surface displayed more severe damage development than those reinforcing GFRP bars with the HW-SC surface. Furthermore, the critical bond damage with respect to the grooved surface was much smaller than that with respect to the HW-SC surface,

which can be attributed to the smaller slip development for the grooved surface when the bond stress reached the maximum. On the other hand, the damage evolutions of the FRC specimens were smaller than that of the plain concrete specimen, indicating that the fiber mixture helps to ameliorate the damage evolution. In addition, the critical bond damage of the FRC specimen was smaller than that of the plain concrete specimen, as well as its corresponding slip.

5.6. References

Achillides, Z., and Pilakoutas, K. (2004). Bond behavior of fiber reinforced polymer bars under direct pullout conditions. Journal of Composites for Construction, 8(2), 173-181.

Akishin, P., Kovalovs, A., Kulakov, V., and Arnautov, A. (2014). Finite element modelling of slipage between FRP rebar and concrete in pull-out test. Paper presented at the The International Scientific Conference „Innovative Materials, Structures and Technologies".

Baena, M., Torres, L., Turon, A., and Barris, C. (2009). Experimental study of bond behaviour between concrete and FRP bars using a pull-out test. Composites Part B: Engineering, 40(8), 784-797.

Ceroni, F., Cosenza, E., Gaetano, M., and Pecce, M. (2006). Durability issues of FRP rebars in reinforced concrete members. Cement and Concrete Composites, 28(10), 857-868.

Chaallal, O., and Benmokrane, B. (1993). Pullout and bond of glass-fibre rods embedded in concrete and cement grout. Materials and Structures, 26(3), 167-175.

Chen, Y., Davalos, J. F., Ray, I., and Kim, H.-Y. (2007). Accelerated aging tests for evaluations of durability performance of FRP reinforcing bars for concrete structures. Composite Structures, 78(1), 101-111.

Committee, A., Institute, A. C., and Standardization, I. O. f. (2008). Building code requirements for structural concrete (ACI 318-08) and commentary.

Cosenza, E., Manfredi, G., and Realfonzo, R. (1995). Analytical modelling of bond between FRP reinforcing bars and concrete. Paper presented at the Non-Metallic (FRP) Reinforcement for Concrete Structures: Proceedings of the Second International RILEM Symposium.

Cosenza, E., Manfredi, G., and Realfonzo, R. (1997). Behavior and modeling of bond of FRP rebars to concrete. Journal of Composites for Construction, 1(2), 40-51.

Damian, K., Thomas, M., Solomon, Y., Kasidit, C., and Tanarat, P. (2001). Finite element modeling of reinforced concrete structures strengthened with FRP laminates. Report for Oregon Department Of Transportation, Salem.

Davalos, J. F., Chen, Y., and Ray, I. (2008). Effect of FRP bar degradation on interface bond with high strength concrete. Cement and Concrete Composites, 30(8), 722-730.

De Nardin, S., Almeida Filho, F., Oliveira Filho, J., Haach, V., and El Debs, A. (2005). Non-linear analysis of the bond strength behavior on the steel-concrete interface by numerical models and pull-out tests. Paper presented at the Proceedings of the ASCE Conference "Structures.

Ding, Y., Ning, X., Zhang, Y., Pacheco-Torgal, F., and Aguiar, J. (2014). Fibres for enhancing of the bond capacity between GFRP rebar and concrete. Construction and Building Materials, 51, 303-312.

Dolbow, J., and Belytschko, T. (1999). A finite element method for crack growth without remeshing. International Journal for Numerical Methods in Engineering, 46(1), 131-150.

Godat, A., Chaallal, O., and Neale, K. W. (2013). Nonlinear finite element models for the embedded through-section FRP shear-strengthening method. Computers & structures, 119, 12-22.

Hawileh, R., Rahman, A., and Tabatabai, H. (2010). Nonlinear finite element analysis and modeling of a precast hybrid beam–column connection subjected to cyclic loads. Applied Mathematical Modelling, 34(9), 2562-2583.

Islam, M., Chowdhury, M., Amin, S., Mitu, S., Bala, M., Islam, Z., et al. (2014). Finite element modeling and analysis of rc beams made of steel fiber reinforced concrete (SFRC): Critical investigation of the flexural and shear capacity enhancements. Paper presented at the Proceedings of the 2nd International Conference on Civil Engineering for Sustainable Development (ICCESD-2014), KUET, Khulna, Bangladesh.

Jianjing, L. X. J. (2003). Analysis for Concrete Structure Under Complex Stress Condition with Solid 65 FEA Element of ANSYS [J]. Building Structure, 6, 007.

Kabir, M. R., and Islam, M. M. (2014). Bond stress behavior between concrete and steel rebar: Critical investigation of pull-out test via Finite Element Modeling.

Kachanov, L. (1958). Time of the rupture process under creep conditions. Isv. Akad. Nauk. SSR. Otd Tekh. Nauk, 8, 26-31.

Kachanov, L. (2013). Introduction to continuum damage mechanics (Vol. 10): Springer Science & Business Media.

Katz, A., and Berman, N. (2000). Modeling the effect of high temperature on the bond of FRP reinforcing bars to concrete. Cement and Concrete Composites, 22(6), 433-443.

Khalaf, J., Huang, Z., and Fan, M. (2016). Analysis of bond-slip between concrete and steel bar in fire. Computers & structures, 162, 1-15.

Kohnke, P. (1999). ANSYS theory reference: Ansys.

Lemaitre, J. (2012). A course on damage mechanics: Springer Science & Business Media.

Lin, X., and Zhang, Y. (2014). Evaluation of bond stress-slip models for FRP reinforcing bars in concrete. Composite Structures, 107, 131-141.

Liu, P.-x., Xiu, Y., and Liu, F.-s. (2007). Realization of RC structure bond-slip analysis with ansys. JOURNAL-SHANDONG AGRICULTURAL UNIVERSITY, 38(1), 125.

Losberg, A. (1963). Force Transfer and Stress Distribution at Anchorage and Curtailment of Reinforcement. Rep, 608.

MacGregor, J. G., Wight, J. K., Teng, S., and Irawan, P. (1997). Reinforced concrete: Mechanics and design (Vol. 3): Prentice Hall Upper Saddle River, NJ.

Malvar, L. J. (1994). Bond stress-slip characteristics of FRP rebars: DTIC Document.

Mazaheripour, H., Barros, J. A., Sena-Cruz, J., Pepe, M., and Martinelli, E. (2013). Experimental study on bond performance of GFRP bars in self-compacting steel fiber reinforced concrete. Composite Structures, 95, 202-212.

Okelo, R., and Yuan, R. L. (2005). Bond strength of fiber reinforced polymer rebars in normal strength concrete. Journal of Composites for Construction.

Polanco-Loria, M., and Sørensen, S. (1994). A Scalar Damage Model Applied to Concrete DIANA Computational Mechanics '94 (pp. 171-180): Springer.

Release, A. (2012). 14.0. Help Guides, ANSYS Europe Ltd.

RILEM/CEB/FIP. (1978). Bond test for reinforcing steel 2: Pullout test. Recommendation RC6, RILEM/CEB/FIP, Bagneux, France.

Robert, M., and Benmokrane, B. (2010). Effect of aging on bond of GFRP bars embedded in concrete. Cement and Concrete Composites, 32(6), 461-467.

Ru-deng, L. (2008). Values of shear transfer coefficients of concrete element Solid65 in Ansys [J]. Journal of Jiangsu University (Natural Science Edition), 2, 018.

Skrzypek, J. J., and Ganczarski, A. (2013). Modeling of material damage and failure of structures: theory and applications: Springer Science & Business Media.

Soh, C., Chiew, S., and Dong, Y. (1999). Damage model for concrete-steel interface. Journal of engineering mechanics, 125(8), 979-983.

Soh, C. K., Liu, Y., Dong, Y. X., and Lu, X. Z. (2003). Damage model based reinforced-concrete element. Journal of Materials in Civil Engineering, 15(4), 371-380.

Tang, B., Bruschi, S., Ghiotti, A., and Bariani, P. (2016). An improved damage evolution model to predict fracture of steel sheet at elevated temperature. Journal of Materials Processing Technology, 228, 76-87.

Tepfers, R. (2006). Bond clause proposals for FRP bars/rods in concrete based on CEB/FIP Model Code 90. Part 1: Design bond stress for FRP reinforcing bars. Structural Concrete, 7(2), 47-55.

WANG, Y.-q., and WANG, F.-z. (2006). Simulation of bond-slip relationship between concrete and reinforcing bar in ANSYS. Journal of Tianjin University, 2, 016.

Wang, Y., Wong, P., and Kodur, V. (2007). An experimental study of the mechanical properties of fibre reinforced polymer (FRP) and steel reinforcing bars at elevated temperatures. Composite Structures, 80(1), 131-140.

Wei-ping, Z. (2011). Local bond-slip numerical simulation based on ANSYS contact analysis. Paper presented at the Electric Technology and Civil Engineering (ICETCE), 2011 International Conference on.

William, K., and Warnke, E. (1975). Constitutive model for the triaxial behavior of concrete.

Yan, F., and Lin, Z. (2016). New strategy for anchorage reliability assessment of GFRP bars to concrete using hybrid artificial neural network with genetic algorithm. Composites Part B: Engineering.

Yan, F., Lin, Z., and Yang, M. (2016 (Under review)). Bond mechanism and bond strength of GFRP bars to concrete: a review. Composites Part B: Engineering.

Yoo, D.-Y., Kwon, K.-Y., Park, J.-J., and Yoon, Y.-S. (2015). Local bond-slip response of GFRP rebar in ultra-high-performance fiber-reinforced concrete. Composite Structures, 120, 53-64.

Zhang, M., and Jivkov, A. P. (2014). Microstructure-informed modelling of damage evolution in cement paste. Construction and Building Materials, 66, 731-742.

6. EVALUATION AND PREDICTION OF BOND STRENGTH OF GFRP-BAR REINFORCED CONCRETE USING ARITIFICIAL NEURAL NETWORK AND GENETIC ALGORITHM

6.1. Introduction

Accurately predicting bond strength between GFRP bars and concrete is of great importance to design GFRP bar reinforced concrete products. Over the past few decades, primary factors influencing bond behavior have been investigated by either beam test or direct pullout test (Benmokrane and Tighiouart, 1996; Masmoudi et al., 2010; Mazaheripour et al., 2013; Okelo and Yuan, 2005; Yoo et al., 2015), and brought into design guidelines of the US, Canada and Japan for considerations (ACI Committee, 2006; Canadian Standards Association, 2002, 2006; Machida and Uomoto, 1997), which are summarized in Table 6-1. These independent variables involve bar diameter (d_b), concrete strength (f_c'), concrete cover (c), bar position, embedment length (l_d), bar surface and transverse reinforcement ratio (ρ). It is clear that some parameters contributing to bond strength are not completely covered. Meanwhile, it has been reported that the bond strength predicted by these design equations exhibited much conservative compared with the actual values (Ametrano, 2011). Experimental-based approaches employ traditional technique of linear or nonlinear regressions. Sometimes, it is feasible to find a simple solution for a univariate problem based on the available data of test results. However, these approaches fail to yield good accuracy and fit with small coefficient of determination (R^2) for multivariate problems when independent variables tend to be enormous or further correlate with each other.

Table 6-1. Variables affecting bond strength considered in existing design codes

Design standards	d_b	f_c'	c	Position	l_d	Surface	ρ
ACI 440.1R-06	√	√	√	√	√	×	×
CSA S806-02	√	√	√	√	×	√	×
CSA S6-06	√	√	√	√	×	√	√
JSCE	√	√	√	√	×	×	√

Thereupon, with the purpose of modeling complex problems referred to highly nonlinearity, the intelligence computing technique, artificial neural network (ANN) is introduced as an ascendant resource. The strategy of the ANN-based modeling is to map complicated nonlinear and indeterminate relationships between a large number of inputs and outputs by a set of interconnected neurons. Particularly, back-propagation neural network (BPNN) has gained popularity due to its powerful nonlinear functions and convenience to use. Golafshani et al. (Golafshani et al., 2015) modeled the bond strength of GFRP bars in concrete associated with the aforementioned independent variables using BPNN. The developed model was proved to be more reliable than the model using traditional multi-linear regression method, and was more accurate and consistent with experimental results compared to the design equations stipulated in ACI 440.1R-06 and CSA S806-02. Dahou et al. (Dahou et al., 2009) developed two BPNN models with six and two inputs for predicting ultimate pullout load between steel ribbed bars and concrete matrix based on pullout test data. Good agreement with experimental data and fairly strong generalization capacity were achieved for the two ANN models. Mashrei et al. (Mashrei et al., 2013) applied the BPNN to predict the bond strength of FRP plate adhered to concrete prisms. Results indicated that the proposed model matched better with test results than those existing models. In spite of these successful applications, inherent defect of back-propagation (BP) algorithm needs to be mentioned. During the ANN training, it is inclined to get stuck in local

minimal solution, as demonstrated in Figure 6-1. Such drawback can be attributed to the searching strategy of ANN, which aims to find the optimal solution along the direction of the maximum gradient descent. Thus, if the step size in search is relatively smaller and the starting point which does not locates near the global minima, all the solutions are prone to point to the local minima repeatedly during the training process and cannot jump out of the loop. This model is not capable of generating global minima. Additionally, iterations trapped locally also results in additional cost due to the longer operational time.

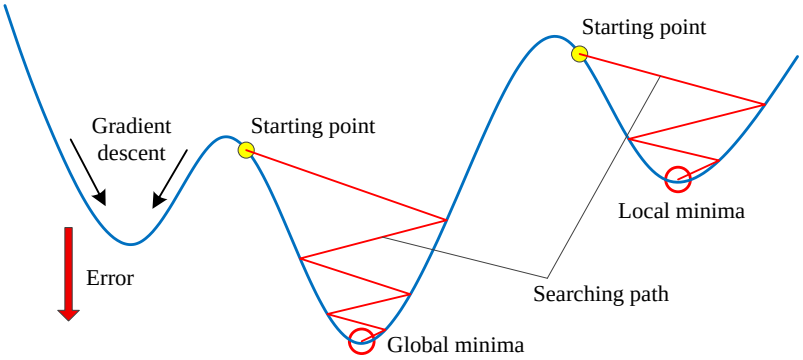

Figure 6-1. Searching strategy of BPNN

To avoid falling into local convergence, genetic algorithm (GA) that provides global stochastic searching ability gets involved to optimize the initial weights and biases of the ANN, helping the ANN to seek out the accurate solution and converge more quickly (Yan and Lin, 2016). GA utilize the evolution process of natural selection to explore more superior solutions for various problems, of which the criteria of judgment could be defined according to different optimization goals. Chandwani et al. (Chandwani et al., 2015) used GA to optimize ANN in modeling the slump of ready mix concrete. Results showed that both accuracy and convergence speed of the ANN-GA model were improved compared to the original ANN model. Irani et al. (Irani and Nasimi, 2011) developed the ANN-GA model for predicting the permeability of the reservoir, and reported that both performance and generalization capability of the hybrid model

presented better than those of the ordinary ANN models. Despite these successful applications of incorporating GA into ANN to assist the training phase, this strategy has yet been used so far for modeling bond strength of GFRP bars in concrete.

Thus, this chapter addresses efforts to combining the strong approximation ability of ANN and global arbitrary searching ability of GA as the hybrid model for bond strength prediction. A database generated from available 157 beam-test specimens in the literature was used to train the proposed models and calibrate the applicability of the prediction. Conventional multi-nonlinear regression (MNLR) method and design equations were used as a comparison to demonstrate the effectiveness of the proposed methods.

6.2. Hybrid Modeling Strategy

6.2.1. Framework of Hybrid Modeling

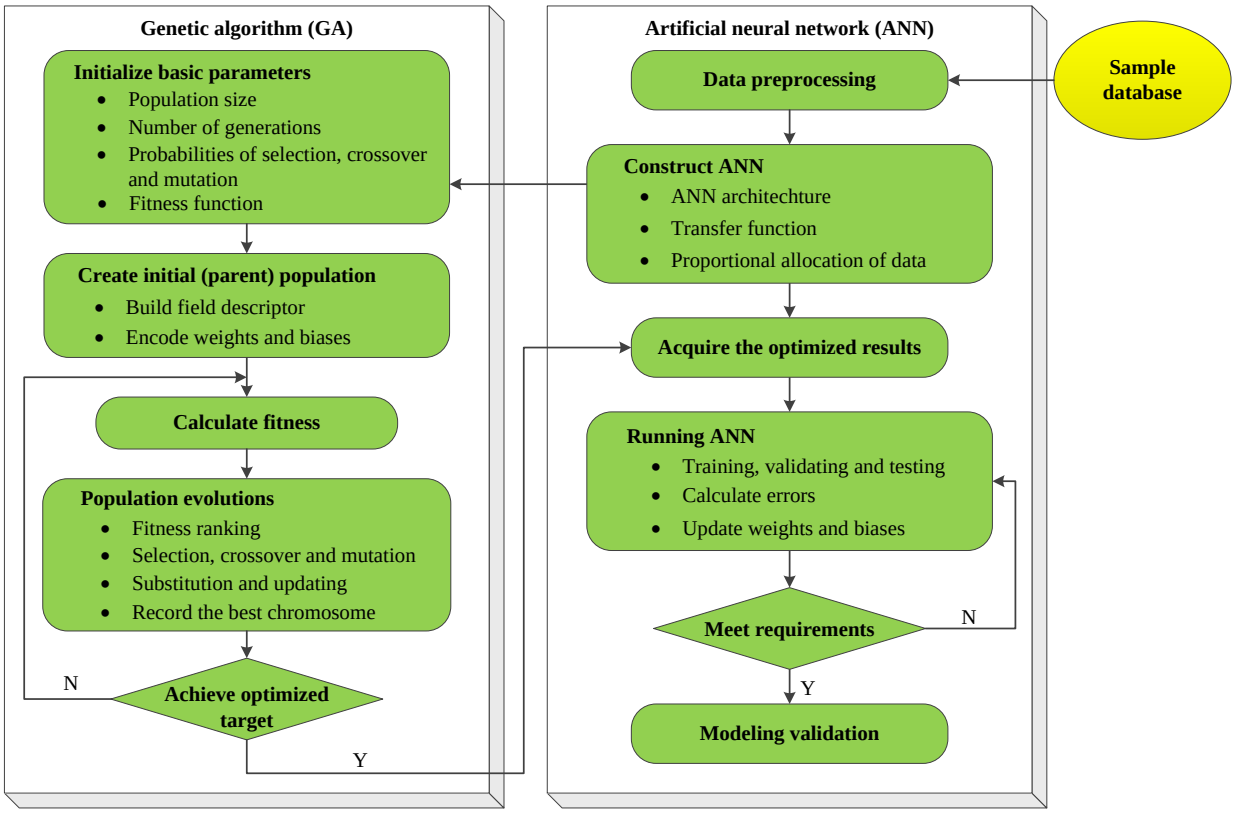

Figure 6-2. Framework of the hybrid modeling strategy

A systematic framework of hybrid modeling for bond strength was proposed, as demonstrated in Figure 6-2. Generally, the strategy is to use ANN to map the relationship between the influencing factors and bond strength and use GA to evolve the initial weights and biases for global minima approximation. First, a database containing the basic factors listed in Table 6-1 and their corresponding bond strengths is created. These data are imported into ANN and normalized into a specific range to be used for network training. Prior to starting GA, the ANN needs to be constructed in advance since the chromosome length in the population is dependent on the network architecture. Some ANN option settings, such as transfer function and proportional allocations of data, can also be set up at this stage. Next, GA is launched to generate and optimize the weights and biases of ANN. Basic parameters in terms of population size, number of generations, probabilities of evolutionary events (i.e. selection, crossover and mutation) are initialized incipiently. Particularly, the fitness is defined as the difference between the predicted and actual values, which is the most critical index during population evolutions. In the following, the weights and biases are first limited within a coding range based on the field descriptor, and then generated randomly and encoded by real numbers, constituting a set of chromosome in the parent population. After that, the fitness of all the chromosomes is calculated. The chromosomes that have better fitness are selected for crossover and mutation to generate new chromosomes that would be more suitable for the problem solution. While those chromosomes that have worse fitness would be replaced by the fitter ones to form a new population for the next evolution. This evolving process keeps repeating until the best fitness is obtained. By this time, the best chromosome involving the best weights and biases is decoded and assigned to the ANN as the initial values for iterations. The ANN follows the normal procedures of training, validating, and testing to adjust weights and biases until the appropriate

solution is found. Toward the end, the final hybrid model can be validated by experimental results or other existing models.

6.2.2. Data Acquisition and Preprocessing

The bond tests are usually classified into two major categories: direct pullout test and beam test. Note that the concrete neighboring the reinforcement is in compression in pullout test, which does not agree with practical situations. On the contrary, the concrete neighboring the reinforcement is in tension in beam tests. It matches well with actual situations and thus, data used for bond strength modeling were collected from the beam tests only. In order to study the general conditions rather than a special scenario, the major failure modes representing the common cases need to be covered when collecting data. A database of 687 specimens was created to investigate the primary failure modes. As shown in Figure 6-3, the pullout and splitting failures account for the majority failure modes, occupying 70.38% and 16.42% respectively. Thus, data derived from these two types of failures are capable of providing a sound basis without loss of generality. Integrating the above principles, the data are collected from the beam tests, and consider pullout and splitting failures. The inputs in the ANN modeling were formatted in terms of bar surface treatment, bar position, bar diameter (d_b), concrete cover to bar diameter ratio (c/d_b), embedment length to bar diameter ratio (l_d/d_b), transverse reinforcement ratio (ρ) and square root of concrete compressive strength ($\sqrt{f_c'}$), while the output is the bond strength (τ_b).

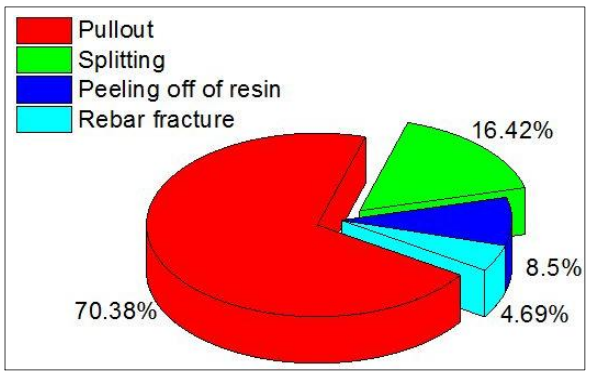

Figure 6-3. Bond failure modes

Considering that the diversity of data helps to enhance the learning ability and generalization ability of the neural network, it is necessary to reduce the similarity of selected data. Thus, the data of both inputs and output are normalized into a range within [-1, 1] or [0, 1]. The algorithm of this normalization is demonstrated in Equation (6-1):

$$x_n = \frac{y_{max}-y_{min}}{x_{max}-x_{min}}(x - x_{min}) + y_{min}, \quad (6\text{-}1)$$

where x_n is the normalized value of variable x; x_{max} and x_{min} are the maximum and minimum of x, respectively; y_{max} and y_{min} are the maximum and minimum of the normalized targets, respectively. For example, when the interval [-1, 1] is used, that is, $y_{max} = 1$ and $y_{min} = -1$. Substituting these values in Equation (6-1) yields:

$$x_n = 2\frac{(x-x_{min})}{x_{max}-x_{min}} - 1. \quad (6\text{-}2)$$

6.2.3. ANN Modeling for Bond Strength

6.2.3.1. Architecture and working principle of ANN

The first step of ANN modeling for bond strength is to determine the network architecture. A typical multi-layer feed-forward neural network is comprised of an input layer, one or more hidden layers and an output layer. Generally, a three-layer network including one hidden layer is enough to solve the most problems, of which the complex nonlinear relationship

could be approximated in accuracy (Bengio and LeCun, 2007; Hornik et al., 1989). In regard to the number of neurons comprising each layer, since the input layer contains the seven independent variables mentioned above, and the output layer corresponds with the bond strength. Thus, as shown in Figure 6-4, a preliminary architecture of the network is determined to be $7-n-1$, where n is the number of neurons in the hidden layer. The remaining problem is to ascertain the number of neurons comprising the hidden layer. It is difficult to define a universal principle that is applicable to general conditions since it is dependent on many factors and variables, such as the complexity of the functions and the number of inputs and outputs (Alshihri et al., 2009). Therefore, the configuration has to be confirmed based on a number of trials.

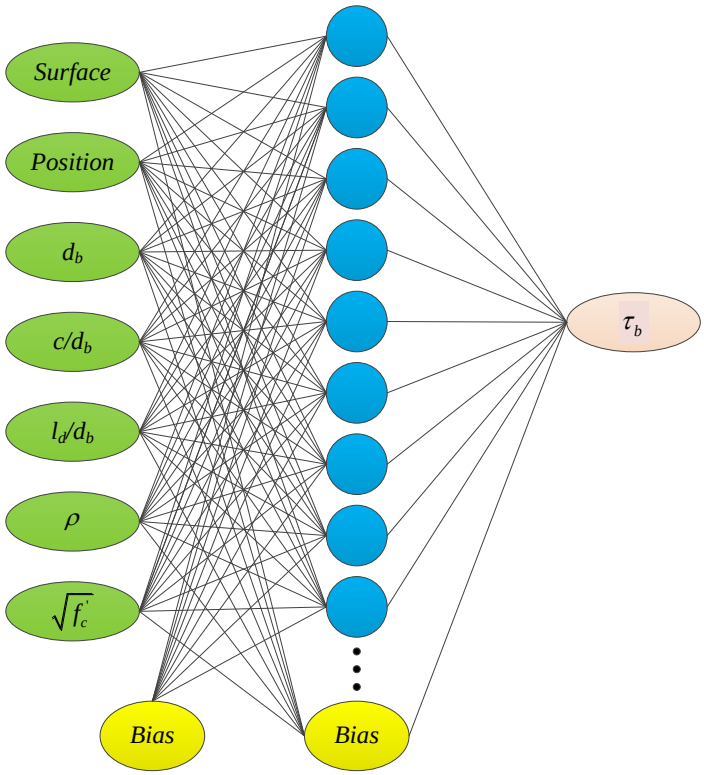

Figure 6-4. Architecture of the ANN model (7-n-1)

To demonstrate the working principle of a multi-layer feed-forward network employed with BP algorithm, a neuron of the hidden layer is taken out to be connected with the inputs and

output, as shown in Figure 6-5. It adopts gradient decent learning to adjust the weights during the training phase, minimizing error between the actual and target outputs.

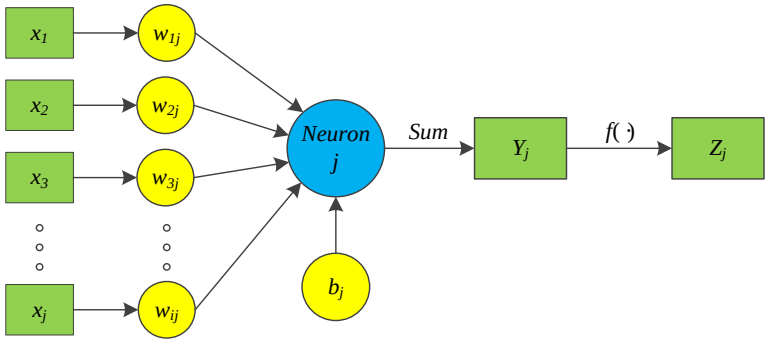

Figure 6-5. Workflow of information transfer

Given a set of inputs $[x_1, x_2, \dots, x_j]$, two basic mathematical operations are conducted successively to solve the final output Z_j. First, the sum of the products of the inputs and their respective weight is added by a bias for each neuron of the hidden layer when information is passing through input layer to the hidden layer, obtaining the receive vector Y_j, as illustrated in Equation (6-3):

$$Y_j = \sum_{i=1}^{n} w_{ij} x_i + b_j, \tag{6-3}$$

where $[w_{1j}, w_{2j}, \dots, w_{ij}]$ is the weight vector of the j^{th} neuron between the input layer and hidden layer, and b_j is the bias of the j^{th} neuron. Next, Y_j is processed by a transfer function $f(\cdot)$ into Z_j as demonstrated in Equation (6-4):

$$Z_j = f(Y_j). \tag{6-4}$$

Thus, consider the specific scenario that the network is used for bond strength modeling, given the architecture is $7 - n - 1$, and the inputs are $X = [X_1, X_2, \dots, X_7]$; then we have the weight matrix evaluating the input layer to the hidden layer should be a n by 7 matrix, which is denoted as W_1; and the weight matrix evaluating the hidden layer to the output layer should be a n by 1 matrix, which is denoted as W_2; the bias vector of the hidden layer should be a n by 1

vector, which is denoted as B_1; and the bias of the output layer should be a 1 by 1 vector, which is denoted as B_2. According to the aforementioned workflow, the receive vector Y_1 and its corresponding output Z_1 from the input layer to the hidden layer are:

$$Y_1 = W_1^T X + B_1, \tag{6-5}$$

$$Z_1 = f_1(Y_1) = f_1(W_1^T X + B_1). \tag{6-6}$$

The receive vector Y_2 and its corresponding output Z_2 from the hidden layer to the output layer are:

$$Y_2 = W_2^T Z_1 + B_2 = W_2^T (f_1(W_1^T X + B_1)) + B_2, \tag{6-7}$$

$$Z_2 = f_2(Y_2) = f_2(W_2^T (f_1(W_1^T X + B_1)) + B_2), \tag{6-8}$$

where, Z_2 is the predicted bond strength of interest.

6.2.3.2. Training parameter settings

Reasonably setting training parameters, such as learning rate, activation function, and training algorithm, is of great importance on enhancing predicted ability of the network. The best parameters seem to vary from different problems. A number of trials have to be conducted to check the performance of different settings. However, there are still some principles that can be utilized to guide the parameter adjustment process. The two most important parameters for network training are demonstrated in the following.

The learning rate is used to control the speed of learning progress during the adjustment of weights and biases. Although a high learning rate speeds up the convergence at the outset, unexpected oscillations may be induced when the solution is close to the optimal point at a later stage, and consequently lead to no convergence. On the other hand, a low learning rate increases the number of steps during the searching of desired error level.

As the primary characteristic element of an ANN, the activation function produces significant influence on the predicted ability in various problems. Nonlinear logistic (hyperbolic tangent sigmoid and log-sigmoid) and linear activation functions comprise the major types of functions applied on all neurons of the network, except the input neurons, whose values assigned those given independent variables. The selection of these activation functions is dependent on the degrees of nonlinearity of the problem solved and the diversity of the training samples. Normally, by setting the hyperbolic tangent sigmoid activation function applying on the hidden neurons and the linear activation function applying on the output neuron is taken as the first choice during trial process.

The selection of the training algorithm depends on many factors, including the scale of the network, complexity of the problem, and error goal (Beale et al., 2012). As one type of BP algorithm, Levenberg–Marquardt algorithm (LMA) is regarded as the preferred choice due to its fast learning ability although it may use more memory resources than other algorithms (Suratgar et al., 2005). Particularly, it performs well when a middle-size neural network is employed.

6.2.3.3. Performance assessment indices

The performance of ANN training is usually validated through several statistical indices in terms of mean absolute error (MAE) and root mean square error (RMSE), and Pearson's correlation coefficient (R-value), as demonstrated through Equations. (6-9) to (6-11):

$$MAE = \frac{1}{N}\sum_{i=1}^{N}|T_i - P_i|, \tag{6-9}$$

$$RMSE = \sqrt{\frac{1}{N}\sum_{i=1}^{N}(T_i - P_i)^2}, \tag{6-10}$$

$$R = \frac{\sum_{i=1}^{N}(T_i-\bar{T})(P_i-\bar{P})}{\sum_{i=1}^{N}(T_i-\bar{T})^2\sum_{i=1}^{N}(P_i-\bar{P})^2}, \tag{6-11}$$

where T_i and P_i are the target and predicted values, respectively; $\bar{T}$ and $\bar{P}$ are the mean of the target and predicted values, respectively; and N is the total number of samples. MAE demonstrates the residual error between the target values and predicted values for each data set; RMSE demonstrates the square root of average residual error between the target values and predicted values for each data set. For the two indices, the smaller value indicates better performance of the ANN model and vice versus. R-value is used for investigate the linear correlation between the target and predicted values. The R-value near one indicates the robustness of the ANN model in bond strength prediction, and the slope of the fitting line is close to forty-five degree.

6.2.4. ANN Optimized by GA

6.2.4.1. Synthesized working principle of ANN-GA

Conventional BP algorithm has inherent drawback, of which the network is prone to be trapped in local minima. GA algorithm, therefore, is introduced due to its favorable feature of global arbitrary searching ability to evolve the initial weights and biases of ANN prior to network training. This methodology utilizes the principle of survival of the fittest in biology, seeking suitable solution in global level and detecting potential better solutions through evolutionary operations applied on the individuals in the population (Michalewicz, 2013). For the purpose of combining GA with ANN, an individual containing the information of weights and biases is expressed in the form of a chromosome, and the information exchange between the ANN and GA is implemented through the operations of encoding and decoding chromosome. As shown in Figure 6-6, a group of weighs and biases $[W_1^i, B_1^i]$ and $[W_2^i, B_2^i]$ are encoded to form a number of chromosomes, where *i* means the i^{th} chromosome, and the length of each chromosome is dependent on the architecture of the network.

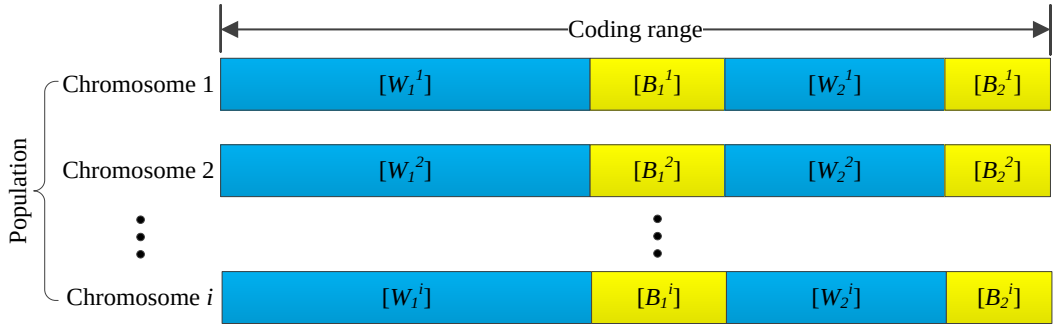

Figure 6-6. Demonstration of constituents of chromosomes

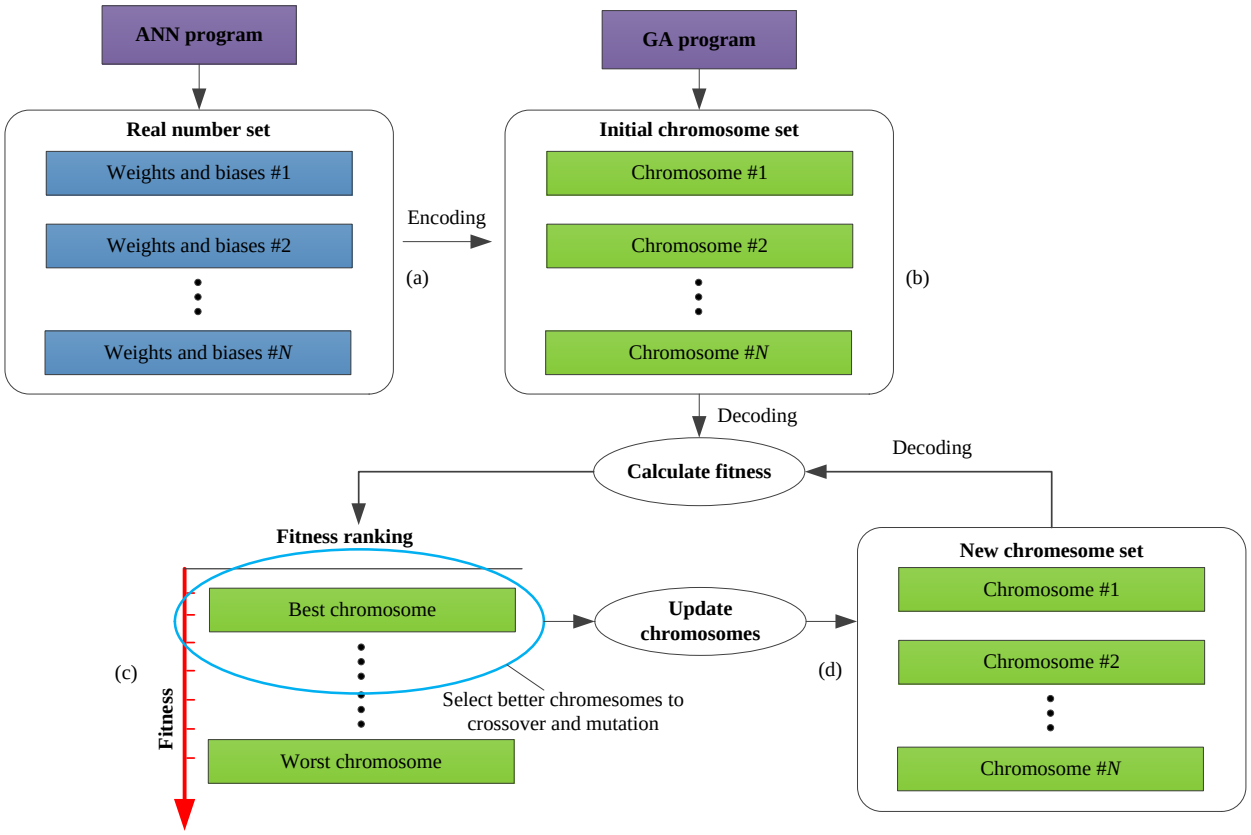

Figure 6-7. Synthesis working principle

The synthesis working principle is demonstrated in Figure 6-7. Basically, each time of evolution by GA needs to invoke ANN to calculate the fitness of the chromosome. Here for convenience, the fitness is defined as the norm of differences between the predicted output vector and actual output vector. Thus, the chromosome with smaller fitness demonstrates smaller

difference. Note that the individuals exhibiting larger fitness hold larger probabilities to participate in the evolutionary operations and thus, it is necessary to sort all the individuals according to the reciprocals of the calculated fitness.

At first, a set of random weights and biases are generated in ANN program and then encoded into the chromosomes, as shown in Figure 6-7 (a) and (b). To evaluate the chromosome performance in terms of predicted accuracy by using the initial weights and biases for the starting point of the network iterations, all the chromosomes are decoded to calculate their respective fitness. According to aforementioned ranking principle, the chromosome with the smaller fitness demonstrates better performance, and those superior chromosomes are selected under a predefined probability to participate in the subsequent evolutions in terms of crossover and mutations, as shown in Figure 6-7 (c). Thereafter, those worse chromosomes in the former population are substituted for those better ones, forming a new superior population for the next evolution loop, as shown in Figure 6-7 (d). The new chromosome set follows the same procedures to the next evolution loop, and those excellent chromosomes are filtered out to evolve to be more advanced ones.

6.2.4.2. Parameters settings of GA

GA aims to find out an optimal solution based on successive population evolutions, and the key parameters of GA, such as the population size, the maximum number of generations, the probability evolutionary event, directly influence the evolutionary results.

The size of the population is dependent on the number of individuals included. Basically, the more individuals the population involves, the more opportunities to find out the more superior solutions. On the other hand, large quantities of individuals lead to the heavy computation cost and long time of evolutions. Thus, it is necessary to achieve a compromise

between the accuracy and efficiency. The maximum number of generations represents the total iterations, which is dependent on the fitness variations. When the fitness remains constant or decrease a little as the number of generation increases, the demarcation point can be taken as an appropriate value of the maximum number of generations. Throughout the evolutionary operations in terms of selection, crossover and mutation, the probabilities of these events need to be preassigned. Generally, the probability of selection is set to be a higher value (greater than 80%), promising most excellent individuals can be selected to evolve; the probability of mutation is usually set to be a smaller value which coincides with the phenomenon in reality; and the probability of crossover is set in between the other events.

6.2.4.3. Fitness function

The fitness is the most important index to assess the superiority of an individual, which is defined as the norm of differences between the predicted output vector and actual output vector. For ease of calculation, the fitness is programmed as a function in terms of a set of independent variables related to the network structure and training data, and has a return value of the norm of those forecast errors. The variables involved in the fitness function are demonstrated in Table 6-2.

Table 6-2. Variables involved in the fitness function

Returned value	Independent variable	Note
	IND	Involving weights and biases
	inputNum	Node number of the input layer
	hiddenNum	Node number of the hidden layer
	outputNum	Node number of the output layer
	net	Pointer of the network
	inputNorm	Input data for network training
	outputNorm	Output data for network training
Error		Norm of difference between predicted and output values

The independent variable IND is defined as a vector containing the values of W_1, B_1, W_2, B_2 in sequence. For a $7-n-1$ ANN, the length of IND is $7n+2n+1$. The independent variable net is a structure type pointer containing all information of the network, and all the operations of the network, such as extracting or assigning weights and biases, are implemented through invoking this pointer. In addition, it is worth noting that both input data and output data used for network training are the normalized values based on the algorithm illustrated in Section 2.2. Thus, in addition to the simulation and prediction operations of the network, the error returned of the fitness function is also a normalized value. From this, as long as the optimized weights and biases are obtained from GA, they are passed into the current network to calculate the forecast error, and then back-transmitted to GA as the judgement for population evolutions.

6.3. Bond Strength Prediction by Other Methods

6.3.1. Multi-nonlinear Regression

Conventional regression method is a convenient and effective statistical way that helps to model the multivariate problems with either linear or nonlinear relationship between a response variable and a set of regressor variables, fitting the observed data using an explicit mathematical formula. Generally, multi-linear regression and multi-nonlinear regression comprise the major types of function approximation approaches, and are adopted frequently in the past work regarding bond strength modeling. Golafshani et al. used multi-linear regression to model the bond strength between GFRP bar and concrete (Golafshani et al., 2015), and Kim et al. used the multi-nonlinear regression to fit the bond strength between deformed steel rebar and recycled coarse aggregate concrete (Kim et al., 2015).

In this study, considering that the bond strength of GFRP bar and concrete can be normalized in the form of $\tau_b/\sqrt{f_c'}$ (ACI Committee, 2006; Canadian Standards Association, 2002; Quayyum, 2010) when evaluating the influences of those independent variables and thus, the multi-nonlinear regression (MNLR) model matches condition for the bond strength modeling, as illustrated in Equation (6-12):

$$\tau_b = (ASurf + BPos + Cd_b + Dc/d_b + El_d/d_b + F\rho + G)\sqrt{f_c'}, \quad (6\text{-}12)$$

where the fitting coefficients A, B, C, D, E, F, G are determined using the least square method to minimize the sum of squared errors, an error being the difference between an actual value and the forecast value provided by the MNLR model (Stigler, 1981).

6.3.2. Design Equations

National and international design specifications to predict the bond strength of GFRP bars to concrete are summarized in Table 6-3. Basically, the key factors, such as the concrete strength, concrete cover, bar diameter and bar position are covered for all these guidelines. Embedment length is taken into account only in ACI 440.1R-06 for bond strength prediction. Differently, the influences of more additional information on bond strength, such as transverse reinforcement ratio, bar surface treatment type, are covered in the Canadian or Japanese codes, which are not involved in ACI 440.1R-06.

In addition, Ametrano reported that the bond strength predicted by ACI 440.1R-06, CSA S806-02, CSA S6-06 and JSCE design recommendations exhibited conservative compared to experimental results (Ametrano, 2011). These design equations are used for comparisons with the developed ANN-GA model and MNLR model.

Table 6-3. Bond strength calculations by design standards

Design standards	Design equations		Notes
ACI 440.1R-06 (ACI Committee, 2006)	$\tau_b = \sqrt{f_c'}(0.332 + 0.025\frac{c}{d_b} + 8.3\frac{d_b}{l_d})$	(6-13)	d_{cs}: the smaller of the distance from concrete surface to the center of the bar or two-thirds the spacing of the bars being developed (mm);
CSA S806-02 (Canadian Standards Association, 2002)	$\tau_b = \frac{d_{cs}\sqrt{f_c'}}{1.15(K_1K_2K_3K_4K_5)\pi d_b}$	(6-14)	K_1: bar location factor; K_2: concrete density factor; K_3: bar size factor; K_4: bar fiber factor; K_5: bar surface profile factor.
CSA S6-06 (Canadian Standards Association, 2006)	$\tau_b = \frac{f_{cr}(d_{cs}+K_{tr}E_{FRP}/E_s)}{0.45\pi d_b K_1 K_5}$	(6-15)	f_{cr}: the cracking strength of concrete (MPa); K_{tr}: transverse reinforcement index (mm); E_{FRP}: elastic modulus of FRP bar (MPa); E_{s}: elastic modulus of steel (MPa);
JSCE (Machida and Uomoto, 1997)	$\tau_b = f_{bod}/\alpha_1$	(6-16)	f_{bod}: designed bond strength of concrete; α_1: a confinement modification factor.

6.4. Modeling Applications

6.4.1. Database Creation and Data Preprocessing

A database consisting of 157 beam-test specimens was created based on the past work (Achillides and Pilakoutas, 2004; Benmokrane and Tighiouart, 1996; Daniali, 1990; Ehsani et al., 1993; Faza and GangaRao, 1991; Kanakubu et al., 1993; Shield et al., 1999; Tighiouart et al., 1998). The statistical characteristics of those collected data are summarized in Table 6-4, in which the bar surface treatments were quantified as 1, 2, 3, representing helical lugged, spiral wrapped, sand coated, respectively; and bar position of bottom and top are quantified as 1 and 2, respectively.

Table 6-4. Statistical characteristics of influencing factors on bond strength

Variables	Minimum	Maximum	Mean	Standard deviations
$Surf$	1.00	3.00	1.71	0.64
Pos	1.00	2.00	1.25	0.44
d_b	9.53	28.70	19.68	5.52
c/d_b	1.00	16.00	3.13	2.49
l_d/d_b	3.54	41.88	15.81	8.92
$\sqrt{f_c'}$	5.25	8.08	5.97	0.72
ρ	0	0.08	0.02	0.02
τ_b	2.40	24.52	7.76	4.55

In this study, Matlab® was used for data preprocessing. To reduce data similarity, the records derived from the database were disordered and then randomly selected to fill the data set, of which the percentage was preassigned to be 60% records for training set, 20% for the validating set and 20% for the testing set. Note that these disrupted data will be used for modeling bond strength by other methods using the corresponding value for comparisons. Thus, the new orders after disturbance need to be recorded additionally. This can be conveniently implemented using the function provided by the ANN toolbox viz., 'dividevec' function, which is capable of returning multiple structure type of the arrays in terms of training samples, validating samples and testing samples. In addition, according to Equation (6-2), all of the data are normalized within the interval [-1, 1].

6.4.2. Modeling Implementations

The architecture of the ANN model is determined to be 7-15-1, of which the size of hidden layer adopting fifteen was proved to be robust in prediction after a number of trials. To optimize the initial weights and biases of ANN with GA, an appropriate number of the maximum number of generations was first investigated through the variations of the best fitness, as demonstrated in Figure 6-8. It can be seen that the best fitness of the chromosome kept

decreasing as the evolution increased until the threshold reached at eighty, and then leveled off toward the end. It indicates that keeping increasing the number of evolutions after eighty does not improve the predicted accuracy anymore. Thus, it is reasonable to take this threshold as the maximum number of generations. To be conservative, the final value is set to be one hundred.

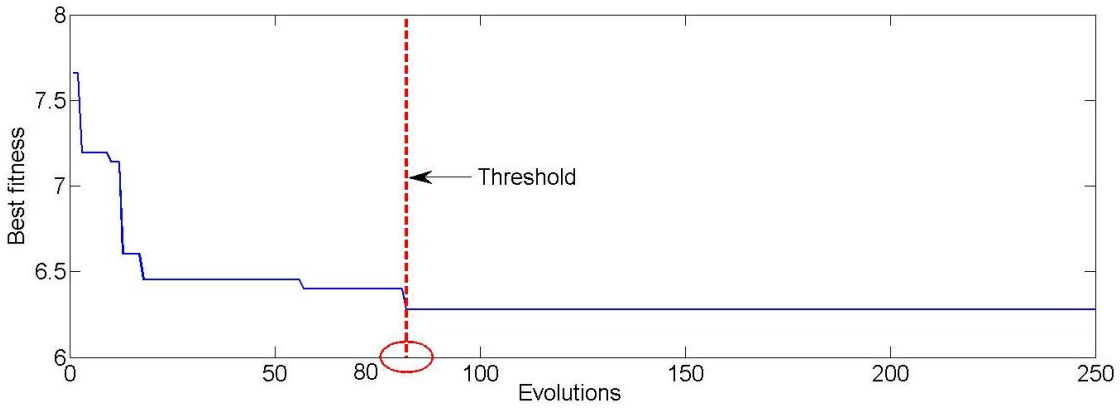

Figure 6-8. Variations of best fitness

In addition, the population consisting of one hundred individuals yields good balance between the accuracy and efficiency on searching the global optimal solution for ANN. The chromosome length of each individual is computed to be 136 according to the architecture of the network (7-15-1). Other parameters of GA were determined based on the principles discussed in section 2.4.2, as summarized in Table 6-5.

Table 6-5. Parameter initializations for GA

Parameters	Values
Population size	100
Chromosome length	136
Maximum number of generations	100
Generation gap	0.9
Crossover probability	0.7
Mutation probability	0.1

Through the optimization of GA, the initial weights and biases of ANN are shown through Equations. (6-17) through (6-20):

$$W_1 = \begin{pmatrix} 0.2962 & -2.3830 & -2.5728 & 0.7975 & -1.1801 & -0.2326 & -0.3091 \\ 0.5035 & 2.4259 & 1.2647 & 1.4374 & 1.2245 & -0.0443 & -0.6801 \\ -1.3899 & -1.8186 & -1.0717 & 0.5119 & 0.6560 & 0.0785 & 1.1670 \\ -0.7095 & 0.2916 & 0.1993 & 1.5352 & -1.5847 & -0.2225 & -1.8852 \\ 1.1773 & -1.6736 & -0.0832 & 0.4004 & 1.5946 & 1.9657 & 1.7593 \\ 0.4197 & 0.5660 & 0.2696 & 0.7513 & 1.1109 & -0.5742 & -0.6710 \\ -0.5040 & -1.0974 & -0.5146 & -0.7092 & 1.2534 & 0.6920 & 0.1325 \\ 0.8403 & -1.2781 & -0.3044 & 0.2560 & 0.4661 & 0.6395 & -0.9856 \\ -0.1101 & -0.1569 & -0.4633 & 1.2631 & -2.0150 & -0.5176 & -1.0738 \\ 0.3133 & 1.4548 & 0.9639 & 1.2551 & 0.0611 & -1.4437 & -0.7686 \\ -1.1654 & 1.2042 & -1.1584 & 1.0507 & -1.1801 & 0.0428 & -1.5924 \\ -0.0244 & -1.1790 & 1.5635 & -0.2422 & -1.2616 & -0.3862 & 0.4054 \\ 0.9327 & 0.5101 & -1.6541 & 0.8513 & 1.1918 & 0.5940 & -1.6972 \\ -0.3995 & -0.3253 & 0.9972 & -2.0682 & 0.3863 & 0.3458 & 0.0372 \\ -0.4007 & 0.4148 & -1.0274 & 0.7343 & 1.4261 & -0.5746 & -1.9444 \end{pmatrix}, \quad (6\text{-}17)$$

$$B_1{}^T = \begin{pmatrix} 1.0087 & -0.4877 & -1.1930 & -1.2309 & 0.5074 & -0.0250 & -1.2035 & 2.0636 \\ -2.4386 & -0.2089 & 0.5468 & 1.6455 & 1.0693 & -1.5222 & -0.5356 & \end{pmatrix}, \quad (6\text{-}18)$$

$$W_2 = \begin{pmatrix} 0.7860 & 0.8990 & -0.8420 & -0.5588 & 0.1552 & -1.1721 & 1.2482 & 0.3092 \\ 1.0962 & 0.7895 & 0.2705 & 0.6490 & -0.4934 & -0.3986 & 0.2998 & \end{pmatrix}, \quad (6\text{-}19)$$

$$B_2 = (-0.5023). \quad (6\text{-}20)$$

In addition, the MNLR model of bond strength prediction is illustrated in Equation. (6-21):

$$\tau_b = (0.2811\mathrm{Surf} - 0.0695\mathrm{Pos} - 0.0210d_b - 0.0075c/d_b - 0.0755l_d/d_b - 4.2048\rho + 2.5810)\sqrt{f'_c}. \quad (6\text{-}21)$$

6.4.3. Performance Assessment

Generally, the performance of the ANN-GA model was assessed through two steps: first, by comparing with the original ANN model to validate its progress by hybrid modeling; secondly, by comparing with MNLR model and design equations to validate its superiority among other forecasting methods.

Using the same data set, the comparison of the ANN-GA model and the original ANN model is illustrated in Figure 6-9, in which the ratio of test bond strength over predicted bond strength was displayed as the measurement index, and the horizontal line located at the vertical coordinate of one was taken as the target line. Basically, the closer distance from the target line

demonstrates the more accurate predictions. It is clear that developed ANN-GA model exhibited lower discreteness than the ANN model. The variations of the ratios of the ANN-GA were limited within the interval of [0.8, 1.2], while the ANN model within [0.2, 1.8] for most records. Meanwhile, the ratios of the ANN-GA model oscillated slightly around the target line, indicating that the predicted values differed little from the test values and gathered near one. Differently, more intensive oscillation around the target line was observed in the ANN model, denoting relatively larger differences between the predicted values and test values. The absolute value of maximum deviation between the test value and predicted value was observed to be 18% in the ANN-GA model, while 81% in the ANN model. Thus, it can be concluded that the accuracy of the ANN-GA model was significantly improved after the optimization of initial weights and biases.

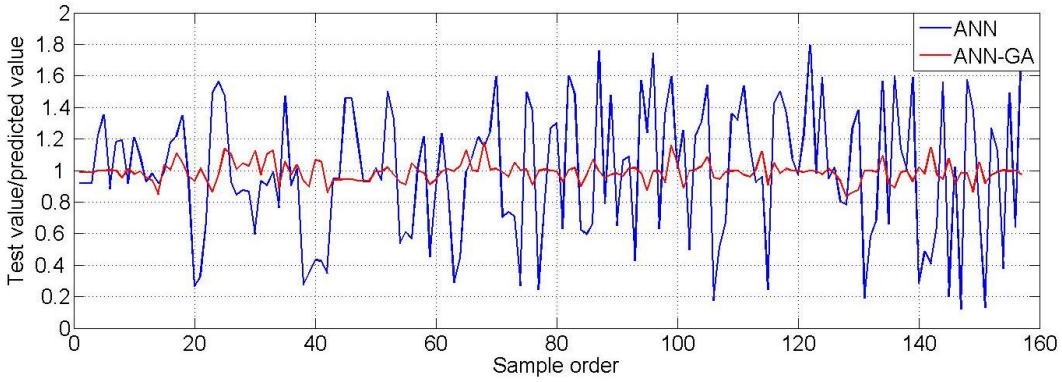

Figure 6-9. Comparisons of ANN-GA and ANN models

The linear regressions of the predicted and target values are calculated using Pearson's correlation coefficient (R) according to Equation. (6-11), as illustrated in Figure 6-10. Basically, the more closely the R-value approaches to one, the better the prediction performs. It was observed that R-value was equal to 0.97, 0.92, 0.92 and 0.94 for the training set, validating set, testing set and all data, respectively, and the slopes of all fitting curves were almost equal to forty-five degrees, indicating the hybrid ANN-GA model fit well with the experimental results.

Specifically, the R-value of the training data denotes excellent training performance of the optimized network on exploring the inherent nonlinear relationship between the inputs and output; the R-value of the validating data denotes the strong ability for preventing the network from overfitting; and the R-value of the testing data denotes the generalization ability to predict a new set of data in accuracy.

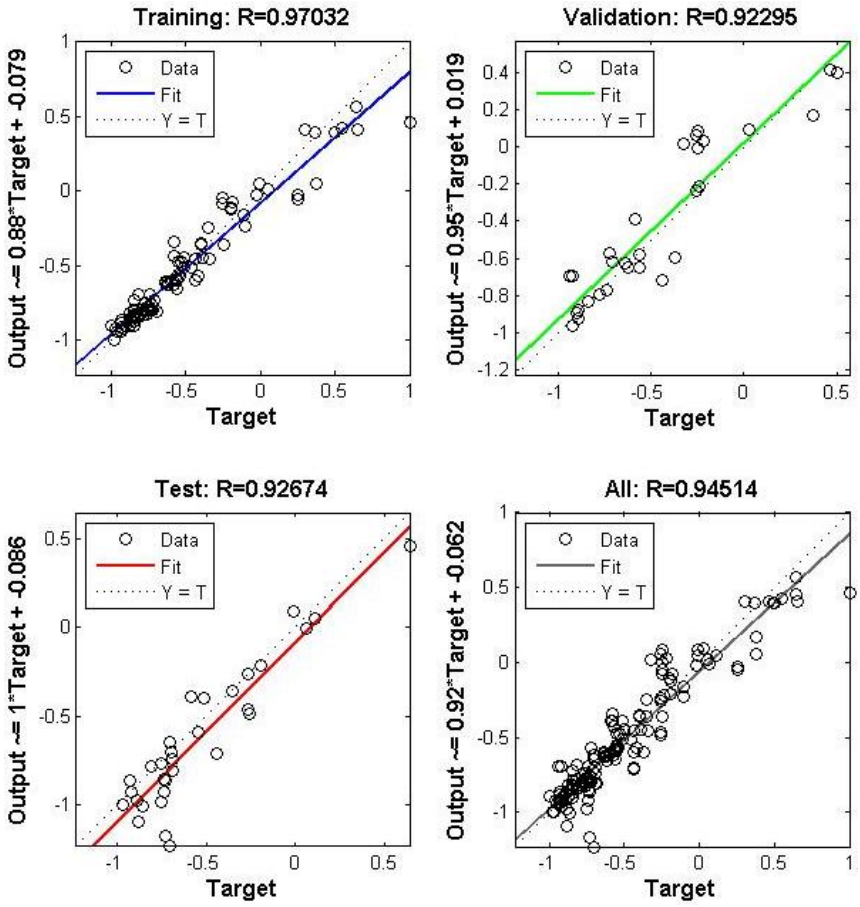

Figure 6-10. Linear regressions of predictions and targets

In the following, the performances of bond strength modeled by other different methods are compared in detail. Figure 6-11 displays the comparisons of the experimental and predicted bond strength with regard to data samples for different models. Generally, it can be seen that the bond strengths of the ANN-GA model were the closest to the experimental results among all models, while those of the CSA S6-06 model exhibited the largest derivations. ACI 440.1R-06

performed better in accuracy, ranking the second place in all models. The MNLR model manifested intensive oscillations in local sections, where relatively larger differences were observed therein. In addition, it is worth noting that except for CSA S6-06 showing excessive predictions, the other design equations provide a conservative modeling method for the bond strength, of which the predicted values lay below the experimental results.

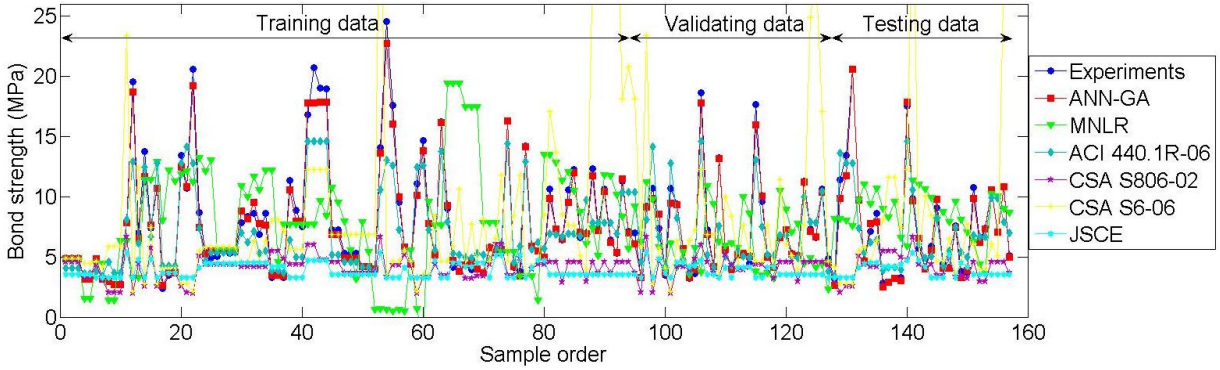

Figure 6-11. Bond strength predictions of different modeling methods

According to Equations (6-9), (6-10) and (6-11), all of the data samples randomly divided into the training set, validating set and testing set are evaluated using MAE, RMSE and R-value, as shown in Figure 6-12, Figure 6-13, and Figure 6-14, respectively. For the training data, the MAEs of the ANN-GA, MNLR, ACI 440.1R-06, CSA S806-02, CSA S6-06 and JSCE models were observed to be 0.66, 3.34, 2.12, 4.13, 8.04 and 6.17, respectively. This indicates that the ANN-GA model demonstrates the most robust ability for data mining. Meanwhile, the same trends of MAEs were also found in the validating data, testing data and all data, confirming the superiority of the ANN-GA modeling method in preventing overfitting, generalization ability and comprehensive ability, respectively. Moreover, note that the MAEs of ACI 440.1R-06 model were observed as 2.12, 2.44, 2.41 and 2.23 for the training data, validating data, testing data and all data, respectively, which all displayed smaller values than the other design models for the same data set. This implies that the bond strength predicted by the ACI code suggests smaller

deviations from the experimental results. Similarly, the RMSEs of the ANN-GA, MNLR, ACI 440.1R-06, CSA S806-02, CSA S6-06 and JSCE models were 1.02, 4.11, 3.08, 5.15, 9.17 and 7.12, respectively for the training data. Also, the same varying patterns of these statistical values were also found in other data sets. The R-values of the ANN-GA model were in accordance with the results shown in Figure 6-10, which were all bigger in contrast to other models for the same data set. Thus, from the above statistical analyses, it can be concluded that the ANN-GA method exhibits more powerful function on exploring the complex relationship between those independent variables and the bond strength than other modeling methods.

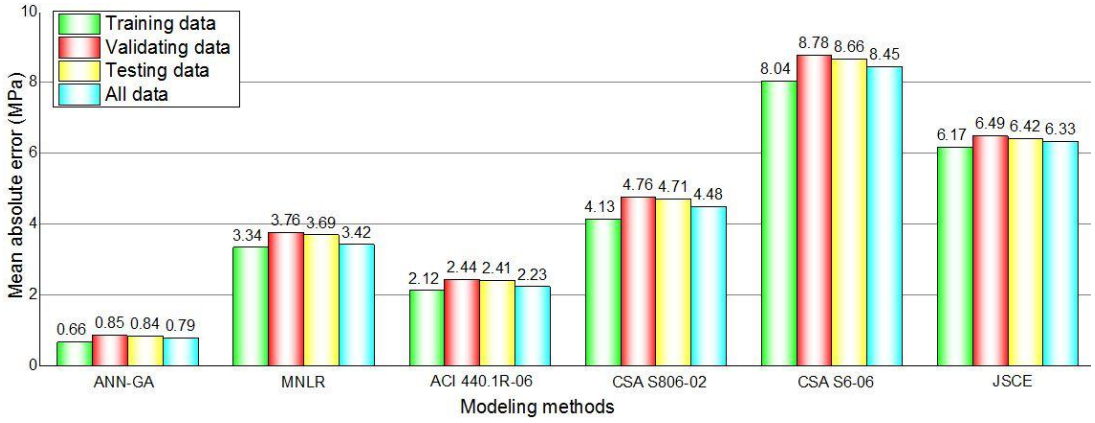

Figure 6-12. Mean absolute errors (MAEs) of different modeling methods

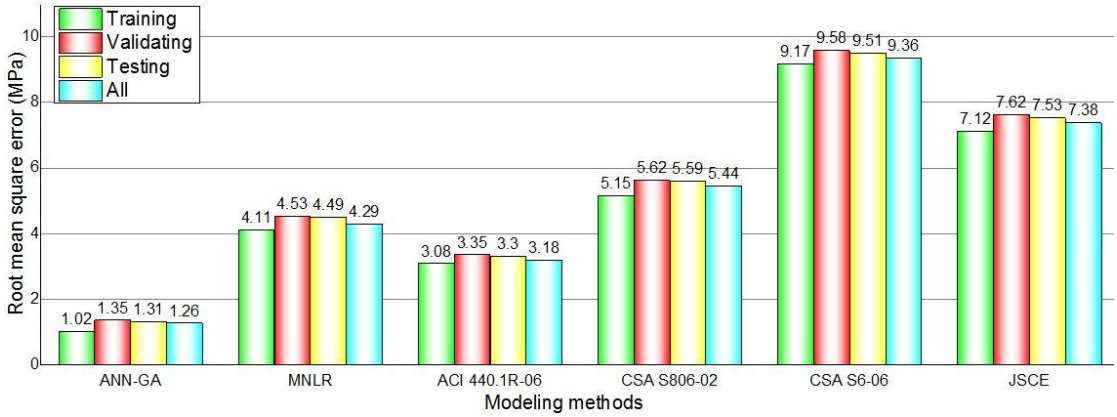

Figure 6-13. Root mean square errors (RMSEs) of different modeling methods

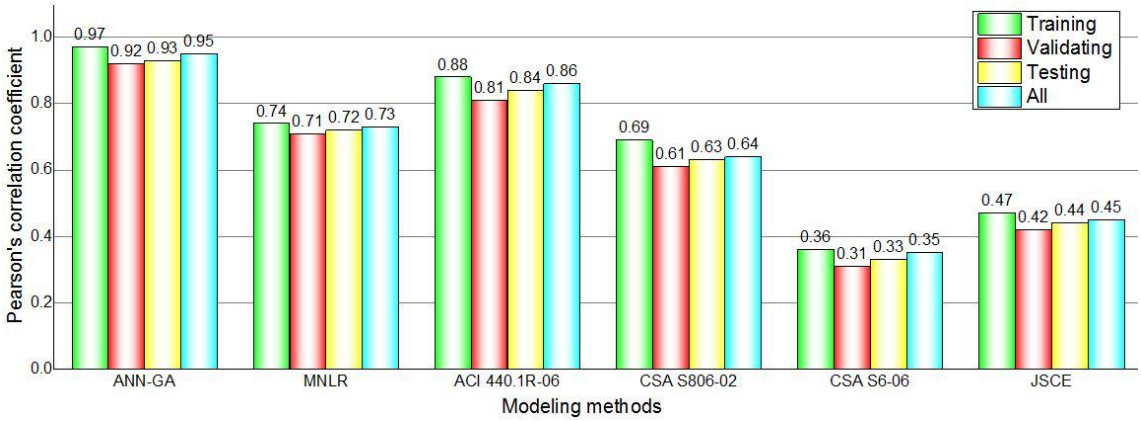

Figure 6-14. Pearson's correlation coefficients (R-values) of different modeling methods

6.5. Conclusions

This chapter introduced a general framework of the hybrid modeling strategy using ANN and GA to predict the bond strength of GFRP bars to concrete. The conceptual design consisted of data processing, modeling methodology and implementation, as well as assessment methods. The complete procedures of the hybrid modeling was demonstrated through an application, of which the experimental results in the literature were used to validate its accuracy, while the comparison to existing MNLR model and design equations further confirms the effectiveness of the proposed method. Specifically, the following conclusions can be drawn:

(1) The essence of the hybrid ANN and GA is to use encoding and decoding the chromosome to implement the information exchange between different algorithms. The optimal number of population evolutions is determined through tracking the variations of the best fitness, and thus it is viable way to optimize the initial weights and biases in the ANN algorithm, thereby yielding a good tradeoff between simplicity and efficiency.

(2) The developed ANN-GA model provides the higher accuracy in bond strength prediction as compared to the conventional ANN model, of which the ratios of test and predicted values were reduced from the interval of [0.2, 1.8] to the interval of [0.8, 1.2], displaying less

scatter in the new model. The largest R-values observed in the ANN-GA model for all sample data sets also confirm the better agreement with experimental results than the other models. Moreover, the ANN-GA model yield the smaller errors in terms of MAE and RMSE for the training data, validating data, and testing data when compared with MNLR model and design equations, thereby more robust for simulation, overfitting prevention, generalization and comprehensiveness.

(3) The bond strength predicted by ACI 440.1R-06 better matches with experimental data than those predicted by other design codes/specifications (Canadian and Japanese codes). It is partially because the embedment length is taken into account only in ACI 440.1R-06 for bond strength prediction. The inverse relation between the bond strength and embedment length cannot be reflected in Canadian and Japanese codes. On the other hand, since the concrete confinement provided by transverse reinforcement was considered only in CSA S6-06 and JSCE, while not covered in ACI 440.1R-06 and CSA S806-02. The diversity of the collected data may lead to the deviation of bond strength prediction. In this respect, more experiments need to be conducted to investigate the influences of those factors that affect bond strength.

6.6. References

Achillides, Z., and Pilakoutas, K. (2004). Bond behavior of fiber reinforced polymer bars under direct pullout conditions. Journal of Composites for Construction, 8(2), 173-181.

ACI Committee. (2006). Guide for the design and construction of structural concrete reinforced with FRP bars. ACI 440.1 R, 6.

Alshihri, M. M., Azmy, A. M., and El-Bisy, M. S. (2009). Neural networks for predicting compressive strength of structural light weight concrete. Construction and Building Materials, 23(6), 2214-2219.

Ametrano, D. (2011). Bond characteristics of glass fibre reinforced polymer bars embedded in high performance and ultra-high performance concrete. Ryerson University, Toronto, Ontario, Canada, 1-132.

Beale, M., Hagan, M., and Demuth, H. (2012). Neural Network Toolbox. User's Guide 2012a. The MathWorks. Inc., Natick, Mass.

Bengio, Y., and LeCun, Y. (2007). Scaling learning algorithms towards AI. Large-scale kernel machines, 34(5).

Benmokrane, B., and Tighiouart, B. (1996). Bond strength and load distribution of composite GFRP reinforcing bars in concrete. ACI Materials Journal, 93(3).

Canadian Standards Association. (2002). Design and construction of building components with fibre-reinforced polymers: Canadian Standards Association.

Canadian Standards Association. (2006). Canadian highway bridge design code: Canadian Standards Association.

Chandwani, V., Agrawal, V., and Nagar, R. (2015). Modeling slump of ready mix concrete using genetic algorithms assisted training of artificial neural networks. Expert Systems with Applications, 42(2), 885-893.

Dahou, Z., Sbarta ï, Z. M., Castel, A., and Ghomari, F. (2009). Artificial neural network model for steel–concrete bond prediction. Engineering Structures, 31(8), 1724-1733.

Daniali, S. (1990). Bond strength of fiber reinforced plastic bars in concrete. Paper presented at the Serviceability and Durability of Construction Materials.

Ehsani, M., Saadatmanesh, H., and Tao, S. (1993). Bond of GFRP rebars to ordinary-strength concrete. ACI Special Publication, 138.

Faza, S. S., and GangaRao, H. V. (1991). Bending and bond behavior of concrete beams reinforced with plastic rebars. Transportation Research Record(1290).

Golafshani, E., Rahai, A., and Sebt, M. (2015). Artificial neural network and genetic programming for predicting the bond strength of GFRP bars in concrete. Materials and Structures, 48(5), 1581-1602.

Hornik, K., Stinchcombe, M., and White, H. (1989). Multilayer feedforward networks are universal approximators. Neural networks, 2(5), 359-366.

Irani, R., and Nasimi, R. (2011). Evolving neural network using real coded genetic algorithm for permeability estimation of the reservoir. Expert Systems with Applications, 38(8), 9862-9866.

Kanakubu, T., Yonemaru, K., Fukuyama, H., Fujisawa, M., and Sonobe, Y. (1993). Bond performance of concrete members reinforced with FRP bars. ACI Special Publication, 138.

Kim, S.-W., Yun, H.-D., Park, W.-S., and Jang, Y.-I. (2015). Bond strength prediction for deformed steel rebar embedded in recycled coarse aggregate concrete. Materials & Design, 83, 257-269.

Machida, A., and Uomoto, T. (1997). Recommendation for design and construction of concrete structures using continuous fiber reinforcing materials (Vol. 23): Research Committee on Continuous Fiber Reinforcing Materials, Japan Society of Civil Engineers.

Mashrei, M. A., Seracino, R., and Rahman, M. (2013). Application of artificial neural networks to predict the bond strength of FRP-to-concrete joints. Construction and Building Materials, 40, 812-821.

Masmoudi, A., Masmoudi, R., and Ouezdou, M. B. (2010). Thermal effects on GFRP rebars: experimental study and analytical analysis. Materials and Structures, 43(6), 775-788.

Mazaheripour, H., Barros, J. A., Sena-Cruz, J., Pepe, M., and Martinelli, E. (2013). Experimental study on bond performance of GFRP bars in self-compacting steel fiber reinforced concrete. Composite Structures, 95, 202-212.

Michalewicz, Z. (2013). Genetic algorithms+ data structures= evolution programs: Springer Science & Business Media.

Okelo, R., and Yuan, R. L. (2005). Bond strength of fiber reinforced polymer rebars in normal strength concrete. Journal of Composites for Construction.

Quayyum, S. (2010). Bond behaviour of fibre reinforced polymer (FRP) rebars in concrete.

Shield, C., French, C., and Hanus, J. (1999). Bond of glass fiber reinforced plastic reinforcing bar for consideration in bridge decks. ACI Special Publication, 188.

Stigler, S. M. (1981). Gauss and the invention of least squares. The Annals of Statistics, 465-474.

Suratgar, A. A., Tavakoli, M. B., and Hoseinabadi, A. (2005). Modified Levenberg-Marquardt method for neural networks training. World Acad Sci Eng Technol, 6, 46-48.

Tighiouart, B., Benmokrane, B., and Gao, D. (1998). Investigation of bond in concrete member with fibre reinforced polymer (FRP) bars. Construction and Building Materials, 12(8), 453-462.

Yan, F., and Lin, Z. (2016). New strategy for anchorage reliability assessment of GFRP bars to concrete using hybrid artificial neural network with genetic algorithm. Composites Part B: Engineering, 92, 420-433.

Yoo, D.-Y., Kwon, K.-Y., Park, J.-J., and Yoon, Y.-S. (2015). Local bond-slip response of GFRP rebar in ultra-high-performance fiber-reinforced concrete. Composite Structures, 120, 53-64.

7. NEW STRATEGY FOR ANCHORAGE RELIABILITY ASSESSMENT OF GFRP BARS TO CONCRETE USING HYBRID ARTIFICIAL NEURAL NETWORK AND GENETIC ALGORITHM

7.1. Introduction

Sufficient development length of reinforcing bars plays an important role in preventing bond premature failure and ultimately ensures the safety of the structures (ACI 408 Committee, 2003). Anchorage reliability of GFRP bars to concrete therein is one of the most critical indices for implementation of such engineered material to the concrete structures. A reasonable reliability index of the development length must be designated to allow the GFRP bar to yield desirable flexural failure prior to anchorage failure.

Anchorage reliability assessment requires a performance function (PF) with respect to a set of design variables, while the PFs are usually implicit in most cases. Although data generated from either numerical simulation or experimental tests are commonly used for determining the PFs (Chiachio et al., 2012; Elhewy et al., 2006), there still remain high challenges: a) Effectiveness of numerical simulation. The GFRP bar bond-slip behavior exhibits a highly nonlinear contact feature between GFRP bars and concrete (Akishin et al., 2014), resulting in high variation in modeling (parameter selection and optimization); and b) Limitation of experimental tests. Most laboratory tests, due to limited facilities, time consuming and cost, may be conducted under certain particular conditions, which in turn do not accommodate all critical design variables (e.g., bar position, bar diameter and concrete cover) commonly experienced in construction. As a result, both numerical simulation and experimental tests neither consider the different characteristics of GFRP materials nor distinguish issues inherent to particular applications to construct the PFs for anchorage reliability analysis.

Alternatively, use of the ANN algorithm enables to approximate the implicit PF through a set of inputs and a desirable output without need of solving explicit function of the PFs (Chau, 2007; Goh and Kulhawy, 2003; Hornik et al., 1990). This technique has been widely accepted in structural reliability analysis, and has been validated to be more comparable over conventional approaches (Deng et al., 2005). Deng et al. (Deng et al., 2005) presented their work on structural reliability analyses through the ANN-based first-order second-moment (FOSM) method and Monte Carlo simulation (MCS) method. The ANN technique in their study was utilized to predict the implicit PFs and determine their partial derivatives with respect to design variables for determining failure probability and reliability index. Their analysis revealed that the results predicted by the ANN-based FOSM and the MCS methods have higher accuracy over conventional reliability analysis methods. Papadrakakis et al. reported the reliability analysis of complex structural system using the ANN-based MCS method. The critical load factor and failure probability considering plastic-hinge collapse were accurately captured (Papadrakakis et al., 1996).

Multi-layer feed-forward neural network with back-propagation (BP) algorithm due to its strong ability of data mining is usually taken as a preferred choice for complex problems with highly nonlinear correlations (Bashir and Ashour, 2012; El Kadi, 2006; Mansouri and Kisi, 2015; Perera et al., 2010). The BP algorithm adopts a local searching technique through the gradient decent method to adjust the weights and biases back from the output layer to the preceding layers iteratively, thereby minimizing the mean square error between the actual and predicted outputs (Chandwani et al., 2015; Varol et al., 2013). However, this algorithm may experience inherent drawback where the training phase is too low to avoid local minima. To overcome this, the genetic algorithm (GA) is embedded into the ANN to post a global searching ability, referred to

the hybrid ANN-GA model for the network training. By taking advantage of the capability of identifying the global optimal solutions, the initial weights and biases in the ANN are evolved firstly, and then assigned to the ANN as the initial values for the subsequent iterations. Cheng and Li (Cheng and Li, 2008) used the ANN-based GA model for structural reliability analysis, in which the ANN model was used to approximate the limit state function, while the GA to estimate the failure probability. The developed method confirmed that the hybrid ANN with GA is more effective, particularly when the failure probability tends to be extremely small. This hybrid modeling strategy has also been used in several engineering fields, such as the slump of ready mix concrete (Chandwani et al., 2015), the permeability of the reservoir (Irani and Nasimi, 2011), and yet has not been applied in reliability analysis of GFRP bars in concrete.

This chapter is to develop a systematic strategy using the hybrid ANN-GA model for the anchorage reliability assessment of GFRP bars to concrete. The developed procedures of the strategy cover the detailed data selection and processing, PF modeling and validation, and the ANN-based reliability assessment in terms of the FOSM and MCS methods. Implementation of the ANN-GA model for GFRP bar anchorage reliability assessment is then exemplified in a step-by-step manner. A graphical user interface (GUI) system in Matlab environment is designed for practical use.

7.2. ANN-based Anchorage Reliability Assessment

7.2.1. Framework of ANN-based Anchorage Reliability Assessment

A systematic framework of the ANN-based reliability analysis is proposed, as demonstrated in a flow chart shown in Figure 7-1 (a) and 1(b). It mainly consists of three phases as shown in Figure 7-1 (a). Firstly, the database for the network training needs to be created, where the design variables $X = (x_1, x_{2,\ldots}, x_n)^T$ and its corresponding response $g(X)$ (i.e., PFs) can

be obtained from experimental results. Statistical characteristics in terms of means and standard deviations are then computed and prepared for the reliability analysis. Secondly, with the predetermined database, the hybrid ANN-GA modeling method is used for determining the PFs of anchorage reliability of GFRP bars in concrete. The computational strategy is to integrate the ANN with the GA to predict the PF and calibrate its effectiveness, thereby resulting in the prerequisite for the subsequent reliability assessment at the third step. Specifically, the ANN is used to map the relationship between the design variables and the PFs, while the GA is used to optimize the initial weights and biases of the ANN. Toward the end, the reliability assessment using the ANN-based FOSM and MCS methods are used to derive reliability index and the failure probability. Note that the development length collected in the database is too short for adequate anchorage, leading to the reliability index to be negative. Thus, the mean of development length is corrected based on a targeted reliability index.

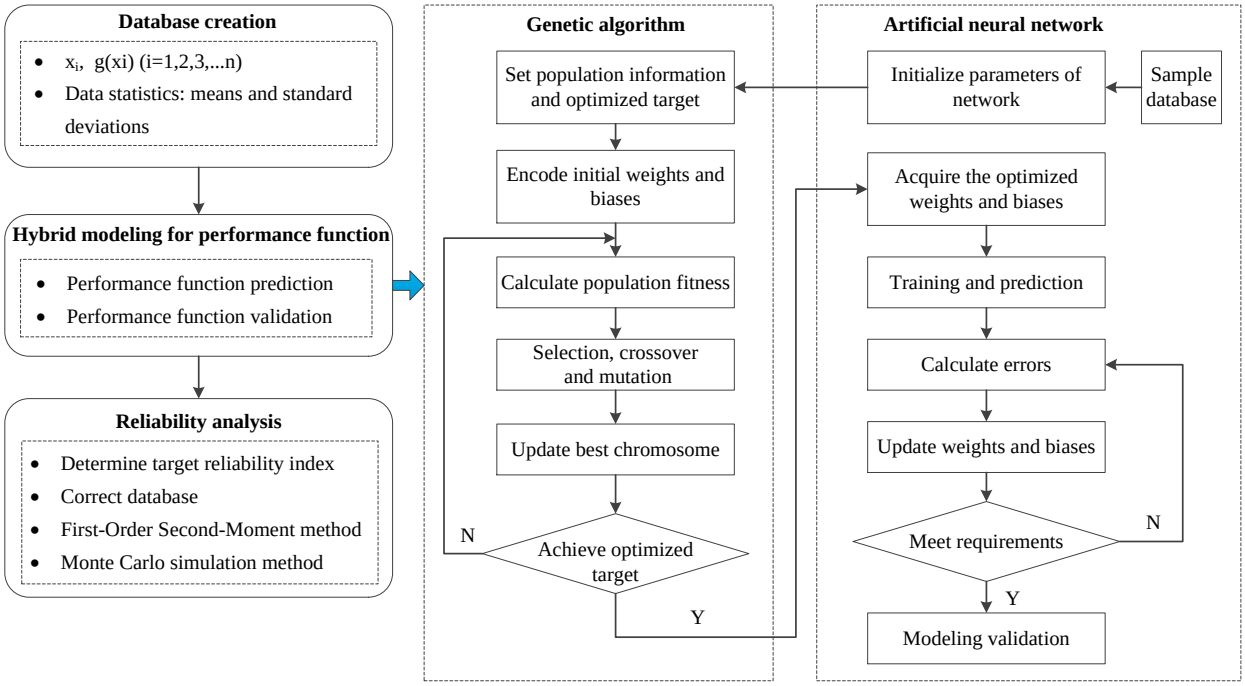

(a) Reliability analysis procedures (b) ANN-GA model

Figure 7-1. Concept of ANN-based anchorage reliability analysis

Among the detailed procedures above, effective prediction of the PFs with respect to the design variables at the second step plays important role in the accuracy of the final reliability assessment. For the hybrid ANN-GA modeling of the PFs, the ANN needs to be constructed in advance due to the fact that the chromosome length in the GA is dependent on the network architecture. As illustrated in Figure 7-1 (b), the basic information, such as the population size and optimized target, is firstly initialized in the GA. The weights and biases of the ANN are encoded to constitute a set of chromosomes, forming an initial population to evolve. The norm of the errors between the predicted output vector and expected output vector is defined as the fitness. The chromosomes with the smaller fitness (i.e., the smaller errors) are selected for crossover and mutation at a certain probability, generating offspring inheriting excellent genes from their parents. With that, the worse chromosomes in the parent population are replaced with these new superior ones, creating a new population. Meanwhile, the best chromosome is decoded and transmitted into the ANN to determine whether the optimal target is achieved. Otherwise, the evolution subjected to the same rules will continue refining the network prediction. As long as the optimized target meets the requirement, the best chromosome containing the best solutions for the ANN prediction are decoded and assigned to the network as the initial weights and biases for training. The weights and biases are then adjusted to gain the relationship between the design variables and the PF. Finally, the predicted PF will be further calibrated through data from either experimental tests or numerical simulation.

7.2.2. Data Selection and Processing

The selected data for the network training must cover the most critical factors for the PF, while eliminating the secondary factors that may cause unexpected disturbance during the network prediction. As one of the most critical factors for the bar anchorage PF, the bond

strength and its influence factors need to be investigated. A preliminary database was collected from existing 179 beam-test specimens in the literature (Aly et al., 2006; Benmokrane and Tighiouart, 1996; Saeed Daniali, 1990; S Daniali, 1992; DeFreese and Roberts-Wollmann, 2002; M. Ehsani et al., 1993; M. R. Ehsani et al., 1996; Faza and GangaRao, 1991; Kanakubu et al., 1993; Mosley, 2000; OH et al., 2007; Shield et al., 1999; Shield et al., 1997; B Tighiouart et al., 1998; Brahim Tighiouart et al., 1999), covering the variables of interest, such as bar diameter, concrete strength and cover, bar position and surface, development length, and transverse confinement. The statistical characteristics are summarized in Table 7-1, where *Surface* denotes the surface treatment of GFRP bars; *Position* denotes the bar position; ρ denotes the transverse reinforcement ratio; d_b denotes the bar diameter; c denotes the concrete cover; l_d denotes the development length; f_c' denotes the concrete compressive strength; f_u denotes the ultimate strength of GFRP bars. In addition, the surface treatments were quantified by 1, 2 and 3 for the helical lugged, spiral wrapped and sand coated, respectively. Bar positions were quantified by 1 and 2 for top and bottom, respectively.

Table 7-1. Statistical characteristics of variables affecting bond strength

Factors	Minimum	Maximum	Mean	Standard deviations
Surface	1	3	1.79	0.69
Position	1	2	1.17	0.38
ρ	0	0.08	0.02	0.02
d_b (mm)	9.53	28.70	18.98	5.48
c (mm)	9.53	406.00	63.43	47.65
l_d (mm)	38.10	799.91	271.02	220.55
f_c' (MPa)	27.56	65.29	34.00	8.41
f_u (MPa)	469.00	931.00	648.14	110.98

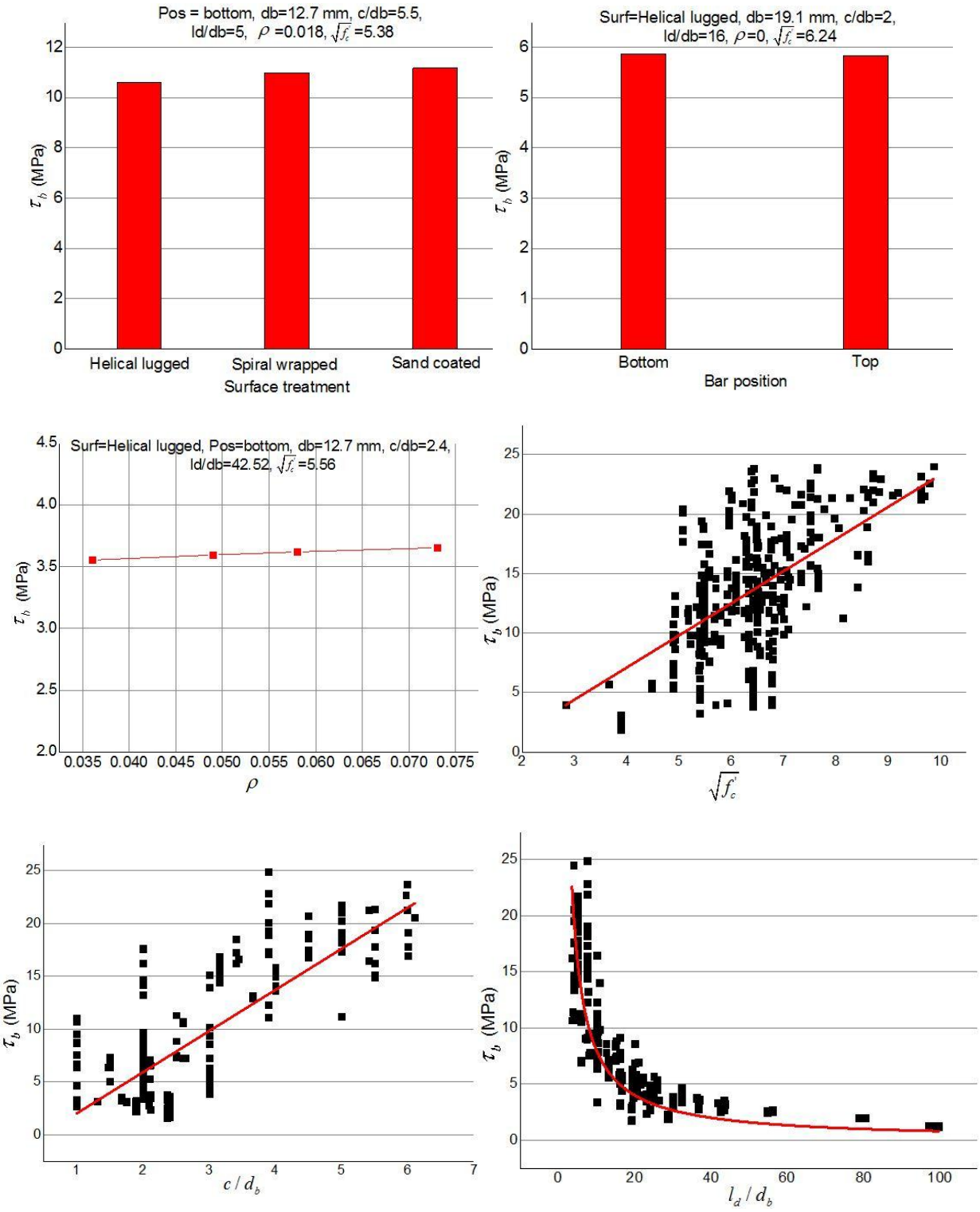

Figure 7-2. Influences of design variables on bond strength

Figure 7-2 displays the influences of those variables on bond strength, τ_b. Generally, it was observed that the bar surface treatment, bar position and transverse reinforcement ratio have

no significant effects on the bond strength. Differently, the concrete compressive strength, the ratio of concrete cover to bar diameter, and the ratio of development length to bar diameter have high impacts on bond strength: as $\sqrt{f_c'}$ and c/d_b increased, τ_b increased linearly; while τ_b decreased nonlinearly as l_d/d_b increased. According to the data diversity principle, *Surface*, *Position*, and ρ will not be included for the network training, while still remaining for the purpose of the PF prediction in design codes for a comparison.

In addition, since the data collected are generally in a big numerical range, it is necessary to normalize them into a regular range to enhance the training efficiency of the network. The algorithm of the data normalization is shown in Equation (7-1):

$$x_n = \frac{y_{max}-y_{min}}{x_{max}-x_{min}}(x - x_{min}) + y_{min}, \tag{7-1}$$

where x_n is the normalized value of variable x; x_{max} and x_{min} are the maximum and minimum of x, respectively; y_{max} and y_{min} are the maximum and minimum of normalized target, respectively. When the normalized target with $y_{max} = 1$ and $y_{min} = -1$ are used, then we have:

$$x_n = 2\frac{(x-x_{min})}{x_{max}-x_{min}} - 1. \tag{7-2}$$

7.2.3. Performance Function Modeling for Anchorage Reliability

7.2.3.1. Performance function definition

The first step of a reliability analysis is to construct the PF in terms of a set of design variables $X=(X_1, X_2, \dots, X_n)^{\mathrm{T}}$, where $X_i(i = 1,2, \dots, n)$ is the i^{th} design variable. In general, the basic items of the PF can be classified into the structural resistance, *R*, which is dependent on the properties of the structure itself, and the load effect, *S*, which is resulted from external loads. As such, the PF of the anchorage reliability are demonstrated in Equation (7-3):

$$Z = g(X) = R - S = \tau_b \pi d_b l_d - f_u \pi d_b^2/4. \tag{7-3}$$

Note that the bond strength has implicit form in terms of the some design variables in existing Canadian and Japanese FRP design codes, which posts a high challenge in conventional reliability analysis as we stated previously. By using the ANN technique, the procedures of solving the implicit bond strength are replace with directly constructing a relationship between the design variables and the PF, while the relationship will be generated, as long as the inputs and its corresponding output are given.

7.2.3.2. Modeling performance function based on design standards

The bond strength of FRP bars to concrete, illustrated in Table 7-2, are given by national and international design codes for constructing the PF. Introducing τ_b in Equation (7-3) yields the PF for its anchorage reliability. However, note that some design variables have implicit form in bond strength equations, which is difficult to deal with for the conventional FOSM method. For example, the contribution of the bar diameter to the bond strength is associated with the coefficient K_3 in Equation (7-5), which is equal to 0.8 when $A_b \leq 300\,mm^2$ and 1.0 for other cases, where A_b denotes the cross sectional area of the bar. It is difficult to solve the partial derivative with respect to d_b due to its implicit form. Similar difficulty are also observed for the concrete cover associated with d_{cs} in Equations (7-5) and (7-6), and the bar diameter and concrete cover associated with α_1 in Equation (7-7). Note that the bond strength prediction in ACI 440.1R-06 code has an explicit form with respect to design variables, and thus demands less efforts for a reliability analysis.

Table 7-2. Bond strength predicted by national and international design standards

Design standards	Design equations		Notes
ACI 440.1R-06 (ACI Committee, 2006)	$\tau_b = \sqrt{f_c'}(0.332 + 0.025\frac{c}{d_b} + 8.3\frac{d_b}{l_d})$	(7-4)	d_{cs}: the smaller of the distance from concrete surface to the center of the bar or two-thirds the spacing of the bars being developed (mm);
CSA S806-02 (Canadian Standards Association, 2002)	$\tau_b = \frac{d_{cs}\sqrt{f_c'}}{1.15(K_1K_2K_3K_4K_5)\pi d_b}$	(7-5)	K_1: bar location factor; K_2: concrete density factor; K_3: bar size factor; K_4: bar fiber factor; K_5: bar surface profile factor.
CSA S6-06 (Canadian Standards Association, 2006)	$\tau_b = \frac{f_{cr}(d_{cs}+K_{tr}E_{FRP}/E_s)}{0.45\pi d_b K_1 K_5}$	(7-6)	f_{cr}: the cracking strength of concrete (MPa); K_{tr}: transverse reinforcement index (mm); E_{FRP}: elastic modulus of FRP bar (MPa); E_s: elastic modulus of steel (MPa);
JSCE (Machida and Uomoto, 1997)	$\tau_b = f_{bod}/\alpha_1$	(7-7)	f_{bod}: designed bond strength of concrete; α_1: a confinement modification factor.

7.2.3.3. Modeling performance function based on the ANN and GA

The hybrid ANN-GA strategy is to use the ANN to predict the PF according to the given design variables, and use the GA to evolve the initial weights and biases of the ANN. There is no need to derive the bond strength compared to the PF modeling based on the design standards.

(I) Key issues of the ANN modeling

The architecture of a network has great influence on the prediction of PF. It has been proved that the performance improvements by adding additional hidden layers (second, third or even more) are very small or even worse. A network containing one hidden layer with adequate neurons is capable of approximating any continuous function with satisfactory precision (Bengio and LeCun, 2007; Cardoso et al., 2008; Gybenko, 1989). While for the number of neurons in hidden layer, it is usually determined through a number of trials (E. Golafshani et al., 2015; E. M. Golafshani et al., 2012). In addition, according to the discussion in Section 2.2, the design variables do not involve the bar surface, bar position and transverse reinforcement ratio in the

input layer, whereas take the bar diameter, concrete cover, development length, concrete compressive strength and bar ultimate strength into account, as shown in Figure 7-3.

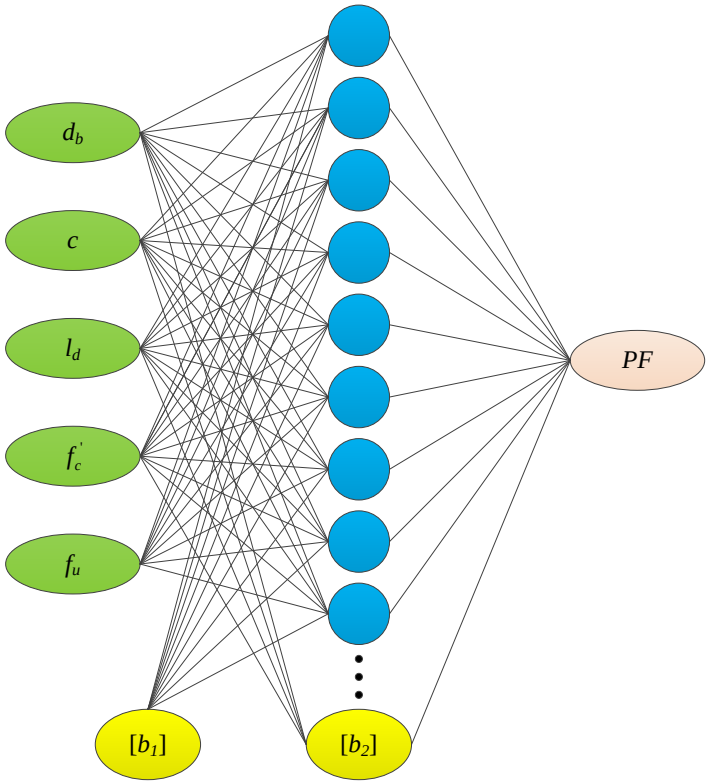

Figure 7-3. Preliminary architecture of the ANN

The data imported from the database to the network is classified into training set, validating set and testing set, respectively. The training data is used for network training by paring a set of inputs with the corresponding expected output. The validating data is used to avoid over-fitting. If the accuracy over the training data yields an increase, but the accuracy over the validating data stays the same or decreases, then over-fitting occurs and training needs to be stopped. The testing data is used to test the final solution that guarantees the predictive capability of the network (Friedman et al., 2001). In addition, the Levenberg–Marquardt algorithm is taken as a preferred choice for network training (Mansouri and Kisi, 2015; Suratgar et al., 2005). The nonlinear hyperbolic tangent sigmoid transfer function is usually used in the hidden layer while

the linear transfer function in the output layer. However, these transfer functions can switch over their positions between the hidden and output layers to achieve best training results.

(II) Hybrid ANN-GA modeling

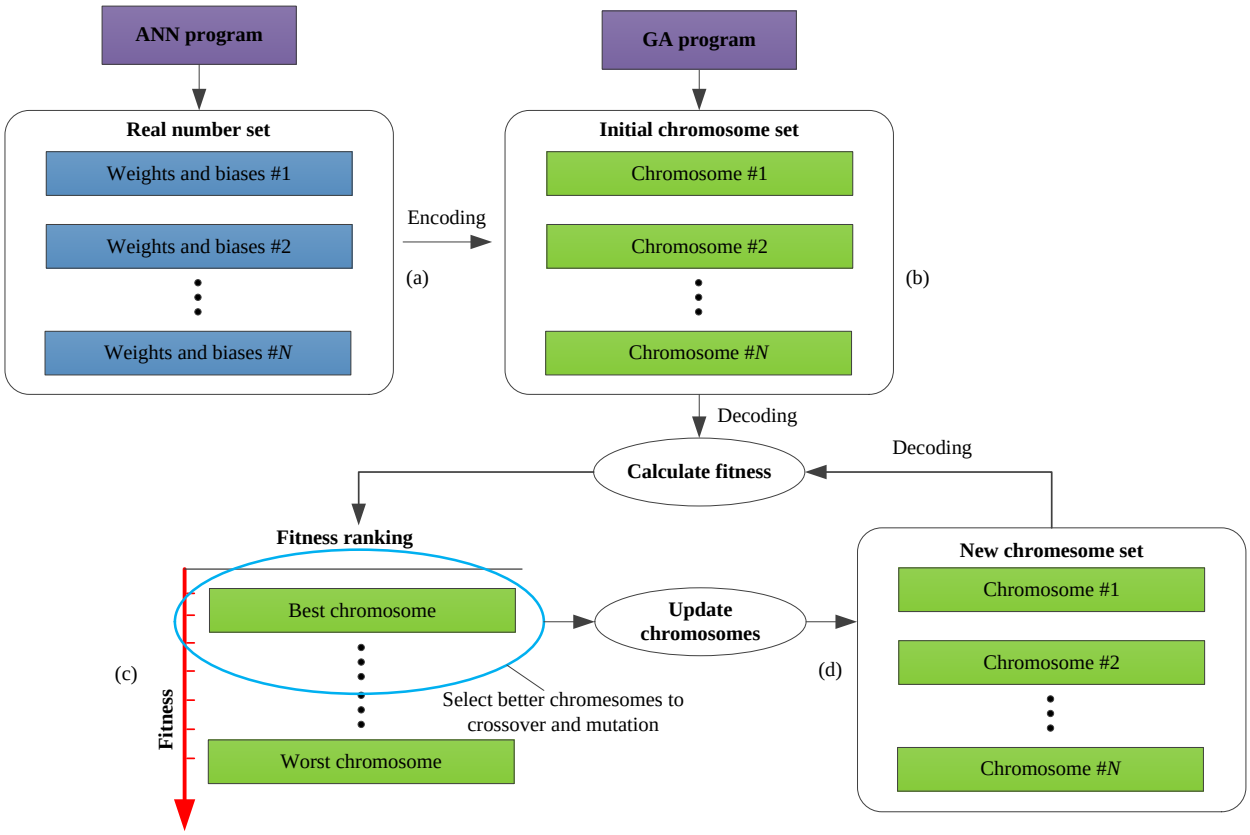

Figure 7-4. Synthesis of workflow of the ANN-GA model

The information exchange between the ANN and GA is implemented through encoding and decoding the chromosome. The synthesis workflow of the ANN-GA model is demonstrated in Figure 7-4. Basically, the actual values of the weights and biases are first randomly generated in the ANN program, and each data set corresponds to a solution to the neural network, as shown in Figure 7-4 (a). These data sets are then encoded into a group of chromosomes, comprising an initial population in the GA program, as shown in Figure 7-4 (b). To evolve the weights and biases, the chromosomes are decoded to calculate their fitness, which is defined as the norm of

the PF differences between the predicted vector and expected vector for convenience. Thus, the best chromosome demonstrates the smaller fitness and vice versa. The superior chromosomes have the larger probabilities to participate in the evolutionary operations in terms of selection, crossover and mutations, creating new chromosomes inheriting the excellent genes from their parent ones, as demonstrated in Figure 7-4 (c). These new inborn chromosomes are compared with the old ones, and substitute those worse chromosomes in the former population, thereby comprising a new superior population, as shown in Figure 7-4 (d). After that, the new population follows the same rules to start a new evolutionary loop until the fitness meet requirement of the allowable error of the prediction.

7.2.3.4. Performance function prediction and validation

Generally, the PF was predicted and validated through two major steps: first, by comparing with the ANN model to demonstrate its optimized effect on the predicted ability; next, by comparing with the model based on design standards to demonstrate its superiority among different modeling methods.

Table 7-3. Parameter initializations for the GA

Parameters	Values
Population size	100
Length of chromosome	78
Maximum number of generations	250
Selection probability	0.9
Crossover probability	0.7
Mutation probability	0.1

The database created in section 2.2 was used for PF modeling. Out of the total 179 samples, 109 records were randomly selected for the training data, 35 records for the validating data, and 35 records for the testing data. For the ANN-based modeling, the architecture of the network adopting 5-11-1 was proved to yield good results. On the other hand, the parameters of the GA were initialized as shown in Table 7-3. , where the length of chromosome was calculated to 78 based on the architecture of the network. During the evolutions, those excellent chromosomes were selected with a probability of 0.9, and then crossed and mutated with a probability of 0.7 and 0.1, respectively.

Figure 7-5 displays the variations of the fitness over the number of evolutions. It is clear that the best fitness decreased as the evolution increased, and leveled off after a threshold near to 200. Thus, the appropriate maximum number of generations of the GA was determined to be 200.

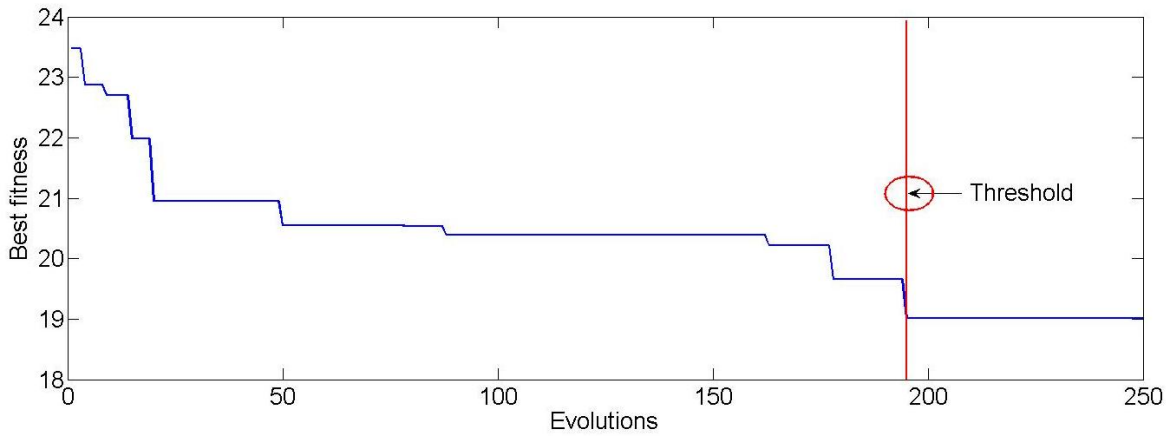

Figure 7-5. Variations of the best fitness

The PF modeled with the ANN-GA was first compared to that modeled with the ANN to demonstrate the optimization effect, as shown in Figure 7-6. The relative error was defined as the ratio of the difference between the predicted result and experimental result to the experimental result. It can be seen that the errors of the ANN-GA model was limited within the interval of [-0.05, 0.05] for all data sets, while those of the ANN model distributed along [-0.10, 0.10]. Thus,

the ANN-GA model significantly improved the accuracy of the predicted PF compared with the ANN model.

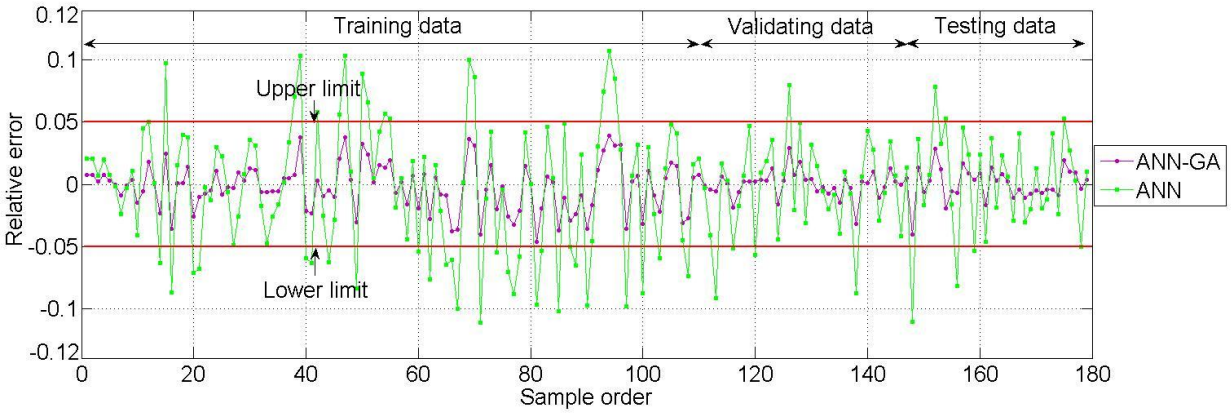

Figure 7-6. Comparisons between the ANN-GA and ANN models

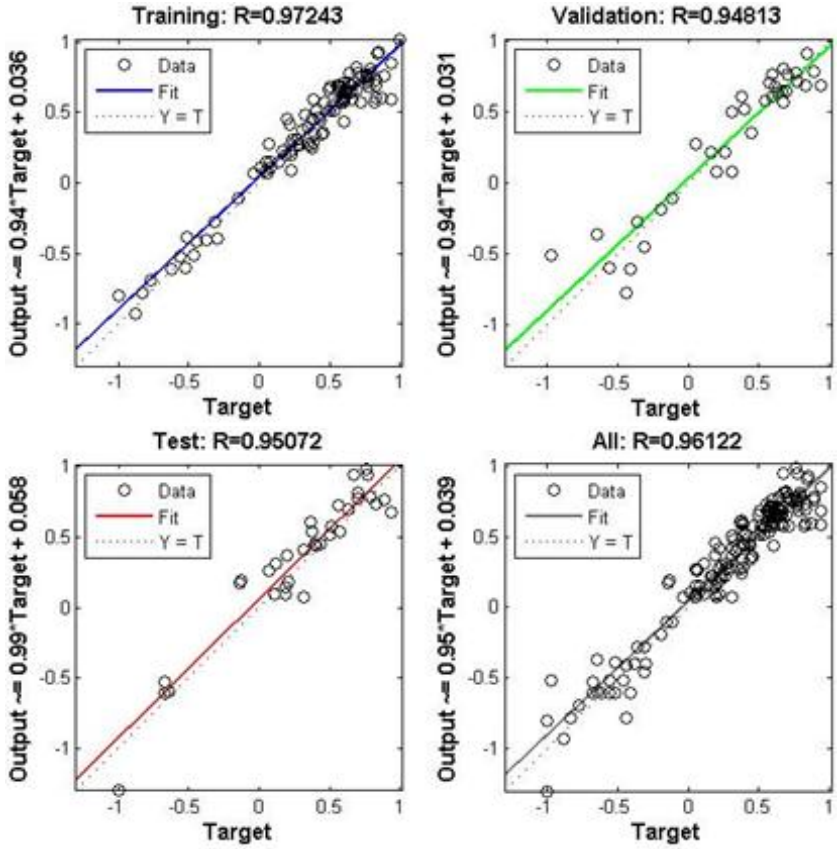

Figure 7-7. Regression analyses of data predicted by the ANN-GA model as compared to experimental results

On the other hand, the linear regression analysis of the predicted and target values is illustrated in Figure 7-7, comprising of training data, validating data, testing data and all data. It can be seen that the Pearson's correlation coefficient (R-value) was 0.97, 0.95, 0.95 and 0.96 for training data, validating data, testing data and all data, respectively. This indicates that the prediction model of the ANN-GA fitted the experimental results very well. Specifically, the R-value of the training data showed good learning ability for the network to approximate the actual values. And the R-value of the testing data represented that the trained network was competent for generalizing data between the design variables and the PF.

In the following, the PFs modeled with different methods were compared in detail, as shown in Figure 7-8. It was observed that the PFs modeled with the ANN-GA exhibited the closest predictions to the experimental results for all data sets, whereas those modeled based on CSA S6-06 displayed the largest deviations. Meanwhile, the model of ACI 440.1R-06 showed good agreement with the experimental results, performing best among other design standards. The models of CSA S806-02 and JSCE manifested the most conservative results compared to the experimental results. Thus, it is reasonable to use the ANN-GA to model the PF for reliability assessment due to its accuracy as well as its convenience.

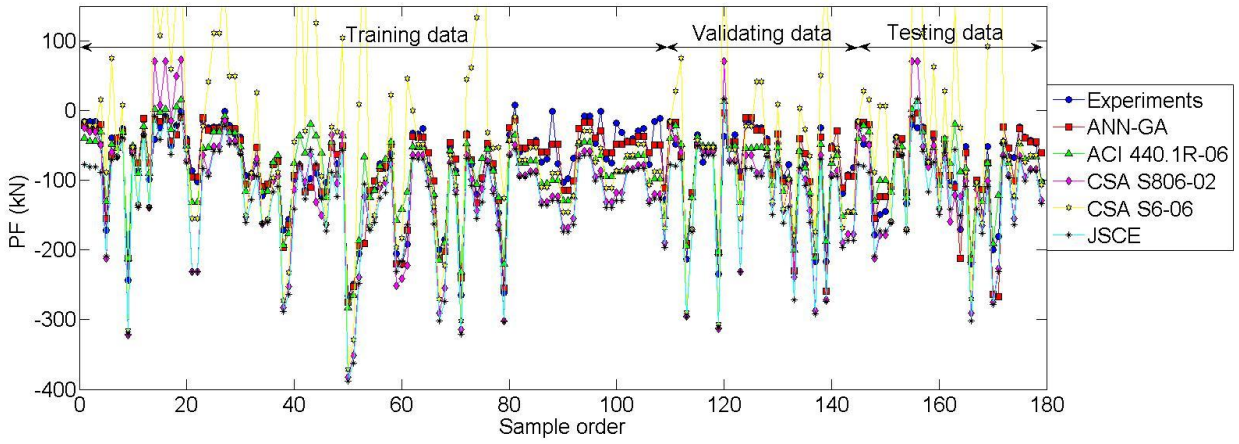

Figure 7-8. PF calculations

Therefore, these comparisons among different modeling approaches and validations by experimental results further confirm that the PFs generated by the proposed ANN-GA algorithm are viable with applications to the subsequent reliability analysis.

7.2.4. ANN-based Anchorage Reliability Assessment

7.2.4.1. ANN-based performance function derivation

As the simplest type of the ANN, the feed-forward neural network with BP algorithm was employed in this study. It consists of the input layer, one or more hidden layers and the output layer, in which each layer has a number of interconnected neurons that send message to each other. Design variables are regarded as the preliminary information to be assigned to the input layer, and then pass through the hidden layer to the output layer. The weights therein are used to measure the contribution that the preceding neuron set to the current one. Biases are added to the sums calculated at each neuron (except input neuron) during the feed-forward process (Alshihri et al., 2009; Davalos et al., 2012). The working principle of a single neuron unit processor is depicted as shown in Figure 7-9.

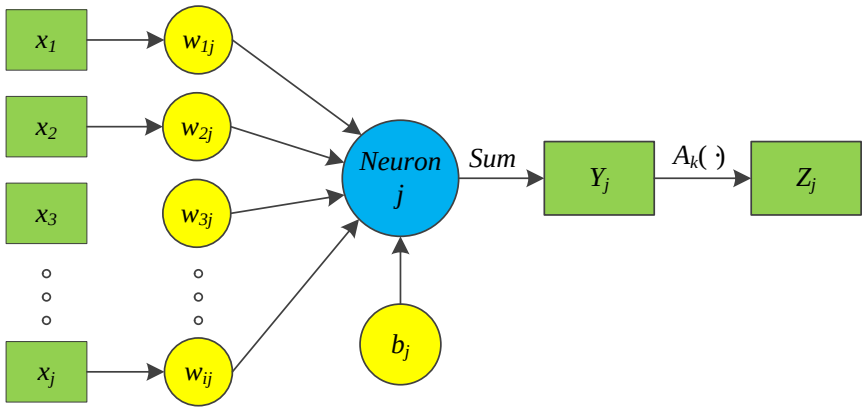

Figure 7-9. Working principle of single neuron

It is assumed that the activation function $A_k(\cdot)$ is applied on all neurons of the k^{th} layer; n_k is the number of neurons of the k^{th} layer; $W_k = [w_{ij}^k]$ is the n_{k-1} by n_k weight matrix between the $(k\text{-}1)^{th}$ layer and the k^{th} layer and hence, the weight vector between the neurons of preceding layer and the j^{th} neuron of current layer can be expressed as $W_k^j = [w_{1j}^k, w_{2j}^k, \dots, w_{in_k}^k]^{\mathrm{T}}$; and $B_k = (b_1^k, b_2^k, \dots, b_{n_k}^k)^{\mathrm{T}}$ is the bias vector of the k^{th} layer. Then the receive vector of the k^{th} layer is expressed as: $Y_k = (Y_1^k, Y_2^k, \dots, Y_{n_k}^k)^{\mathrm{T}}$, in which the value of the j^{th} neuron Y_j^k is,

$$Y_j^k = \sum_{i=1}^{n} w_{ij}^k x_i + b_j^k. \tag{7-8}$$

The vector Y_k is transformed to the same dimensional output vector, $Z_k = (Z_1^k, Z_2^k, \dots, Z_{n_k}^k)^{\mathrm{T}}$, as shown below:

$$Z_k = A_k(Y_k) = (A_k(Y_1^k), A_k(Y_2^k), \dots, A_k(Y_{n_k}^k))^{\mathrm{T}}. \tag{7-9}$$

The partial derivative matrix is by the form:

$$D_{Z_k Y_k} = \frac{\partial Z_k}{\partial Y_k} = diag\left[\frac{dZ_1^k}{dY_1^k}, \frac{dZ_2^k}{dY_2^k}, \dots, \frac{dZ_{n_k}^k}{dY_{n_k}^k}\right] = diag[A_k'(Y_1^k), A_k'(Y_2^k), \dots, A_k'(Y_{n_k}^k)]. \tag{7-10}$$

Specially, for a network with one hidden layer, the receive vector Y_1 and output vector Z_1 between the input layer and hidden layer are illustrated as:

$$Y_1 = W_1^T X + B_1 \tag{7-11}$$

$$Z_1 = A_1(Y_1) = A_1(W_1^T X + B_1) \tag{7-12}$$

The receive vector Y_2 and output vector Z_2 between the hidden layer and output layer are derived from:

$$Y_2 = W_2^T Z_1 + B_2 = W_2^T (A_1(W_1^T X + B_1)) + B_2, \tag{7-13}$$

$$Z_2 = A_2(Y_2) = A_2(W_2^T (A_1(W_1^T X + B_1)) + B_2), \tag{7-14}$$

where, Z_2 herein is exactly the PF, $g(X)$.

Moreover, the gradient vector of the PF is given as:

$$\nabla g(X) = W_1 D_{Z_1 Y_1} W_2 D_{Z_2 Y_2}. \quad (7\text{-}15)$$

7.2.4.2. ANN-based FOSM method

The conventional FOSM method is based on a first-order Taylor series approximation of the PF linearized at the point located on the failure surface (Nowak and Collins, 2012). The limit state function is:

$$Z = g(X) = 0. \quad (7\text{-}16)$$

If $x^* = (x_1^*, x_2^*, \dots, x_n^*)^{\mathrm{T}}$ is a point located on the limit state surface, which is satisfied with:

$$g(x^*) = 0. \quad (7\text{-}17)$$

Then the PF is approximated by a Taylor series at x^* as expressed:

$$Z = g(x^*) + \sum_{i=1}^{n} \frac{\partial g(x^*)}{\partial X_i}(X_i - x_i^*) = g(x^*) + (\nabla g(x^*))^T (X - x^*). \quad (7\text{-}18)$$

The mean and standard deviation of the PF herein is:

$$\mu_Z = g(x^*) + \sum_{i=1}^{n} \frac{\partial g(x^*)}{\partial X_i}(\mu_{X_i} - x_i^*) = g(x^*) + (\nabla g(x^*))^T (\mu_X - x^*), \quad (7\text{-}19)$$

$$\sigma_Z = \sqrt{\sum_{i=1}^{n} [\frac{\partial g(x^*)}{\partial X_i}]^2 \sigma_{X_i}^2} = ||\nabla g(x^*) \sigma_X||. \quad (7\text{-}20)$$

The sensitivity coefficient is defined as:

$$\alpha_X = -\frac{\nabla g(x^*)\sigma_X}{||\nabla g(x^*)\sigma_X||}. \quad (7\text{-}21)$$

The reliability index can be gained as follows:

$$\beta = \frac{\mu_Z}{\sigma_Z} = \frac{g(x^*) + (\nabla g(x^*))^T (\mu_X - x^*)}{||\nabla g(x^*)\sigma_X||}. \quad (7\text{-}22)$$

For the ANN-based FOSM, the reliability index needs to be solved by iterations, in which the steps are described as follows:

Step 1. Assume that the initial checking point $x^* = \mu_X = (\mu_{X_1}, \mu_{X_2}, \dots, \mu_{X_n})^T$, and $\sigma_X = (\sigma_{X_1}, \sigma_{X_2}, \dots, \sigma_{X_n})^T$;

Step 2. Calculate $g(x^*)$ and $\nabla g(x^*)$, in which $g(x^*)$ can be directly obtained through the network simulation, and $\nabla g(x^*)$ can be calculated according to Equations (7-10) and Equation (7-15);

Step 3. Calculate β according to Equation (7-22);

Step 4. Calculate the new x^* according to the equation below, in which α_X can be derived from Equation (7-21),

$$x^* = \mu_X + \beta \sigma_X \alpha_X; \tag{7-23}$$

Step 5. Repeat steps 2 through 4 until the difference of $||x^*||$ is smaller than a threshold.

7.2.4.3. ANN-based MCS method

Traditional MCS method is commonly used to solve complex problem involving random variables of known or assumed probability distributions. For the ANN-based MCS, the PF can be easily obtained through network simulation and hence, the failure probabilistic estimated by MCS method is illustrated in the following equation (Cardoso et al., 2008; Papadrakakis and Lagaros, 2002),

$$p_f = \int_{g(X)\leq 0} f(X)dx = \int_{-\infty}^{\infty} I[g(X)]f(X)\,dx = \frac{1}{N}\sum_{i=1}^{n} I[g(X)], \tag{7-24}$$

where $f(X)$ is the joint probability density function; $I[g(X)]$ is the indicator function defined as: $I[g(X)] = 1$ when $g(X) < 0$, while $I[g(X)] = 0$ when $g(X) \geq 0$. This direct sampling method of MCS is denoted as MCS-DS.

However, the direct sampling points X mostly locate at the neighborhood of the maximum of joint probability density function, which lead to few occurrences for $g(X) < 0$ when the failure probability is extremely small. Thus, the efficiency and precision of MCS by

direct sampling is relatively lower. To overcome such weakness, importance sampling (IS) is introduced accordingly, and denoted as MCS-IS. By modifying Equation (7-24), the failure probability is calculated as follows (Papadrakakis and Lagaros, 2002; Papadrakakis et al., 1996):

$$p_f = \int_{g(V)\le 0} \frac{f(V)}{p(V)} p(V) dv = \int_{-\infty}^{\infty} \frac{I[g(V)]f(V)}{p(V)} p(V) dV = \frac{1}{N}\sum_{i=1}^{n} I[g(V_i)] \frac{f(V_i)}{p(V_i)}, \quad (7\text{-}25)$$

where $p(V)$ is the importance sampling function; and $V = (V_1, V_2, \dots, V_n)^T$ is generated samples according to $p(V)$. Note that the most probable failure point is the design checking point x^*. Thus, the new variable V can use x^* as the mean of the generated samples, specifying $\mu_V = x^*$ and $\sigma_V = \sigma_X$. The procedures for the MCS-IS method is detailed in the following steps.

Step 1. Calculate the design checking point x^* by the aforementioned steps in the ANN-based FOSM method;

Step 2. Generate samples of the design variables V, in which $\mu_V = x^*$ and $\sigma_V = \sigma_X$;

Step 3. Calculate the sum of the probability density function (PDF) of all samples, in which the PDF of each design variable is equal to $f(V_i)/p(V_i)$;

Step 4. Calculate the failure probability according to Equation (7-25).

7.3. Implementation to GFRP Bar Anchorage Reliability Assessment

7.3.1. Target Reliability Index

The limit state for anchorage of GFRP bars in concrete is defined as the state that the bond stress τ achieves to the maximum bond strength τ_b as the bar stress σ at loaded end reaches the ultimate strength f_u, i.e., $\sigma = f_u$ and $\tau = \tau_b$ occur simultaneously. The corresponding probability of the anchorage limit state is denoted as:

$$p_{fa} = P(\sigma = f_u, \tau = \tau_b) = P(\sigma = f_u) \cdot P(\tau = \tau_b | \sigma = f_u) = p_f \cdot p_{fc}, \quad (7\text{-}26)$$

where, p_{fa} is the failure probability of anchorage; p_f is the failure probability of bar stress reaches the maximum; p_{fc} is the conditional failure probability of the bond stress reaches the

maximum given that bar stress has reached the maximum. Note that the bar stress at loaded end is determined based on the concrete flexural capacity of normal section, the reliability index β_f and its corresponding p_f can be determined according to the suggestions by ACI 440.1R-06 and Szerszen et al. (ACI Committee, 2006; Szerszen and Nowak, 2003), as shown below:

$$\beta_f = 3.5 \text{ and } p_f = 2.326 \times 10^{-4}. \tag{7-27}$$

Moreover, it is necessary to stipulate the reliability index of anchorage relatively higher than that of both strength limit state and serviceability limit state for higher reliability. Thus, β_{fa} is raised to an upper level, and its corresponding p_{fa} are shown below:

$$\beta_{fa} = 4.0, \text{ and } p_{fa} = 3.167 \times 10^{-5}. \tag{7-28}$$

Introducing Equations (7-27) and (7-28) back into Equation (7-26) yields

$$\beta_{fc} = 1.098, \text{ and } p_{fc} = 1.362 \times 10^{-1}, \tag{7-29}$$

which means that in order to make $\beta_{fa} = 4.0$, it is necessary to attach $\beta_{fc} = 1.098$ on the basis of $\beta_f = 3.5$. β_{fc} is the target reliability index for determining the development length of GFRP bars to concrete.

7.3.2. Development Length Estimation

The development lengths in the literature are relatively smaller than those should be for sufficient anchorage to concrete, leading to most points calculated by Equation (7-3) fall into the negative domain. The further results in the reliability index to be negative. Therefore, statistical parameters of the development length cannot be directly used for anchorage reliability analysis. In order to apply the proposed ANN-based methods to reliability analysis, it is necessary to recalculate the development length. For another, some design variables contributing to bond strength have no explicit expressions in both Canadian and Japanese design standards, and also had relatively larger difference between the test results compared with ACI 440.1R-06. Thus, it

is reasonable to employ ACI 440.1R-06 for the development length estimation. The target reliability index $\beta_{fc} = 1.098$ is used as the terminating condition for iterations.

The flow chart of the calculation is illustrated in Figure 7-10. Firstly, the means of the design variables of d_b, c, l_d, f_c' and f_u adopted the values listed in Table 7-1.. Meanwhile, in order to reduce the discrete range of the design variables, standard deviation is assumed to be $\sigma = 0.1 \cdot \mu$. Next, an array was created for the storage of development length with an increment with 0.01 mm. Meanwhile, the target reliability index and error tolerance were initialized for subsequent iterations. Thereafter, reliability analysis was carried out based on the steps specified in the ANN-based FOSM method. The development length kept increasing until the reliability index was larger than the target reliability index. Finally, the estimated development length was calculated to be 1133.05 mm with the corresponding reliability index of 1.098. The mean and standard deviation of the development length are $\mu_{l_d} = 1133.05$ and $\sigma_{l_d} = 0.1 \cdot \mu_{l_d} = 113.31$ respectively.

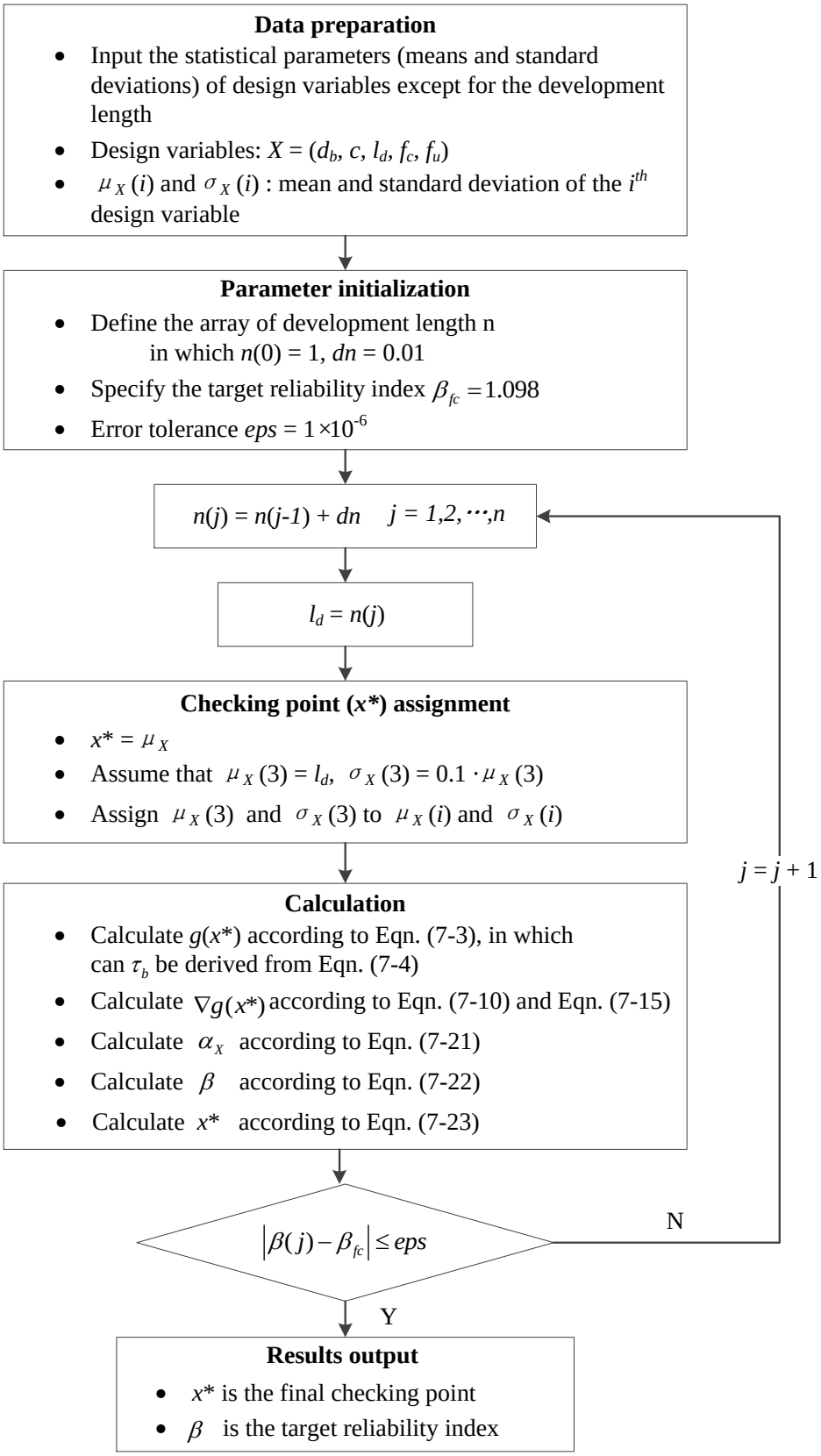

Figure 7-10. Development length calculation based on the targeted reliability index

7.3.3. Reliability Index Estimation

7.3.3.1. Performance function modeling with the ANN-GA model

The ANN-based methods are used to estimate the anchorage reliability index of GFRP bars to concrete. It is assumed that all the design variables follow the normal distribution. Both mean and St. of the development length adopted the new calculated values $\mu_{l_d} = 1133.05$ and $\sigma_{l_d} = 113.31$. Meanwhile, the means and St. of the other design variables followed the same rule as that of section 3.2, in which $\sigma = 0.1 \cdot \mu$. All information is summarized in Table 7-4. In addition, for the randomly generated variables, there are no test results that can be used as the corresponding targets. Considering that ACI 440.1R-06 display better performance in the aforementioned discussions, it was reasonable to use it to calculate the PF as the target output of the network. Also, the nonlinear transfer function was used in the hidden layer, and the linear transfer function in the output layer.

Table 7-4. Corrected statistical characteristics of design variables

Design variables	Distribution type	Mean	Standard deviation
d_b	Normal	18.98	1.90
c	Normal	63.43	6.34
l_d	Normal	1133.05	113.31
f_c'	Normal	34.00	3.40
f_u	Normal	648.14	64.81

One hundred samples were generated for networking learning, in which the training, validating and testing sets account for 60%, 20% and 20% respectively. As demonstrated in Figure 7-11, the training data and validating data displayed the PF predicted by the ANN-GA in solid lines and the target PF in dash lines. Clearly, the results of the ANN-GA model matched well with those calculated by ACI 440.1R-06, with less than 0.01% difference. Meanwhile, for

the testing data, the predicted and actual output differ little, with the maximum difference of 0.03% and hence, the network is capable of predicting output accurately according to the design variables that conforms to the respective probabilistic distributions.

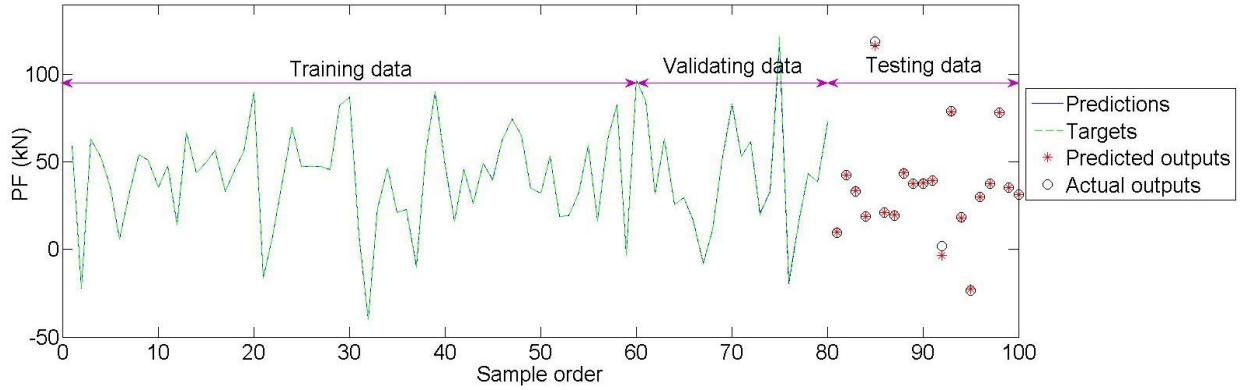

Figure 7-11. Training and validating of the ANN-GA model

7.3.3.2. ANN-based FOSM method

For the ANN-based FOSM method, the key step is to derive both $g(X)$ and $\nabla g(X)$ from the network. The calculation procedures were detailed in the following steps. First, assigning the means of design variables to the initial checking point x^*,

$$x^* = \mu_X = (\mu_{X_1}, \mu_{X_2}, \dots, \mu_{X_n})^T = (18.98,63.43,1133.05,34.00,648.14)^T \quad (7\text{-}30)$$

Also, the vector of the standard deviations of design variables was denoted as:

$$\sigma_X = (1.90,6.34,113.31,3.40,64.81)^T \quad (7\text{-}31)$$

Next, the weights of the input layer (W_1) and biases from the input layer to the hidden layer (B_1), and the weights of the hidden layer (W_2) and biases from the hidden layer to the output layer (B_1) were derived from the network, as shown in the following:

$$W_1 = \begin{pmatrix} -0.8537 & 0.2486 & -0.8818 & -0.3274 & 1.4514 \\ 0.0778 & 0.9255 & -0.4445 & -0.2479 & 0.5890 \\ 0.5801 & -0.3983 & 0.3394 & -0.3280 & -0.0382 \\ -0.5762 & -0.1051 & 0.5454 & -0.0512 & -0.5662 \\ -0.2205 & 0.2168 & -0.4198 & -0.3398 & 0.7984 \\ -0.2195 & 1.1514 & -0.5824 & 0.0426 & 0.5410 \\ 0.1619 & 0.8293 & 0.7387 & -1.8839 & 1.7730 \\ 0.4595 & 0.0687 & 0.7245 & -0.4512 & 1.1714 \\ -0.2387 & 0.1005 & 0.7975 & 0.2413 & 0.1357 \\ -0.8262 & -0.3569 & 1.5100 & -0.0667 & 1.2506 \\ -1.3065 & 1.2610 & -0.5053 & -0.0474 & 0.4526 \end{pmatrix}, B_1 = \begin{pmatrix} 1.5615 \\ -0.6552 \\ -0.7526 \\ 0.5366 \\ 0.1107 \\ -0.5510 \\ 0.3937 \\ 1.5450 \\ -0.2673 \\ -1.4895 \\ 1.0291 \end{pmatrix}. \quad (7\text{-}32)$$

$$W_2 = \begin{pmatrix} -0.3038 \\ -0.4138 \\ -0.6789 \\ 0.7506 \\ -0.6196 \\ 0.4053 \\ 0.0205 \\ 0.0776 \\ 0.4045 \\ -0.0041 \\ 0.0396 \end{pmatrix}^T, B_2 = (-0.6572). \quad (7\text{-}33)$$

By substituting Equation (7-32) into Equation (7-11) and Equation (7-12), Y_1 and Z_1 were calculated as follows:

$$Y_1 = \begin{pmatrix} 1.8412 \\ -0.5242 \\ -1.1639 \\ 0.2784 \\ 0.1563 \\ -0.2057 \\ -1.4637 \\ 0.1131 \\ -1.1532 \\ -3.6431 \\ 1.4214 \end{pmatrix}, Z_1 = \begin{pmatrix} 0.9509 \\ -0.4809 \\ -0.8223 \\ 0.2715 \\ 0.155 \\ -0.2029 \\ -0.8984 \\ 0.1126 \\ -0.8188 \\ -0.9986 \\ 0.8899 \end{pmatrix}. \quad (7\text{-}34)$$

By substituting Equation (7-34) into Equation (7-13), Y_2 was calculated to be (-0.4649). Meanwhile, the partial derivatives of the nonlinear transfer function and linear transfer function were deduced according to Equation (7-10), as shown below:

$$D_{Z_1Y_1} = \begin{pmatrix} 0.0958 \\ 0.7687 \\ 0.3238 \\ 0.9263 \\ 0.9760 \\ 0.9588 \\ 0.1929 \\ 0.9873 \\ 0.3295 \\ 0.0027 \\ 0.2081 \end{pmatrix}, D_{Z_2Y_2} = 1 \quad (7\text{-}35)$$

Thus, upon substitution of Equation (7-35) into Equation (7-15), the solution of the gradient of the PF can be deduced, as shown below:

$$\nabla g(x^*) = (-0.4868 \quad 0.0616 \quad 0.6598 \quad 0.3367 \quad -0.7688)^T \quad (7\text{-}36)$$

Since $\nabla g(X)$ is the normalized result, the actual value can be derived from inversing normalization, and α_X was obtained according to Equation (7-21) as shown below:

$$\alpha_X = (-0.0002 \quad -0.0024 \quad -0.9780 \quad -0.0007 \quad -0.2087)^T \quad (7\text{-}37)$$

Then the reliability index β is deduced according to Equation (7-22),

$$\beta = 0.2662 \quad (7\text{-}38)$$

After that, the first new x^* was calculated according to Equation (7-23),

$$x^* = (19.0000 \quad 0.0634 \quad 1.1589 \quad 0.0340 \quad 0.6442\ )^T \quad (7\text{-}39)$$

It needs to take a number of iterations until the norm of the difference between the current and last x^* is smaller than the allowable error. The final reliability index was calculated to be $\beta = 1.098$, and the final checking point was:

$$x^* = (20.07 \quad 62.81 \quad 1071.78 \quad 32.76 \quad 691.02\ )^T. \quad (7\text{-}40)$$

It is clear that β exactly coincides with that calculated by ACI 440.1R-06.

7.3.3.3. ANN-based MCS method

One hundred thousand samples of the each design variable were generated according to the statistical characteristics listed in Table 7-4, and were used to form a matrix that would be feed into the trained network as the input vectors. By using the MCS-DS method, the failure probability was easily obtained according to Equation (7-23), in which the samples of the PF less than zero were counted. The final solution was: $p_f = 0.134$, and the corresponding reliability index $\beta = 1.106$. While for the MCS-IS method, by using the x^* in Equation (7-24), the PDF of all samples was calculated according to $f(V_i)/p(V_i)$. Then the final solutions were deduced as: $p_f = 0.135$, and the corresponding reliability index $\beta = 1.105$. Thus, it can be observed that the relative errors of reliability index between the ANN-based MCS-DS and MCS-IS and ACI 440.1R-06 were 0.7% and 0.6%, respectively.

7.4. Designed Graphical User Interface (GUI) System for FRP Bar Anchorage Reliability Assessment

A GUI toolbox in Matlab environment was developed for both development length estimation and the ANN-based reliability analysis, as shown in Figure 7-12 and Figure 7-13. The development length is predicted based on the target reliability index as long as the means and standard deviations of design variables are known. The computational kernel follows the principles demonstrated in Figure 7-10. Figure 7-13 displays the ANN-based reliability analysis, including the ANN-based FOSM, MCS-DS and MCS-IS methods. It mainly consists of five toolbars. The upper toolbar was used for statistical characteristics inputs, referred to preprocessor. The two toolbars located in the middle window were used for parameter settings with regard to the ANN and GA respectively. After running of the program, results are directly plotted from the

buttons located at lower left side. Reliability index using the ANN-based FOSM, MCS-DS and MCS-IS methods will be generated for users.

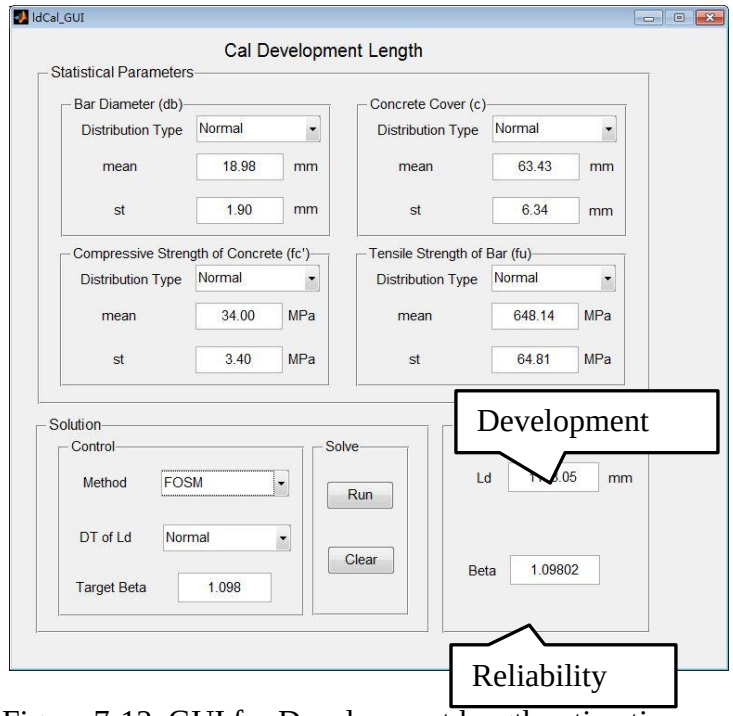

Figure 7-12. GUI for Development length estimation

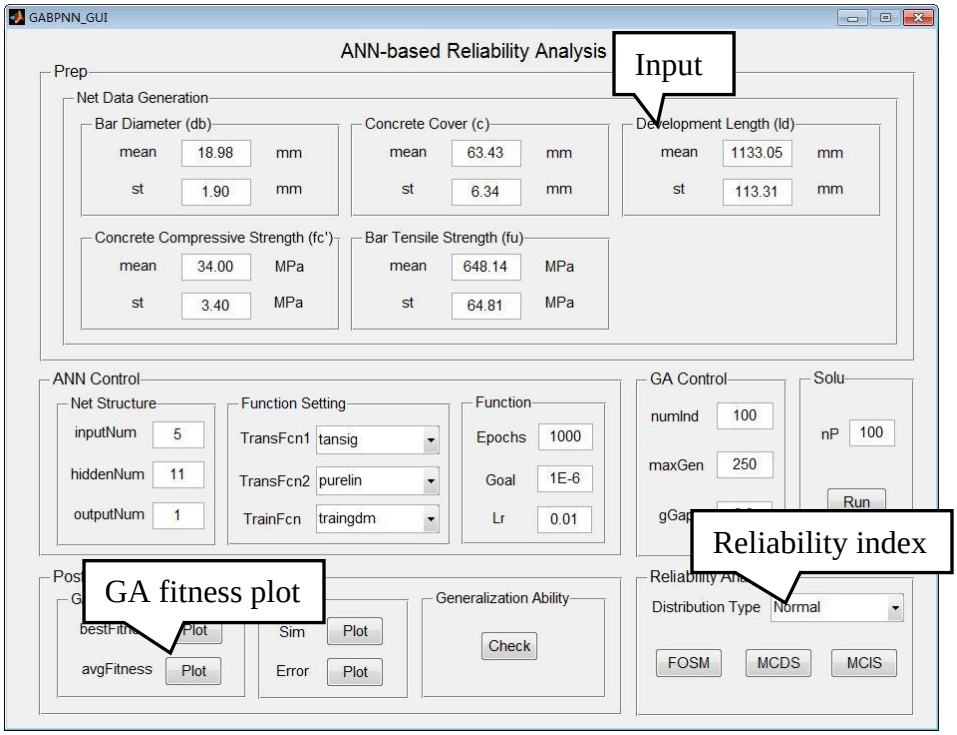

Figure 7-13. GUI for the ANN-based reliability analysis

7.5. Conclusions

This chapter introduced a new strategy for the ANN-based anchorage reliability assessment of GFRP bars to concrete. Some conclusions can be drawn as follows:

(1) The proposed hybrid modeling methodology integrates the respective superiorities of the nonlinear mapping ability of the ANN and global searching ability of GA. It provides an effective way to approximate the PF and solve its partial derivatives in terms of the design variables, yielding higher accuracy over conventional methods. The relative errors between the predicted and actual values of the ANN-GA model reduced within ± 5%. Moreover, the PFs calculated based on ACI 440.1R-06 were observed to be closer to the test results than those calculated based on other codes, where the Canadian design code CSA S6-06 exhibited the largest deviations.

(2) Both analytical formulations and numerical implementations of the ANN-based GFRP bar anchorage reliability analysis were presented in detail. A reasonable targeted reliability index for determining the development length of GFRP bars to concrete was demonstrated to be 1.098, which ensures that the anchorage failure would not occur before the flexural failure during structural service life. Note that the reliability index predicted by the ANN-based FOSM method is 1.098, 1.106 by the MCS-DS method, and 1.105 by the MCS-IS method, respectively. The proposed strategy in this study can also be used to assess both reliability index and required development length for five given design variables of the PF. In addition, the designed GUI system was developed under a Matlab environment based on the proposed modeling strategy, which can be directly applied in practical use.

7.6. References

ACI 408 Committee. (2003). Bond and Development of Straight Reinforcing Bars in Tension (ACI 408R-03). American Concrete Institute, Detroit, Michigan, US.

ACI Committee. (2006). Guide for the design and construction of structural concrete reinforced with FRP bars. ACI 440.1 R, 6.

Akishin, P., Kovalovs, A., Kulakov, V., and Arnautov, A. (2014). Finite element modelling of slipage between FRP rebar and concrete in pull-out test. Paper presented at the The International Scientific Conference „Innovative Materials, Structures and Technologies".

Alshihri, M. M., Azmy, A. M., and El-Bisy, M. S. (2009). Neural networks for predicting compressive strength of structural light weight concrete. Construction and Building Materials, 23(6), 2214-2219.

Aly, R., Benmokrane, B., and Ebead, U. (2006). Tensile lap splicing of fiber-reinforced polymer reinforcing bars in concrete. ACI Structural Journal, 103(6), 857.

Bashir, R., and Ashour, A. (2012). Neural network modelling for shear strength of concrete members reinforced with FRP bars. Composites Part B: Engineering, 43(8), 3198-3207.

Bengio, Y., and LeCun, Y. (2007). Scaling learning algorithms towards AI. Large-scale kernel machines, 34(5).

Benmokrane, B., and Tighiouart, B. (1996). Bond strength and load distribution of composite GFRP reinforcing bars in concrete. ACI Materials Journal, 93(3).

Canadian Standards Association. (2002). Design and construction of building components with fibre-reinforced polymers: Canadian Standards Association.

Canadian Standards Association. (2006). Canadian highway bridge design code: Canadian Standards Association.

Cardoso, J. B., de Almeida, J. R., Dias, J. M., and Coelho, P. G. (2008). Structural reliability analysis using Monte Carlo simulation and neural networks. Advances in Engineering Software, 39(6), 505-513.

Chandwani, V., Agrawal, V., and Nagar, R. (2015). Modeling slump of ready mix concrete using genetic algorithms assisted training of artificial neural networks. Expert Systems with Applications, 42(2), 885-893.

Chau, K. (2007). Reliability and performance-based design by artificial neural network. Advances in Engineering Software, 38(3), 145-149.

Cheng, J., and Li, Q. (2008). Reliability analysis of structures using artificial neural network based genetic algorithms. Computer methods in applied mechanics and engineering, 197(45), 3742-3750.

Chiachio, M., Chiachio, J., and Rus, G. (2012). Reliability in composites–A selective review and survey of current development. Composites Part B: Engineering, 43(3), 902-913.

Daniali, S. (1990). Bond strength of fiber reinforced plastic bars in concrete. Paper presented at the Serviceability and Durability of Construction Materials.

Daniali, S. (1992). Development length for fiber-reinforced plastic bars. Paper presented at the Advanced Composite Materials in Bridges and Structures.

Davalos, J. F., Chen, Y., and Ray, I. (2012). Long-term durability prediction models for GFRP bars in concrete environment. Journal of Composite Materials, 46(16), 1899-1914.

DeFreese, J. M., and Roberts-Wollmann, C. L. (2002). Glass fiber reinforced polymer bars as top mat reinforcement for bridge decks.

Deng, J., Gu, D., Li, X., and Yue, Z. Q. (2005). Structural reliability analysis for implicit performance functions using artificial neural network. Structural Safety, 27(1), 25-48.

Ehsani, M., Saadatmanesh, H., and Tao, S. (1993). Bond of GFRP rebars to ordinary-strength concrete. ACI Special Publication, 138.

Ehsani, M. R., Saadatmanesh, H., and Tao, S. (1996). Design recommendations for bond of GFRP rebars to concrete. Journal of Structural Engineering, 122(3), 247-254.

El Kadi, H. (2006). Modeling the mechanical behavior of fiber-reinforced polymeric composite materials using artificial neural networks—A review. Composite Structures, 73(1), 1-23.

Elhewy, A. H., Mesbahi, E., and Pu, Y. (2006). Reliability analysis of structures using neural network method. Probabilistic Engineering Mechanics, 21(1), 44-53.

Faza, S. S., and GangaRao, H. V. (1991). Bending and bond behavior of concrete beams reinforced with plastic rebars. Transportation Research Record(1290).

Friedman, J., Hastie, T., and Tibshirani, R. (2001). The elements of statistical learning (Vol. 1): Springer series in statistics Springer, Berlin.

Goh, A. T., and Kulhawy, F. H. (2003). Neural network approach to model the limit state surface for reliability analysis. Canadian Geotechnical Journal, 40(6), 1235-1244.

Golafshani, E., Rahai, A., and Sebt, M. (2015). Artificial neural network and genetic programming for predicting the bond strength of GFRP bars in concrete. Materials and Structures, 48(5), 1581-1602.

Golafshani, E. M., Rahai, A., Sebt, M. H., and Akbarpour, H. (2012). Prediction of bond strength of spliced steel bars in concrete using artificial neural network and fuzzy logic. Construction and Building Materials, 36, 411-418.

Gybenko, G. (1989). Approximation by superposition of sigmoidal functions. Mathematics of Control, Signals and Systems, 2(4), 303-314.

Hornik, K., Stinchcombe, M., and White, H. (1990). Universal approximation of an unknown mapping and its derivatives using multilayer feedforward networks. Neural networks, 3(5), 551-560.

Irani, R., and Nasimi, R. (2011). Evolving neural network using real coded genetic algorithm for permeability estimation of the reservoir. Expert Systems with Applications, 38(8), 9862-9866.

Kanakubu, T., Yonemaru, K., Fukuyama, H., Fujisawa, M., and Sonobe, Y. (1993). Bond performance of concrete members reinforced with FRP bars. ACI Special Publication, 138.

Machida, A., and Uomoto, T. (1997). Recommendation for design and construction of concrete structures using continuous fiber reinforcing materials (Vol. 23): Research Committee on Continuous Fiber Reinforcing Materials, Japan Society of Civil Engineers.

Mansouri, I., and Kisi, O. (2015). Prediction of debonding strength for masonry elements retrofitted with FRP composites using neuro fuzzy and neural network approaches. Composites Part B: Engineering, 70, 247-255.

Mosley, C. (2000). Bond performance of fiber reinforced plastic (FRP) reinforcement in concrete. master's thesis, Purdue University, West Lafayette, IN.

Nowak, A. S., and Collins, K. R. (2012). Reliability of structures: CRC Press.

OH, H., SIM, J., and JU, M. (2007). An experimental study for flexural bonding characteristics of GFRP rebar. Paper presented at the Proceedings of the 8th international symposium fiber reinforced polymer reinforcement for concrete structures (FRPRCS–8), University of Patras, Patras.

Papadrakakis, M., and Lagaros, N. D. (2002). Reliability-based structural optimization using neural networks and Monte Carlo simulation. Computer methods in applied mechanics and engineering, 191(32), 3491-3507.

Papadrakakis, M., Papadopoulos, V., and Lagaros, N. D. (1996). Structural reliability analyis of elastic-plastic structures using neural networks and Monte Carlo simulation. Computer methods in applied mechanics and engineering, 136(1), 145-163.

Perera, R., Barch ń, M., Arteaga, A., and De Diego, A. (2010). Prediction of the ultimate strength of reinforced concrete beams FRP-strengthened in shear using neural networks. Composites Part B: Engineering, 41(4), 287-298.

Shield, C., French, C., and Hanus, J. (1999). Bond of glass fiber reinforced plastic reinforcing bar for consideration in bridge decks. ACI Special Publication, 188.

Shield, C., French, C., and Retika, A. (1997). Thermal and mechanical fatigue effects on GFRP rebar-concrete bond. Paper presented at the Proceedings of the 3rd international symposium on non-metallic (FRP) reinforcement for concrete structures (FRPRCS-3), Sapporo.

Suratgar, A. A., Tavakoli, M. B., and Hoseinabadi, A. (2005). Modified Levenberg-Marquardt method for neural networks training. World Acad Sci Eng Technol, 6, 46-48.

Szerszen, M. M., and Nowak, A. S. (2003). Calibration of Design Code for Buildings (ACI 318): Part 2? Reliability Analysis and Resistance Factors. ACI Structural Journal, 100(3).

Tighiouart, B., Benmokrane, B., and Gao, D. (1998). Investigation of bond in concrete member with fibre reinforced polymer (FRP) bars. Construction and Building Materials, 12(8), 453-462.

Tighiouart, B., Benmokrane, B., and Mukhopadhyaya, P. (1999). Bond strength of glass FRP rebar splices in beams under static loading. Construction and Building Materials, 13(7), 383-392.

Varol, T., Canakci, A., and Ozsahin, S. (2013). Artificial neural network modeling to effect of reinforcement properties on the physical and mechanical properties of Al2024–B 4 C composites produced by powder metallurgy. Composites Part B: Engineering, 54, 224-233.

8. CONCLUSIONS AND RECOMMENDATIONS

This dissertation presents both experimental and analytical studies on the GFRP-concrete bond under harsh environmental conditions. The critical durability indices were measured and investigated for the simulated environmental aging tests. Based on the experimental data, the widely used analytical models accounting for the bond development were calibrated by considering environmental effects to better demonstrate GFRP-concrete bond. The study was further extended to GFRP-FRC bond, in which a systematic framework for long-term bond degradation prediction was developed using the Arrhenius relation and TSF method. The bond strength retentions for both GFRP-plain concrete and GFRP-FRC over 75 years of service lifetime was predicted with consideration of different environmental temperatures and relative humidity. Moreover, a bond damage assessment approach in terms of the damage evolution at the GFRP bar-concrete interface was proposed and implemented by FE simulations. In addition, a new strategy using ANN and GA techniques were developed for both bond strength prediction and anchorage reliability assessment for GFRP bars. The contributions and conclusions of this dissertation are summarized in the following.

8.1. Conclusions

8.1.1. Durability Performance and Bond Degradation Prediction

8.1.1.1. Experimental investigation

The durability tests for GFRP-plain concrete specimens considered the environmental conditions of individual and coupled effects of FT cycles and AS solutions on the their durability performance, and we can draw the conclusions as follows.

The combined wreathing of FT cycles and AS solutions was noticed to cause the largest degradation for both concrete and bar-concrete interface. The surface scaling of the specimens

subjected to the coupled FT cycles and AS solution was obvious, where the flaking of the surface mortar and exposure of the coarse aggregate were clearly observed. Also, the weight loss of those coupled conditioned specimens was the largest among all scenarios, with 1.23% and 1.34% for the specimens having $c = 3.0d_b$ and $c = 4.5d_b$, respectively. By comparison, the specimens conditioned with AS solution exhibited minor weight losses, with 0.24% and 0.21% for the specimens having $c = 3.0d_b$ and $c = 4.5d_b$, respectively.

The concrete cover $c = 3.0d_b$ was not sufficient to resist the environmental agents when exposed to weathering including FT cycles (temperatures ranging from -18 ± 2 ℃ and 4 ± 2 ℃), in which all the pullout specimens failed by concrete splitting. In contrast, pullout failure was observed in the specimens having concrete cover $c = 4.5d_b$. Such observations were consistent with the stipulations of ACI 440.1R-06, of which the bond equation accounts for pullout failure by limiting c/d_b to 3.5. On the other hand, the specimens having $c = 3.0d_b$ showed the smallest DF value of 51.21% under the coupled weathering, which requires attention for design considerations.

On the other hand, the durability test for GFRP-FRC specimens revealed that The FRC specimens exhibited distinctly better bond durability than the plain concrete specimens under saline solutions. When the same fiber volume fraction was used, steel fibers demonstrated larger enhancement on bond performance than PVA fibers. The reduction of bond strength due to weathering was about 10% for the steel FRC specimens with fiber contents of 1.0% as compared to 12% for the plain concrete specimens.

8.1.1.2. Analytical investigation

The widely used analytical models accounting for the bond-slip development were calibrated by considering environmental effects and matched well with the experimental results

for both plain concrete and FRC specimens. The curve-fittings using the CMR model performed better than those using the mBPE model. The R^2 values fitted with the CMR model were all greater than 0.98, indicating rather close predictions to the test results. Moreover, from the perspective of design, the average values of the curve-fitting parameters were given. For GFRP-plain concrete considering combined effect of FT cycles and AS solutions, α and p of mBPE model were suggested to be 0.4064 and 0.0897, and s_r and β of CMR model were 0.7365 and 0.7266, respectively. For GFRP-FRC considering the individual saline solutions under 70 ℃, steel FRC with 1.0% of fiber volume fraction, these parameters are suggested to be 0.4379 and 0.0536 for mBPE model, and 0.5954 and 0.7317 for CMR model, respectively.

In addition, the developed procedure for long-term bond degradation prediction based on the Arrhenius relation and the TSF method can be conveniently adjusted to meet conditions of different environmental temperatures and relative humidity. As a case study, the bond strength retentions of both plain concrete and FRC in cold and warm regions were predicted using the developed method. Generally, the FRC demonstrates evident superiority on the bond durability over the plain concrete according to the predictions over 75 years of service lifetime. In particular, the steel FRC with 1.0% of fiber content will have largest bond strength retention. In cold regions with a temperature of 10 ℃, the 75-year bond strength retentions will be 96.76, 92.88, and 74.47% for the dry, moist, and saturated humidity conditions, respectively; while in warm regions under 40 ℃, these predictions will decreased to 95.83, 90.85, and 67.19 %, respectively.

8.1.2. Bond Damage Evolution

A systematic bond damage assessment approach for the GFRP bar-concrete interface was presented in this study. The damage evolution equations are proposed based on the strain

equivalence principle of damage mechanics, where the variations of the secant modulus of the bond-slip curve are utilized to evaluate the interface deterioration against slip. Numerical analyses are conducted with the ANSYS FE program to simulate the bond behavior of pullout test. Nonlinear material behaviors of the GFRP composite and concrete matrix with respect to plain concrete and FRC are implemented using appropriate constitutive models. The interfacial bond-slip behavior is implemented using nonlinear spring elements. Numerical predictions are validated by the experimental results and compared with the widely used analytical models accounting for the FRP-concrete bond.

For both plain concrete and FRC specimens, their damage evolution patterns strictly followed the lognormal distribution and Weibull distribution. Based on this, the respective governing mechanisms for both pre-peak and post-peak bond development were distinguished according to damage evolution stage. It reveals that damage governed the failure progress at the pre-peak bond stage whereas displacement governed the failure progress at the post-peak bond stage. Especially, considering the abrupt features of the bond-slip relation in terms of the descending branch, large displacement usually takes place in the form of brittle failure regardless of the remaining damage that the interface can further sustain.

In addition, the damage evolution curves of GFRP bars having different surface treatment were compared and investigated. The plain concrete specimens with grooved surface displayed more severe damage development than those reinforcing bars with the HW-SC surface. Moreover, the critical bond damage in reference to the grooved surface was much smaller than that in reference to the HW-SC surface, which can be attributed to the smaller slip development for the grooved surface when the bond stress reached the maximum. On the other hand, the damage evolutions of the FRC specimens were smaller than that of the plain concrete specimen,

indicating that the fiber mixture helps to ameliorate the damage evolution. In addition, the critical bond damage of the FRC specimen was smaller than that of the plain concrete specimen, as well as its corresponding slip.

8.1.3. New Strategy for Bond Behavior Modeling and the Application in Practical Use

The hybrid ANN-GA modeling strategy for bond behavior was developed in details. First, the framework of bond strength between GFRP bars and concrete was presented. The prediction results demonstrated apparent optimized effect when compared to the conventional ANN model, where the absolute value of maximum deviation between the test value and predicted value was observed to be 18% in the ANN-GA model, whereas 81% in the ANN model. Meanwhile, the proposed ANN-GA model yield the smaller errors in terms of MAE and RMSE for the training data, validating data, and testing data when compared with MNLR model and design equations, thereby more robust for simulation, overfitting prevention, generalization and comprehensiveness.

This modeling strategy was further extended to anchorage reliability assessment of GFRP bars to concrete. The methodology harnesses not only the strong nonlinear mapping ability in the ANN to approximate the PF and solve its partial derivatives in terms of the design variables, but also global searching ability in the GA to explore the optimal initial weights and biases of the ANN to avoid falling into local minima during the network training. The ANN-based FOSM and MCS methods were first derived. Implementation of the proposed hybrid ANN-GA procedures for GFRP bar anchorage reliability analysis were then achieved by the targeted reliability index and development length. Both the ANN-based FOSM and MCS methods were utilized for determining the reliability index and probability of failure of GFRP bar anchorage. In particular, a reasonable targeted reliability index for determining the development length of GFRP bars to

concrete was demonstrated to be 1.098, which ensures that the anchorage failure would not occur before the flexural failure during structural service life.

8.2. Recommendations

Based on the experimental-analytical results presented in this study, the following recommendations can be drawn for further research:

1. The accelerated aging test carried out in this study mainly considered environmental attack without considering the impact of stress level of GFRP bars on the durability performance. To more approximate the stress conditions of field RC structures, it is necessary to further include different loading levels to correspond to respective strength limit and service limit design. Indeed, tensile and fatigue stresses may lead to microcracks of the resin matrix, which in turn provides access to environmental agents that can degrade the embedded fibers. Thus, future research combining the effects of corrosive agents and sustained loads is encouraged to provide more comprehensive insights. Furthermore, the predictive models for long-term bond degradation should be calibrated accordingly, in order to account for the coupled stress-chemical influences.

2. The developed damage evolution curves have revealed the surface treatment of GFRP bars plays critical role in the bond damage development. Also, GFRP-FRC demonstrates smaller critical bond damage than GFRP-plain concrete. Upon this, GFRP bars embedded in FRC deserve extensive studies on more types of bar surface treatment.

3. The developed hybrid ANN-GA modeling strategy used previous beam test results for the network training, in which the numerical range of transverse reinforcement ratio was limited. In this respect, more experiments need to be conducted to investigate the influences of those factors contributing to bond strength. On the other hand, the ANN-based anchorage reliability

assessment is time invariant reliability analysis that assumes the means and standard deviations do not change with time. The variations of critical time-dependent variables of the PFs, such as the concrete compressive strength and GFRP tensile strength, should be investigated to demonstrate the influences of material degradation over time on the reliability index and probability of failure.